UNIVERSITY OF STRATHCLYDE
DEPARTMENT OF PHYSICS

Radiation generation and high-field physics phenomena in ultra-intense laser-solid interactions

by

Matthew James Duff

in partial fulfilment of the requirements for the degree of Doctor of Philosophy in Physics

2019

Copyright Declaration

This thesis is the result of the author's original research. It has been composed by the author and has not been previously submitted for examination which has led to the award of a degree.

Signed:

Date:

Abstract

This thesis reports on experimental and numerical investigations of the radiation produced via ultra-intense laser-solid interactions. Laser intensities in the range $10^{18} - 10^{24}$ Wcm^{-2} are explored, enabling these interactions to be investigated at current laser facilities (at the lower end of this intensity range), and predictions to be made about the properties of the emitted radiation, which will be measured at upcoming multi-petawatt laser facilities (for which intensities exceeding 10^{23} Wcm^{-2} should be accessible). The associated laser fields have sufficiently strong magnitudes that quantum electrodynamics (QED) effects play a significant role in the interaction. There are two key effects which will be considered within the context of this thesis. The first is prolific production of high energy radiation from electrons that are accelerated by the laser fields. This radiation emission is necessarily accompanied by a back-reaction, or radiation reaction (RR) force. The second key effect is the production of electron-positron pairs, from the interaction of the high energy radiation with the laser fields. These QED effects will, in turn, impact relativistic plasma physics processes, enabling insight to be gained into interactions in the QED-plasma regime. Ion acceleration will be influenced, as well as the production of radiation, which may enable the realisation of ultra-bright radiation sources (with brightness $\sim 10^{24}$ ph$\cdot$s$^{-1}\cdot$mm$^{-2}\cdot$mrad$^{-2}\cdot$(0.1% bandwidth)$^{-1}$) from laser-solid interactions. Exploiting these QED effects will enable exotic states of matter, such as electron-positron pair-plasmas, to be produced in the laboratory enabling, for example, the study of fundamental astrophysical phenomena.

The results presented in this thesis form three distinct studies. The first investigates the process of relativistic self-induced transparency (RSIT) during the interaction of an ultra-intense laser pulse (10^{20} Wcm^{-2}) with an ultra-thin foil target (which is tens of nanometers thick). RSIT is a plasma physics process which is predicted to be heavily influenced by QED effects. During this investigation of RSIT, it was found that the light detected at the rear of ultra-thin foil targets is converted into higher order spatial modes, at both the laser frequency and its second harmonic. It is found that it is possible to produce a radially polarised mode, of high intensity ($\sim 10^{18}$ Wcm^{-2}). Such a mode has applications in the efficient acceleration of electrons and positrons, and in the generation of radiation sources which are optimised in terms of their average photon energy and beam divergence. It is highly difficult to generate these modes at high intensity, using conventional solid-state optics, given their damage thresholds.

The second study is a numerical and analytical investigation of the effects of RSIT and RR on the acceleration of thin foil targets (hundreds of nanometers thick) interacting with ultra-intense laser pulses (10^{23} Wcm^{-2}). It is demonstrated that the magnitude of the RR force is sensitive to the target thickness, thus indicating that it may be possible to control the properties of the emitted radiation, and the partition of laser energy between the plasma species, at upcoming laser facilities. For targets in which the magnitude of the RR force is weak, the emitted radiation is nearly isotropic, whereas for strong RR, distinct peaks appear in the photon angular distribution. Given that the magnitude of the RR force is also reduced by early onset RSIT, it will be possible to diagnose this process via changes in the radiation distribution, at upcoming laser facilities. In this study, an analytical model was developed which, for the first time, describes the target velocity in the light sail regime of radiation pressure acceleration, under the influence of the RR force. The predictions of this model, in terms of the target velocity and the photon conversion efficiency, are found to be in good agreement with numerical simulations.

The final study proposes a multi-stage scheme for the investigation of non-linear pair-production, utilising a laser-solid interaction. By employing numerical modelling, it is demonstrated that this set-up enables an enhancement in the number and energy of positrons produced during ultra-intense laser-solid interactions, compared to conventional experimental set-ups. The first stage is the generation and optimisation of a γ-ray beam (in terms of the average photon energy and divergence half-angle) from an ultra-intense (10^{23} Wcm^{-2}) laser-solid interaction. In the second stage, this beam interacts with dual counter-propagating laser pulses, inducing non-linear pair-production. It is shown that a significant number of positrons are produced by employing this scheme, with an anisotropic energy-angle distribution. This study will assist in the design of future experiments aiming to generate QED plasmas in the laboratory.

Acknowledgements

First and foremost, I would like to express my deepest thanks to my PhD supervisor, Prof Paul McKenna, for providing me with the opportunity to embark on this PhD journey. The work presented in this thesis would not have been possible without with his continued support and guidance. He leads by example, demonstrating the values that any great scientist should possess, and encouraging those around him to achieve their full potential. His patience, kindness and vast knowledge cannot be overstated. I am also extremely grateful to Rémi Capdessus for his encouragement and advice. The work in this thesis has benefited from many vibrant discussions with him. He is a passionate and enthusiastic teacher, and has an unparalleled intuition across a wide range of topics in physics. If I have gained even a fraction of his knowledge, I would count myself extremely fortunate.

The excellence achieved at Strathclyde is the result of a diverse and skilled group of researchers, whom I have had the pleasure of working with. I would like to thank Robbie Wilson, for guiding me through numerous experimental campaigns and for sharing his vast knowledge of experimental physics. This thesis has been enhanced by his feedback and suggestions, for which I am hugely appreciative. I would also like to thank Ross Gray and Martin King for their support in all things Matlab and EPOCH related, and for providing excellent examples of the qualities inherent in the very best researchers. Thanks to Tim, Jonathan, Harry and Nick B for the company and for many interesting physics discussions. In addition I would like to thank many colleagues I have worked with over the years; Adam, Bruno, Chris A, Sam and Zoe, as well as the staff at the Central Laser Facility, and especially Prof David Neely, whose knowledge and expertise have contributed to the success of many experimental campaigns.

I am grateful to have studied at a number of universities leading up to this PhD, and I would like to express my thanks to the many people who have joined me along the way. First, to all my friends in Edinburgh; KB, Andy, Luke and Nick W. Those endless hours spent battling our way through MfP assignments have finally paid off. Thank you all for your companionship, support and many great adventures. In particular I'd like to express my gratitude to KB for teaching me so much over the last eight years, not just physics but also about cooking and the dangers of buying cheap fan heaters. I am also extremely grateful for the inspiration and life advice he has provided, and for being like a brother all these years. Thank you very much to Thomas and Josh at York for their friendship and many great times. It is rare to find anyone with the same affinity for coffee as I have, but in York I managed to find two.

I would also like to offer my sincere thanks to Dario and Chris Ridgers, who I have had the pleasure of collaborating with. Both have provided unique insight and intriguing discussions, which have aided in the work presented in this thesis. I am also thankful to Mohamed Babiker, Brian Pendleton, Joan Simon and Stanislas Pamela, who offered guidance at various stages of this journey and who have inspired me to continue studying.

I am extremely grateful to my parents, Johnnie and Wendy, for the continued support and encouragement they have provided. At every point, they have fostered my intellectual curiosity, whether it be through painstakingly searching for scientifically correct dinosaur models, providing an endless supply of reading material, or taking me on bird-watching weekends. I'd also like to thank my brother, Josh, and grandparents, Tom, Anne, Jack and Betty, for their encouragement through the years. I owe a great deal of gratitude to the Falkners, who have welcomed me into their family and provided immeasurable hospitality. They have also provided vast quantities of coffee and beer which have made this research possible. I am also grateful to Katie for all the baking she has provided, as well as being there to offer advice and support.

The biggest thanks of all goes to my amazing wife, Danielle. She has been there for the highs and lows, offering unconditional love, support and encouragement. I am truly grateful to have a partner who I can share every aspect of my life with; all the places I have studied, lived and traveled to I have been truly lucky to have her by my side. Who would have imagined that so much good fortune could come from a maths tutorial. In short, I could not have completed this PhD without her.

Role of Author

The experimental results presented in this thesis are the result of work by the author, in collaboration with a team of researchers led by Prof Paul McKenna and assisted by the staff at the Central Laser Facility. The author was responsible for the analysis of the experimental data in chapter 5, and played a key role in its interpretation. The author conducted and analysed all of the simulations presented in chapters 6 and 7, and interpreted the results with helpful insight from Dr Rémi Capdessus. In addition, the author made significant contributions to the inception and writing of the publications arising from the research in this thesis.

Chapter 5 - The author played a role in the planning and delivering of the experiment, by assisting Dr Bruno Gonzalez-Izquierdo with the set-up and operation of the Stokes polarimeter. The experiment was executed by Dr Robbie Wilson (TAO) and Dr Adam Higginson (DTAO). The author analysed the corresponding experimental data, and designed and implemented the analysis method employed to interpret the experimental measurements. 3D PIC simulations were performed by Dr Martin King, with input from the author, Dr Bruno Gonzalez-Izquierdo and Prof Paul McKenna. The analysis of the PIC simulations was performed by Dr Martin King and the author. The author played a key role in the conception and writing of the associated publication, in collaboration with Dr Martin King and Prof Paul McKenna.

Chapters 6 and 7 - All 1D and 2D PIC simulations were designed and run by the author. All of the simulation results were analysed and interpreted by the author, under the supervision of Dr Rémi Capdessus and Prof Paul McKenna. The analytical model in chapter 6, and the analytical estimate in chapter 7, were developed by the author in collaboration with Dr Rémi Capdessus. The author played a lead role in the writing and preparation of the corresponding publications.

Publications

Publications directly resulting from the research presented in this thesis

1. **Modelling the effects of the radiation reaction force on the interaction of thin foils with ultra-intense laser fields**
   M. J. Duff, R. Capdessus, D. Del Sorbo, C. P. Ridgers, M. King and P. McKenna, *Plasma Physics and Controlled Fusion*, **60**, 064006 (2018)

2. **Multi-stage scheme for non-linear Breit-Wheeler pair-production utilising ultra-intense laser-solid interactions**
   M. J. Duff, R. Capdessus, C. P. Ridgers and P. McKenna, *Plasma Physics and Controlled Fusion*, **61**, 094001 (2019)

3. **Tunable high power laser mode conversion in relativistic plasma**
   M. J. Duff, R. Wilson, M. King, B. Gonzalez-Izquierdo, R. J. Gray, A. Higginson, S. D. R. Williamson, Z. E. Davidson, R. Capdessus, N. Booth, S. Hawkes, D. Neely and P. McKenna, *Under review* (2019)

Additional publications resulting from this PhD work

4. **Experimental evidence of radiation reaction in the collision of a high-intensity laser pulse with a laser-wakefield accelerated electron beam**
   J. M. Cole, K. T. Behm, E. Gerstmayr, T. G. Blackburn, J. C. Wood, C. D. Baird, **M. J. Duff**, C. Harvey, A. Ilderton, A. S. Joglekar, K. Krushelnick, S. Kushel, M. Marklund, P. McKenna, C. D. Murphy, K. Poder, C. P. Ridgers, G. M. Samarin, G. Sarri, D. R. Symes, A. G. R. Thomas, J. Warwick, M. Zepf, Z. Najmudin and S. P. D. Mangles, *Physical Review X*, **8**, 011020 (2018)

5. **Experimental signatures of the quantum nature of radiation reaction in the field of an ultraintense laser**

   K. Poder, M. Tamburini, G. Sarri, A. Di Piazza, S. Kuschel, C. D. Baird, K. Behm, S. Bohlen, J. M. Cole, D. J. Corvan, **M. J. Duff**, E. Gerstmayr, C. H. Keitel, K. Krushelnick, S. P. D. Mangles, P. McKenna, C. D. Murphy, Z. Najmudin, C. P. Ridgers, G. M. Samarin, D. R. Symes, A. G. R. Thomas, J. Warwick and M. Zepf, *Physical Review X*, **8**, 031004 (2018)

6. **Relativistic Doppler-boosted γ-rays in High Fields**

   R. Capdessus, M. King, D. Del Dorbo, **M. J. Duff**, C. P. Ridgers and P. McKenna, *Scientific Reports*, **8**, 9155 (2018)

7. **Efficient ion acceleration and dense electron-positron plasma creation in ultra-high intensity laser-solid interactions**

   D. Del Sorbo, D. R. Blackman, R. Capdessus, K. Small, C. Slade-Lowther, W. Luo, **M. J. Duff**, A. P. L. Robinson, P. McKenna, Z. M. Sheng, J. Pasley and C. P. Ridgers, *New Journal of Physics*, **20**, 033014 (2018)

8. **A spectrometer for ultrashort gamma-ray pulses with photon energies greater than 10 MeV**

   K. T. Behm, J. M. Cole, A. S. Joglekar, E. Gerstmayr, J. C. Wood, C. D. Baird, T. G. Blackburn, **M. J. Duff**, C. Harvey, A. Ilderton, S. Kuschel, S. P. D. Mangles, M. Marklund, P. McKenna, C. D. Murphy, Z. Najmudin, K. Poder, C. P. Ridgers, G. Sarri, G. M. Samarin, D. R. Symes, J. Warwick, M. Zepf, K. Krushelnick and A. G. R. Thomas, *Review of Scientific Instruments*, **89**, 113303 (2018)

Conference proceedings

9. **Modelling the effect of the radiation reaction force on the acceleration of ultra-thin foils**

   M. J. Duff, R. Capdessus, D. Del Sorbo, C. P. Ridgers, M. King and P. McKenna, *Proceedings of SPIE*, 10241 (2017)

10. **Ion acceleration with radiation pressure in quantum electrodynamic regimes**

    D. Del Sorbo, D. R. Blackman, R. Capdessus, K. Small, C. Slade-Lowther, W.

Luo, **M. J. Duff**, A. P. L. Robinson, P. McKenna, Z. M. Sheng, J. Pasley and C. P. Ridgers, *Proceedings of SPIE*, 10241 (2017)

Contents

List of Figures

Chapter 1

Introduction

Since the discovery of the laser by Theodore Maiman, in 1960 [1], it has proved an invaluable tool in the exploration of high energy density physics (HEDP). Research into HEDP encompasses multiple branches of physics, including plasma physics, nuclear and particle physics, condensed matter physics, and astrophysics. In the context of this thesis, the high energy density system under investigation is the dense, hot plasma formed via the interaction of an ultra-intense laser pulse with a solid target. To illustrate why this constitutes a HEDP environment, consider the definition provided in Ref. [2] which states that a threshold energy density $\geq 10^7$ Jcm^{-2}, is required. The laser pulses considered in this thesis have intensities ranging between 10^{20} and 10^{24} Wcm^{-2}, whilst the current achievable intensity frontier sits at $\sim 10^{22}$ Wcm^{-2} [3]. In addition, these laser pulses have ultra-short duration, of approximately tens of femtoseconds. Taking the example of a pulse at the current intensity frontier, this amounts to delivering an energy density of 30×10^7 Jcm^{-2}, well above the threshold which classifies HEDP phenomena.

Harnessing the physics which occurs at such high energy densities may enable a wide range of potential applications to be realised, such as the development of an abundant source of energy via the process of nuclear fusion. In addition, studies of HEDP may lead to enhanced understanding of aspects of theoretical physics, including the processes which occur in extreme astrophysical phenomena (such as the propagation of shocks from protogalactic structures [4] and generation of cosmic rays [5]), and the theory of non-linear quantum electrodynamics (QED). With lasers at the current intensity frontier, it is possible to explore both of these topics in the laboratory.

1.1 Why laser-solid interactions?

Laser-solid interactions represent a rich sub-field of HEDP, which developed rapidly in the intervening years since the discovery of the laser. The advent of sub-picosecond laser pulses in the late 1960s subsequently led to the observation of a wide range of exotic phenomena within laser-solid interactions. These included; the self-generation of strong magnetic fields, ionisation mechanisms, electron and ion acceleration, neutron production, and the generation of radiation in the form of X-rays, γ-rays, high harmonics and THz emission. It is the process of radiation generation during laser-solid interactions which is of most interest in this thesis.

The dynamics of laser-solid interactions have proved to be highly complex, given that different phenomena emerge at different times throughout the interaction, and these phenomena are further dependent on both the laser and target parameters. Take, for example, the coupling of laser energy to the target. There are multiple mechanisms by which this coupling can occur, depending on the incident laser intensity and target density. In addition, the dominant mechanism may switch during the interaction, depending on the temporal profile of the laser. Nevertheless, the aim of this introduction section is to give the reader an overview of the key processes which occur during laser-solid interactions, and which will be discussed in more detail throughout this thesis.

A good starting point is to build up the interaction from scratch. Laser-solid experiments tend to employ metal targets, such as aluminium foils, due to their ease of manufacture and durability. During the first few cycles of the laser interacting with the foil, the intense laser fields cause ionisation of the target front surface, producing a dense plasma. The thermal pressure within the plasma causes it to expand, resulting in an exponentially decreasing density profile. The spatial extent of the density gradient is known as the scale length, and is an important parameter in determining the dominant mechanism by which the laser energy is coupled into the plasma. The laser then penetrates into the expanding plasma, until it reaches the so-called ‘critical density’. Here, the number density of electrons within the plasma is sufficiently high to reflect the laser pulse, preventing it from propagating any further. There is, however, a short region beyond the critical density, over which the laser fields decay in amplitude exponentially. This is known as the skin depth, and again plays a crucial role in the interaction dynamics. For example, if the target is compressed by the laser to a thickness less than the skin depth, then laser light may appear at the target rear, impacting the dynamics of electrons accelerated through the target.

The interplay between the effects of the scale length, skin depth, and critical density, on the propagation of the laser pulse necessarily lead to a wide range of behaviour. In early laser-solid interactions, employing nanosecond long laser pulses, the increased heating time resulted in long scale lengths, and deposition of the laser energy at, or below, the critical density [6]. In subsequent years, emerging technologies led to a decrease in the laser pulse duration [7, 8]. A consequence of this development was shorter scale lengths, enabling the laser to interact with the peak target density. It was then discovered that the laser resonantly excites electron oscillations around the critical density; some of these electrons are subsequently pushed into the skin depth, where the restoring force of the laser is weaker, enabling them to propagate deep into the plasma [9–12]. This leads to a bulk transfer of laser energy to dense regions of the plasma, which previously could not be accessed with long pulse lasers.

This coupling of laser energy to the plasma species generates a population of energetic electrons, whose temperature scales as a function of the laser irradiance, $I_L\lambda_L^2$, which is the product of the laser intensity (I_L) and wavelength (λ_L) [13, 14]. These hot electrons were at the fore-front of laser-plasma interactions for many years, due to their potential application in the fast ignition approach to inertial confinement fusion. Due to the high energy, and therefore low collisional cross-section of these electrons, it was believed they could be applied to penetrate deep into a compressed hydrogenic target, heating it to the required temperature of $\sim$10 keV necessary to ignite thermonuclear fusion [15, 16]. The acceleration of hot electrons through solid targets induces ion acceleration, by mechanisms such as the target normal sheath acceleration (TNSA) scheme, which has been studied extensively in Refs. [15, 17–19]. In this scheme, a fraction of the hot electrons reach the target rear and subsequently escape, thus leaving a net positive charge. This leads to an accumulation of electrons at the target rear to screen the positive charge, establishing a strong electrostatic sheath field, with a magnitude of TVm^{-1} [20]. This is sufficient, not only to ionise the target rear surface, but also to accelerate ions. These ions are emitted in a highly laminar beam with a wide energy spread [21, 22]. In addition, the spatial distribution of the sheath field means that its magnitude peaks along the laser axis [23, 24]. Thus, the highest energy ions are emitted along the laser axis (the target normal direction), whilst the ion beam as a whole has an energy-dependent divergence. The maximum ion energy achievable using TNSA scales with the square root of the laser irradiance [14], thus it is predicted that ion energies in excess of hundreds of MeV will be generated at upcoming multi-petawatt (PW) laser facilities.

The focus of this thesis is the production of radiation in laser-solid interactions. For the intensities at which TNSA is the dominant ion acceleration mechanism ($10^{18} - 10^{22}$ Wcm^{-2}), this radiation may be generated in the form of high harmonics, coherent synchrotron emission, or terahertz (THz) emission. The interaction of relativistic picosecond (ps) duration pulses with solid targets has demonstrated the generation of XUV and X-ray harmonic radiation, via the relativistic oscillating mirror process [25–28]. Here, the relatively long ps-scale pulse induces a scale length, such that the laser can then drive oscillations at the critical density. The laser light reflecting off this 'oscillating mirror' is strongly Doppler-shifted, leading to the generation of high order harmonics $\gtrsim 100^{th}$ order, which for a 1054 nm laser corresponds to XUV emission [29, 30]. In the case of ultra-short scale lengths, it has been demonstrated that XUV radiation is produced via the process of coherent synchrotron emission [31]. This is caused by the acceleration of nanobunches of electrons through the target, producing a synchrotron-like harmonic spectrum. Finally, the generation of THz radiation, which falls in the frequency range between microwaves and IR in the electromagnetic spectrum, has been demonstrated from laser-solid interactions. This radiation has applications in homeland security, as well as for probing the internal structure of crystals, and as a non-invasive medical imaging technique. There is still debate as to the exact mechanism by which this radiation is produced in laser-solid interactions, however proposed mechanisms include: low frequency emission due to lateral electron transport along the target surface [32, 33], emission caused by the ponderomotively induced space-charge force [34] and coherent emission from electrons accelerated through the target rear surface [35, 36]. Later chapters of this thesis will demonstrate the generation of radiation in the form of higher order transverse electromagnetic modes, at the laser frequency and second harmonic frequency, caused by electron bunches accelerated through a thin foil target.

A promising development in the field of laser-solid interactions is the prospect of directly accelerating targets via radiation pressure from ultra-intense laser pulses. As early as 1966, it was proposed that radiation pressure from a laser could be used to drive a 'sail' to relativistic velocities, offering a means of interstellar transport [37]. It was later discovered that the equation of motion describing such a sail can be applied to the field of laser-solid interactions [38]. There has been substantial interest in using radiation pressure to accelerate ions in recent years, due to the high mechanical efficiency of such a process, and the prospect of generating quasi-monoenergetic ion bunches, which have applications in proton oncology [39] and radiography [40, 41]. In addition, it is predicted that the maximum ion energy in the regime of radiation pressure acceleration (RPA) scales with the laser irradiance, as opposed to the square root of the irradiance as is the case for TNSA. To-date, signatures of RPA have been observed in laser-solid interactions, but for this to become the dominant acceleration mechanism it is necessary to suppress the expansion of the target via the coupling of laser energy to the plasma electrons [42]. The direct acceleration of ions via radiation pressure requires intensities exceeding 10^{24} Wcm^{-2}. At current intensities, the ions are accelerated in the electrostatic fields generated as a result of the electrons being preferentially accelerated by the laser. If RPA is to become the dominant ion acceleration mechanism however, intensities beyond the current frontier will be required. For example, the threshold intensity at which RPA dominates over TNSA is predicted in Ref. [43] to be $\geq 10^{23}$ Wcm^{-2}.

The discussion thus far has only considered interactions in which the solid target remains opaque to the laser throughout the entirety of the interaction. With the advent of relativistic laser pulses, it has become possible for the target to undergo a process known as relativistic self-induced transparency [44–48]. In this case, a combination of relativistic electron motion in the laser fields, and heating of the target during irradiation with an ultra-intense laser pulse, causes a region of plasma within the focal spot of the laser to become transparent to the laser light. The transmitted laser light may then influence the motion of electrons accelerated through the target, enabling some degree of control over the charge contained within the electron bunch, as well as its dynamics [49]. Transparency has become an active area of research in recent years, due to its implications for ion acceleration. It is predicted that this process will limit the efficiency of RPA, given that the laser will penetrate into the target and interact with electrons in the bulk, as opposed to reflecting off the target surface and driving it via radiation pressure. This direct interaction of the laser with the bulk electrons may, however, lead to additional ion acceleration mechanisms which are enhanced by the process of transparency, such as those described in Refs. [50–53]. The onset of transparency during laser-solid interactions is a recurring theme within this thesis. As higher laser intensities are achieved, it will be possible for targets which are initially extremely dense (with electron number density hundreds of times greater than the critical density) to undergo transparency. In addition, this process is predicted to be strongly influenced by quantum electrodynamics (QED) effects [54] for laser intensities $\geq 10^{22}$ Wcm^{-2}. An aim of this thesis is therefore to investigate transparency effects at currently available laser intensities, and to predict how these effects will be impacted by QED at upcoming laser facilities.

1.2 QED effects in laser-solid interactions

At the intensities for which RPA becomes the dominant ion acceleration mechanism, the theory of QED predicts that the emission of high energy radiation will begin to influence the collective electron dynamics within the system. There are two main QED processes which must be considered in the context of laser-plasma interactions; the first is the emission of high energy radiation by accelerating electrons, which is necessarily accompanied by a back-reaction force. The second effect is the production of electron-positron pairs via the interaction of this high energy radiation with either the strong laser fields, or the Coulomb fields from the nuclei of targets with a high mass number. There are two important questions which must now be addressed; when do these QED effects become important, and what is their impact on the laser-plasma interaction?

1.2.1 When do QED effects become important?

To answer this first question, it is necessary to introduce the concept of the QED critical field (sometimes called the Schwinger field, after Julian Schwinger, one of the founding fathers of QED) [55]. This is the field strength at which QED becomes non-linear; the energy density associated with such a field is strong enough to pull electron-positron pairs from the vacuum. This fundamentally changes the properties of the vacuum, such that electromagnetic waves propagating through it may be scattered. This also marks the point at which perturbation theory is predicted to break down, and marks a frontier of our current knowledge of theoretical physics. A simple estimate of the magnitude of the Schwinger field is obtained by equating the work done by the electromagnetic field, over a distance equal to the Compton wavelength, $\bar{\lambda}_c = \hbar/m_e c$, to the rest mass of the electron, $m_e c^2$:

$$E_{Sch} = \frac{m_e^2 c^3}{e\hbar} = 1.6 \times 10^{16} \text{ Vcm}^{-1} \tag{1.1}$$

Equivalently, this can be stated in terms of an intensity, as follows:

$$I_{Sch} = \frac{1}{2}\epsilon_0 c E_{Sch}^2 = 4.6 \times 10^{29} \text{ Wcm}^{-2} \tag{1.2}$$

As discussed, the current intensity frontier sits at around 10^{22} Wcm^{-2}, with upcoming laser facilities expected to achieve focused intensities of $\sim 10^{23}$ Wcm^{-2} within the next few years, and facilities in the distant future planning to produce peak intensities around 10^{25} Wcm^{-2}. Even the highest planned intensities are thus four orders of magnitude below the Schwinger limit, which raises the question of why it is important to study QED effects at the present time.

It has been demonstrated that lasers operating at the current intensity frontier can accelerate electrons up to GeV energies, via the process of laser wakefield acceleration [56, 57]. If these are then collided in a head-on geometry with an ultra-intense laser pulse, the magnitude of the electric field in the electron rest frame is Doppler-shifted, such that the electron experiences a boosted intensity. The importance of QED effects are therefore expressed in terms of a Lorentz invariant parameter, χ_e, which measures the ratio of the magnitude of the electric field in the electron rest frame, to that of the Schwinger field. For a head-on collision between a relativistic electron beam (where the electron energy $\gamma_e m_e c^2$ is characterised by the electron Lorentz factor, γ_e) and an ultra-intense laser pulse, this parameter is expressed in practical units as:

$$\chi_e \sim 0.1 \left(\frac{\gamma_e m_e c^2}{500 \text{ MeV}}\right) \left(\frac{I_L}{10^{21} \text{ Wcm}^{-2}}\right)^{1/2} \tag{1.3}$$

Therefore, during the interaction of a 5 GeV electron beam with a laser pulse at the current intensity frontier, the electric field experienced in the electron rest frame will be the same order of magnitude as the Schwinger field. In principle, it is therefore possible to study non-linear QED effects at present laser facilities. In reality, conducting such an experiment is a difficult task. Both the accelerated electron beam and the colliding laser pulse experience temporal and spatial fluctuations, making it difficult to optimise the overlap between the two, and therefore to maximise the amplitude of QED effects.

A similar effect can be exploited during laser-solid interactions, in order to boost the electric field strength of the laser in the electron rest frame. During the interaction with an initially highly overdense target, the leading edge of an ultra-intense laser pulse is reflected from the target surface, producing a standing wave as it interferes with the remainder of the incoming pulse. Electrons oscillating in this standing wave experience an enhanced intensity, increasing the probability of observing QED effects. In general, higher laser intensities than are available at present are required to observe QED effects in laser-solid interactions, given that the electrons are not accelerated to GeV energies as is the case for beam-beam interactions.

1.2.2 Why are QED effects important in laser-solid interactions?

Having demonstrated that QED effects are important in laser-plasma interactions at the current intensity frontier, it is fitting to discuss the impact of these effects on the plasma dynamics. The immediate consequence of electron oscillations in ultra-intense laser fields is the generation of prolific synchrotron-like radiation. This is emitted in the form of high energy photons, which carry away a significant fraction of the electron energy. As a result of photon emission, a back-reaction force acts on the electron, so-called ‘radiation reaction’ (RR). Numerical studies have demonstrated that RR leads to enhanced coupling of the laser energy into high energy radiation. For example, in Refs. [58, 59] it is predicted that 10% of the laser energy will be converted in to γ-ray radiation during the interaction of a laser pulse at an intensity of 4×10^{23} Wcm^{-2} with thick aluminium foils, which are likely to be employed on experimental campaigns.

This enhanced radiation production comes at the cost of a lower laser-to-ion energy conversion efficiency [60, 61], which may in turn limit the efficiency of laser-induced ion acceleration mechanisms, such as RPA. For thick targets, RR is known to reduce the target velocity, a result which was demonstrated in Refs. [62, 63]. Thus RR is predicted to slow the scaling of the maximum ion energy with increasing laser intensity in the RPA regime. This has important consequences for proposed applications of ion acceleration, such as proton oncology, which requires ion energies in the range 200-250 MeV [64].

The radiation produced in ultra-intense laser-solid interactions is typically of high enough energy to induce electron-positron pair-production. To-date, pair-production has been observed via the scattering of such high energy photons off the Coulomb fields of high-Z nuclei. It will be possible to probe more fundamental pair-production mechanisms at upcoming laser facilities, in which the high energy γ-ray photons interact directly with the laser fields. Pair-production means that the laser energy is increasingly coupled to electrons and positrons, again reducing the laser-to-ion energy conversion efficiency. In Ref. [58], it is predicted that at a laser intensity of 10^{24} Wcm^{-2}, up to 40% of the laser energy is converted to γ-rays, with a further 10% converted into electron-positron pairs. The impact of pair-production on ion acceleration mechanisms within thick targets was demonstrated theoretically in Ref. [65] and later demonstrated numerically in Ref. [66]. These studies suggest that the production of a dense pair-plasma at the laser-target interface shields the target from the peak laser fields, therefore reducing the efficiency of ion acceleration. It is proposed that the ion energy is reduced by up to 50% for an incident intensity of 5×10^{24} Wcm^{-2} [66]. There is also the possibility that the electron-positron pairs produced in laser-solid interactions will emit further high energy photons as they are accelerated in the laser fields, which then trigger additional pair-production events. This process is known as an electromagnetic cascade, and is perhaps the most troubling QED effect for the future development of ultra-intense laser pulses. This process may place a limit on the maximum achievable intensity, given that it is predicted to rapidly deplete a laser pulse with intensity approaching the Schwinger limit, and can be seeded from a single electron accelerated within the fields of an ultra-intense laser pulse [67].

1.2.3 Applications of QED processes in laser-solid interactions

Potential applications of the aforementioned QED processes which occur in laser-solid interactions are discussed in this final section. Whilst the enhanced coupling of laser energy to high energy radiation is detrimental to ion acceleration mechanisms, it opens up a range of new applications for ultra-intense laser-solid interactions. The synchrotron-like radiation emitted during such interactions is in the form of a compact beam, with an opening angle inversely proportional to the Lorentz factor of the radiating electrons. The divergence of such a beam can be further reduced through the application of strong, self-generated magnetic fields within the target, such that a divergence half-angle $\leq 10°$ may be achieved (an idea which is explored further in chapter 7). In addition, the average energy of photons within the emitted γ-ray beam may be enhanced via the relativistic Doppler effect, which can be tuned via the choice of laser and target parameters. Thus laser-solid interactions can be employed to generate sources of radiation with a brightness of $\sim 10^{24}$ ph$\cdot$s$^{-1}\cdot$mm$^{-2}\cdot$mrad$^{-2}\cdot$(0.1% bandwidth)$^{-1}$ [68, 69]. This brightness is comparable to conventional synchrotron sources, however the average photon energy ($\sim$10 MeV) is an order of magnitude higher. It is possible that the radiation generated via laser-solid interactions could edge in on the territory of conventional synchrotron sources, with potential applications including: macro-molecular imaging, structural analysis of stress and strain in materials, and non-destructive probing of palaeontological and archaeological samples [70].

These bright γ-ray beams can also be exploited to investigate pair-production mechanisms. Whilst pair-production is, again, detrimental to the efficiency of ion acceleration, it is a research topic of great importance in the fields of theoretical physics and astrophysics, for example. The collision of two of the aforementioned γ-ray beams, at a high angle of incidence, may enable the first observation of pair-production via the linear Breit-Wheeler process [71, 72], which is important in the dynamics of active galactic nuclei, stellar winds, and pulsars. Alternatively, the interaction of such a γ-ray beam with counter-propagating laser pulses may generate electron-positron plasmas with a sufficiently high density that collective effects can be observed, thus enabling laboratory astrophysics experiments to be conducted [4, 73]. Such experiments may aim to address fundamental questions in astrophysics, such as determining the mechanism by which γ-ray bursts occur in neutral electron-positron plasmas, and investigating the generation of cosmic rays from Fermi acceleration within such a plasma [5].

1.3 Thesis outline

The unifying theme of this thesis is the generation of radiation via laser-solid interactions. The results of both experimental and numerical investigations of the properties of this radiation are presented. These studies cover a range of laser intensities and target thicknesses; from experimental investigations at current laser intensities (10^{20} Wcm^{-2}) with ultra-thin foils, through to numerical studies of the interaction of ultra-intense laser pulses ($\geq 10^{23}$ Wcm^{-2}) with micron thick slabs of plasma. The structure of this thesis is as follows:

- **Chapter 2 -** Explores the dynamics of a single electron moving in an electromagnetic field, including QED effects such as RR and pair-production.

- **Chapter 3 -** Investigates the collective electron dynamics, and the propagation of electromagnetic waves, within a plasma.

- **Chapter 4 -** The experimental and numerical tools employed to obtain the data presented in this thesis are described, along with a review of the technology which will enable upcoming, ultra high intensity laser facilities to be realised.

- **Chapter 5 -** The first results chapter of this thesis details experimental and numerical investigations of relativistic transparency and mode conversion in the light detected at the rear of ultra-thin foils, interacting with laser pulses at intensities of $\sim 10^{20}$ Wcm^{-2}. The key result of this chapter is the demonstration of high intensity, radially polarised mode generation, at the laser second harmonic frequency.

- **Chapter 6 -** A numerical and analytical investigation of RR and relativistic transparency effects during the acceleration of thin-foil targets, at intensities of 10^{23} Wcm^{-2}, is presented. It is found that the magnitude of the RR force is highly sensitive to the target thickness, such that the properties of the emitted radiation, and the target dynamics, may be controlled.

- **Chapter 7 -** The properties of the radiation emitted via the interaction of an ultra-intense laser pulse with a thick plasma slab are explored, leading to the generation of a compact γ-ray beam. This beam then interacts with dual counter-propagating laser pulses, in various geometric configurations, to induce non-linear pair-production. This two-stage interaction scheme is demonstrated to produce a higher number of positrons, with an anisotropic energy-angle distribution, compared to conventional configurations.

- **Chapter 8 -** Finally, the results of chapters 5, 6 and 7 are summarised, and potential future work is discussed, including the possibility of experimentally testing the predictions of chapters 6 and 7 at upcoming multi-PW laser facilities.

Chapter 2

Theory: Single electron motion in electromagnetic fields

2.1 Classical electrodynamics

Describing ultra-intense laser-plasma interactions, in terms of the collective electron dynamics within the electromagnetic fields of a laser is a difficult task. It is often more informative to first consider the relatively simple case of a single electron moving in an electromagnetic plane wave, which will be the focus of this chapter. The relevant equations are then Maxwell's equations, which describe the generation of electric and magnetic fields from sources of charges and current density, and the Lorentz force equation of motion, which describes the motion of a charged particle in an electromagnetic field. The starting point is to write down Maxwell's equations, as follows:

$$\nabla \cdot \mathbf{E} = \frac{\rho}{\epsilon_0} \tag{2.1}$$

$$\nabla \cdot \mathbf{B} = 0 \tag{2.2}$$

$$\nabla \times \mathbf{E} = -\frac{\partial \mathbf{B}}{\partial t} \tag{2.3}$$

$$\nabla \times \mathbf{B} = \mu_0 \mathbf{j} + \mu_0 \epsilon_0 \frac{\partial \mathbf{E}}{\partial t} \tag{2.4}$$

First, Eqn. (2.1) describes the generation of an electric field from a source of charge density, ρ, where ϵ_0 is the vacuum permittivity. Eqn. (2.2) represents the conservation of magnetic flux, whilst Eqn. (2.3) describes the relation between spatially varying electric fields and temporally varying magnetic fields. Finally Eqn. (2.4) shows how electric current leads to the generation of magnetic fields, where μ_0 is the vacuum permeability.

The motion of a charged particle in an electromagnetic field is described by the Lorentz force equation of motion, which is written:

$$\frac{d\mathbf{p}}{dt} = q(\mathbf{E} + \mathbf{v} \times \mathbf{B}) \tag{2.5}$$

where $\mathbf{v}$ and q denote the velocity and the charge of the particle, respectively. The momentum is given by $\mathbf{p} = \gamma m_e \mathbf{v}$, where m_e is the mass (in this case the electron mass), $\gamma = (1 - \boldsymbol{\beta}^2)^{-1/2}$ is the Lorentz factor, and $\boldsymbol{\beta} = \mathbf{v}/c$ is the velocity normalised to the speed of light. From Eqn. (2.5), the $\mathbf{v} \times \mathbf{B}$ term can be neglected in the case where $v \ll c$, such that the electron undergoes oscillations in the direction of the electric field. The $\mathbf{v} \times \mathbf{B}$ force introduces a drift term to the electron motion, which becomes significant as $v \to c$, and is described in detail in section 2.1.2.

Maxwell's equations can be reformulated as a wave equation, whose solutions are electromagnetic waves which propagate at a characteristic speed, $c = (\epsilon_0 \mu_0)^{-1/2}$, which also turns out to be the speed of light. This can be shown by taking the curl of Eqn. (2.3), as follows:

$$\nabla \times (\nabla \times \mathbf{E}) = -\frac{\partial}{\partial t}(\nabla \times \mathbf{B}) \tag{2.6}$$

$$\nabla(\nabla \cdot \mathbf{E}) - \nabla^2 \mathbf{E} = -\frac{\partial}{\partial t}(\nabla \times \mathbf{B}) \tag{2.7}$$

To obtain solutions for waves propagating in vacuum, it is assumed that there is no charge or current density. Substitution of Eqns. (2.1) and (2.4) into the above expression yields the following wave equation:

$$\nabla^2 \mathbf{E} = \frac{1}{c^2} \frac{\partial^2 \mathbf{E}}{\partial t^2} \tag{2.8}$$

This equation may be solved using the method of characteristics, such that the general solution (in 1D) is a superposition of functions of the form $f(x, t) = f(x \pm ct)$, traveling in the positive and negative directions. A particular solution to Eqn. (2.8) is the plane wave. This is a monochromatic wave (i.e. composed of a single frequency), whose amplitude is described by sinusoidal oscillations, and whose wave fronts are infinite, parallel planes. A 3D plane wave solution may be written as follows:

$$\mathbf{E}(\mathbf{r},t) = \mathbf{E}_0 \cos(\mathbf{k}\cdot\mathbf{r} - \omega t - \psi) \tag{2.9}$$

where $\mathbf{r}$ is the Cartesian position vector and $\mathbf{E}_0$ is the amplitude of the wave. The direction of wave propagation is defined by the wave vector, $\mathbf{k}$, whose magnitude is given by $|\mathbf{k}| = 2\pi/\lambda$. The angular frequency of the wave is ω, the wavelength is λ, and the term ψ is a phase shift. It is typically easier to manipulate the plane wave solutions by expressing them using the polar representation. This produces the following solutions to Maxwell's equations (in Fourier space), which describe the propagation of electric and magnetic waves in vacuum:

$$\mathbf{E}(\mathbf{r},t) = \mathbf{E}_0 \exp[i(\mathbf{k}\cdot\mathbf{r} - \omega t - \psi)] \tag{2.10}$$

$$\mathbf{B}(\mathbf{r},t) = \mathbf{B}_0 \exp[i(\mathbf{k}\cdot\mathbf{r} - \omega t - \psi)] \tag{2.11}$$

In the above expressions, the amplitudes of the fields are related to the real parts of $\mathbf{E}(\mathbf{r},t)$ and $\mathbf{B}(\mathbf{r},t)$. From the plane wave solutions, it is possible to determine the relative orientation and magnitudes of the electric and magnetic fields. Substituting the plane wave solutions into Maxwell's equations (in vacuum) yields:

$$i\mathbf{k}\cdot\mathbf{E} = 0 \quad \text{and} \quad i\mathbf{k}\cdot\mathbf{B} = 0 \tag{2.12}$$

$$i\mathbf{k}\times\mathbf{B} = \frac{-i\omega}{c^2}\mathbf{E} \quad \Rightarrow \quad |\mathbf{B}| = \frac{|\mathbf{E}|}{c} \tag{2.13}$$

where the wave vector is expressed in terms of the unit normal vector, such that $\mathbf{k} = k\hat{\mathbf{n}}$. From Eqn. (2.12) it is clear that the electric and magnetic fields are mutually perpendicular, and also perpendicular to the direction of wave propagation, whilst Eqn. (2.13) indicates that the magnitude of the magnetic field is weaker than that of the electric field, by a factor c.

Finally, it is useful to define the intensity of an electromagnetic wave, which is given by the Poynting vector, $\mathbf{S}(\mathbf{r},t) = \mathbf{E}\times\mathbf{B}/\mu_0$. This vector describes the intensity in terms of the instantaneous values of the electric and magnetic fields, which, in the case of a laser pulse, vary sinusoidally over a laser period. It is therefore more useful to average the Poynting vector over a laser cycle, which provides the average intensity.

Substituting the real parts of Eqns. (2.10) and (2.11) into the Poynting vector yields:

$$|\mathbf{S}(\mathbf{r},t)| = \frac{|\mathbf{E}_0|^2}{\mu_0 c}\cos^2(\mathbf{k}\cdot\mathbf{r} - \omega t - \psi) \tag{2.14}$$

Averaging this over a laser cycle, $\langle\cos^2(x)\rangle = \frac{1}{2\pi}\int_0^{2\pi}\cos^2(x)dx = 1/2$,yields $\langle|\mathbf{S}|\rangle = I_L = \epsilon_0 c E_0^2/2$, where I_L is the laser intensity. The magnitude of the electric field is typically normalised using the parameter a_0, defined as follows:

$$a_0 = \frac{eE}{m_e c\omega} \sim \frac{v_{osc}}{c} \tag{2.15}$$

where v_{osc} is the velocity of electron oscillations in the laser field. The relation $a_0 \sim v_{osc}/c$ only holds for non-relativistic motion, where the contribution from the $\mathbf{v}\times\mathbf{B}$ force is negligible. From this relation, however, it is immediately clear that the electron motion becomes relativistic when $a_0 \geq 1$. This condition can be re-stated as:

$$a_0 = \frac{e}{m_e c\omega}\left(\frac{2I_L}{\epsilon_0 c}\right)^{1/2} \sim 0.85\left(\frac{I_L\lambda^2[\mathrm{Wcm}^{-2}\mu\mathrm{m}^2]}{1.37\times10^{18}}\right)^{1/2} \geq 1 \tag{2.16}$$

The above condition defines a threshold irradiance ($I_L\lambda^2$), beyond which the electron motion becomes relativistic. The threshold also depends on the incident laser polarisation; for linear polarisation, averaging over a laser period results in a reduction of the a_0 value by a factor $\sqrt{2}$ compared to circular polarisation.

2.1.1 Polarisation of plane waves

A key property of light which can, for example, be used to infer information about laser-plasma interactions, is the polarisation. The aim of chapter 5 is to measure the polarisation state of the light detected at the rear of ultra-thin foil targets, whilst the influence of polarisation on high-field physics effects, such as radiation reaction and pair-production, is explored in chapters 6 and 7. It is therefore necessary to introduce the concept of polarisation in this section, and describe how it affects the motion of electrons.

The polarisation of a plane wave describes the orientation of the electric field oscillations. Light is considered to be polarised if the electric field oscillations are confined to the same plane during propagation of the wave. On the other hand, for unpolarised light the electric field oscillates in many different directions, and can thus be considered a superposition of many randomly oriented polarised waves. The total electric field vector for an unpolarised wave therefore changes direction (outwith the polarisation plane) rapidly throughout the course of its propagation. To describe the polarisation state of light, consider an orthogonal basis, in which the wave vector is aligned with the x axis. It follows from Eqn. (2.12) that the electric field only has components in the y-z plane, the so-called 'polarisation plane'. For any point along the wave propagation direction, the total electric field is then composed of two orthogonal components, described as follows:

$$\mathbf{E}(\mathbf{r},t) = E_{0,y}\cos(\phi+\phi_y)\hat{\mathbf{y}} + E_{0,z}\cos(\phi+\phi_z)\hat{\mathbf{z}} \tag{2.17}$$

where $\phi = \mathbf{k}\cdot\mathbf{r} - \omega t$ is the phase, and $\phi_y - \phi_z$ describes the difference in phase between the two components of the electric field. The amplitudes of these two components are given by $E_{0,y}$, $E_{0,z}$, and are related by the following trigonometric identity (for more details see Ref. [74]):

$$\sin^2(\phi_y - \phi_z) = \left(\frac{E_y}{E_{0,y}}\right)^2 + \left(\frac{E_z}{E_{0,z}}\right)^2 - 2\left(\frac{E_y}{E_{0,y}}\right)\left(\frac{E_z}{E_{0,z}}\right)\cos(\phi_y - \phi_z) \tag{2.18}$$

where $E_y = E_{0,y}\cos(\phi+\phi_y)$, with E_z defined in the same way. The polarised wave is then described by two key parameters; the ratio of the magnitudes of the two electric field components, and their relative phase. From Eqn. (2.18), it can be seen that the total electric field vector traces out an ellipse in the polarisation plane, the so-called 'polarisation ellipse'. The polarisation state is then quantified by the ratio of the semi-minor to the semi-major axis (which is related to the ratio of the magnitudes of the electric field components), and the angle between the semi-major axis and one of the axes in the polarisation plane. This ellipse is illustrated in Fig. 2.1.

In general, the semi-minor and semi-major axes of the polarisation ellipse will be rotated through some angle, θ, with respect to the axes of the polarisation plane. In this case, it is useful to express the electric field components with respect to the rotated co-ordinates (y′ and z′), as shown in Eqns. (2.19) and (2.20), below.

$$E_y = E'_y\cos\theta - E'_z\sin\theta \tag{2.19}$$

$$E_z = E'_y\sin\theta + E'_z\cos\theta \tag{2.20}$$

The rotation angle can subsequently be expressed in terms of the ratio of the amplitudes

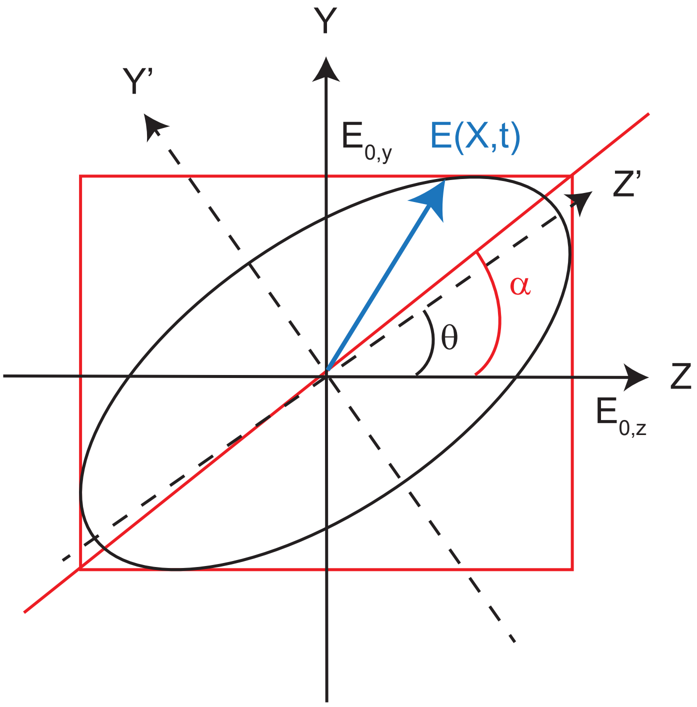

Figure 2.1: Representation of polarised light using the polarisation ellipse. The key parameters of the ellipse are related to the ratio of the magnitudes of the two electric field components in the polarisation plane, and their relative phase.

of the field components, $\alpha = E_{0,y}/E_{0,z}$, such that $\tan 2\theta = \cos(\phi_y - \phi_z)\tan 2\alpha$. Any polarisation state which can be visualised using the aforementioned ellipse is referred to as elliptically polarised, however there are two special cases which are frequently referred to in this thesis. The first is linear polarisation, in which $(\phi_y - \phi_z) = 0$ or $n\pi$. The elliptical relationship described by Eqn. (2.18) then becomes linear, and the characteristic angles are related by $\theta = \alpha$. Thus the electric field vector oscillates purely along the semi-major axis of the ellipse, as illustrated in Fig. 2.2 (b). The second case of interest is when the magnitude of the two electric field components are equal, and the relative phase between these components is $(\phi_y - \phi_z) = n\pi/2$. The total electric field vector therefore traces out a circle in the polarisation plane, leading to circular polarisation. Again, this is illustrated in Fig. 2.2 (c).

2.1.2 Single electron motion in a plane wave

It is now possible to describe the motion of a single electron oscillating in a polarised, electromagnetic plane wave, propagating along the positive x axis. The motion is described by a combination of the Lorentz force equation (Eqn. (2.5)) and the relativistic

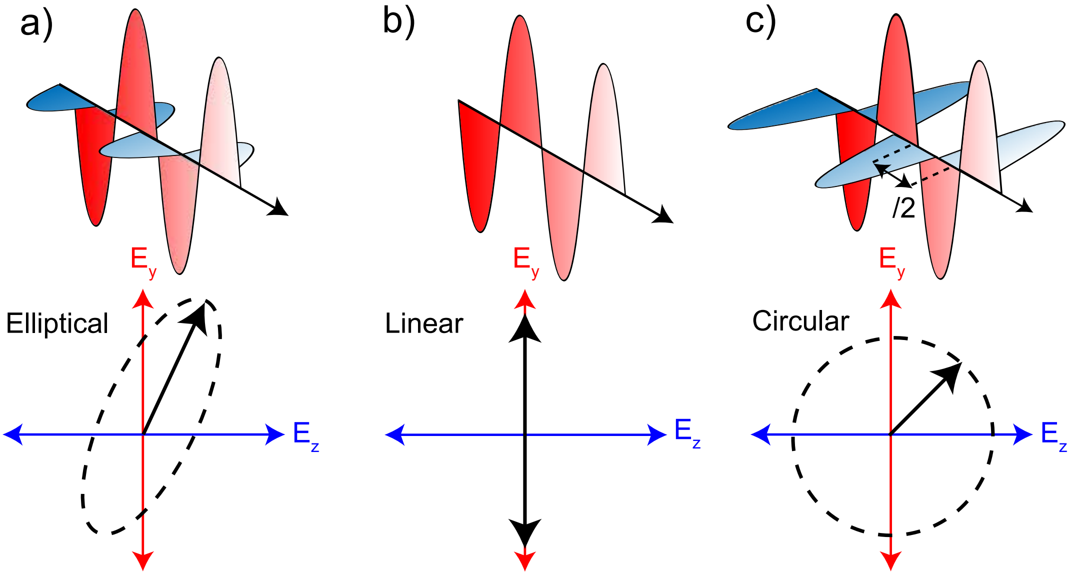

Figure 2.2: Illustration of elliptical polarisation (a), and two special cases, linear (b) and circular (c) polarisations. The representation of these states is additionally illustrated using the polarisation ellipse.

energy equation, which is obtained by taking the scalar product of Eqn. (2.5) with the electron velocity.

$$\frac{1}{2}\frac{d}{dt}(\gamma m_e \mathbf{v}^2) = -e(\mathbf{v}\cdot\mathbf{E}) \tag{2.21}$$

The electric field in which the electron oscillates is described in terms of the vector potential, as follows:

$$\mathbf{A} = (0, \delta a_0 \cos\phi, (1-\delta^2)^{1/2} a_0 \sin\phi) \tag{2.22}$$

where $a_0 = eE/m_e c\omega$ is the normalised amplitude of the laser vector potential, and δ is a term which describes the polarisation state, such that $\delta = 0$ corresponds to linear polarisation along the z axis, $\delta = \pm 1$ corresponds to linear polarisation in the y axis, and $\delta = \pm 1/\sqrt{2}$ describes the circular right and left handed polariation states. The symbol ϕ denotes the phase.

The electromagnetic fields are expressed in terms of the vector potential, such that $\mathbf{E} = -\partial\mathbf{A}/\partial t$ and $\mathbf{B} = \nabla\times\mathbf{A}$. It is also important to note that in the proceeding analysis, the momenta are normalised, such that $p \equiv |\mathbf{p}|/m_e c$, and the vector potential is similarly normalised to $A \equiv e|\mathbf{A}|/m_e c$. Following the method presented in Ref. [6], the first step in determining the electron motion is to decompose the Lorentz force and energy equations into the longitudinal (along the x axis) and transverse (in the

y-z plane) components. Such a decomposition is useful as it enables the motion in the polarisation plane to be decoupled from the motion along the wave propagation direction. Starting with the transverse equation, the magnetic field components are:

$$\mathbf{B} = \left(0, -\frac{\partial A_z}{\partial x}, \frac{\partial A_y}{\partial x}\right) \tag{2.23}$$

Leading to the following expression for the transverse Lorentz force:

$$\frac{dp_\perp}{dt} = \frac{\partial A}{\partial t} - v_x\frac{\partial A_y}{\partial x} - v_x\frac{\partial A_z}{\partial x} \tag{2.24}$$

Integrating this equation provides the first constant of motion, $p_\perp - A = c_1$. Subsequently, the second constant of motion is obtained by simultaneously solving the energy and longitudinal Lorentz force equations. These are written as follows:

$$\frac{d\gamma}{dt} = -v_y\frac{\partial A_y}{\partial t} - v_z\frac{\partial A_z}{\partial t} \tag{2.25}$$
$$\frac{dp_\parallel}{dt} = v_y\frac{\partial A_y}{\partial x} + v_z\frac{\partial A_z}{\partial x} \tag{2.26}$$
$$\frac{d\gamma}{dt} - \frac{dp_\parallel}{dt} = -v_y\left(\frac{\partial A_y}{\partial t} + \frac{\partial A_y}{\partial x}\right) - v_z\left(\frac{\partial A_z}{\partial t} + \frac{\partial A_z}{\partial x}\right) \tag{2.27}$$

Subtracting Eqn. (2.26) from (2.25) yields Eqn. (2.27), above. Given that the electric field is a plane wave propagating along the x direction, it follows that $(x - ct)$ is a constant, and the right hand side of Eqn. (2.27) vanishes. This enables the second constant of motion to be determined by integrating the left hand side, such that $\gamma - p_\parallel = c_2$. Using the definition of the normalised relativistic momentum, $\gamma^2 = 1 + p_\perp^2 + p_\parallel^2$, this relation may be re-written:

$$p_\parallel = \frac{1 - c_2^2 + p_\perp^2}{2c_2} \tag{2.28}$$

To evaluate the trajectory of the electron, in the laboratory frame of reference, the constants of motion are first determined by the initial conditions. It is assumed that the particles start from rest, such that $c_1 = 0$ and $c_2 = 1$. The set of equations describing the momenta, in the laboratory frame of reference (denoted by subscript *lab*), are as follows:

$$p_{x,lab} = \frac{a_0^2}{4}(1 + \cos 2\phi(2\delta^2 - 1)) \tag{2.29}$$

$$p_{y,lab} = \delta a_0 \cos\phi \tag{2.30}$$

$$p_{z,lab} = (1 - \delta^2)^{1/2} a_0 \sin\phi \tag{2.31}$$

which can be integrated to yield expressions for the electron trajectory in the laboratory frame of reference.

$$x_{lab} = \frac{a_0^2}{4}\left[\phi + (2\delta^2 - 1)\frac{\sin 2\phi}{2}\right] \tag{2.32}$$

$$y_{lab} = \delta a_0 \sin\phi \tag{2.33}$$

$$z_{lab} = -(1 - \delta^2)^{1/2} a_0 \cos\phi \tag{2.34}$$

There are a number of interesting points to note about the above sets of equations. First examining the set of equations describing the momenta, it is clear that the longitudinal momentum is proportional to a_0^2, whilst the transverse momentum is proportional to a_0. Looking to the equations which describe the electron trajectory, Eqn. (2.32) shows that the electron motion in the longitudinal plane oscillates at twice the frequency of the motion in the polarisation plane. Another interesting feature of this equation is that it has a non-oscillatory component. This term is proportional to ϕ, and therefore grows with time, leading to a drift of the electron along the propagation direction. The trajectory described by the above equations is plotted in Fig. 2.3 for increasing values of the electric field strength (normalised to a_0). The electric field in Fig. 2.3 is linearly polarised in the y direction, however it is clear that the same motion arises in the x-z plane if the electric field is instead linearly polarised in the z axis.

Since the electron position drifts in the laboratory frame of reference, it is often convenient to evaluate the electron motion in its rest frame. To achieve this, the longitudinal momentum is set to zero and the drift motion necessarily vanishes; this amounts to setting $p_{\|} = 0$ in Eqn. (2.28), and $c_1 = 0$, such that the second constant of motion becomes $c_2 = 1 + A^2$. From this expression, the vector potential is averaged over a laser period, so the oscillating terms may be simplified to $\langle\cos^2\phi\rangle = 1/2$. It is then assumed that, since the electric field is linearly polarised, $c_2 = \gamma \sim \sqrt{1 + a_0^2/2}$. This enables the relation between the longitudinal and transverse momenta to be expressed

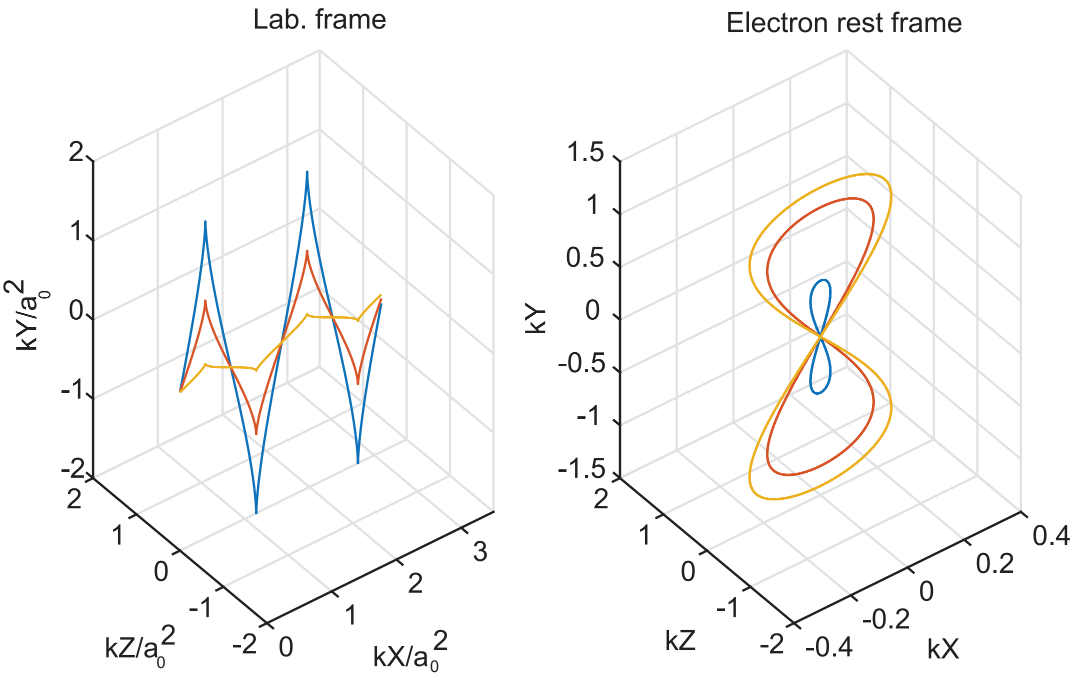

Figure 2.3: Plot of the trajectory of a single electron moving in a linearly polarised plane wave, in the laboratory frame (left) and the electron rest frame (right). The colours correspond to a_0 *values of 0.5 (blue), 1 (orange) and 5 (yellow). Note that due to the normalisation used in the left hand plot, the trends appear to reverse between the two reference frames.*

as:

$$p_{\|} = \frac{p_{\perp}^2 - a_0^2/2}{2\gamma} \tag{2.35}$$

The trajectories in the rest frame (denoted by a subscript, *rest*) are then obtained by integrating Eqn. (2.35), producing the following set of equations:

$$x_{rest} = \left(\delta^2 - \frac{1}{2}\right)\frac{a_0^2}{4\gamma^2}\sin 2\phi \tag{2.36}$$

$$y_{rest} = \frac{a_0}{\gamma}\sin\phi \tag{2.37}$$

$$z_{rest} = -\frac{a_0}{\gamma}(1-\delta^2)^{1/2}\cos\phi \tag{2.38}$$

For the case of a linearly polarised electric field, such that $\delta = 1$, the trajectory in the electron rest frame is the well-known figure-of-eight trajectory, which drives oscillations along the propagation direction, at twice the wave frequency. This is illustrated in Fig. 2.3 for a range of a_0 values. If the plane wave is instead circularly polarised, the trajectory in the rest frame is simply a circular orbit.

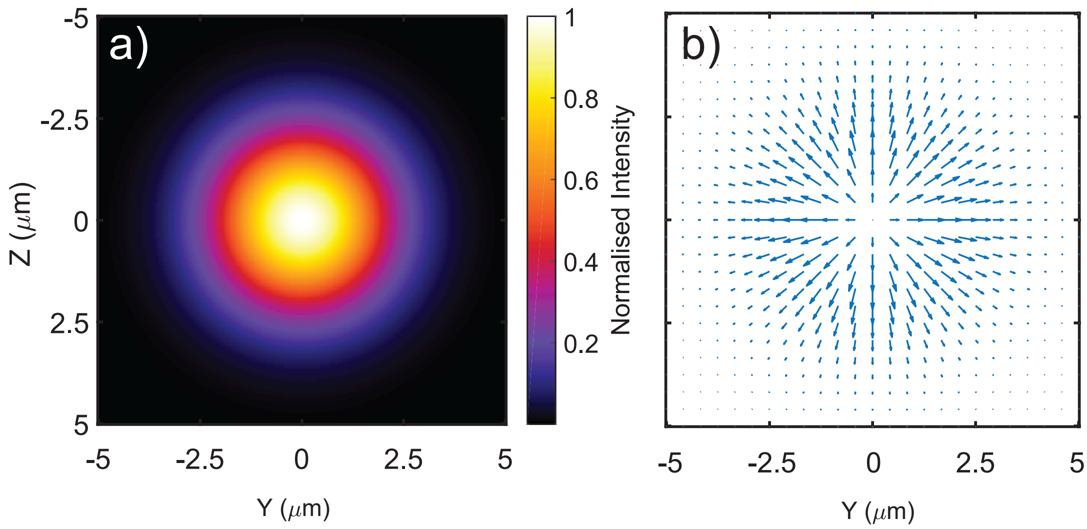

Figure 2.4: Plot of the spatial intensity distribution of a fundamental Gaussian (TEM_{00}) mode, normalised to its maximum value. (b) Illustration of the ponderomotive force exerted by the TEM_{00} mode. The arrows indicate the magnitude and direction of the ponderomotive force, which pushes electrons from regions of high to low intensity.

2.1.3 The ponderomotive force

The preceeding section detailed the motion of a single electron in an electromagnetic plane wave. However, the electric fields associated with realistic laser pulses have finite spatial and temporal profiles, which give rise to steep gradients in the intensity [75–78]. These gradients are particularly important in the case of tight focusing, and short (femtosecond duration) laser pulses, leading to the rapid ejection of electrons from the laser focal spot. The effects of these gradients in the spatial distribution of the laser intensity will be explored in this section.

During the interaction of a single electron with a spatially homogeneous plane wave, the electron will oscillate in the plane of the electric field, always returning to its starting position at the end of the wave cycle. In this configuration, it is not possible for the electron to gain net energy from the laser [79, 80]. However, if the laser electric field is spatially inhomogeneous, the situation is very different. During the initial interaction, the electron oscillates in the polarisation plane, where the ponderomotive force pushes it into a region of lower intensity. At this position, when the laser fields reverse direction, the restoring force on the electron is weaker than it was at its starting position, due to the spatial gradient in the electric field. The electron therefore does not return to its starting position, and can gain net energy from the laser pulse. This effect accumulates over the course of many laser cycles, with the electron being pushed into regions of progressively weaker field strength, resulting in an overall drift of the electron out of the laser focal spot, where the fields are strongest.

It has been proposed that the ponderomotive force can be employed as an electron acceleration mechanism, as opposed to merely inducing a drift in the electron velocity. For example, in Ref. [81] it is demonstrated that the component of the ponderomotive force along the laser propagation direction drives electrons from the focal spot, such that they can gain net energy from the laser. For an $a_0 \geq 1$, energy gains of $\geq$MeV can be realised. However, this study assumes that the Rayleigh range of the laser is much larger than the focal spot size, therefore enabling the effect of a changing beam waist to be neglected. In Ref. [82], an additional case is considered in which the focal spot is comparable in size to the laser wavelength. This leads to the same MeV gain in electron energy, which is found to scale linearly with a_0 for $a_0 \geq 2$. The ponderomotive force can be therefore be employed as an acceleration mechanism, such that tightly focused laser pulses may generate MeV electrons in a forwards directed beam.

In the non-relativistic case, the average energy associated with an electron oscillating in a laser field, over the course of a laser period, is the so-called 'quiver potential', written as follows:

$$U_p = \frac{1}{2} m_e v_{osc}^2 = \frac{e^2}{2 m_e \omega_L^2} \langle E^2 \rangle \tag{2.39}$$

where $v_{osc} = eE/m_e\omega_L$ is the velocity of electron oscillations in the laser electric field and ω_L is the laser frequency. An expression for the ponderomotive force is then obtained by taking the gradient of the quiver potential:

$$\mathbf{F}_p = -\frac{e^2}{2 m_e \omega_L^2} \langle \nabla \mathbf{E} \cdot \mathbf{E} \rangle = -\frac{e^2}{4 m_e \omega_L^2} \langle \nabla E^2 \rangle \tag{2.40}$$

The above expression demonstrates that the ponderomotive force is independent of the sign of the charge, however it is inversely proportional to the mass of the particle under consideration, and is therefore much weaker for ions compared to electrons. It is also important to note that Eqn. (2.40) does not take into account the motion which arises due to the influence of the magnetic field on the electron, and is therefore restricted to the non-relativistic regime. In the relativistic formulation, the ponderomotive potential is written $U_p = m_e c^2 \langle \gamma \rangle$. This leads to the following expression for the relativistic ponderomotive force [6, 83–85]:

$$\mathbf{F}_p = -\frac{dU_p}{dt} = -m_e c^2 \nabla \gamma \tag{2.41}$$

A consequence of the drift acquired by a relativistic electron is that it has components of its motion in the longitudinal and transverse directions, resulting in the ejection of the electron from the laser focal spot at an angle with respect to the propagation direction of the laser. This ejection angle is obtained from energy conservation, as follows. The relativistic kinetic energy of the electron when it leaves the focal spot is $E_k = (\gamma - 1)m_e c^2$, which is equal to the kinetic energy imparted to the electron via interaction with n photons of the laser, with energy $\hbar\omega_L$. In the longitudinal direction, this yields:

$$p_{\parallel} = n\hbar\omega_L/c = (\gamma - 1)m_e c \tag{2.42}$$

Then, using the condition derived in Eqn. (2.28), the ejection angle is calculated as follows:

$$\tan\theta = \frac{p_\perp}{p_\parallel} = \sqrt{\frac{2}{\gamma - 1}} \tag{2.43}$$

Given that the average electron Lorentz factor is related to the temporal intensity profile of the laser, both the ponderomotive force and the ejection angle also have a temporal dependence. An illustration of the ponderomotive force is provided in Fig. 2.4, in which the spatial intensity profile of a Gaussian pulse is plotted in panel (a). The arrows in panel (b) indicate the magnitude and direction of the resulting ponderomotive force; it is clear that an electron initially located at the origin will be pushed towards regions of weaker fields.

2.2 Radiation from accelerating charges

It is well established that the acceleration of charged particles leads to the generation of radiation [86, 87]. Perhaps the first demonstration of this principle was the discovery of X-rays from electrons accelerated through evacuated glass tubes (or Crookes tubes, which will be discussed again in the context of the discovery of plasmas) by Rontgen in 1895 [88]. The generation of radiation from accelerating charges has many applications, from the broadcasting of radio waves in the case of low energy radiation, to the probing of the structure of matter using synchrotron radiation, in the case of high energy

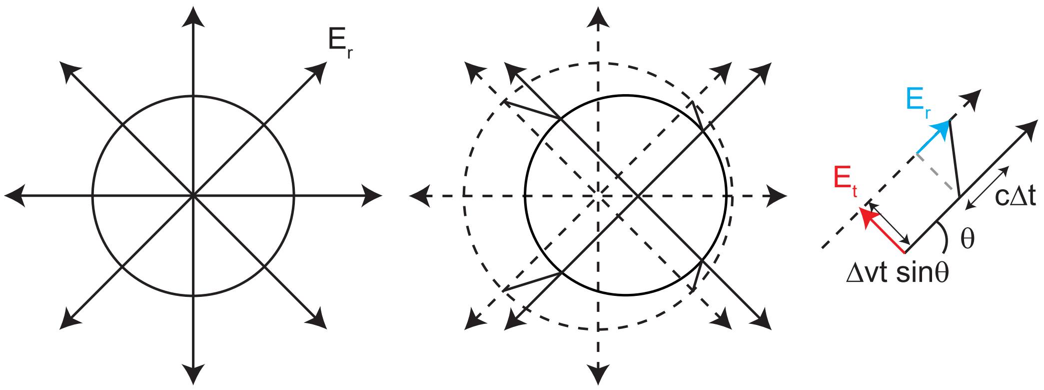

Figure 2.5: Illustration of the generation of radiation from an accelerating charge. Initially at rest, the field lines extend radially outwards from the charge. As the charge accelerates during a time interval Δt, the field lines which are at a distance greater than cΔt remain unchanged. The discontinuity in the field lines produces a tangential component of the electric field, and leads to the emission of radiation. Adapted from Ref. [91].

radiation.

A rigorous mathematical description of this process is typically obtained using the method prescribed by Liénard and Wiechart [89, 90], in which the fields associated with an accelerating point charge, with some motion relative to a distant observer, are expressed in terms of retarded potentials (see, for example, Ref. [86]). A less rigorous, but more intuitive description is provided in this section, following the arguments provided in Ref. [91].

The starting point here is to consider a charged particle, initially at rest. The electric field lines extend radially outwards from the location of the charge, with the magnitude of the field at some radial distance r given by $E_r = q/4\pi\epsilon_0 r^2$. If the charge now accelerates over a time interval, Δt such that it gains a velocity Δv, a pulse of electromagnetic radiation will be generated. The field lines move along with the charge, however the information that the charge has accelerated (and hence that the field lines have moved) can only propagate out to a distance $c\Delta t$. At distances greater than this, the field lines remain unperturbed, corresponding to the configuration of the charge at rest. The field lines must be continuous, in which case there will be some region in which they are perturbed, as seen in Fig. 2.5. Since the field lines are bent, in a region of radial extent $c\Delta t$, there will be components of the electric field in both the radial and tangential directions, denoted E_r and E_t, respectively. The ratio of the fields is as follows:

$$\frac{E_t}{E_r} = \frac{t\Delta v \sin\theta}{c\Delta t} = \frac{r|a|\sin\theta}{c^2} \tag{2.44}$$

where $|a|$ is the magnitude of the acceleration and $t = r/c$. The angle θ is the angle between the observer and the direction of acceleration. The tangential field is then obtained by substituting the radial field into the above expression, yielding:

$$E_t = \frac{q|a|\sin\theta}{4\pi\epsilon_0 r c^2} \tag{2.45}$$

The temporal variation of the tangential field as the charge continues to accelerate leads to the generation of a magnetic field in the perpendicular direction. This production of electromagnetic radiation has an associated energy flux, described by the Poynting vector. The magnitude of the Poynting vector is $|\mathbf{S}| = |\mathbf{E} \times \mathbf{B}/\mu_0|$, where the relevant field components are E_t and $B_\perp = E_t/c$. The magnitude of the Poynting vector describes the flux of electromagnetic energy through an area $r^2 d\mathbf{\Omega}$ subtending a solid angle, $d\mathbf{\Omega}$, at a distance r along the radial direction. The associated power of the emitted radiation, P_γ, is written:

$$P_\gamma r^2 d\mathbf{\Omega} = \frac{q^2|a|^2\sin^2\theta}{16\pi^2\epsilon_0 c^3 r^2} r^2 d\mathbf{\Omega} \tag{2.46}$$

where, to be explicit, P_γ is associated with a loss of energy by the electron. It is then possible to obtain the total radiated power by integrating over the area, subtended by solid angle $d\mathbf{\Omega}$, and associated with the change $\theta \to \theta + d\theta$. In this case $d\mathbf{\Omega} = 2\pi \sin\theta d\theta$, such that:

$$P_\gamma = \int_0^{2\pi} \frac{q^2|a|^2\sin^2\theta}{16\pi^2\epsilon_0 c^3} 2\pi \sin\theta d\theta = \frac{q^2|a|^2}{6\pi\epsilon_0 c^3} \tag{2.47}$$

The total radiated power is a Lorentz invariant parameter. The covariant expression of Eqn. (2.47) is then obtained by replacing the acceleration vector with the corresponding 4-vector (see appendix for more details). The square of the 4-acceleration is invariant under a Lorentz transformation, meaning that it does not depend on the observer's frame of reference. The square of the 4-acceleration in the observer's reference frame, a^2, is equated with the same quantity in the rest frame of the charge, s^2, (in which it is assumed the zeroth component is negligibly small) as follows:

$$-s^2 = \left(\frac{\mathbf{v}\cdot\mathbf{a}}{c}\right)^2 \gamma^8 - \left[\gamma^2 \mathbf{a} + \left(\frac{\mathbf{v}\cdot\mathbf{a}}{c^2}\right)\gamma^4 \mathbf{v}\right]^2 \tag{2.48}$$

which yields the result:

$$s^2 = \gamma^4\left(\mathbf{a}^2 + \gamma^2\left(\frac{\mathbf{v}\cdot\mathbf{a}}{c}\right)^2\right) \tag{2.49}$$

Finally, replacing a^2 with s^2 in Eqn. (2.47) (i.e. substituting in the square of the 4-acceleration in the rest frame of the charge), and noting that $a^\mu = dv^\mu/d\tau$, gives the covariant formulation of the radiated power [92]:

$$P_\gamma = \frac{q^2}{6\pi\epsilon_0 c^3}\left(\frac{dv^\mu}{d\tau}\cdot\frac{dv^\mu}{d\tau}\right) \tag{2.50}$$

$$= \frac{q^2}{6\pi\epsilon_0 c^3}\gamma^4\left(\mathbf{a}^2 + \gamma^2\left(\frac{\mathbf{v}\cdot\mathbf{a}}{c}\right)^2\right) \tag{2.51}$$

2.2.1 Radiation from a charge accelerating in a constant magnetic field

The radiation of most interest in this thesis is the synchrotron radiation generated by charged particles accelerating in magnetic fields (see section 4.3.3 for details on why synchrotron radiation is dominant over Bremsstrahlung radiation in simulations of laser-plasma interactions). To describe the generation of synchrotron radiation, it is easiest to start from the simple case of a charge accelerating in a constant magnetic field [86, 91]. The relativistic equation of motion is written:

$$\frac{d}{dt}(\gamma m_e \mathbf{v}) = q(\mathbf{v}\times\mathbf{B}) \tag{2.52}$$

$$m_e\gamma\frac{d\mathbf{v}}{dt} + m_e\mathbf{v}\left(\frac{\mathbf{v}\cdot\mathbf{a}}{c}\right)\gamma^3 = q(\mathbf{v}\times\mathbf{B}) \tag{2.53}$$

To obtain the second equation, the relativistic momentum is differentiated via the product rule, and the following result substituted: $\frac{d\gamma}{dt} = (\mathbf{v}\cdot\mathbf{a}/c)\gamma^3$. During the motion of a charge in a constant magnetic field, the velocity and acceleration are always perpendicular, and so the second term on the left of Eqn. (2.53) vanishes. The equation of motion can then be separated into its perpendicular and transverse components:

$$m_e\gamma\frac{dv_\parallel}{dt} = qvB\cos\theta_p = 0 \tag{2.54}$$

$$m_e\gamma\frac{dv_\perp}{dt} = qvB\sin\theta_p = qv_\perp B \tag{2.55}$$

Here, $\theta_p = \arctan(v_\parallel/v_\perp)$ is the pitch angle, i.e. the angle between the particle velocity and the magnetic field [91]. From Eqn. (2.54), it is clear that the charge moves along the magnetic field direction with a constant velocity. In the perpendicular direction, Eqn. (2.55) shows that the charge accelerates as it completes circular orbits around the magnetic field line. The radius of this orbit is obtained by equating $dv_\perp/dt$ with the centripetal acceleration, yielding the Larmor radius, $r_L = \gamma m_e v_\perp / qB$. The total motion of the charge is then a helical path, centered around the magnetic field direction.

To obtain the radiated power in this case, it is necessary to decompose the square of the 4-acceleration into its parallel and perpendicular components, as follows:

$$\mathbf{a}^2 + \gamma^2(\mathbf{v}\cdot\mathbf{a})^2 = |a_{||}|^2 + |a_\perp|^2 + \gamma^2(va_{||}/c)^2 \tag{2.56}$$

$$= |a_\perp|^2 + |a_{||}|^2\gamma^2 \tag{2.57}$$

If there is no parallel acceleration (as in the case of Eqn. (2.54)), then the expression for the synchrotron radiated power is obtained by substituting $a_\perp = q|v|B\sin\theta_p/m_e\gamma$ into Eqn. (2.47). The radiated power is then written:

$$P_\gamma = \frac{q^4\gamma^2B^2}{6\pi\epsilon_0c^3m_e^2}v^2\sin^2\theta_p \tag{2.58}$$

There are a few important points to note about the emission of synchrotron radiation. Due to the $\sin^2\theta_p$ term in the expression for the radiated power, the distribution of the radiated power in the rest frame of the accelerating charge is in the form of a symmetric dipole. In the context of electron acceleration in ultra-intense laser fields, the electrons acquire relativistic velocities, and so a Lorentz transformation must be applied to view the radiation in the reference frame of the observer. This transformation means the radiation experiences a significant relativistic aberration, in which case it appears beam-like in the frame of the observer. The radiation is viewed when the velocity of the electron points along the line of sight of the observer, such that it is contained within a cone of opening angle $\theta \sim 1/\gamma$, and thus it appears as a brief pulse.

2.2.2 The synchrotron radiation spectrum

Deriving the spectrum of the synchrotron radiation emitted from a charged particle is a task which requires a more rigorous approach than the quantitative description provided in the previous section. Full details of the derivation of the synchrotron spectrum are provided, for example, in Refs. [86, 93]. Here, the key aspects of the spectrum will be highlighted.

In theoretical descriptions of laser-plasma interactions, it is common practice to assume that the laser field can be treated as a constant, static background field, over the time scale of the radiation emission. Under this assumption, it is possible to take the background field to be a static magnetic field [94–97]. The advantage of this approach is that the rate of photon emission from an electron radiating in such a field is well known within the context of astrophysics. As such, the synchrotron spectrum can be obtained by first considering the rate of photon emission from an electron accelerating in a constant magnetic field, which is given in Refs. [65, 98] as:

$$\frac{d^2N_\gamma}{d\chi_\gamma dt} = \frac{\sqrt{3}\alpha c}{\lambda_c}\frac{cE}{B}\frac{F(\chi_e,\chi_\gamma)}{\chi_\gamma} \tag{2.59}$$

where α is the fine structure constant and λ_c is the Compton wavelength. The parameters χ_e and χ_γ parameterise the electron and photon energies, respectively, and are described in detail in section 2.3.2. The most important aspect for this discussion is the function, $F(\chi_e,\chi_\gamma)$, the so-called 'quantum synchrotron function', which describes the shape of the radiated photon spectrum. This function is defined in Refs. [98, 99] and written as follows:

$$F(\chi_e,\chi_\gamma) = \frac{4\chi_\gamma^2}{\chi_e^2}yK_{2/3}(y) + \left(1-\frac{2\chi_e}{\chi_\gamma}\right)y\int_y^\infty K_{5/3}(x)dx \tag{2.60}$$

where $y = 4\chi_\gamma/[3\chi_e(\chi_e-2\chi_\gamma)]$ and K denotes a Bessel function of the second kind. The quantum synchrotron function only has values when $0<\chi_\gamma<\chi_e/2$, which is equivalent to the condition that the energy of the emitted photon must be less than the energy of the radiating electron. This can be seen more clearly by stating that, assuming the photon is emitted along the direction of the electron momentum, the quantum parameters are related as follows: $\chi_e \sim \chi_\gamma\hbar\omega_\gamma/\gamma m_e c^2$. The aforementioned restriction on the energy of the emitted photon leads to a hard cut-off in the energy spectrum, which is illustrated in Fig. 2.6.

In the above discussion, the quantum nature of the photon spectrum is considered, i.e. the radiation is assumed to be composed of a finite number of photons. If instead, a large number of incoherent photons are emitted, it is possible to describe the radiation using a semi-classical description, in which the radiating electron emits a large number of photons in a continuous process. The semi-classical regime applies when $\chi_\gamma \ll \chi_e<1$,

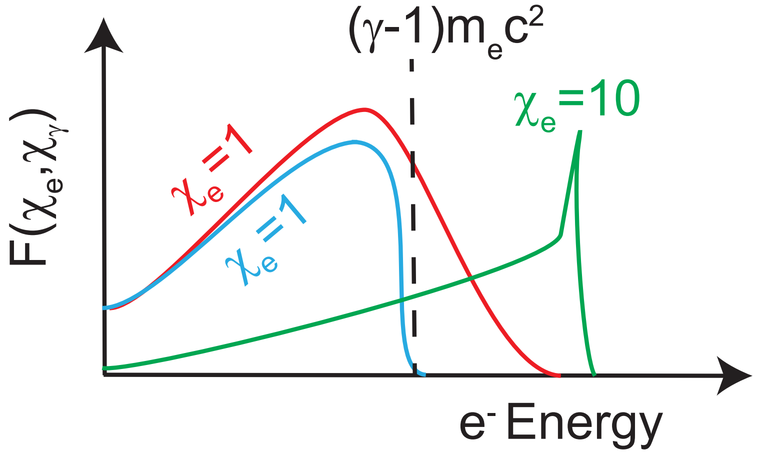

Figure 2.6: Illustration of the classical and quantum synchrotron functions, for a range of χ_e *values. The red curve is the classical synchrotron function, plotted for a radiating electron with* $\chi_e = 1$. *The blue curve is the quantum synchrotron function for the same* χ_e *value. Finally, the green curve is the quantum synchrotron function for an electron with* $\chi_e = 10$.

such that the classical synchrotron function may be approximated as [98]:

$$F_{cl} = y_c \int_{y_c}^{\infty} K_{5/3}(x)dx \tag{2.61}$$

where $y_c \equiv \frac{\omega}{\omega_{cr}}$, such that ω_{cr} is the critical frequency (or peak) of the spectrum. This is related to the frequency of electron oscillations in the laser field (ω_r) or, in this equivalent geometry, the frequency of the electron oscillations in the constant background magnetic field, such that $\omega_r = |\mathbf{p}_e \times \mathbf{F}_L|/\mathbf{p}_e^2$ and $\mathbf{F}_L$ is the Lorentz force. The critical and rotation frequencies are related by $\omega_{cr} = (3/2)\omega_r\gamma_e^2$. Thus the semi-classical synchrotron function may be written:

$$F_{cl} = \frac{2}{3}\frac{\omega|\mathbf{p}|^2}{\gamma_e^3|\mathbf{p} \times \mathbf{F}_L|} \int_{\omega/\omega_{cr}}^{\infty} K_{5/3}(x)dx \tag{2.62}$$

The semi-classical synchrotron function predicts higher photon energies than the quantum function, given that there is no cut-off in energy. These differences are illustrated in Fig. 2.6, for various energy values of the radiating electron, and their consequences will be discussed further in section 2.3.2. For classical descriptions of the radiation it makes sense to consider the spectral intensity of the emitted radiation, as opposed to the number of photons emitted into a given energy range as in Eqn. (2.59). The intensity of the synchrotron radiation emitted by a single electron, per unit frequency and solid angle, denoted by I_γ, is given by:

$$\frac{dI_\gamma}{d\omega d\mathbf{\Omega}} = \frac{P_\gamma}{\omega_{cr}} \delta\left(\mathbf{\Omega} - \frac{\mathbf{p}_e}{|\mathbf{p}_e|}\right) F_{cl} \tag{2.63}$$

The delta function in Eqn. (2.63) ensures that the synchrotron radiation is emitted into a narrow cone, pointing along the direction of the electron momentum, with an opening angle of $\sim 1/\gamma$, as was discussed in the previous section. Finally, the term P_γ is the radiated power from a single electron, which is written:

$$P_\gamma = \frac{2\alpha c}{3\bar{\lambda}_c} m_e c^2 \chi_e^2 \tag{2.64}$$

2.3 Radiation reaction

It has been demonstrated in section 2.1.2 that the motion of an electron in an electromagnetic field is described by the Lorentz force equation of motion, Eqn. (2.5). Whilst the acceleration of charged particles within an electromagnetic field has been shown to generate radiation, the Lorentz force equation of motion does not account for the radiated power of the electron, which is expected to affect its trajectory. The loss of energy as a result of radiation emission may be interpreted, in the classical framework, as a back-reaction (or friction) force acting on the electron. Note that the terminology 'back-reaction' refers to the fact that the radiation emitted by the electron subsequently affects its own motion. This back-reaction force is referred to as the radiation reaction (RR) force [86, 100, 101] throughout this thesis.

Obtaining an equation of motion for a radiating electron, which self-consistently accounts for the loss of energy via photon emission, remains an outstanding problem in electrodynamics [102–104]. Whilst many such equations have been posed over the years, many of these predict unphysical behaviour, or fail to account for the quantum nature of photon emission. In this section, a brief history of the equations of motion which attempt to describe RR are presented; from the first formulation by Dirac [100], through to the widely accepted Landau-Lifshitz equation [101]. Excellent review articles on RR can be found in Refs. [104, 105].

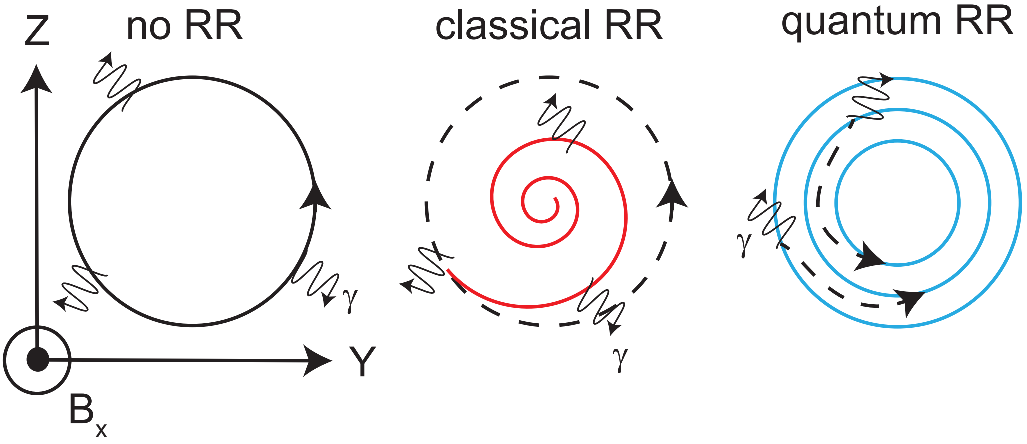

Figure 2.7: Illustration of the trajectory of an electron in a constant magnetic field, comparing the cases with no RR (black), classical RR (red) and quantum RR (blue). The small curved lines indicate the emission of photons.

2.3.1 The classical radiation reaction force

First, consider the dynamics of an electron in an ultra-intense laser field, such that $a_0 \gg 1$. In this case, the photon formation length (the spatial extent of the region in which radiation is produced, given by $\ell_{photon} \sim \lambda_L/a_0$) is assumed to be small relative to the laser wavelength [65, 106, 107]. As discussed, the emission of radiation leads to the exertion of a back-reaction, or RR force, on the electron. Its trajectory then depends on both the Lorentz force, and the RR force, as follows [104]:

$$m_e\mathbf{a} = -e(\mathbf{E}_{ext} + \mathbf{v} \times \mathbf{B}_{ext}) + \mathbf{F}_{RR} \tag{2.65}$$

where $\mathbf{E}_{ext}, \mathbf{B}_{ext}$ refer to the external electromagnetic fields, in this case associated with the laser, and $\mathbf{F}_{RR}$ is the RR force. For now, only the non-relativistic formulation is considered.

The RR force term can be evaluated by applying the principle of energy conservation, i.e. the total power radiated by an electron over a given time interval must be equal to the work done by the RR force. The electron radiated power is given by $P_\gamma = m_e\tau_r|\mathbf{a}|^2$, where $\tau_r = e^2/6\pi\epsilon_0 m_e c^3 \sim 6.2 \times 10^{-24}$ s is the radiation time, a parameter which corresponds to 2/3 the time it takes for light to cross the classical electron radius. Energy conservation leads to the following equation:

$$\int_{t_0}^{t_1} \mathbf{F}_{RR} \cdot \mathbf{v}dt = -\int_{t_0}^{t_1} P_\gamma dt \tag{2.66}$$

Substituting the above expression for P_γ, and integrating the right hand side, yields the following expression:

$$-m_e\tau_r\int_{t_0}^{t_1}\frac{d\mathbf{v}}{dt}\cdot\frac{d\mathbf{v}}{dt}dt=-m_e\tau_r\left[\frac{d\mathbf{v}}{dt}\cdot\mathbf{v}\right]_{t_0}^{t_1}+m_e\tau_r\int_{t_0}^{t_1}\frac{d\mathbf{a}}{dt}\cdot\mathbf{v}dt \tag{2.67}$$

If it is then assumed that the motion is periodic, for example, evaluated at the start and end of the interaction with an electromagnetic wave, then the first term on the right vanishes and Eqns. (2.66) and (2.67) are combined to give:

$$\int_{t_0}^{t_1}\left(\mathbf{F}_{RR}-m_e\tau_r\frac{d\mathbf{a}}{dt}\right)\cdot\mathbf{v}dt=0 \tag{2.68}$$

From the above it is clear that $\mathbf{F}_{RR}=m_e\tau_r\frac{d\mathbf{a}}{dt}$. This leads to a non-relativistic formulation of the electron motion, known as the Lorentz-Abraham equation [108, 109], given below.

$$m_e\mathbf{a}=-e(\mathbf{E}_{ext}+\mathbf{v}\times\mathbf{B}_{ext})+m_e\tau_r\frac{d\mathbf{a}}{dt} \tag{2.69}$$

As discussed in Refs. [104, 105], the fact that the classical RR force depends on the time derivative of the acceleration (or the third order derivative of the electron position), leads to two interesting cases of unphysical behaviour, known as runaway solutions and pre-acceleration. For example, in the absence of external fields, Eqn. (2.69) becomes:

$$m_e\mathbf{a}=m_e\tau_r\frac{d\mathbf{a}}{dt} \tag{2.70}$$

which has a solution of $\mathbf{a}(t)=\mathbf{a}(t_0)\exp(t/\tau_r)$. This solution grows exponentially on a time scale of 10^{-24} s, even in the absence of any external fields to accelerate the electron; clearly this is unphysical behaviour, known as a runaway solution.

Alternatively, it is possible to solve Eqn. (2.69) using an integrating factor. Multiplying this equation through by the factor $\exp(-t/\tau_r)$ yields the following differential equation [102, 104]:

$$\frac{d}{dt}\left[\mathbf{a}\exp(-t/\tau_r)\right]=-\mathbf{F}_{ext}\exp(-t/\tau_r) \tag{2.71}$$

$$\mathbf{a}=-\frac{\exp(t/\tau_r)}{m_e\tau_r}\int_{t_0}^{t_1}\mathbf{F}_{ext}\exp(-t'/\tau_r)dt' \tag{2.72}$$

In which the boundary condition $a(t_0)\rightarrow 0$ as $t_0\rightarrow\infty$ is assumed. Finally, a change of variable to $s = (t' - t)/\tau$ enables the above equation to be written as:

$$\mathbf{a}(t) = \frac{1}{m_e} \int_0^\infty \mathbf{F}_{ext}(s\tau_r + t) \exp(-s) ds \tag{2.73}$$

Eqn. (2.73) again demonstrates unphysical behaviour in the Lorentz-Abraham equation; the acceleration of the electron at some time, t, depends on the force exerted on it from some future time, $t + s\tau_r$. In the upcoming sections, alternative models which aim to remove the unphysical behaviour inherent in Eqn. (2.69), will be explored.

The Lorentz-Abraham-Dirac (LAD) equation

The LAD equation is the relativistic generalisation of Eqn. (2.69) and was the first covariant description of RR. This was derived by Dirac in 1938 [100] under the assumption of energy conservation. To obtain this equation the velocity and acceleration vectors in Eqn. (2.69) are replaced with 4-vectors, such that $\mathbf{v} \to v^\mu$ and $\mathbf{v} \cdot \mathbf{v} \to -v_\mu v^\mu$ (see the appendix for more details). In addition, the 4-velocity satisfies the normalisation $v_\mu v^\mu = c^2$, which upon differentiating twice with the chain rule, yields the following relation: $\dot{v}^\mu \dot{v}_\mu = -v_\mu \ddot{v}^\mu$. The Lorentz force equation is generalised by re-writing in terms of the electromagnetic tensor, $F^{\mu\nu}$, such that a first attempt at the equation of motion becomes:

$$m_e \frac{dv^\mu}{d\tau} = \frac{e}{c} F^{\mu\nu} v_\nu + m_e \tau_r \ddot{v}^\mu \tag{2.74}$$

The above equation is unphysical in the same way as the non-relativistic version in Eqn. (2.69). To see why this is the case, it is necessary to multiply through by v_μ, to obtain:

$$\frac{1}{2} \frac{d}{d\tau} v_\mu v^\mu = \frac{e}{m_e c} F^{\mu\nu} v_\mu v_\nu + \tau_r v_\mu \ddot{v}^\mu \tag{2.75}$$

The left hand side of Eqn. (2.75) equals zero due to the normalisation condition, whilst the first term on the right vanishes due to the fact that it is the product of a symmetric and anti-symmetric tensor. The equation is therefore unphysical, given that the term $v_\mu \ddot{v}^\mu \neq 0$. A quick fix is to simply subtract the non-vanishing term so that Eqn. (2.75) satisfies the normalisation condition. The term which is subtracted must then vanish in the non-relativistic limit; dimensional analysis shows that the additional term is therefore $\tau_r v^\mu v_\nu \ddot{v}^\nu / c^2 = -\tau_r v^\mu \dot{v}_\nu \dot{v}^\nu / c^2$. The corrected LAD equation is then:

$$m_e \frac{dv^\mu}{d\tau} = \frac{e}{c} F^{\mu\nu} v_\nu + m_e \tau_r \left(\ddot{v}^\mu - \frac{v^\mu}{c^2} \dot{v}_\nu \dot{v}^\nu \right) \tag{2.76}$$

The above equation contains the same problems as the non-relativistic formalism in Eqn. (2.69); the $\ddot{v}^\mu$ term represents a third order derivative of position, which as discussed earlier leads to runaway solutions and pre-acceleration.

The Landau-Lifshitz equation

To remove the unphysical behaviour inherent in the LAD equation, it is necessary to reduce the order of the equation, i.e. to eliminate the third order derivative of the electron position. This is achieved by assuming that the magnitude of the Lorentz force, evaluated in the reference frame of the accelerating electron, is much weaker than that of the RR force. In this case, $m_e \mathbf{a} = \mathbf{F}_{ext} + \mathbf{F}_{RR} \sim \mathbf{F}_{ext} = -e(\mathbf{E}_{ext} + \mathbf{v} \times \mathbf{B}_{ext})$. Re-injecting this into the right hand side of Eqn. (2.69) gives:

$$\begin{aligned} m_e \mathbf{a} &= \mathbf{F}_{ext} - m_e \tau_r \frac{d}{dt} \left[\frac{e}{m_e} (\mathbf{E}_{ext} + \mathbf{v} \times \mathbf{B}_{ext}) \right] && (2.77) \\ &= \mathbf{F}_{ext} - \tau_r e \left[\frac{d\mathbf{E}_{ext}}{dt} + \mathbf{v} \times \frac{d\mathbf{B}_{ext}}{dt} + \mathbf{B}_{ext} \times \frac{d\mathbf{v}}{dt} \right] && (2.78) \\ &= \mathbf{F}_{ext} - \tau_r e \left[\frac{d\mathbf{E}_{ext}}{dt} + \mathbf{v} \times \frac{d\mathbf{B}_{ext}}{dt} + \frac{\mathbf{B}_{ext}}{m_e} \times \mathbf{F}_{ext} \right] && (2.79) \end{aligned}$$

where higher order terms which scale as τ_r^2 are assumed negligibly small and therefore are omitted. The above equation is the non-relativistic Landau-Lifshitz equation. The relativistic generalisation is obtained from (2.76) by expressing the acceleration as follows: $\dot{v}^\mu = \frac{e}{m_e} F^{\mu}{}_{\nu} v^\nu$,. The derivative of the acceleration with respect to the proper time is then written:

$$\begin{aligned} \ddot{v}^\mu &= \frac{e}{m_e} (F^{\mu}{}_{\nu} \dot{v}^\nu + \dot{F}^{\mu}{}_{\nu} v^\nu) && (2.80) \\ &= \frac{e}{m_e} v^\gamma \partial_\gamma F^{\mu}{}_{\nu} v^\nu + \left(\frac{e}{m_e} \right)^2 F^{\mu}{}_{\nu} F^{\nu}{}_{\gamma} v^\gamma && (2.81) \end{aligned}$$

Substituting this term into Eqn. (2.76) yields the following result:

$$m_e \frac{dv^\mu}{d\tau} = \frac{e}{c} F^{\mu\nu} v_\nu + m_e \tau_r \left(\frac{e}{m_e} v^\gamma \partial_\gamma F^{\mu}_{\nu} v^\nu + \frac{e^2}{m_e^2} F^{\mu}{}_{\nu} F^{\nu}{}_{\gamma} v^\gamma + \frac{v^\mu}{c^2} \dot{v}_\nu \dot{v}^\nu \right) \tag{2.82}$$

known as the Landau-Lifshitz (LL) equation, which is regarded as the most correct, and widely used, equation of motion for a point-like radiating electron, provided the magnitude of the RR force is sufficiently weak. It does not suffer from the same unphysical solutions as the LAD equation, and has been demonstrated to be consistent with the classical limit of strong field QED [110, 111]. In addition, it has been shown in Ref. [112] that the set of solutions to the LL equation also includes all physical solutions to the LAD equation.

For the purposes of modelling the RR force analytically in later chapters of this thesis, it is possible to approximate the LL equation by keeping the dominant term proportional to $a_0^2\gamma^2$, as outlined in Ref. [113]. In this case, the LL equation can be expressed in 3-vector form, as follows:

$$\frac{d\mathbf{p}}{dt} = \mathbf{F}_L + \mathbf{F}_{RR} \tag{2.83}$$

where $\mathbf{F}_{RR} = -P_\gamma \boldsymbol{\beta}/c$ is an approximation of the RR force, which is assumed to be oriented in the direction opposite to the radiating electron's momentum. Here P_γ is the single electron radiated power, which was previously defined in Eqn. (2.64).

It is important to note that the classical description of RR provided by the LL equation is valid provided that the electromagnetic field under consideration has a magnitude less than the classical critical field, $E_{cr} = E_{Sch}/\alpha$, where E_{Sch} is the Schwinger field (as described in section 1.2.1) and α is the fine structure constant. Given that $\alpha \sim 1/137$, the classical critical field actually imposes a less stringent condition on the magnitude of the fields which can be considered within the classical framework. To derive the magnitude of the classical critical field, the work done by this field, over a distance equal to the classical electron radius ($r_e \sim 10^{-15}$ m) is equated to the electron rest mass. Given that this distance is much less than the equivalent characteristic length in QED, which is the Compton wavelength, it follows that the classical critical field is stronger than the equivalent field in QED, the Schwinger field. However, whilst the LL equation is predicted to be valid up to the classical critical field strength, it is restricted by the fact that it neglects quantum aspects of RR, which will be discussed in section 2.3.2.

2.3.2 Quantum aspects of radiation reaction

The LL equation described in Eqn. (2.82) is a classical interpretation of RR, and therefore neglects QED effects which can impact the electron dynamics [114]. In this section, these relevant effects will be investigated, as well as the threshold at which they become important.

The importance of quantum effects can be parameterised by two Lorentz invariant quantities, χ_e and χ_γ, which are referred to in this thesis as the electron and photon quantum parameters, respectively. The electron quantum parameter is expressed as follows:

$$\chi_e = \frac{\gamma_e}{eE_{Sch}}\sqrt{\mathbf{F}_L^2 - (\mathbf{F}_L \cdot \boldsymbol{\beta}_e)^2} = \frac{\gamma_e}{E_{Sch}}|\mathbf{E}_\perp + \mathbf{v} \times \mathbf{B}| \tag{2.84}$$

where $E_{Sch} = m_e^2c^3/e\hbar$ is the Schwinger field (defined in section 1.2.1), $\mathbf{F}_L$ is the Lorentz force and $\mathbf{E}_\perp$ is the electric field perpendicular to the electron velocity. The parameter χ_e therefore describes the magnitude of the electric field experienced by the electron, in its rest frame, relative to that of the Schwinger field. In general, as $\chi_e \gtrsim 0.1$, the stochastic nature of photon emission becomes important [114], whilst higher order QED effects such as pair-production become important for $\chi_e \sim 1$.

Analogously, the photon quantum factor is defined as follows:

$$\chi_\gamma = \frac{\hbar\omega}{2m_ec^2}\frac{|\mathbf{E}_\perp + \hat{\mathbf{k}}_\gamma \times c\mathbf{B}|}{E_{Sch}} \tag{2.85}$$

where $\mathbf{E}_\perp$ is the electric field in the direction perpendicular to the unit wave vector, $\hat{\mathbf{k}}_\gamma$, which describes the direction of photon propagation.

These quantum parameters can be used to calculate the rate of QED processes in terms of Lorentz invariants. In general, there are other Lorentz invariants which can be calculated, however in this thesis the weak field approximation is assumed such that the only relevant parameters for evaluating the rate of QED processes are χ_e and χ_γ. This assumption is outlined in Refs. [65, 106] and is generally considered to be valid for ultra-intense laser fields in which $E/E_{Sch}<10^{-3}$. The reasoning behind this assumption is that, if the laser field can be considered to be a constant background field on the time scale of the QED processes involved in the interaction, then the rates of these processes depend only on the local χ_e and χ_γ values. In addition, the configuration in which the rates of the QED processes (i.e. photon emission and pair-production) are calculated is interchangeable with any other configuration which has the same values of the quantum parameters, χ_e and χ_γ. This enables the rates of photon-emission and pair-production to be calculated for the case of a constant background magnetic field, as discussed in section 2.2.2

It is now possible to investigate the electron dynamics in the case where quantum effects become important, i.e. a regime in which $\chi_e \gtrsim 0.1$. The move from classical to quantum RR means that the stochastic nature of the emitted radiation becomes significant, and must be taken into account [58, 114–118]. In the classical description, the RR force acts on the radiating electron continuously during its motion, analogously to a friction force. In the quantum description, there is a probability of photon emission occurring at all points along the electron trajectory. When this emission occurs, the electron experiences an instantaneous recoil force, causing a discontinuity in its trajectory. The electron path is then considered to be ‘smooth’ (i.e. continuous) in between instances of photon emission [119]. This description is semi-classical, as the concept of a trajectory in quantum mechanics is replaced by the path-integral formulation. However, the semi-classical behaviour associated with stochastic photon emission can be considered to approximate the electron dynamics. The stochastic recoil force exerted on the radiating electron is the quantum equivalent of the RR force [58, 115, 120]. The differences between the classical and quantum descriptions of RR are illustrated in Fig. 2.7.

There are two key quantum effects which impact the electron dynamics. The first is known as the straggling effect, which enables electrons to penetrate into regions of high fields which they could not reach classically [116, 121–123]. For example, in the classical description, an electron radiates continuously, at all points on its trajectory. It may then lose all of its kinetic energy to photon emission and become reflected by the laser field. If the photon emission process is now stochastic, there is a probability that the electron will not emit a photon until it has reached the most intense region of the field. In this case, a higher energy photon will be emitted than would be predicted classically. This effect has been reported to boost the rate of pair-production in QED-PIC simulations [113, 116], for focused laser intensities $\leq 10^{24}$ Wcm^{-2} (for intensities greater than this threshold, the average photon energies are sufficiently high that they can produce large numbers of electron-positron pairs without assistance from the straggling effect).

The second important quantum effect arises due to a cut-off in the photon energy spectrum in the quantum case relative to that of the classical case. In the quantum description, it is not possible for a radiating electron to emit a photon with energy higher than the kinetic energy of the electron, whereas this is possible in the classical description (since there are no restrictions on the frequency of photons which can be emitted). This difference is observed in the classical and quantum synchrotron functions, as illustrated in Fig. 2.6. In addition, the classical synchrotron function neglects photon spin and polarisation effects, which also enable the photons emitted to have a higher energy than the electron from which they were radiated [124, 125]. Since it is the emission of such high energy photons which impart the greatest RR force on the electron, the amplitude of the electron radiated power, and therefore the magnitude of the RR force, is overestimated in the classical description compared to the quantum description.

It is possible to construct a semi-classical description of the RR force by modifying the LL equation (Eqn. (2.82)) to account for the hard cut-off in the photon energy. This is achieved by scaling the electron radiated power by the so-called 'Gaunt factor', $g(\chi_e)$, defined as follows [58, 98, 120]:

$$g(\chi_e) = \frac{3\sqrt{3}}{2\pi\chi_e^2} \int_0^{\chi_e/2} F(\chi_e, \chi_\gamma) d\chi_\gamma \tag{2.86}$$

where $F(\chi_e, \chi_\gamma)$ is the quantum synchrotron function [98], introduced in section 2.2.2. Eqn. (2.86) may be approximated as follows: $g(\chi_e) \sim [1 + 4.8(1+\chi_e)\ln(1+1.7\chi_e) + 2.44\chi_e^2]^{-2/3}$ [65, 126]. This approximation demonstrates that even for only moderate values of $\chi_e \sim 0.1$, the Gaunt factor is 0.66, and so the magnitude of the radiated power is reduced by a third relative to the classical description. A consequence is that it should be possible to observe quantum aspects of RR using current laser systems [107, 117, 127–129], given that even fields which are significantly weaker than the Schwinger field will produce non-negligible quantum effects.

2.3.3 Experimental observations of radiation reaction

It is important to note that experimental signatures of RR can be observed using current laser systems, which operate at focused intensities of approximately 10^{20} Wcm^{-2}. Two recent experimental campaigns at the Astra-Gemini laser system have demonstrated RR effects during the collision of a relativistic electron beam with an ultra-intense counter-propagating laser, as detailed in Refs. [130, 131]. The counter-propagating geometry employed in these experiments boosts the magnitude of the electric field in the electron reference frame, up to $\sim 25\%$ of E_{Sch}. As demonstrated in Eqn. (2.86), this is sufficient not only to induce RR, but also to trigger the onset of stochastic effects.

In the aforementioned experiments, GeV electron beams were generated via the interaction of one of the dual Astra-Gemini lasers with a gas jet/cell. This interaction produces a low density plasma, through which the electrons are accelerated by the process of laser wakefield acceleration. On exiting the gas jet, these relativistic electrons were collided with the second Astra-Gemini laser, tightly focused using an $F/2$ parabola. At the point of overlap, the laser a_0 was calculated to be ≈ 10, sufficiently high intensity to observe RR.

In both experiments, a combination of an electron spectrometer and a Cesium-Iodide (CsI) array were employed to obtain measurements of the electron and γ-ray spectra [132]. Using these diagnostics, RR is evidenced by a reduction in the electron energy, which coincides with a high flux of γ-rays on the CsI detector. RR is a fundamental process which is present in every collision between the electron beam and the counter-propagating laser pulse. However, it may not be observed on every shot, due to spatial and temporal drifts in the electron beam. These reduce the overlap between the electron beam and the laser at the collision point, reducing the magnitude of RR effects below the threshold which can be detected. The difficulties in achieving spatial and temporal overlap in such a set-up are detailed in Ref. [133].

Despite the technical challenges, both experiments observed a significant reduction in the electron energy, with a reported decrease of 30% in the peak energy in Ref. [131]. This was correlated with a high flux of γ-rays; in Ref. [130] these were observed to have a characteristic energy >30 MeV, which should impart a moderate RR force on the emitting electrons. Interestingly, both studies concluded that the electron energy loss was more consistent with a quantum description of RR, compared to a classical description. The quantum model referred to in these studies is the LL equation, scaled by the Gaunt factor to approximate quantum aspects of the photon emission process. This means that even at currently achievable laser intensities, it is possible to see the breakdown of the LL equation. In addition, Ref. [131] discusses the disparity between the experimental results and QED-PIC simulations, hinting that the constant cross fields approximation (CCFA) employed in these simulations may also breakdown. The next generation of ultra-intense laser systems will enable quantum RR to be probed further, and may shed light on physics beyond the CCFA approximation and the LL model of electron motion.

2.4 Pair-production mechanisms in ultra-intense laser-plasma interactions

Thus far, the generation of radiation from accelerating charges, and the accompanying RR force, has been described in detail. Another important QED process which must be considered is the possibility of the emitted radiation producing electron-positron pairs. As $\chi_e \sim 1$, it is possible for electron-positron pairs to be formed from the vacuum, in a process known as Schwinger pair-production [55, 134]. These pairs may be accelerated by the laser fields, subsequently depleting the energy of the pulse. It has been proposed in Ref. [67] that the process of Schwinger pair-production may place a fundamental limit on the maximum achievable laser intensities. However, the current intensity frontier is seven orders of magnitude below the Schwinger limit; given that the probability of Schwinger pair-production decreases exponentially for intensities below this limit, it will not be possible to observe this process for some time [113].

There are however pair-production mechanisms which can be observed at current laser intensities. These do not involving pulling pairs from the vacuum, but rather arise from the interaction of high energy photons with the Coulomb fields of high-Z nuclei, or via non-linear interactions with multiple photons from the laser. The dominant pair-production mechanisms at current laser intensities will be detailed in this section.

2.4.1 The Bethe-Heitler and trident processes

Recent experiments have demonstrated the possibility of generating electron-positron pairs via the Bethe-Heitler and single photon trident processes. These processes are written explicitly below, with first order Feynman diagrams provided in Figs. 2.8 (a) and (b).

$$\omega_\gamma + Z \to Z + e^+ + e^- \quad \text{Bethe-Heitler} \tag{2.87}$$

$$e^- + Z \to Z + e^+ + 2e^- \quad \text{trident} \tag{2.88}$$

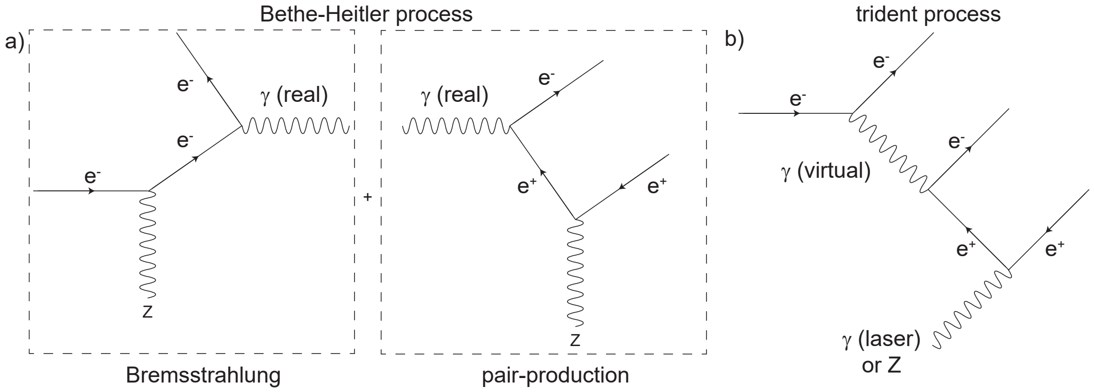

Figure 2.8: Feynman diagrams representing two pair-production mechanisms. (a) The Bethe-Heitler process occurs in two stages; an electron first interacts with the Coulomb field of an ion, producing a Bremsstrahlung photon (a real photon) which decays into an electron-positron pair. (b) In the trident process, a virtual photon decays in the Coulomb field of the ions, or within the laser field, to produce an electron-positron pair.

where ω_γ represents a photon and Z is the atomic number of the scattering nucleus. In the Bethe-Heitler process, hard photons (typically associated with Bremsstrahlung radiation) scatter off the Coulomb field of high-Z nuclei, producing electron-positron pairs [135, 136]. Pair-production is more likely to occur in the Coulomb field of a nucleus compared to occurring in vacuum since there are more ways in which the hard photon can partition its energy, for example, via excitation of the nucleus. This process has been experimentally verified in Refs. [73, 137] during intense laser-solid interactions. In Ref. [73], the experimental set-up involved first generating a relativistic electron beam via the process of wakefield acceleration. This beam was then collided with a solid Pb target, producing high energy Bremsstrahlung photons. The photons then scatter off the Pb nuclei in the target, generating a dense, neutral, electron-positron plasma. This study is particularly significant, as it marks the first time in which a sufficiently high density of electron-positron pairs was produced ($n_{pos} \sim 10^{15}$ cm^{-3}), thus enabling collective effects within such a plasma to be observed. These pair plasmas are important for laboratory astrophysics experiments, and may enable questions, such as how γ-ray bursts are generated, to finally be answered.

Laser induced pair-production may also occur via the trident process, in which an energetic electron (with energy $\geq 2m_ec^2$) scatters off a high-Z nucleus, producing a virtual photon, which subsequently decays into an electron-positron pair [96, 138]. There are many definitions of this process in the literature, for example, the process can occur in the field of the laser as opposed to the Coulomb field of the nucleus.

The trident process has been observed to some degree, in that it contributed to the positrons produced in the well-cited SLAC E144 experiment [139, 140]. It is difficult to experimentally isolate positrons which come from the trident process, as the probability of pair-production is lower than that of the Bethe-Heitler process for the targets which are typically employed experimentally. The probability of trident pair-production, P_t, is proportional to the number of ions within the target material (which the energetic electrons scatter off), the target thickness, d, and the trident process cross-section, which is estimated in Ref. [141] to be proportional to Z^2. This gives a probability $P_t \propto n_i Z^2 d$ [142]. The probability for Bethe-Heitler pair-production (P_{BH}) is the product of the probabilities of first generating a Bremsstrahlung photon, and this photon decaying into an electron-positron pair [142]. These two probabilities are functions of the ion density, the target thickness and Z^2, such that the total probability is $P_{BH} \propto n_i^2 Z^4 d^2$. This expression demonstrates that the Bethe-Heitler process is the dominant pair-production mechanism for ultra-intense laser interactions with thick, high-Z targets.

2.4.2 The linear and non-linear Breit-Wheeler processes

The previously described processes detail pair-production in the presence of high-Z nuclei. The aim of upcoming laser facilities is to investigate fundamental QED processes, such as pair-production via photon-photon collisions (i.e. without the intermediate step of interacting with the Coulomb fields in a solid target). A common experimental set-up for such an interaction involves generating a low divergence, high energy beam of photons and colliding this with a counter-propagating laser (for example, the dual pulse interaction scheme proposed in chapter 7). In such an interaction, the dominant pair-production mechanism is the non-linear Breit-Wheeler process, described below [106, 143–145].

$$\omega_\gamma + n\omega_L \rightarrow e^+ + e^- \tag{2.89}$$

Here, ω_γ represents a photon emitted by a radiating electron or within a γ-ray beam, whilst ω_L represents a laser photon. It can be seen that the non-linearity in the process arises due to both the high energy of the probe photon (the γ-ray photons produced via ultra-intense laser solid interactions typically have an average energy $\sim$ 10 MeV), and the fact that this probe photon interacts with n photons of the laser, due to the high photon flux within the focal spot.

The non-linear Breit-Wheeler process was famously observed during the SLAC E144 experiment, in which a beam of electrons was accelerated to 46.6 GeV in a linac, before colliding with a relativistic laser pulse [139, 146]. The interaction of multiple photons of the laser with the hard photons radiated by the accelerated electrons then produced a small number (∼100) of positrons via the non-linear Breit-Wheeler process. Exotic schemes have been proposed to observe this process during laser-solid interactions. For example, in Ref. [147] a set-up is presented in which two counter-propagating ultra-intense laser pulses each interact with a thin foil. As the foil becomes transparent to the laser, both the laser light and the accelerated electrons are transmitted through, and collide with the species from the second foil. This scheme predicts a large number of pairs ($\sim 1.6 \times 10^{10}$ per shot, with a density of $\sim 2.5 \times 10^{22}$ cm^{-3}) can be generated using achievable laser intensities of 10^{23} Wcm^{-2}.

There is also a linear Breit-Wheeler process, which describes the production of an electron-positron pair through the interaction of a probe photon with a single photon from the laser (or equivalently, the interaction of two high energy photons) [148]. This is a QED process of the lowest order (i.e. represented by a Feynman diagram with two vertices) which is predicted to be prevalent in extreme astrophysical environments such as pulsars and the accretion discs around active galactic nuclei. Despite the importance of this process, it has yet to be observed experimentally, due to two challenges. The first is that during the interaction of a γ-ray beam with an ultra-intense laser pulse (which is necessary to generate the high energy photons), the large flux of photons means that the non-linear process is much more likely to occur. Even during the collision of two high energy γ-ray beams, another challenge which must be overcome is that to achieve a non-negligible cross-section requires the head-on interaction of two high energy photons, with an energy threshold given by [71, 72, 149]:

$$E_1 E_2 > \frac{2m_e^2c^4}{1-\cos\phi} \tag{2.90}$$

where E_1 and E_2 are the energies of the interacting photons and ϕ is the angle between the colliding light sources. To illustrate the difficulty in observing this process experimentally, consider the interaction of a typically achievable γ-ray beam, with average photon energy ∼10 MeV, colliding head on (ϕ=180°) with an ultra-intense laser pulse. Whilst the photons in the γ-ray beam have energies much greater than the rest mass of the electron, the laser photons have an energy ∼keV, such that Eqn. (2.90) is barely satisfied.

A number of schemes have been proposed to observe this process. In Refs. [71, 72] it is suggested that two laser-solid interactions can be used to produce multi-MeV photon sources, which are collided at a high angle of incidence. Such schemes are predicted to produce 10^4 pairs, at achievable laser intensities $\sim 10^{23}$ Wcm^{-2}. Alternatively, Ref. [150] proposes interacting a γ-ray beam, generated via a laser-solid interaction, with the black body radiation produced in a laser heated hohlraum.

2.4.3 Pair-production cascades

The acceleration of electrons in ultra-intense laser fields also leads to the exciting prospect of pair-production via an electromagnetic cascade. A fascinating aspect of cascade pair production is that it can be triggered by a single electron, with an initially low energy, as it accelerates in the laser fields. In this process, an accelerated electron emits high energy photons, which decay into electron-positron pairs in the presence of the laser fields. These electrons and positrons are subsequently accelerated by the laser, radiating more high energy photons in the process. These photons then decay into more electron-positron pairs, triggering a runaway reaction known as an electromagnetic cascade [67, 128, 151–153]. It is predicted that this process could completely deplete the energy of ultra-intense laser pulses which have intensities close to the Schwinger limit [67].

Determining the conditions necessary for an electromagnetic cascade is an area of extensive research, due to concern that this process could present a fundamental limit to the laser intensities which can be achieved. Ref. [152] has observed a cascade from a single electron positioned at the focal spot of two counter-propagating, circularly polarised laser pulses, each with an intensity of 10^{24} Wcm^{-2}. The complete depletion of two colliding pulses is predicted to occur at an intensity of 6×10^{26} Wcm^{-2} in Ref. [67]. An important point to note in this study is that the rate of cascade pair production was found to depend on the amount of time that the seeded electron-positron pairs spend in the focal spot of the laser, thus it may be possible to reduce the magnitude of this process by moving to short duration, tightly focused pulses.

2.5 Conclusions

The focus of this chapter has been to describe the dynamics of a single electron in an electromagnetic wave, such as that of a laser pulse. Starting from the Lorentz force equation of motion, the electron trajectory, in both the laboratory and electron rest frame, was derived. It was further demonstrated that the acceleration of an electron leads to the generation of electromagnetic radiation. Specifically, the properties of synchrotron radiation, such as its angular dependence and energy spectrum, were discussed.

For sufficiently strong electromagnetic fields, the energy lost by the electron in the form of radiation leads to the action of a back-reaction (or RR) force on the electron. A number of equations of motion for a radiating electron were compared, with particular focus on the LL equation, since this is adapted for the analysis presented in chapter 6 of this thesis. Upcoming laser facilities will achieve sufficiently high laser intensities that quantum aspects of RR, such as stochastic photon emission, will be observed. The impact of these quantum effects on the electron dynamics was explored in section 2.3.2, along with a brief discussion on the possibility of observing such effects experimentally. A particularly important QED process, which will be investigated in chapter 7, is electron-positron pair-production. A number of pair-production processes were discussed in this chapter, along with proposed experiments for the generation of electron-positron pairs via photon-photon interactions, which will finally be possible utilising upcoming laser systems.

Chapter 3

Theory II: Collective electron dynamics in ultra-intense laser-plasma interactions

The previous chapter provided a description of the motion of a single electron in a plane wave, including the generation of high energy radiation and the onset of QED effects. In this chapter, the investigation will be extended in order to describe the interaction of an intense laser pulse with a quasi-neutral system of many charged particles, i.e. a plasma. The collective dynamics of the particles within such a system lead to interesting plasma physics effects, such as quasi-neutrality and wave propagation, which will be explored in detail. For the ultra-intense pulses considered in this thesis, relativistic effects also impact the collective electron dynamics enabling, for example, the propagation of laser pulses through plasmas which are opaque in the non-relativistic regime. This phenomenon, known as relativistic transparency, is of particular importance in chapters 5 and 6 of this thesis, in which it leads to the generation of transverse electromagnetic modes, and impacts the magnitude of the RR force.

3.1 Plasma as a state of matter

The plasma state (often referred to as 'the fourth state of matter') was first observed by William Crookes in 1879, by passing a strong electric current through a partially evacuated glass tube. The name 'plasma' was later coined by Irving Langmuir to describe this state, given its analogy with plasma in the blood. In everyday life, the plasmas which are typically encountered can be broadly divided into the categories of naturally or artificially occurring. Natural plasmas are observed in weather phenomena, such as lightning, St Elmo's fire, and the Aurora Borealis. Artificial plasmas tend to have technological applications, such as neon signs and television displays. Less well known applications of plasmas include energy generation via nuclear fusion [14, 154, 155], rocket propulsion [156], etching of electrical components [157, 158], and as an optical medium which can be used to control the properties of light [159–161].

Plasma is produced by ionising a gas, therefore generating a complex state of matter in which it is assumed the number of positive and negative charges are equal. The feature which makes a plasma distinct to an ionised gas, is that a plasma is dominated by collective behaviour, arising due to long-range electrostatic interactions between the constituent charges. It is clear then, that not every ionised gas constitutes a plasma. In general, there are three conditions which must be satisfied for an ionised gas to be classified as a plasma. These are:

- $L \gg \lambda_D$ - The dimensions of the plasma (L) must exceed the Debye length (λ_D), the distance over which the plasma is considered to be electrically neutral.
- $N = (4/3)\pi\lambda_D^3 \gg 1$ - There must be a sufficiently large number of particles contained within the sphere, whose radius is equal to the Debye length, in order to screen out any changes in electrostatic potential within the plasma.
- $\omega_p > \omega_{coll}$ - The characteristic frequency (ω_p, the so-called 'plasma frequency'), at which density perturbations within the plasma oscillate, must be greater than the frequency of collisions between the electrons and neutral particles, ω_{coll}.

A final point to note is that the plasmas considered in this thesis are collisionless. This means that the interactions between charged species within the plasma are dominated by long-range electrostatic forces, as opposed to binary collisions. More rigorously, a collisionless plasma refers to the condition that the average distance a particle travels between collisions, the mean free path, is much greater than the dimensions of the plasma. The aforementioned conditions, which differentiate between a plasma and an ionised gas, will be explored further in this chapter.

3.1.1 The Debye length and quasi-neutrality

A distinguishing feature of a plasma is a property known as quasi-neutrality, namely that a plasma is electrically neutral when viewed over distances greater than a characteristic length, known as the Debye length. This feature is typically described by considering the addition of a positive charge to the plasma. The electrons within the plasma respond quickly to the change in electrostatic potential, arranging themselves in a ‘cloud’ around the charge, which shields its potential from the rest of the plasma. In contrast, the much heavier ions are unable to respond quickly to the change in electrostatic potential, and so remain static on the time scales over which the electrons screen the charge. Given that the electrons have a temperature associated with their thermal motion, they oscillate about their positions around the charge, and so its potential can ‘leak’ through the electron cloud. The magnitude of the potential decays exponentially over a characteristic distance, known as the Debye length.

Following the arguments described in Ref. [162], an expression for the Debye length is obtained by considering a 1D model in which a test charge, with an electrostatic potential ϕ, is introduced to a plasma containing equal numbers of positive and negative charges. The charge balance within the plasma is described by Poisson’s equation:

$$\nabla^2\phi = \frac{e}{\epsilon_0}(n_e - n_i) \tag{3.1}$$

Given that the ions remain static over the time scale of the electron motion, it is assumed that the ion density, $n_i = n$, remains constant throughout the interaction. The electron density is described by a Boltzmann distribution, such that $n_e = n\exp(e\phi/k_BT)$. Substituting this term into Eqn. (3.1) yields:

$$\frac{d^2\phi}{dx^2} = \frac{ne}{\epsilon_0}\Big(\exp(e\phi/k_BT) - 1\Big) \tag{3.2}$$

If it is assumed that the electrostatic potential is small, such that $e\phi \ll k_BT$, the exponential term may be approximated as $\exp(x) = 1 + x + \mathcal{O}(x^2)$, and Eqn. (3.2) is re-written:

$$\frac{d^2\phi}{dx^2} = \frac{ne^2}{\epsilon_0}\frac{e\phi}{k_BT} \equiv \frac{\phi}{\lambda_D^2} \tag{3.3}$$

A solution to Eqn. (3.3) is obtained by converting to polar co-ordinates, which yields:

$$\phi = \frac{\phi_0}{r} \exp(-|x|/k_B T) \tag{3.4}$$

where $\phi_0 = e/4\pi\epsilon_0$ is a constant of integration, associated with the 'bare' Coulomb potential of the charge introduced to the plasma [163]. From this solution, the Debye length (λ_D) is a characteristic distance over which the magnitude of the electrostatic potential decreases exponentially. It is therefore the distance over which charge is screened within the plasma. This length is described as:

$$\lambda_D = \sqrt{\frac{\epsilon_0 k_B T}{n e^2}} \tag{3.5}$$

There are two key dependencies within the expression for the Debye length. The first is that it is proportional to the square root of the electron temperature. As this temperature increases, the electron thermal oscillations increase in amplitude, shielding the test charge less effectively and enabling more of the electrostatic potential to leak into the plasma. The second key dependence is on the electron number density. As this parameter increases, the larger number of electrons are able to screen the charge more efficiently, over a smaller distance.

The plasma is then electrically neutral over distances greater than the Debye length, a condition known as quasi-neutrality. Thus, for an ionised gas to behave like a plasma, the system must have dimensions greater than the Debye length. It is also necessary that there are a sufficient number of particles, N, within the Debye length (or, in 3D, within the Debye sphere) to effectively screen any changes in the electrostatic potential, i.e. $N = (4/3)\pi\lambda_D^3 \gg 1$.

3.1.2 Plasma kinetic theory

The most complete description of a plasma is obtained using kinetic theory, which aims to describe the macroscopic properties of a plasma by accounting for the motion of every particle within it [164, 165]. The starting point for such a description is in terms of a density functional, $N = N(\mathbf{x}, \mathbf{v}, t)$, which describes the set of all locations of a single particle in 6D phase space. Generalising to a system of N particles, the number density in phase space is given by:

$$N(\mathbf{x}, \mathbf{v}, t) = \Sigma_{k=1}^{N} \delta(\mathbf{x} - \mathbf{X}_k)\delta(\mathbf{v} - \mathbf{V}_k) \tag{3.6}$$

where $\mathbf{X}_k, \mathbf{V}_k$ are the position and velocity co-ordinates of particle k, and δ is the Dirac delta function, which takes a non-zero value only when $\mathbf{x} = \mathbf{X}_k$ and $\mathbf{v} = \mathbf{V}_k$. Note that for a system of multiple species, labelled by index s (such as a plasma composed of electrons and ions), the density functional must be defined for each species in turn. The evolution of the density functional is given by a continuity equation, known as the Klimontovich equation [166]. This equation assumes that the number of particles are conserved (i.e. no collisions which act as sources and sinks), and is written as follows:

$$\frac{\partial N_s}{\partial t} + \mathbf{v} \cdot \nabla N_s + \frac{q_s}{m}(\mathbf{E}^m + \mathbf{v} \times \mathbf{B}^m) \cdot \nabla_v N_s = 0 \tag{3.7}$$

where q_s is the charge of the species and ∇_v is the gradient with respect to the velocity vector. Eqn. (3.7) provides a completely self-consistent description of the plasma, since the velocity is defined as $\mathbf{V}_k = d\mathbf{X}_k/dt$ and $d\mathbf{V}_k/dt$ is determined by the Lorentz force (and can be generalised to include the RR force, as per Eqn. (2.83)). The electric and magnetic fields which appear in Eqn. (3.7) are the microscopic fields, obtained from the total charge and current densities, which are defined below.

$$\rho(\mathbf{x}, t)^m = \Sigma_s q_s \int N_s(\mathbf{x}, \mathbf{v}, t)\mathbf{dv} \tag{3.8}$$

$$\mathbf{j}(\mathbf{x}, t)^m = \Sigma_s q_s \int \mathbf{v} N_s(\mathbf{x}, \mathbf{v}, t)\mathbf{dv} \tag{3.9}$$

where m denotes a microscopic property. The Klimontovich equation is exact, in that it describes the position and velocity of every particle in the system at every time. This provides much more information than is necessary, given that only the macroscopic properties of the plasma are of interest. As such, this equation is no easier to solve than an N-body problem.

A way around this cumbersome equation is to define a distribution function for each species, $f_s = f_s(\mathbf{x}, \mathbf{v}, t)$, which counts the number of particles located in a volume $\Delta\mathbf{x}\Delta\mathbf{v}$ of phase space, centered on a co-ordinate ($\mathbf{x}$,$\mathbf{v}$), at a given time. The number of particles located within this finite volume of phase space can vary with time, leading to fluctuations in the electromagnetic fields. These fluctuations are described as follows:

$$N_s(\mathbf{x},\mathbf{v},t) = f_s(\mathbf{x},\mathbf{v},t) + \delta N_s(\mathbf{x},\mathbf{v},t) \tag{3.10}$$

where the distribution function is related to the density functional by averaging over phase space, as follows: $f_s(\mathbf{x},\mathbf{v},t) = \langle N_s(\mathbf{x},\mathbf{v},t)\rangle$. The electric field is $\mathbf{E}^m = \mathbf{E} + \delta\mathbf{E}$, (similarly for the $\mathbf{B}$ field), where the $\mathbf{E}$ term is the 'smooth' field associated with the averaged number of particles within the phase space volume. These quantities are then substituted back into Eqn. (3.7), and an ensemble average is taken. This means averaging over all configurations which give the same distribution, i.e. averaging over the degenerate configurations which give the same number of particles within a given phase space volume. This leads to the following kinetic equation:

$$\frac{\partial f_s}{\partial t} + \mathbf{v}\cdot\nabla f_s + \frac{q}{m}(\mathbf{E} + \mathbf{v}\times\mathbf{B})\cdot\nabla_v f_s = -\frac{q}{m}\langle(\delta\mathbf{E} + \mathbf{v}\times\delta\mathbf{B})\cdot\nabla_v \delta N\rangle \tag{3.11}$$

where $\langle\rangle$ denotes an ensemble average, and this process eliminates the fluctuating components of the fields, i.e. $\langle\delta\mathbf{E}\rangle$=0. The right hand side of Eqn. (3.11) describes the discrete, particle-like nature of the plasma, and therefore describes the effect of collisions between the constituent particles. In the context of high intensity laser-plasma interactions, it is typically sufficient to neglect the collision terms; the right hand side of Eqn. (3.11) then vanishes and is commonly referred to as the Vlasov equation.

Whilst the Klimontovich equation provides the exact description of the motion of particles within the plasma it provides too much information and is not practically solvable. Instead, the Vlasov equation (Eqn. (3.11)) equation provides a kinetic description of the plasma through the evolution of the distribution functions describing averaged quantities. Whilst this reduces the complexity of the description, the distribution function is not a quantity which is easily measurable. In the next section, an even simpler model will be introduced, which is remarkably useful in terms of describing the plasma in terms of experimentally measurable quantities.

3.1.3 The fluid model

A way of working through the problems inherent in the kinetic equation is to take averages (or so-called 'moments') of the Vlasov equation. This enables the plasma to be described in terms of equations which relate to macroscopic variables, such as pressure, temperature and density. Such quantities are experimentally measurable and therefore provide a more concise description of the plasma (compared to Eqn. (3.11)), referred to as the fluid description [162, 163]. The starting point for this approach is to write down the equation which describes the evolution of the distribution function (assuming for now only one plasma species). In the absence of collisions, this equation is the Vlasov equation, written:

$$\frac{\partial f}{\partial t} + (\mathbf{v} \cdot \nabla) f + \frac{1}{m}(\mathbf{F} \cdot \nabla_v) f = 0 \tag{3.12}$$

where $\nabla_v = (\partial/\partial v_x, \partial/\partial v_y, \partial/\partial v_z)$ and $\mathbf{F}$ is the Lorentz force. The k^{th} moment of the distribution is computed by multiplying the distribution function through by k factors of $\mathbf{v}$ and integrating over the velocity co-ordinates. As an example, the first moment is described below:

$$n\mathbf{u} = \int \mathbf{v} f(\mathbf{x}, \mathbf{v}, t) \mathbf{dv} \tag{3.13}$$

where n is the number density and $\mathbf{u}(\mathbf{x}$,t) is the flow velocity of the plasma as a whole, whereas $\mathbf{v}(\mathbf{x}, t)$ is the velocity of a single particle within the plasma. Following the steps outlined in Ref. [162], taking the first moment of the Vlasov equation yields a continuity equation:

$$\frac{\partial n}{\partial t} + \nabla \cdot (n\mathbf{u}) = 0 \tag{3.14}$$

where the above equation is a statement of particle conservation. Repeating this process for the second moment of the Vlasov equation yields an expression for force balance:

$$mn\left(\frac{\partial \mathbf{u}}{\partial t} + (\mathbf{u} \cdot \nabla)\mathbf{u}\right) = -\nabla P + nq(\mathbf{E} + \mathbf{v} \times \mathbf{B}) \tag{3.15}$$

where it is necessary to introduce the pressure tensor, P. It can be seen that taking higher order moments of the Vlasov equation generates an equation for a fluid variable, which subsequently depends on the next moment. For example, the continuity equation describes the number density, but it requires the introduction of a new quantity, the flow. Similarly, the second moment of the Vlasov equation describes the flow, but it now depends on the pressure. In order to obtain a self-consistent description, it is then necessary to close the set of equations, in this case by describing the pressure without introducing a new moment. In the plasma fluid model, this is achieved by applying the ideal gas law, $pV^{\gamma} = C$, where C and γ are constants. If the plasma behaves adiabatically, this ideal gas law may be expressed as [163, 167]:

$$\left(\frac{\partial}{\partial t} + \mathbf{u} \cdot \nabla\right) \rho n^{-\gamma} = 0 \tag{3.16}$$

The set of Eqns. (3.14), (3.15) and (3.16), combined with Maxwell's equations, enables macroscopic properties of the plasma to be determined. In practical applications, the fluid is composed of a species of ions and electrons, each of which is described by a distribution function. Maxwell's equations are then defined in the usual way, with the charge and current densities obtained by summing over the charged species, $s \in [e, i]$ as follows:

$$\rho = \Sigma_s q_s \int f_s(\mathbf{x}, \mathbf{v}, t) \mathbf{dv} \tag{3.17}$$

$$\mathbf{j} = \Sigma_s q_s \int \mathbf{v} f_s(\mathbf{x}, \mathbf{v}, t) \mathbf{dv} \tag{3.18}$$

Whilst the fluid equations produce a less complex description of a plasma, compared to the kinetic equation, this approach is still difficult to apply given that the set of equations are coupled and represent non-linear behaviour. For many practical applications, it is necessary to first linearise the set of equations, which will be detailed in the next section.

3.1.4 The plasma frequency

It has been discussed previously that a distinguishing feature of a plasma, as opposed to an ionised gas, is that it facilitates collective behaviour. A key example is the propagation of waves at a characteristic frequency, known as the plasma frequency. The interaction of an intense laser pulse with a plasma drives perturbations in the electron density. A population of electrons within the plasma then responds to the electric field associated with the density perturbations (arising from a charge imbalance within the plasma). Through Poisson's equation, the density and frequency of the electron oscillations can be related to the amplitude of the electric field, by assuming that the ions remain static. To derive an expression for the plasma frequency, the typical starting point is to consider the displacement of a volume of electrons driven, for example, by the ponderomotive force of the laser. The perturbation in density produces a charge imbalance, and therefore an electrostatic restoring force, which pulls the displaced volume of electrons back to their equilibrium position. As this volume accelerates, it gains inertia, and overshoots the equilibrium. This leads to oscillations of the electron population at the characteristic plasma frequency.

It is possible to obtain the expression for the plasma frequency by employing a fluid model, in which the plasma is composed of an electron and ion population (i.e. a two-fluid model). Again, the key assumption is that the ions remain static on the time scale of the electron oscillations. Perturbed fluid quantities, for example the density, are expressed in terms of an equilibrium value plus a perturbation, as shown in Eqn. (3.19) below. The perturbations may be written as a linear combination of sine and cosine waves, which accounts for any temporal dependence of the perturbed quantities. These are known as harmonic perturbations, and are expressed in Eqn. (3.20), below.

$$n_e \approx n_e^{(0)} + n_e^{(1)} \tag{3.19}$$

$$n_e^{(1)} = n_e^{(0)} \exp(-i\omega t) \exp(i\mathbf{k} \cdot \mathbf{x}) \tag{3.20}$$

To derive the plasma frequency it is sufficient to work in a 1D geometry, such that the spatial derivative of a fluid quantity becomes: $\nabla \rightarrow ik_x$, and temporal derivatives become $\partial/\partial t \rightarrow -i\omega$. It is further assumed that the perturbation terms are small compared to the equilibrium values, such that the product of two perturbation terms is negligibly small; this is known as linearisation. Applying the above assumptions to Eqns. (3.14) and (3.15), and applying Gauss' law, leads to the following set of linearised equations:

$$-i\omega n_e^{(1)} = -i n_e^{(0)} k_x u_x^{(1)} \tag{3.21}$$

$$\omega m_e u_x^{(1)} = -ieE_x^{(1)} \tag{3.22}$$

$$ik_x E_x^{(1)} = \frac{-e}{\epsilon_0} n_e^{(1)} \tag{3.23}$$

The plasma frequency describes the frequency at which the electron density perturbations oscillate. This is obtained by first rearranging Eqn. (3.22) for $u_x^{(1)}$ and substituting this into Eqn. (3.21). From here, the electric field is eliminated by rearranging Eqn. (3.23) for $E_x^{(1)}$ and substituting this back into Eqn. (3.21). This leads to the following expression:

$$\left(1 - \frac{n_e^{(0)} e^2}{m_e \epsilon_0 \omega^2}\right) n_e^{(1)} = 0 \Rightarrow \omega \equiv \omega_p = \sqrt{\frac{n_e e^2}{m_e \epsilon_0}} \tag{3.24}$$

where ω_p is the plasma frequency, as defined for electrons. The ion plasma frequency is obtained by replacing $n_e{=}Zn_i$ and $m_e{=}m_i$. This frequency is much smaller than the electron plasma frequency, due to the much higher ion mass, and is therefore ignored in many practical applications.

It was previously described that, for a plasma to exhibit collective behaviour, the plasma frequency must be greater than the frequency of electron collisions with neutral species within the plasma. The collision frequency is the inverse of the average time between collisions, τ_{coll}, estimated as follows:

$$\tau_{coll} = \frac{1}{v_{th} n_e^{1/3}} = \sqrt{\frac{m_e}{2k_B T_e}} \frac{1}{n_e^{1/3}} \tag{3.25}$$

where $v_{th} = \sqrt{2k_B T_e / m_e}$ is the electron thermal velocity, and n_e is the electron number density, which is assumed to approximately equal the number density of the neutral species. Given that $\omega_p{>}\omega_{coll}$, and substituting the expression for the plasma frequency (Eqn. 3.24), the following condition can be derived which describes whether collective effects are dominant within the plasma:

$$\Gamma = \sqrt{\frac{e^2}{2\epsilon_0 k_B T_e}} n_e^{1/6} {>} 1 \tag{3.26}$$

Assuming that the electon density is approximately $n_e = 10^{28}$ m^{-3}, which is typical of laser-solid interactions employing thin aluminium foils, and that the bulk electrons in the target remain cold (relative to the population of fast electrons with energy ∼1 MeV) such that $k_B T_e \sim 10$ eV, the parameter $\Gamma = 1.4$. This demonstrates that for the laser-solid interactions considered within this thesis, the electron dynamics are dominated by collective behaviour, and can be considered to be collisionless. From Eqn. (3.26), the collective behaviour is lost in the case of high temperature electrons in the target bulk (which occur during prolonged interaction with an ultra-intense laser pulse) and low electron density (for example, in laser-gas experiments or targets which undergo thermal expansion in a picosecond length laser pulse).

3.2 Propagation of electromagnetic waves in plasma

3.2.1 The plasma dispersion relation

The propagation of a laser pulse into a plasma can drive electron currents, which then act as a source of electromagnetic waves within the plasma. The relationship between the frequency and the wave vector of these electromagnetic waves is given by the dispersion relation. Assuming that the plasma is collisionless, i.e. that the average distance between electron-ion collisions is much greater than the dimensions of the plasma, the dispersion relation is written:

$$\omega^2 = c^2k^2 + \omega_p^2 \tag{3.27}$$

From the above expression, it is possible to define the group and phase velocities of waves propagating through the plasma, as follows:

$$v_g = \frac{d\omega}{dk} = \frac{c^2}{\sqrt{c^2 + \omega_p^2/k^2}} \tag{3.28}$$

$$v_p = \frac{\omega}{k} = \sqrt{c^2 + \omega_p^2/k^2} \tag{3.29}$$

The group and phase velocities are thus related by the expression $c^2 = v_g v_p$. From Eqns. (3.28) and (3.29), the refractive index can be derived, which describes how fast the wave propagates in vacuum, relative to how fast it propagates through the plasma. Assuming there are no dissipative effects, the refractive index is expressed in terms of the phase velocity as follows:

$$\eta = \frac{c}{v_p} = \sqrt{1 - \left(\frac{\omega_p}{\omega}\right)^2} \tag{3.30}$$

Eqn. (3.30) demonstrates that for light with a frequency less than the plasma frequency, the refractive index becomes imaginary, and the incident light is attenuated by the plasma. As the light interacts with the plasma, it drives perturbations in the electron density. However, if the incident light has a frequency less than the plasma frequency, the electrons are able to respond quickly enough to the perturbations to cancel them out, such that the associated wave cannot propagate.

Laser light at a frequency ω_L can therefore only propagate up to a critical density,

n_c, at which point the plasma frequency will equal that of the incident light. The critical density is defined as follows:

$$n_c = \frac{m_e \epsilon_0 \omega_L^2}{e^2} \tag{3.31}$$

The refractive index in Eqn. (3.30) can be re-written in terms of the ratio of the electron density to that of the critical density, yielding $\eta = \sqrt{1 - n_e/n_c}$, in which case it is clear that the refractive index becomes imaginary for plasmas with density exceeding the critical value. It is possible to classify a plasma as being overdense or underdense, depending on whether the electron density of the plasma is greater than, or less than, the critical density. The results chapters of this thesis will focus on plasmas produced via laser-solid interactions, which are initially highly overdense, but which become near critical density during the interaction. Whilst laser light may only propagate as far as the critical density surface in an overdense plasma, there is additionally a short region beyond the critical surface, over which the magnitude of the laser field decays exponentially (to $1/e$ of the peak value). This region is called the plasma skin depth, and is defined as $\ell_s = c/\omega_p$ [168].

3.2.2 Relativistic self-induced transparency

In the previous section, it was demonstrated that laser light at a frequency ω_L cannot penetrate much further than the critical density. However, the definition of the critical density in Eqn. (3.31), highlights an interesting phenomenon in relativistic laser-plasma interactions, known as relativistic transparency. As the a_0 of the laser pulse increases, the electron oscillations in the laser fields increase in magnitude, as does the electron Lorentz factor. For a linearly polarised laser pulse, these quantities are related by $\gamma_e \sim \sqrt{1 + a_0^2/2}$. The relativistic motion of an electron in an intense laser field means its mass increases by a factor γ_e, thus increasing the critical density defined in Eqn. (3.31). The relativistic critical density (n_e') is related to the non-relativistic expression as follows: $n_c' = \gamma_e n_c$. This increase in the critical density means that the laser can penetrate deeper into the plasma, and it is therefore more transparent than the non-relativistic prediction.

This transparency occurs when the electron density drops to a value $n_e \leq \gamma_e n_c$. There are then two ways by which this phenomenon can occur; via an increase in the electron Lorentz factor due to relativistic oscillations in the laser pulse, or by expansion of the target due to heating by the laser, causing a reduction in the electron density. Under experimental conditions, it is a combination of these effects which enable the target to go transparent, hence the process is referred to as relativistic self-induced transparency (RSIT).

For the discussion which follows, it is assumed that the laser has a Gaussian temporal intensity profile, which is typically true for the laser pulses employed experimentally. This temporal profile also means that the laser a_0 varies throughout the interaction, along with the γ_e value, therefore influencing the degree of transparency. As the laser rising edge interacts with the target, the surface is ionised. For laser-foil interactions, this produces an initially overdense plasma, in which thermal pressure causes it to expand into the vacuum. The number density of the plasma decreases exponentially with distance from the target surface. This plasma may then undergo RSIT by two different mechanisms, depending on whether the target thickness is comparable to, or much greater than, the plasma skin depth.

In the case of a thick target, whose dimensions exceed the plasma skin depth (i.e. $\ell \gg \ell_s$), the rising edge of the laser pulse is reflected from the overdense plasma when it encounters the critical density. As the intensity increases, the plasma electrons are pushed into the skin depth, forming a compressed layer of electrons. This results in a density increase within the skin depth, which prevents the target undergoing transparency at this point in the interaction [169]. The process of RSIT happens much later, around the peak of the pulse, at which point the Lorentz factor is sufficiently high, and the target has expanded to such a degree, that the condition for transparency is satisfied.

The process of RSIT is different in the case of thin targets [38, 47], where the intense laser radiation pressure may compress the target thickness to less than the skin depth [45]. Given that the relativistically corrected skin depth, $\ell_s' = \sqrt{\gamma_e}\ell_s$, has a dependence on the Lorentz factor, this process also occurs around the peak of the pulse. Skin depth transparency has been described via an analytical model in Ref. [170], in which the condition for the onset of this process is defined in terms of the areal density, ξ, as follows:

$$a_0 \sim \xi = \pi \frac{n_e}{n_c} \frac{\ell}{\lambda_L} \tag{3.32}$$

Investigations of the effects of RSIT on ion acceleration have motivated many recent studies. RSIT is expected to place a limitation on the maximum ion energies which can be achieved during pure radiation pressure acceleration, in which the radiation pressure exerted by the laser pulse is sufficient to drive the target to high velocities. It is clear that such an acceleration process requires that the target remain overdense throughout the interaction; if RSIT occurs at some point then the laser pulse will interact directly with the electrons in the target bulk, rather than reflecting off the target critical surface, therefore reducing the ion acceleration efficiency. However, studies of RSIT have also indicated that this direct interaction of the laser with the plasma electrons can enhance additional acceleration mechanisms, such as the break-out afterburner [50, 171], and transparency enhanced acceleration schemes [51–53].

3.3 Coupling of laser energy to plasma species

In this section, the mechanisms by which energy from the laser can be coupled to species within the plasma will be investigated. It is discussed in Ref. [6] that laser energy absorption is a complex topic, given that it typically is not the result of a single mechanism. Rather, the absorption mechanism may vary throughout the interaction, with the dominant mechanism depending on the laser parameters, such as intensity and pulse duration, as well as target parameters such as the electron density. Another key parameter on which the absorption depends is the spatial extent of the density gradient, the so-called 'scale length'.

As discussed in section 3.2.2, the interaction of the laser rising edge with the surface of an initially overdense target leads to rapid ionisation and the formation of a dense plasma. The thermal pressure within this plasma causes it to expand, at a speed approximately equal to the ion acoustic velocity, c_s.

$$c_s = \sqrt{\frac{Z^* k_B T_e}{m_i}} \tag{3.33}$$

Here, Z^* is the effective charge state, k_B is the Boltzmann constant and m_i is the ion mass. If the plasma is assumed to expand isothermally during heating by the laser [172, 173], then the density will drop off with an exponential profile over a characteristic distance known as the scale length, $L = c_s \tau_L$, where τ_L is the pulse duration.

The dominant absorption mechanism depends on whether the plasma is collisional or collisionless, a classification which again is related to the scale length. Collisionless plasmas are typically associated with a short scale length. On the contrary, plasmas with a long scale length, such as those heated with long nanosecond or picosecond duration laser pulses, tend to be collisional. In the context of this thesis, only collisionless plasmas will be considered. This is due to the fact that the electron-ion collision frequency scales as $T_e^{-3/2}$ [85]; since the electrons are strongly heated during interaction with an ultra-intense laser pulse, the electron-ion collision frequency, and therefore the role of collisions, is negligible for the laser parameters under consideration in this thesis.

3.3.1 Collisionless heating mechanisms

Resonance absorption

The resonance absorption mechanism occurs when an intense, linearly polarised laser pulse interacts with an overdense target at an oblique angle of incidence (with respect to the density gradient) [9–12]. As previously discussed, this intensity is sufficiently high to ionise the target surface, generating an expanding plasma with a density profile characterised by a scale length. Due to the oblique angle of incidence, and the linear polarisation, there will be a higher density on one side of the pulse compared to the other, as it propagates into the plasma. From Eqn. (3.30), it is clear that this means the refractive index differs on either side of the pulse, causing its path to curve. Complete reflection of the pulse occurs at a lower density for an obliquely incident laser pulse, compared to one which propagates at zero degrees (which is reflected at the critical density). The critical density for a laser pulse at an oblique angle of incidence is obtained as follows. The dispersion relation in Eqn. (3.27) must be modified to account for the fact that the wave vector now has components in the x and y directions:

$$\omega^2 = c^2(k_x^2 + k_y^2) + \omega_p^2 \tag{3.34}$$

It is then assumed that the deflection in the y direction is small, such that $k_y = (\omega/c)\sin\theta$ is approximately constant, with θ the angle of incidence. Similarly, the wave is assumed to be approximately parallel to the x direction, in which case $k_x = (\omega/c)\cos\theta{=}0$. This leads to the following modified dispersion relation:

$$\omega_p^2 = \omega^2(1 - \sin^2\theta) = \omega^2\cos^2\theta \tag{3.35}$$

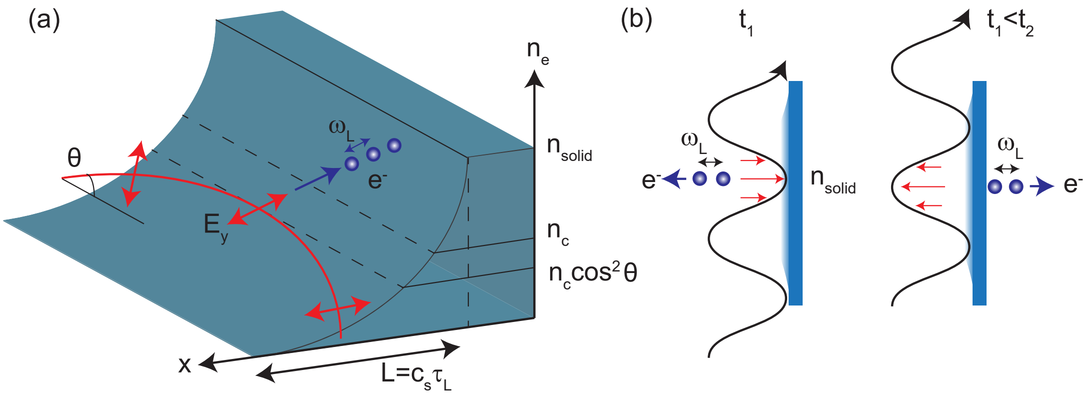

Figure 3.1: Illustrations of two collisionless absorption mechanisms. (a) Resonance absorption occurs for a plasma with sufficiently long scale length, irradiated at oblique incidence. (b) For much shorter scale lengths, $v_{osc}/\omega_L>L$, vacuum heating is the dominant absorption mechanism. The vacuum heating process is represented at two times in the interaction, t_1 and t_2, where $t_2>t_1$.

which yields the critical density for an obliquely incident pulse, n_{ob}, by substituting $\omega_p/\omega = n_e/n_c$, such that $n_{ob} = n_c \cos^2\theta$. In this expression, n_c is the previously defined critical density for a pulse incident at zero degrees. The incident laser pulse is then reflected when it encounters a density of n_{ob}, such that the laser electric field will point along the density gradient of the plasma, exciting a plasma wave. The oscillations of this wave propagate beyond the critical density surface, driving electron motion beyond the restoring force of the laser and enabling a net transfer of energy to the plasma bulk. This mechanism is illustrated in Fig. 3.1 (a).

Resonance absorption becomes the dominant heating mechanism when the scale length is sufficiently long, i.e. $L>v_{osc}/\omega_L$, and the intensity is in the range $10^{12}-10^{17}$ Wcm^{-2}. Beyond this intensity, relativistic effects become important, and alternative heating mechanisms such as $\mathbf{j}\times\mathbf{B}$ heating dominate the interaction.

Vacuum heating

If the scale length is small (i.e. when $L<v_{osc}/\omega_L$), an alternative heating mechanism known as vacuum heating, or ‘not so resonant’ absorption, becomes more efficient than the mechanism described in the previous section [174]. This vacuum heating becomes the dominant heating mechanism for a linearly p polarised laser interacting with a highly overdense target (with a sharp density gradient), at an oblique angle of incidence. Again, the laser is reflected when it encounters a density of n_{ob}, at which point the electric field points along the direction of the density gradient.

During the first half wave cycle, electrons are pulled out of the plasma into the vacuum. When the field reverses direction in the second half cycle, these electrons are re-injected into the plasma, with an energy equal to the ponderomotive potential (Eqn. (2.39)). These electrons propagate into the target beyond the critical density, where the restoring force of the laser pulse is weak, such that there is a net energy transfer to the plasma. A schematic of this process is provided in Fig. 3.1 (b) for two times in the interaction, t_1 and t_2, such that $t_2 > t_1$. The seminal paper on this mechanism, Ref. [174], predicts that vacuum heating becomes the dominant heating mechanism at an intensity of 10^{16} Wcm^{-2} (for a λ_L=1 μm laser), interacting with a sufficiently short scale length. The fraction of energy absorbed by vacuum heating is inversely proportional to the cosine of the angle of incidence, with respect to target normal. This highlights that this mechanism is most efficient when $\theta \sim 90°$.

$\mathbf{j} \times \mathbf{B}$ heating

For relativistic laser pulses, in which $I_L \geq 10^{18}$ Wcm^{-2} (at a wavelength λ_L=1 μm), the $\mathbf{v} \times \mathbf{B}$ component of the Lorentz force equation becomes comparable in magnitude to the electric field component. As described in section 2.1.2, this drives electron motion at a frequency of $2\omega_L$ along the laser propagation direction, in the form of a figure-of-eight trajectory in the average rest frame. The ponderomotive force associated with such motion may be expressed as [175]:

$$\mathbf{F}_p = -\frac{e^2}{4m_e\omega_L^2}\nabla\langle E^2\rangle\left(1 - \frac{1-\varepsilon}{1+\varepsilon}\cos 2\omega_L t\right)\hat{\mathbf{x}} \tag{3.36}$$

where ε is the degree of ellipticity of the laser polarisation, and $\hat{\mathbf{x}}$ is the propagation direction. The first term in Eqn. (3.36) is the (non-relativistic) ponderomotive force term which was introduced in section 2.1.3, which pushes electrons from regions of high to low laser intensity. It is the second term which is of most interest for electron heating and which describes the acceleration of electron bunches, at a frequency of $2\omega_L$, into the target. This process may accelerate electrons beyond the plasma critical density, where the laser fields decay in amplitude exponentially. The weaker restoring force on the electrons in this region enables them to propagate deeper into the target, again resulting in a net energy transfer to the plasma.

The second term in Eqn. (3.36) exhibits a strong dependence on the polarisation of the laser pulse. For example, employing circular polarisation, in which ε=1, causes this oscillating component of the ponderomotive force to vanish. Consequently, the degree of target expansion decreases, enabling the generation of a strong electrostatic field within the target. As will be discussed in section 3.4, it is this field which is responsible for accelerating the ions, and so circular polarisation is generally beneficial for ion acceleration.

Given that the focus of this thesis is the interaction of ultra-intense laser pulses ($\geq 10^{20}$ Wcm^{-2}) with overdense targets, at normal incidence, $\mathbf{j} \times \mathbf{B}$ heating is the dominant absorption mechanism.

3.4 Plasma based ion acceleration mechanisms

High-intensity laser-plasma interactions open up the exciting new possibility of directly accelerating solid targets to high velocities, using laser radiation pressure. As early as 1924, it was first proposed that radiation pressure from the Sun could be used to drive a sail, thus enabling interstellar transport [176]. This idea was developed theoretically by Marx in 1966 [37], in which the method of propulsion was instead a laser. Major interest was fueled in this potential method of transport, due to the prediction that the mechanical efficiency of such a system (i.e. the ratio of the energy of the 'sail' to that of the driving laser) tends to unity as the velocity of the sail approaches the speed of light [37, 177].

The principle of radiation pressure acceleration (RPA) can be described via a semi-classical argument, by considering the flux of momentum imparted to a solid target as it interacts with photons (in this case, photons of intense laser light). In this simplified description, the target is assumed to be rigid and completely reflecting, such that the incident light cannot be transmitted or absorbed, nor can it deform the surface of the target. These assumptions clearly break down for realistic laser-solid interactions, a caveat which will be discussed in detail in chapter 6. The number of photons incident on the target is an invariant quantity, however the photon energy depends on the frame of reference. In the laboratory frame, in which the target is boosted to velocities close to the speed of light, the reflected light will be Doppler-shifted to lower frequencies, and therefore lower energies. The relation between the frequency of the incident and reflected photons is as follows:

$$\omega_r = \omega_i \frac{1-\beta}{1+\beta} \tag{3.37}$$

where $\beta = v/c$ is the target velocity normalised to the speed of light. The difference in energy between the incident and transmitted light is then imparted to the target, causing it to accelerate. Thus, the mechanical efficiency of this process, η_m, may be written:

$$\eta_m = \frac{2\beta}{1+\beta} \tag{3.38}$$

It is then clear that in the ultra-relativistic regime, in which $\beta \to 1$, that the mechanical efficiency also tends to unity. This means that all of the incident laser energy can be used to accelerate the target.

Achieving ion acceleration via RPA is thus extremely desirable for experimentalists, as it may offer a means of producing ions with energies of hundreds of MeV [43, 178]. Theoretically, it is possible to access the RPA regime with current laser systems; for example in Ref. [179] it is stated that a 1 PW, 1 ps duration laser pulse could accelerate bunches of carbon ions to 0.8c. However, the above argument makes many limiting assumptions, the main issue being the assumption that the target behaves as a perfectly reflecting mirror. In reality this is not the case, since a typical overdense, solid target can still transmit laser light via the process of RSIT or skin depth transparency. The target may also absorb some of the laser light, coupling this into the heating of electrons, and the subsequent expansion of the plasma. Ref. [179] also assumes that the laser pulse has a step-like temporal profile; this inhibits the formation of a pre-plasma and enhances the efficiency of the acceleration process. Realistic laser pulses have a Gaussian temporal profile, and contain pre-pulses, which cause the target to pre-expand before the peak of the pulse arrives. This again leads to electron heating, and ion acceleration via the process of target normal sheath acceleration (TNSA). This has been studied extensively (see, for example, Refs. [15, 17–19]), and it is known that the maximum ion energy for this process scales with the square root of the laser irradiance. In the coming sections, it will be shown that the maximum ion energy during RPA scales with the laser irradiance, i.e. it exhibits a faster scaling than for TNSA. Whilst it is favourable then to operate in the RPA regime of ion acceleration, it has been calculated that intensities $\geq 10^{23}$ Wcm^{-2} are required before this becomes the dominant acceleration mechanism.

For RPA to become the dominant acceleration mechanism at currently achievable laser intensities, it is necessary to suppress the process of TNSA. One method by which this may occur is by employing circularly polarised laser pulses [180–182] to reduce the degree of target expansion. However, using circular polarisation raises an additional problem of target surface deformation. The Gaussian spatial profile of the pulse can deform the target surface, driving enhanced resonance absorption, which occurs due to the oblique angle of incidence between the laser field and the plasma density gradient. This is an even larger problem in the case of tight focusing, due to steep spatial gradients in the laser electric field, and is predicted to limit the efficiency of RPA in the case of the high intensities achieved by low F-number optics [183].

The process of RPA is broadly classified into two regimes, depending on the target thickness. Thin targets, with thickness only slightly greater than the plasma skin depth, are accelerated in the light sail regime of RPA. For targets in which $\ell \gg \ell_s$, acceleration occurs in the hole boring regime. Both will be described in the upcoming sections, whilst QED effects in these regimes are discussed in detail in chapters 6 and 7.

3.4.1 Radiation pressure acceleration: Light sail

The light sail regime occurs for targets with a thickness $\ell \sim \ell_s$. Experimentally, signatures of light sail acceleration have been observed for target thicknesses of 10 nm, interacting with laser pulses of intensity 3×10^{20} Wcm^{-2} [184]. This regime of RPA is highly favourable for ion acceleration, due to the prediction of high ion energies, emitted with a quasi-monoenergetic energy spectrum [38, 185].

The process of light sail acceleration is detailed in Refs. [38, 170, 185, 186] and summarised here as follows. As the laser pulse interacts with the front surface of the target, ponderomotive acceleration of the electrons drives them into the plasma skin depth. This produces a highly overdense layer of electrons known as the sail, which is driven forwards by laser radiation pressure. Since the ponderomotive force is inversely proportional to the mass of the accelerated species, it acts much more strongly on the electrons compared to the ions. For this reason, the ions are typically considered to be stationary on the time scale of electron ponderomotive acceleration. The separation of the accelerated electrons and the stationary ions leads to the formation of a region of depleted electron density, and the generation of an electrostatic field. The ions located

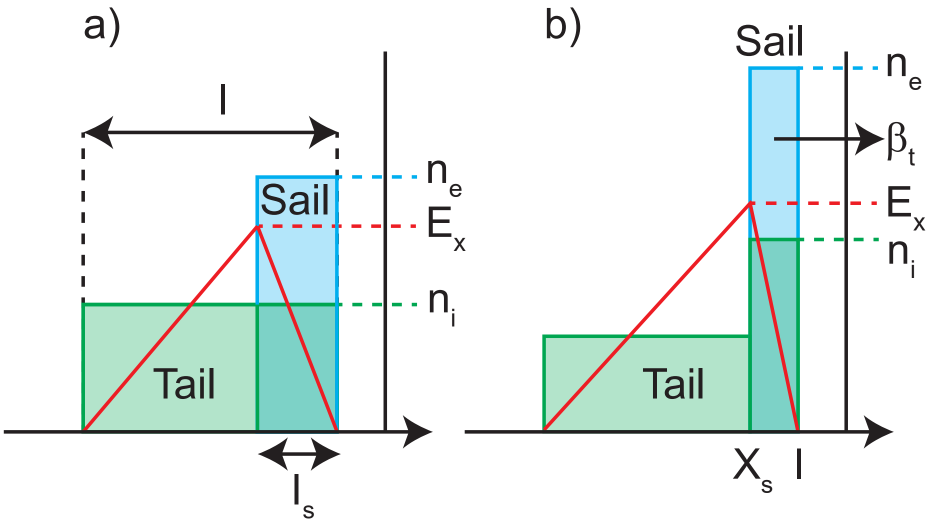

Figure 3.2: Cartoon illustrating the process of light sail acceleration. Ions within the target skin depth are accelerated as part of the sail, whereas the ion population located in the charge depletion zone, the so-called 'tail', is accelerated by space-charge effects. Adapted from Ref. [170].

within this depletion zone form a population known as the tail. Given the charge imbalance in the tail, these ions are accelerated by their own space-charge via a process known as Coulomb explosion [187].

Meanwhile, the compression of the electron sail proceeds until the electrostatic pressure within this layer balances the ponderomotive push of the laser. When equilibrium is achieved, the sail is driven efficiently by radiation pressure, such that ions within this region are pulled along at the light sail velocity, β_t. Since all of these ions originate from the same localised region, i.e. within the sail, they have approximately the same energy, and produce the desired highly peaked energy spectrum. It is important to note that the ions accelerated by their own space-charge are also present in the spectrum, leading to a pedestal-like feature; the entire spectrum is thus referred to as quasi-monoenergetic. The dynamics of the light sail process are illustrated in Fig. 3.2.

The equation of motion for a target undergoing light sail acceleration is derived as follows. The radiation pressure due to a laser of intensity I_L and frequency ω_L incident on a rigid target is given by $P_{rad} = 2\mathcal{R}I'_L/c$, where $\mathcal{R} \equiv \mathcal{R}(\omega')$ is the reflection coefficient of the target in its rest frame, denoted with a prime. In the target rest frame, the equation of motion is expressed in terms of the radiation pressure, as follows:

$$\frac{d}{dt}(\gamma_t\beta_t) = \frac{2I'_L\mathcal{R}(\omega')}{c^2}\frac{S}{M_t} \tag{3.39}$$

where $\gamma_t = (1-\beta_t^2)^{-1/2}$ is the target Lorentz factor and β_t is the light sail velocity normalised to the speed of light. Here, M_t is the total target mass and S is the target surface area, such that the mass per unit surface area can be replaced with the areal density, $\rho\ell$. Eqn. (3.39) is then transformed into the laboratory frame by Doppler-shifting the intensity, such that $I'_L = I_L(1-\beta_t)/(1+\beta_t)$. This yields the equation of motion described in Ref. [38]:

$$\frac{d}{dt}(\gamma_t\beta_t) = \frac{2}{\rho\ell c^2}I_L(t-X/c)\mathcal{R}(\omega')\frac{1-\beta_t}{1+\beta_t} \tag{3.40}$$

In Eqn. (3.40), $dX/dt = \beta_t c$, and it is assumed for this case that $\mathcal{R} = 1$. This integral may then be re-written using separation of variables, as follows:

$$\int_{-1}^{1}\gamma_t^3 d\beta_t = \int_0^t \frac{2I_L}{\rho\ell c^2}\frac{1-\beta_t}{1+\beta_t}dt \tag{3.41}$$

which is solved by a change of variable to the retarded time, $\phi = t(1-\beta_t)$, and following the method outlined in Ref. [177].

$$\int_{-1}^{1}\gamma_t^3 d\beta_t(1+\beta_t) = \int_0^{\phi}\frac{2I_L(\phi')}{\rho\ell c^2}d\phi' \tag{3.42}$$

The term on the right of Eqn. (3.42) is referred to as the laser fluence, $F = \int_0^{\phi} I_L(\phi')d\phi'$, whilst the left hand side can be solved analytically, yielding the following result for the light sail velocity [38]:

$$\beta_t = \frac{(1+\xi)^2-1}{(1+\xi)^2+1} \quad \text{where} \quad \xi \equiv \xi(\phi) = \frac{2F(\phi)}{\rho\ell c^2} \tag{3.43}$$

The time dependence of the light sail velocity is introduced through the expression for the fluence, which can account for a pulse with any chosen temporal profile. The target velocity can then be used to determine the ion energy per nucleon, as follows:

$$E_i(\phi) = m_i c^2\frac{\xi(\phi)^2}{2(\xi(\phi)+1)} \tag{3.44}$$

Given that $\xi \sim I_L \tau_L$ for a top-hat pulse (where τ_L is the pulse duration), it is clear that the scaling of ion energy with the laser intensity is more favourable in the light sail regime, compared to that of TNSA (in which $E_i \propto \sqrt{I_L \lambda_L}$).

The above discussion has focused on the case where the target acts as a perfectly reflecting mirror, via the assumption that $\mathcal{R} = 1$. For light sail to become the dominant acceleration mechanism at current laser intensities, it is necessary to employ ultra-thin foils, of thickness $\ell{\sim}10$ nm. These targets are likely to undergo RSIT during the interaction, which effectively switches off RPA since the laser no longer has a rigid target to reflect off. The effect of RSIT may be accounted for by expressing the reflection coefficient, $\mathcal{R} \leq 1$, as a non-linear function of the target areal density and the normalised laser intensity. Such a function is derived in Ref. [38], by modelling the target foil density in terms of a delta function. The reflection coefficient in this case becomes:

$$\mathcal{R} = \left\{ \begin{array}{ll} \zeta^2/(1+\zeta^2), & \text{for } a_0 \leq \sqrt{1+\zeta^2} \\ \zeta^2/a_0^2, & \text{for } a_0 \geq \sqrt{1+\zeta^2} \end{array} \right\}$$

where $\zeta = \pi \frac{n_e}{n_c} \frac{\ell}{\lambda_L}$ is the target areal density. In Ref. [38], it is concluded that the threshold at which RSIT occurs is when $\zeta \sim a_0$. It is further demonstrated that the effect of the non-linear reflection coefficient on the light sail velocity is significant when $a_0 {>} \zeta \approx 1$. This condition is typically not satisfied experimentally, given that achieving $\xi \sim 1$ requires nanometer thick foils.

Finally, it is worth noting that different behaviour emerges for targets with thickness $\ell \leq \ell_s$. This regime is referred to as the 'leaky light sail', and has been experimentally observed in Qiao *et al* [188]. Here, the laser electric fields do not decay in magnitude within the target, since the thickness is less than the skin depth. In the most intense region of the focal spot, the target is transparent to the laser light, and so the electrons in the target bulk are ponderomotively accelerated by the transmitted laser light. In addition, the laser fields which appear at the rear then pull electrons from the target rear surface, causing them to 'leak' into the vacuum. For a target made of a single ion species, this is disastrous in terms of ion acceleration; the electrons are ejected from the focal spot, rather than being compressed into the skin depth and forming a sail. The situation is different if the target is composed of multiple ions species, especially if the target contains a high and low Z component. Qiao *et al* [188] suggests that the surplus of electrons from the high Z ions stabilise the low Z species against space-charge effects, leading to more stable acceleration than the standard light sail case. It is predicted that 100 MeV protons can be generated via this scheme, by irradiating nanometer thick CH targets with a laser pulse at an intensity of 10^{20} Wcm^{-2} [188].

3.4.2 Radiation pressure acceleration: Hole boring

The hole boring regime occurs for targets which are much thicker than the skin depth $\ell \gg \ell_s$ [179, 189–193]. In an analogous manner to the light sail regime, the laser ponderomotive force drives the electrons into the plasma. This leaves a region of depleted electron density, across which an electrostatic field forms, and subsequently accelerates the ions. Within the dense layer of electrons, an equilibrium between the ponderomotive force and electrostatic pressure is established, and the entire layer is driven forwards by radiation pressure. However, unlike in the light sail regime, the compressed electron layer is not localised to the rear of the target and is instead driven into the target bulk at a velocity known as the hole boring velocity. As this layer propagates into the target, it drives an electrostatic shock, which reflects the ions downstream. The hole boring regime is then characterised by a double layered structure of electrons and ions, which is maintained by radiation pressure. This structure is illustrated in Fig. 3.3, whilst an example from a 1D PIC simulation is provided in Fig. 3.4. In many cases, this structure is referred to as the laser-piston. As pointed out in Ref. [190, 191], there is a subtle difference between the hole boring and laser-piston regimes. The laser-piston refers to a specific case in which the laser pulse is completely reflected from the compressed electron layer, driving a quasi-static structure with an extremely high Mach number $\simeq$6.5. For Mach numbers greater than this value, it is not possible for electrostatic shocks to develop [194], thus it is more correct to refer to this as the laser-piston regime.

An expression for the piston velocity can be derived by balancing the electromagnetic and mass momentum flows (assuming a planar geometry). These equations are written as follows:

$$(1-\mathcal{R})(1-\beta_p)I_L = (\gamma_i - 1)Mn_i\beta_p c^3 \tag{3.45}$$

$$(1+\mathcal{R})(1-\beta_p)\frac{I_L}{c} = Mc^2\gamma_i\beta_p\beta_i \tag{3.46}$$

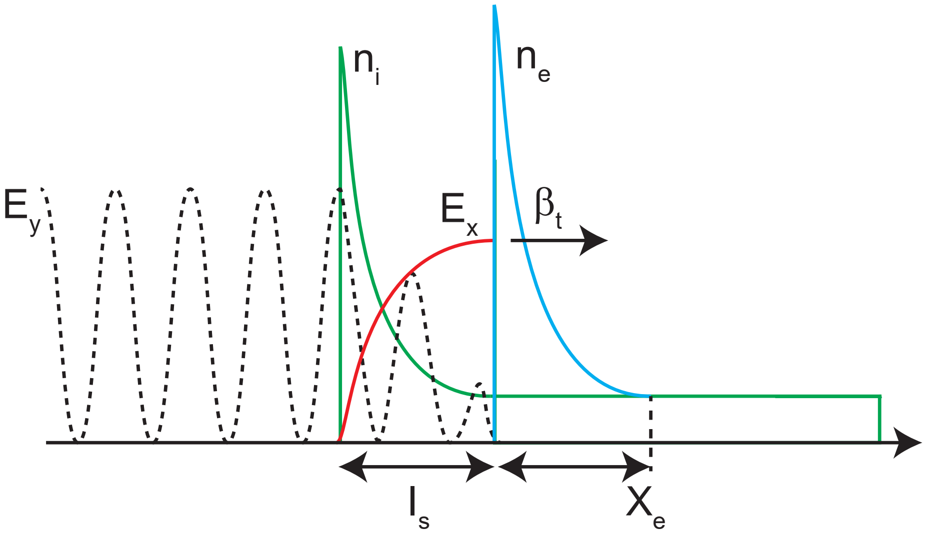

Figure 3.3: Cartoon illustrating the double layered laser-piston. Laser radiation pressure drives the piston structure into the target bulk at a velocity β_t, associated with a high Mach number $\simeq 6.5$. *Adapted from Ref. [190].*

where β_p is the velocity of the piston which reflects the ions (and which is assumed to have a quasi-stationary structure), $\gamma_i = (1-\beta_i^2)^{-1/2}$ is the ion Lorentz factor and $\mathcal{R}$ is the reflection coefficient. This set of equations is reduced by expressing the ion Lorentz factor in terms of the piston velocity, as follows:

$$\gamma_i - 1 = \frac{1+\beta_p^2}{1-\beta_p^2} - 1 = \frac{2\beta_p^2}{1-\beta_p^2} \tag{3.47}$$

The laser intensity may be normalised such that $I = \alpha m_e c^3 n_c a_0^2$, where n_c is the critical density and $\alpha = 1, 1/2$ for circular and linear polarisations, respectively. The energy and momenta equations are then written:

$$(1-\mathcal{R})(1-\beta_p) = \frac{2\beta_p^2}{1-\beta_p^3}\frac{Mn_i}{m_e n_c a_0^2} \tag{3.48}$$

$$(1+\mathcal{R})(1-\beta_p) = \frac{2\beta_p^2}{1-\beta_p^2}\frac{Mn_i}{m_e n_c a_0^2} \tag{3.49}$$

The above equations are further simplified by re-writing them in terms of a dimensionless piston parameter, B, which is defined as follows:

$$B = \sqrt{\frac{n_c}{n_i}\frac{m_e}{m_e + Zm_i}a_0^2} = \frac{I_L}{\rho c^3} \tag{3.50}$$

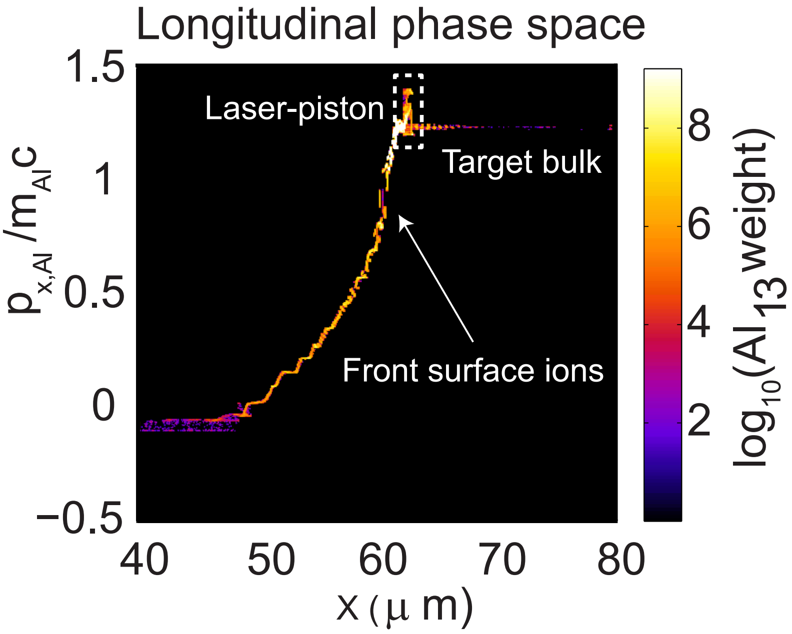

Figure 3.4: Simulation result demonstrating the acceleration of ions in the laser-piston regime. This piston appears as a localised region of high momentum in the longitudinal phase space distribution. The target in this case is a 500 nm thick Al foil, interacting with a laser of intensity 10^{23} *Wcm*$^{-2}$

The velocity is obtained by adding Eqns. (3.48) and (3.49) to eliminate $\mathcal{R}$. This produces a quadratic equation, with a physical root given in Eqn. (3.51), below.

$$\beta_p = \frac{B}{1+B} \tag{3.51}$$

The above equation describes the fully relativisitic piston velocity in the absence of QED effects. It is important to note that for intensities $\geq 10^{23}$ Wcm^{-2}, a substantial fraction of the laser energy is converted into radiation. To generalise the above results to a regime in which QED effects are important, it is therefore necessary to include the photon energy and momenta in the conservation equations [62, 63]. A detailed description of QED effects within the hole boring regime is provided in chapter 7.

A key difference between the two regimes of RPA is that the light sail velocity (Eqn. (3.43)) has an explicit dependence on the target thickness, whilst in the hole boring regime the target is assumed to be infinite, and so the velocity (Eqn. (3.51)) must be independent of the target thickness.

3.5 Conclusions

In this chapter, the collective dynamics of electrons within a plasma have been described. The key differences between a plasma and an ionised gas were discussed, along with the parameters which can be used to classify a plasma, such as the Debye length, the plasma frequency and the critical density. A number of important processes, such as wave propagation, laser energy absorption, ion acceleration and transparency, were also discussed in detail. At ultra-high intensities, these plasma physics processes will become strongly intertwined with QED effects. Theories investigating the interplay between these are still in their infancy, and do not completely describe the predicted phenomena. The research which follows in chapters 6 and 7 may help in this regard, by probing the energy partition, particle dynamics and pair-production rates in QED plasmas (i.e. plasmas in which high energy radiation generation, RR and pair-production will influence the collective electron dynamics).

Chapter 4

Methodology

The results presented in this thesis are obtained via a combination of experimental studies, numerical simulations, and theoretical modelling. The aim of this chapter is to describe the techniques used, and to tie together the experimental and numerical aspects. First, a description of the laser technology employed in current high power systems is provided. This is followed by a specific example, the Astra-Gemini laser system, which is used to make the measurements presented in chapter 5. Technologies which will enable the realisation of ultra-high intensity ($\geq 10^{22}$ Wcm^{-2}), high repetition rate systems ($\geq$ 10 Hz) will be briefly reviewed, followed by descriptions of two upcoming multi-petawatt (PW) lasers, namely APOLLON and ELI-NP. These will provide the ultra-high intensities required to investigate the strong-field QED effects forming the work explored in chapters 6 and 7. The second part of this chapter will focus on the diagnostic techniques used throughout this thesis, including the technique of polarimetry used extensively in chapter 5. The final part of this chapter is then devoted to numerical tools, namely numerical simulations utilising the particle-in-cell (PIC) approach, which are employed in all three results chapters. The physics underlying QED-PIC codes, along with the limitations of this approach, are explored in detail.

4.1 High power laser technology

4.1.1 Current laser technology

From the inception of the laser in the 1960s [1], up until 1985, the peak intensity achievable by laser systems was limited to $\sim 10^{16}$ Wcm^{-2}, well below the threshold for relativistic electron motion in the laser fields, which occurs at $\geq 10^{18}$ Wcm^{-2} (for λ_L=1

μm). This restriction was imposed by the damage threshold of optics within the system, such as the neodymium-glass typically employed as a gain medium (at that time, however titanium-sapphire (Ti:S) has become a popular gain medium in more recent years). Propagating pulses with short duration through these optics deposits an energy fluence which is sufficiently high that it can cause serious damage to the laser chain. Even for laser pulses with intensities orders of magnitude below the damage threshold, it was found that non-linear optical effects, such as self-focusing (which results in an enhancement of the peak laser intensity) [78, 195, 196] and self-phase modulation (which can lead to pulse duration compression) [195, 197] cause the propagating laser pulses to approach the damage threshold.

The importance of non-linear effects is characterised by the so-called 'B-integral', a parameter which corresponds to the non-linear component of the refractive index, and is defined as follows:

$$B = \frac{2\pi}{\lambda_L} \int_0^L n_2 I_L(z) dz \tag{4.1}$$

where $n_2 I_L$ is the component of the refractive index which depends on the laser intensity, I_L. The dimensionless B-integral defined in Eqn. (4.1) can be considered to be the additional phase acquired by a laser pulse, propagating over a path length L, through a medium.

It was the application of the chirped pulse amplification (CPA) technique to laser systems, in 1985, which finally enabled focused intensities to be pushed into the relativistic regime [198]. The key principle of CPA is that the pulse is temporally stretched, from femtoseconds to nanoseconds in duration, before it enters the amplifiers. Since the energy of the pulse remains approximately constant, temporal stretching reduces the intensity of the pulse, leading to a reduction in the amplitude of non-linear effects which previously restricted the peak intensity of high power laser systems. After amplification, the pulse is re-compressed down to a pulse duration in the range ten femtoseconds to picoseconds, enabling the generation of short, relativistically-intense laser pulses.

The stretching of the laser pulse by a factor of $10^3 - 10^5$ is achieved by introducing group velocity dispersion to the propagating light (for example, by employing a diffraction grating or prism). This separates the wavelengths of the incident laser light, such that the shortest wavelengths can be sent along a longer path than the long wavelengths. This relative delay of the wavelengths (and therefore the frequencies) within the pulse is known as chirping, hence the scheme is referred to as chirped pulse amplification. After amplification, the pulse is compressed again by reversing the group velocity dispersion, such that the initial chirping effect is reversed. A schematic diagram of CPA is provided in Fig. 4.1.

CPA is a technique which is employed routinely in high power laser systems, and has revolutionised the field of laser-plasma physics. The importance of this work is reflected by the fact that its pioneers were recently awarded the Nobel Prize in Physics [199]. It does, however, have limitations. For example, the diffraction gratings typically used to stretch and compress the laser pulses are still restricted by damage thresholds. In addition, CPA causes amplification of all the light which passes through the system; this leads to the amplification of the spontaneous emission which arises during pumping of the gain medium. This produces so-called 'amplified spontaneous emission' (ASE), which is undesirable as it is incoherent, and reduces the gain within the system. In addition, ASE reduces the temporal intensity contrast of the laser pulse. This describes the ratio of the intensity at the peak of the pulse, to the intensity typically at picosecond and nanosecond scales before and after the peak of the pulse. Typically, the peak is preceded by a pedestal in the temporal intensity contrast, which arises due to ASE and uncompensated dispersion. A high level of ASE means the intensity of light in the pedestal is sufficiently high that it can, for example, induce early heating of ultra-thin foil targets before the peak of the laser pulse arrives. CPA systems are therefore restricted by high levels of ASE, and poor contrast, in comparison to the additional techniques that will be discussed.

To improve the laser temporal intensity contrast, the technique of optical parametric chirped pulse amplification (OPCPA) is often employed in high power laser systems [200–202]. This is a non-linear process by which energy is resonantly transferred from a high-intensity pump beam into a lower frequency signal beam. Energy conservation leads to the production of a third beam, named the idler, such that the sum of the frequencies of the idler and the signal beams equals the frequency of the pump beam. This process is illustrated in Fig. 4.2. The non-linear crystals used in OPCPA schemes are typically beta-barium borate (BBO) [203], which are employed as they offer high bandwidth amplification and high damage thresholds, as well as amplification over a wider range of central wavelengths, compared to the Ti:S crystals typically used in CPA [200].

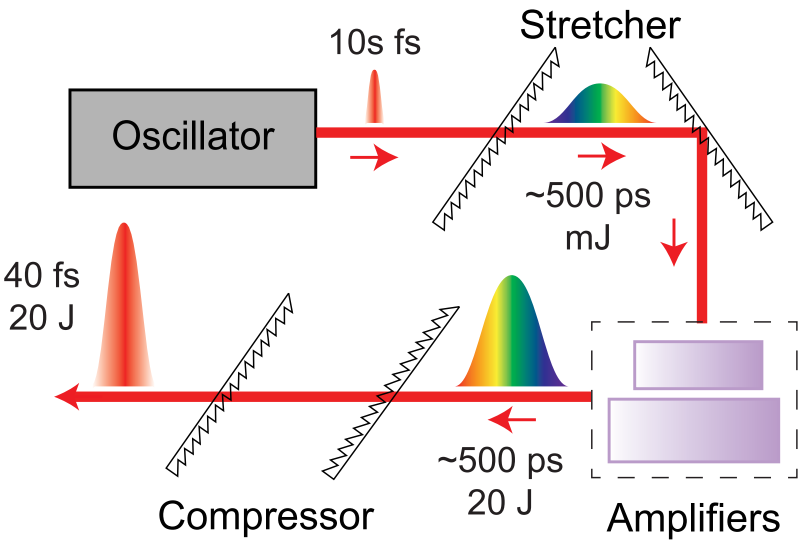

Figure 4.1: Schematic diagram illustrating the process of chirped pulse amplification (CPA). The laser parameters in this case are similar to those of the Astra-Gemini laser system.

An OPCPA set-up generally includes a diode pumped CPA stage in order to provide the pump pulse [202]. For example, Fig. 4.2 shows a scheme in which a low energy, short duration pulse emerging from an oscillator is first temporally stretched and then split, such that part of the pulse is passed to the OPCPA crystal, whilst the other is diverted to a CPA stage, for example a Ti:S or Yb-based amplifier. This amplifier is pumped by a high-repetition rate diode pump laser. The light produced in the CPA stage is then frequency-doubled, and used in turn to pump the OPCPA crystal [204]. This frequency-doubled pulse acts as the pump beam, which is then used to amplify the signal beam (i.e. the short pulse generated by the oscillator).

OPCPA has a number of advantages over CPA. Firstly, the amplification only significantly occurs when the pump and signal beams are phase matched. Any other light in the system therefore remains unamplified, thus significantly reducing the level of ASE. This mechanism also works for a much wider range of wavelengths than CPA (the only restriction is the range of wavelengths which can be transmitted through the non-linear crystal). This process is also very efficient; the energy is resonantly transferred from the pump to the signal and idler beams, without depositing a significant amount of energy in the crystal as heat. Finally, OPCPA also enables much higher gain during a single pass, reducing the need for multi-pass and regenerative amplifiers. The disadvantage of this approach is that, in order to access the required non-linear effects within the crystal, it is necessary that the pump beam has a high intensity.

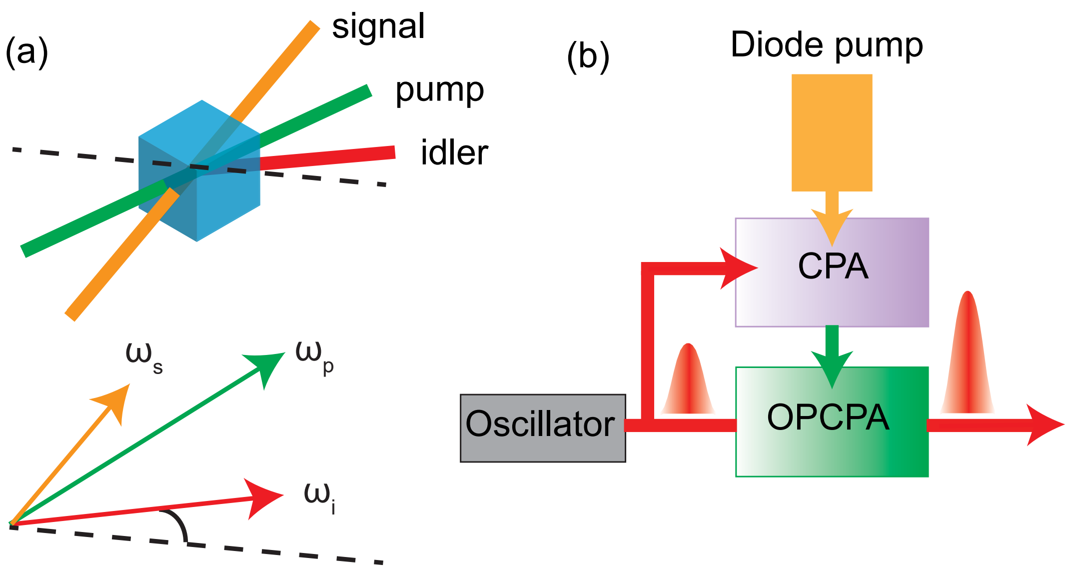

Figure 4.2: A schematic of the OPCPA process (a) The pump and signal pulse overlap within the OPCPA crystal, amplifying the output signal and generating an idler pulse. (b) An illustration of a diode pumped CPA stage being used as the pump pulse in an OPCPA amplifier.

This is typically achieved by either focusing the pump beam to a small spot within the crystal, or by pumping with high energy, hence the necessity of CPA to drive the OPCPA process. Examples of OPCPA based laser systems include the PHELIX laser at GSI, Darmstadt, and the Vulcan laser at the Central Laser Facility. Currently this system operates at 1 PW, however there are plans to upgrade to 10 PW operation in the future [205]; this demonstrates that OPCPA is an example of high power laser technology which will enable the next generation of lasers to be realised.

4.1.2 Current laser systems: The Astra-Gemini laser system

The experimental results presented in chapter 5 of this thesis were obtained using the Astra-Gemini laser system at the Rutherford Appleton Laboratory [206, 207]. This system is capable of delivering two short, 40 fs laser pulses, with energies of up to 15 J, leading to a peak power of 0.5 PW in each of the laser pulses. These pulses have a central wavelength of λ_L=800 nm, with a bandwidth of 40 nm, such that the laser is in the near-IR region of the electromagnetic spectrum. The system operates with a repetition rate of one full power shot every 20 seconds. A unique aspect is that it can be used in a dual beam configuration. This makes it highly applicable for QED experiments employing beam-beam interactions. For example, one of the beams can be focused using a relatively long F-number optic ($F/20$ to $F/40$) to generate a relativistic electron beam, which then collides with the second laser beam, focused to high intensity with a short F-number optic ($\sim F/2$) [130, 131]. The dual beam configuration also enables the exploration of exotic experimental set-ups, such as colliding lasers with different polarisations, as well as using one of the beams for ultra-fast probing of the plasma dynamics by frequency doubling, delaying, or temporally stretching the pulse. Astra-Gemini is an ideal choice of laser for the experimental campaign described in chapter 5, which measured changes in the polarisation state of light detected at the rear of ultra-thin foil targets. Intense laser interactions with such foils require a laser with a high temporal intensity contrast, and short pulse duration, to prevent a significant degree of target pre-heating before the peak of the pulse arrives. Astra-Gemini has a temporal intensity contrast ratio of 10^8 at 5 ps before the peak of the pulse (after reflecting from dual plasma mirrors, as will be described in section 4.1.3), which is sufficient to enable ultra-thin foils to be employed.

In common with many high power laser systems, Astra-Gemini uses an oscillator to generate a low energy seed pulse, which is subsequently amplified using the technique of chirped pulse amplification (CPA) [198]. The oscillator is composed of a Ti:S crystal, which is then mode-locked to produce a train of short pulses. Mode-locking is a process by which a fixed phase is introduced between the longitudinal modes within a laser cavity. Constructive interference between these modes then produces a short pulse of light. Mode-locking within the Astra-Gemini oscillator enables a train of 12 fs duration pulses to be produced, with an average power of 550 mW. These pulses are then stretched to a duration of ~500 ps before amplification, in the first stage of the CPA process. The Astra-Gemini laser uses transmission gratings to stretch the pulses, which reduce the level of ASE compared to a diffraction grating, therefore producing pulses with a higher temporal intensity contrast. These are then sent to the pre-amplifier, which consists of a multi-pass Ti:S crystal, pumped by a green neodymium YLF laser. The pre-amplifier boosts the energy of the pulses to 800 mJ, and a combination of a Pockels cell and polarisers are used to cut the pulse train down to a frequency of 10 Hz, with these pulses then being passed to the main amplifier chain.

The stretched pulses then enter a chain of three amplifiers, which increase in size successively, along with the beam diameter, in order to reduce the fluence below the damage threshold of the optics. The first amplifier is a 10 mm thick Ti:S crystal, pumped on both sides by a frequency-doubled neodymium YAG (Nd:YAG) laser with an energy of 90 mJ. The pulses pass through the crystal four times, to extract as much energy as possible, reaching 4 mJ on the final pass. These are then passed through a spatial filter, and expanded in diameter so they can continue into the next amplifier. Improvements to the beam quality are achieved by using wedged optics to eliminate internal reflections. The second amplifier is another multi-pass TiS crystal, this time pumped with 300 mJ of energy by a frequency-doubled Nd:YAG laser. This amplifier boosts the pulse energy to 120 mJ, after which it is expanded to a diameter of 18 mm before it enters the third amplifier. The third multi-pass amplifier again uses a Ti:S crystal, now pumped by four frequency-doubled Nd:YAG lasers, which impart a maximum energy of 4.5 J to the crystal. In this final Astra amplifier, the energy of the pulse is boosted to 1.2 J, with the quality of the pulse improved through the use of another spatial filter, and expanded to a diameter of 31 mm.

At this stage, the pulses are sent to the Gemini amplifiers, in a pulse train operating at 5 Hz. The energy of the laser can be controlled via a slide in attenuator, enabling a reduction in the energy by two orders of magnitude if necessary. The pulses which enter the Gemini chain are split into two paths, each of which is then amplified by a multi-pass amplifier to an energy of ∼20 J. The final stage in the chain is to then re-compress the pulse via another transmission grating, which reduces the duration down to 40 fs. Finally, the alignment of the Astra-Gemini system is maintained through the application of a series of deformable mirrors, which account for changes in the pointing and central position of the beam. These deformable mirrors allow for pointing and wavefront errors, arising from thermal effects due to extended use of the system, to be controlled.

4.1.3 Future laser technology

As mentioned in section 4.1.1, the invention of CPA enabled a rapid increase in focused laser intensities, from 1985 onwards. Similarly, the invention of mode-locking, in the 1960s, was the first step towards the development of laser pulses with progressively shorter duration [7, 8]. Subsequent developments in laser technology (such as mode-locking via the non-linear Kerr effect [8]) have enabled pulse durations to decrease from picoseconds, down to tens of femtoseconds. It is proposed that attosecond laser pulses will be generated at the Extreme Light Infrastructure [208], which have applications in ultra-fast imaging, such as probing the dynamics of electrons during chemical reactions. Decreasing the pulse duration is one method by which ultra-intense laser pulses will be generated at future laser facilities.

As well as moving towards shorter pulse durations, future laser systems will also operate at higher repetition rates. In particular, laser pulses with nanosecond duration, produced at high repetition rates of $\geq$10 Hz, are required in order to pump the CPA stages in OPCPA amplifiers. Currently, the repetition rates of laser systems are restricted by the flash lamps which are used to pump the amplifiers. Typical nanosecond amplifiers driven by flash lamps can achieve repetition rates of only a few shots per minute for pulses with an energy $\sim$10 J [209]. In addition to producing low repetition rates, flash lamps give rise to extremely low electrical-to-optical efficiency, in most cases <1%. It is therefore crucial that multi-PW laser systems and beyond replace flash lamp technology with diode pumped solid state lasers, which rely on gain media such as Nd:YAG. Such systems can achieve higher efficiencies of 10-50%, however there are numerous technological limitations which must be overcome in order for them to become widely used. These include a slightly reduced beam quality, and less efficient harmonic generation, in comparison to flash lamps [209].

The potential for diode pumped laser technology has been demonstrated by the DiPOLE (Diode Pumped Optical Laser for Experiments) system at the Central Laser Facility [210], which has delivered 100 J of energy in 10 ns laser pulses, at a repetition rate of 10 Hz. This has achieved the highest efficiency recorded to-date for a diode pumped laser, at $\sim$22.5%. The DiPOLE amplifier consists of four Yb:YAG discs, placed inside an insulated pressure vessel, through which cryogenic helium is passed. The amplifier is then pumped by two diode pumped lasers at 940 nm, and produces amplified light with a central wavelength of 1030 nm. DiPOLE has demonstrated the technology of high energy, diode pumped lasers, which are extremely likely to be key components in upcoming multi-PW lasers.

Plasma mirror technology

In addition to increasing the power of laser pulses, the intensity frontier may be pushed further by employing low F-number ($\leq F/1$) focusing optics to achieve tight-focusing conditions, i.e. a focal spot with a size near the diffraction limit of the laser wavelength. As the peak intensities of multi-PW systems increases, it is also necessary to improve the

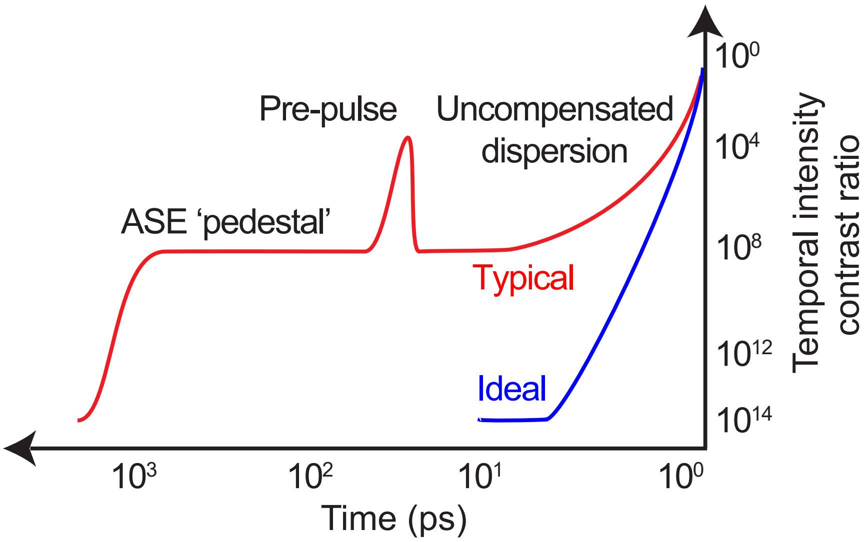

Figure 4.3: Plot of the temporal intensity contrast ratio as a function of time, comparing the ideal case (blue) and the case for a typical high power laser pulse (red).

temporal intensity contrast of the laser pulse. In this section, the plasma mirror and the focusing plasma mirror will be discussed, since the latter optic provides an enhancement of both the peak intensity and the temporal intensity contrast of a high power laser pulse. This will enable the realisation of laser pulses which could be employed to experimentally test the QED effects presented in chapters 6 and 7.

As discussed in section 4.1.2, the temporal intensity contrast is the ratio of the peak laser intensity, to the intensity on the scale of nanoseconds and picoseconds before or after the peak of the pulse arrives, as illustrated in Fig. 4.3. In a high power laser system, ASE and uncompensated dispersion together produce a pedestal in the temporal intensity contrast, a region of intensity at $\sim 10^{12}$ Wcm^{-2}, which arrives nanoseconds before the peak of the pulse. This is undesirable as it leads to heating of a target before the peak of the laser arrives; in the case of ultra-thin foils, it may result in the target undergoing significant expansion during interaction with the rising edge of the laser pulse, such that the peak of the pulse interacts with an underdense plasma. Typical high power lasers achieve a temporal intensity contrast ratio ranging from $<10^8$ at the 5 ps level, and $<10^{11}$ at 1 ns in the case of Astra-Gemini, up to $<10^{12}$ at 1 ns for lasers such as APOLLON [211], which will be introduced in the next section. The importance of this parameter becomes clear when considering next generation facilities such as ELI-NP, which are expected to produce peak intensities exceeding 10^{23} Wcm^{-2}. Even with an exceptional contrast, the pedestal will be of the order $\sim 10^{12}$ Wcm^{-2}, which when focused onto a target will cause a significant degree of pre-ionisation and expansion prior to the main pulse.

Experimentally, one method by which the temporal intensity contrast can be improved is by employing a plasma mirror, a tool described in detail in Refs. [212–214]. This is typically a slab of optical quality glass or plastic with an anti-reflective coating (in order to enhance the transmission in its non-plasma state), which improves the contrast by removing the pedestal. The plasma mirror is positioned such that the rising edge of the laser pulse is below the ionisation threshold of the mirror when it arrives, and is therefore transmitted. As the rising edge of the laser pulse interacts with the mirror, it causes the surface to rapidly ionise, producing a dense plasma. The remainder of the pulse then reflects off this overdense plasma, continuing on to interact with the target. The key point is that the pedestal has been suppressed such that the target is less likely to undergo significant heating during interaction with the rising edge of the laser pulse. This improvement, however, comes at a cost, since it results in a reduction in the laser energy which arrives on target. This is because the laser pulse is not only transmitted through the optic, but is also absorbed and used to ionise the surface of the plasma mirror. For example, the double plasma mirror set-up employed in chapter 5 reduces the energy arriving on target by ∼52%.

An extension of this idea has been presented in Refs. [215, 216], in which an ellipsoidally curved, focusing plasma mirror was developed to not only improve the temporal intensity contrast of the pulse, but also focus it to a focal spot size comparable to the laser wavelength. In this case, the optic is a plastic slab in the shape of an ellipsoid. One of the foci of the ellipse is positioned at the focal spot of the laser system (focused using a conventional off-axis parabola, OAP), enabling re-imaging of the spot at the second focus, where the target is placed. The re-imaged spot is demagnified by a factor determined by the parameters of the ellipse; in Ref. [216], this is ∼3x, for a laser of wavelength λ_L=1054 nm. The demagnification of the focal spot results in a significant intensity enhancement, relative to the input focal spot. These optics are single-use and disposable; this offers a huge advantage over focusing using a solid-state $F/1$ optic, which would otherwise be damaged by debris or high intensity back reflections, as a result of the relatively short focal length. These focusing plasma mirrors will be crucial at upcoming laser facilities, both for delivering ultra-intense laser pulses, as well as cleaning the temporal intensity contrast such that ultra-thin foil targets can be employed.

4.1.4 Future laser systems

Multi-Petawatt laser systems: APOLLON and ELI-NP

The current generation of PW lasers have enabled the first investigations into QED effects such as radiation reaction [130, 131], and pair-production via the Bethe-Heitler process [73, 217]. To further investigate these processes, and to explore higher order QED effects, it will be necessary to employ multi-PW lasers. For example, the high-field physics effects described in chapters 6 and 7 are observed at focused laser intensities of $\geq 10^{23}$ Wcm^{-2}. These intensities are expected to be achieved at multi-PW laser facilities, including APOLLON [211, 218] and ELI-NP [219]. In this section, a brief description of these facilities, and the expected laser parameters (which are employed in the simulation studies presented later in this thesis), will be discussed. These systems, in particular, are explored since they will offer the first means by which the predictions of chapters 6 and 7 can be tested experimentally.

The first system of interest is APOLLON, located in Saclay, France [211, 218]. The goal of this facility is to produce a 10 PW laser pulse, by delivering 150 J of energy into an extremely short pulse duration of 15 fs. The resulting intensity will exceed 2×10^{22} Wcm^{-2}, enabling the generation of intense radiation and relativistic particles, along with enabling the investigation of QED effects in ultra-intense laser-plasma interactions. In a similar manner to Astra-Gemini, APOLLON is a multi-beam laser. In addition to the main 10 PW beamline, this system also aims to deliver a secondary 1 PW beam for collision experiments, as well as a 20 fs, 10 TW probe beam, and an uncompressed long pulse beam with nanosecond duration. The features which make APOLLON unique are that it will produce an exceptionally high temporal intensity contrast ratio of $>10^{11}$, enabling the investigation of laser-solid interactions employing ultra-thin foil targets, and at repetition rates of up to one shot per minute. These objectives are achieved by increasing the bandwidth of the light to support ultra-short pulse generation, using spectral-phase control to enhance the contrast, and limiting the energy after compression to 150 J, to support a short time interval between shots.

The front end of the APOLLON laser is based on a Ti:S oscillator which produces laser pulses with at a central wavelength of λ_L=800 nm [204]. To achieve short pulses, the spectrum is necessarily very broad. The pulses from the oscillator are separated into two components; the part centered on 800 nm is spectrally broadened, and the spectral-phase is controlled via a Dazzler (i.e. an opto-acoustic device which enables properties of the pulse, such as the duration, to be varied). These pulses are stretched to 6 ps in duration, and passed to the OPCPA chain as a signal pulse.

The second component of the pulse from the oscillator, centered on 1030 nm and with energy on the pJ level, is stretched to 1.5 ns and amplified by diode pumped Yb-doped amplifiers, before being compressed and frequency-doubled to produce green light at 515 nm. The output at this stage is a green 12 ps duration pulse, with energy on the order ∼10 mJ (at a repetition rate of up to 100 Hz), which is then used as the pump pulse in the OPCPA stage. The OPCPA stage generates a mJ pulse, with the high bandwidth necessary for the production of 15 fs pulses. These are subsequently stretched to nanosecond duration and passed to the amplification stage.

APOLLON employs a chain of five multi-pass Ti:S amplifiers to boost the energy of the pulse to 300 J before the compressor [218]. This requires a significant amount of pumping energy, especially in the later stages of amplification. The pump lasers used are Nd:glass amplifiers, which are liquid cooled to enable a shot rate of one full power shot per minute. Finally these pulses are passed to the compressor, which consists of four diffraction gratings.

The second multi-PW system referenced in this thesis is ELI-NP. This is one of four pillars of the Extreme Light Infrastructure (ELI) project, which aims to push the frontiers of high intensity laser and radiation science [209, 219–222]. The four pillars have the following objectives; ELI-Beamlines (pillar 1) will investigate the generation of secondary radiation from ultra-intense laser interactions, ELI-ALPS (pillar 2) aims to generate high bandwidth, ultra-short attosecond laser pulses, ELI-NP (pillar 3) aims to combine ultra-intense laser pulses with a high energy gamma-ray source to probe nuclear physics, and ELI high intensity (pillar 4) aims to produce laser pulses at intensities up to 10^{25} Wcm^{-2}. The focus in this thesis is on ELI-NP, as the construction of this facility is close to completion at the time of writing, and is the most likely source of the 10^{23} Wcm^{-2} intensities necessary for the investigation of the high-field physics effects which are described in chapters 6 and 7.

The beam architecture of ELI-NP is similar to that of APOLLON, and is described in detail in Ref. [219]. The front end consists of two identical Ti:S oscillators, producing short pulses with a central wavelength of 820 nm, and which are pre-amplified using the aforementioned OPCPA technique. These pulses are passed to two identical amplification arms, which boost the pulses in three stages to 0.1 PW, 1 PW and 10 PW. At each of these amplification stages, the two beams can be siphoned off to separate experimental areas for various applications.

All three amplifiers use Ti:S crystals pumped with green light. Amplifiers one and two produce pulses at a rate of 10 Hz, with compression of the pulse to 25 fs after each amplification stage. The final amplifier produces 220 J pulses at a rate of one per minute, which are then compressed down to 20 fs. The two 10 PW pulses produced at this stage can be directed into a number of experimental areas. The so-called 'E1' interaction area enables these beams to be used for nuclear physics experiments, whilst in the 'E6' area these can be used for colliding pulse and QED experiments. A unique capability of ELI-NP is that the pulses can be interacted with a high energy gamma-ray beam, for example, to investigate all optical QED set-ups.

The gamma-ray beam at ELI-NP [219, 222] is produced via the interaction of high energy electrons with a high-repetition rate laser. Two diode pumped lasers produce 200 mJ pulses at a rate of 100 Hz, which then collide with electrons accelerated via a linac. The first stage of the linac produces 300 MeV electrons, which are collided with the laser to generate up to 3 MeV gamma-ray photons via inverse Compton scattering (a scattering process in which energy is transferred from the electron to the photon). Alternatively, these electrons can be passed to a second linac stage, boosting them to 720 MeV. When these collide with the laser they produce gamma-rays of up to ∼20 MeV. This gamma-ray source is extremely high energy, and has an exceptionally high peak brilliance ($\geq 10^{19}$ photons$\cdot$s$^{-1}\cdot$mm$^{-2}\cdot$mrad$^{-2}\cdot$(0.1% bandwidth)$^{-1}$) [208, 219]. This is comparable to the peak brightness of conventional radiation sources, such as undulators, however the average photon energy in the ELI-NP gamma-ray beam is at least an order of magnitude higher than these conventional sources [223]. This is highly advantageous for investigating non-linear QED processes, such as electron-positron pair-production. It should be noted that upcoming light sources, such as the European XFEL, are predicted to achieve peak brightness $\sim 10^{33}$ photons$\cdot$s$^{-1}\cdot$mm$^{-2}\cdot$mrad$^{-2}\cdot$(0.1% bandwidth)$^{-1}$ [224].

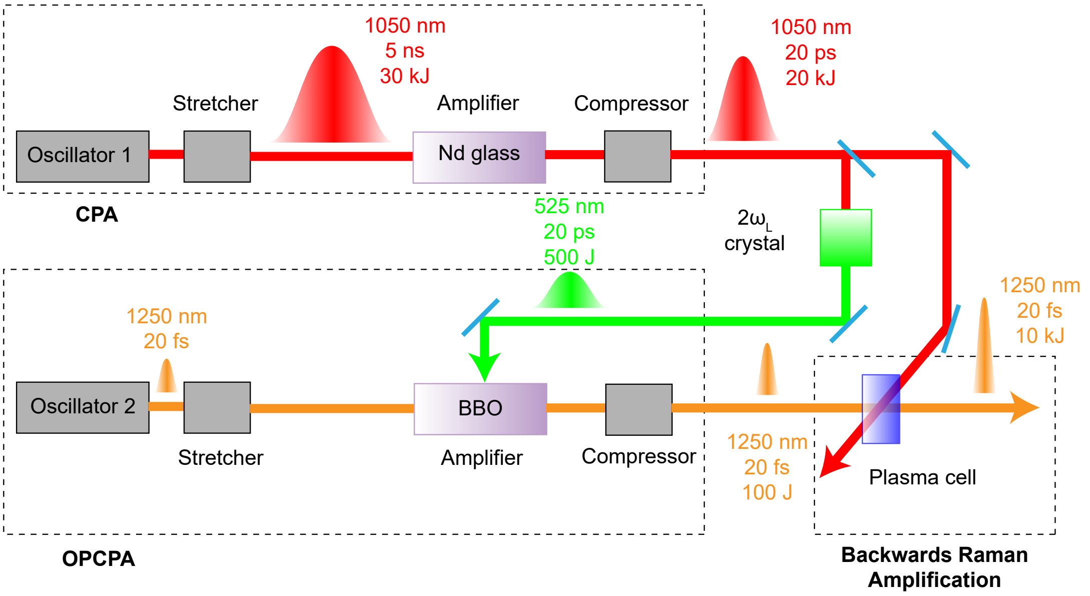

Figure 4.4: A schematic of the C^3 scheme which may enable the generation of Exawatt laser pulses, adapted from Ref. [225]. This scheme combines the methods of CPA, OPCPA and Backwards Raman Amplification.

Exawatt and Zetawatt laser systems

Finally, it is interesting to look much further into the future, towards laser systems which will produce intensities within a few orders of magnitude of the Schwinger limit ($\sim 10^{29}$ Wcm^{-2}). For example, a scheme has been proposed by Gerard Mourou, one of the pioneers of CPA, for the generation of exawatt (1000 PW) pulses [225, 226]. For such high energy laser pulses, the energy fluence incident on the diffraction gratings becomes a limiting factor. To avoid the damage threshold of such components, they must be built to larger sizes than currently feasible, meaning they will become unrealistically wieldy and expensive. It is therefore necessary to employ plasma photonics to boost the intensity, for example by shortening the pulse duration, and resonantly transferring energy between plasma waves and high energy pump pulses [227, 228].

To reach the exawatt level, it has been proposed that the total energy of a system like NIF (National Ignition Facility) or LMJ (Laser MégaJoule), which produce 10 kJ-MJ pulses with nanosecond duration, could be compressed down to 10 fs. It is not possible to achieve this level of compression using CPA or OPCPA alone, since the diffraction gratings required could be up to 100 m^2 and necessarily have a large bandwidth. Instead, a three stage process based on CPA, OPCPA and Backwards Raman Amplification (BRA), has been proposed in Ref. [225]. This final process, BRA, is a method by which a probe pulse transfers energy to a lower frequency wave via resonant excitation of a plasma wave [227]. It is not possible to use the process of BRA on its own to compress the pulse from nanoseconds to tens of femtoseconds in duration, as such a large step requires that the plasma stay uniform in density over a distance of 75 cm, which is currently not feasible. The proposed three stage process, called Cascaded Conversion Compression (or C^3) is illustrated in Fig. 4.4, and described in detail below.

The first stage in the C^3 process is the application of CPA to compress a NIF-like pulse, with a central wavelength λ_L=1050 nm, at an energy of 30 kJ and 5 ns duration, down to a pulse duration of 20 ps. The important point here is that this step can be achieved with currently available diffraction gratings. The resulting pulse is then split in two, with one component used to pump the OPCPA stage, and the second used to pump the BRA stage.

Looking now at the OPCPA stage, the source is a 20 fs pulse with a central wavelength of λ_L=1250 nm, which has been generated in Ref. [229] using a Cr:Fosterite oscillator. This pulse enters an OPCPA stage, pumped by frequency-doubled light from the CPA stage, with an energy of 500 J. The output of the OPCPA stage is then a 20 fs pulse, with an energy of up to 100 J.

Finally, the beam from the OPCPA stage is passed into a uniform density plasma cell (of density 10^{25} m^{-3} and diameter 2.5 cm) to amplify the pulse via the process of BRA. This driving pulse resonantly transfers energy to the pulse incident on the opposite side of the cell, which comes from the CPA stage. BRA enables the generation of a 10 kJ, 20 fs pulse at a wavelength of λ_L=1250 nm, which has a power of the order 1000 PW. It is proposed that this could then be focused to an intensity of 10^{26} Wcm^{-2} using a low F-number optic, either in the form of a conventional solid state OAP, or a focusing plasma optic.

4.2 Experimental Methods

4.2.1 Polarimetry

In chapter 5 of this thesis, the technique of polarimetry is employed, to measure the polarisation state of the light detected at the rear of ultra-thin foil targets. Typically, polarimetry is used as a technique to probe light passing through a strong magnetic field, such as those employed in studies of magnetic confinement fusion [230]. In the context of laser-plasma interactions, polarimetry enables measurement of the spatial distribution of the magnetic fields, as well as the charge and current densities, within an underdense plasma. In general, it is assumed that the change in polarisation (due to the magnetic fields) can be decomposed into contributions from Faraday rotation, in which case the polarisation of light propagating parallel to the magnetic field undergoes a rotation, or from the Cotton-Mouton effect, where the ellipticity of light propagating perpendicular to the magnetic field, is modified [231, 232]. It should be noted that in chapter 5, it is discovered that the polarisation state of light detected at the rear of an ultra-thin foil is not modified by either of these effects, but rather through the process of mode conversion. Nevertheless, the general technique of polarimetry can be used to measure the polarisation state. Specifically, the method of Stokes polarimetry is applied, in which the polarisation state is determined via measurements of the so-called 'Stokes parameters', which will be described in this section.

Stokes polarimetry

To interpret the experimental measurements presented in chapter 5, it is necessary to adopt a description of polarised light which easily enables shifts in the polarisation state to be quantified. Following the analysis presented in Refs. [230, 233–236], the Stokes representation will be employed, in which the polarisation state is described in terms of a four component vector. Each component in this vector is an experimentally measurable quantity, referred to as a Stokes parameter. The first parameter, S_0, describes the total intensity of the light, whilst the remaining three components describe the difference in relative intensities of degenerate polarisation states. The term 'degenerate states' here refers to the six states commonly used in polarimetry, these being; linear polarisations at 0°, 90°, 45°and 135° (where the angle is defined as a rotation in the plane orthogonal to the direction of light propagation), and left and right handed circular polarisations.

The Stokes parameters are defined as follows:

$$S_0 = I_0 + I_{90} = I \equiv 1 \tag{4.2}$$

$$S_1 = I_0 - I_{90} = Ip\cos 2\psi \cos 2\chi \tag{4.3}$$

$$S_2 = I_{45} - I_{135} = Ip\sin 2\psi \cos 2\chi \tag{4.4}$$

$$S_3 = I_{RCP} - I_{LCP} = Ip\sin 2\chi \tag{4.5}$$

where I is the total intensity of the light and I_n is the intensity of light in the degenerate state 'n'. Here, p is the degree of polarisation, such that $0 \leq p \leq 1$, and 2ψ, 2χ are characteristic angles, related to those of the polarisation ellipse introduced in section 2.1.1. In the context of plasma polarimetry, it is common to assume that the light is completely polarised and maintains its total degree of polarisation, such that p=1 [230]. In this case, the reduced Stokes parameters are used such that S_0=1. This is the convention which will be used throughout this thesis. Given that the total degree of polarisation is constant, the Stokes parameters are related as follows: $\sqrt{S_1^2 + S_2^2 + S_3^2}/S_0^2 = 1$.

From an experimental perspective, a typical set up for measuring the Stokes parameters involves splitting the light which is under investigation (for example, the light which appears at the rear of an ultra-thin foil target) into three separate paths, each one enabling measurement of one of the Stokes parameters. Each path contains a Wollaston prism, with the angles set to 0°, 45° and 0°, respectively, such that the orthogonal polarisation states can be separated. In addition, one of the paths should include a quarter waveplate, enabling the left and right handed circular states to be separated. This set-up then splits the light into the six degenerate states mentioned previously. Each pair of degenerate states is then recorded on a camera, with the relative intensity of the states giving a measurement of the corresponding Stokes parameter. The experimental implementation of such a diagnostic on the Astra-Gemini laser system is described in detail in chapter 5.

The Stokes parameters may be visualised as co-ordinates in the so-called 'Poincaré sphere', in which they form an orthonormal basis, as illustrated in Fig. 4.5. In this interpretation, changes in the polarisation are seen as rotations of the Stokes vector, such that its tip moves to a different point on the surface of the Poincaré sphere. Consider for example linear p polarisation, which is represented by a unit vector pointing along the positive S_1 axis, and whose tip is given by the co-ordinate (1,0,0). A change in the

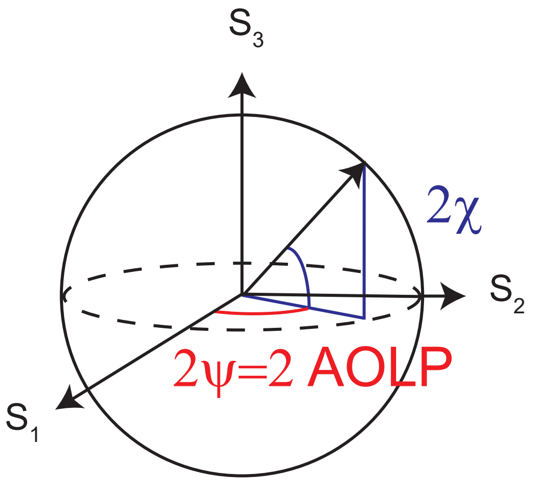

Figure 4.5: An illustration of the Poincaré sphere representation of polarised light, and the angle of linear polarisation (AOLP).

linear polarisation state is then visualised as a rotation of this vector along the equator of the sphere, whilst a change in the circular polarisation state is a rotation along a line of latitude. Elliptical polarisation is represented by a Stokes vector whose tip lies on the unit sphere, but not along the equator or the poles. In this representation, it is clear that the angles which appear in the definition of the Stokes parameters (2ψ and 2χ) are the angles of longitude and latitude in the Poincaré sphere. If the degree of polarisation is not constant, such that $p \neq 1$, then the tip of the Stokes vector need not lie on the unit sphere. The Stokes parameters can be combined to define an angle, called the angle of linear polarisation (AOLP), which is used to quantify the magnitude of shifts between linear polarisation states. The AOLP is defined as follows [234, 235]:

$$\text{AOLP}(^\circ) = \frac{1}{2}\arctan\left(\frac{S_2}{S_1}\right) = \frac{1}{2}\arctan\left(\frac{I_{45} - I_{135}}{I_0 - I_{90}}\right) \tag{4.6}$$

For light which is completely polarised in the linear 0°-90° plane, i.e. the linear p and s states, the AOLP=0°. For linear polarisation at an angle, the magnitude of the AOLP increases proportionally with the polarisation angle, up to a maximum value of 45°. This angle describes shifts of the linear polarisation state, and for completely polarised light is equal to the latitude in the Poincaré sphere (see Fig. 4.5).

The Stokes representation is employed in this thesis due to the advantages it offers over alternatives, such as the Jones representation [230]. For example, the Stokes parameters are quantities which can be measured directly experimentally, whereas in the Jones representation, it is necessary to determine the relative amplitudes of the orthogonal components of the electric field, and their relative phase, in order to measure the polarisation state. The Jones description is also limited to completely polarised light, whereas the Stokes representation can be applied to fully and partially polarised light, as well as completely unpolarised light.

4.3 PIC simulations

It is increasingly common to employ numerical simulations to complement results obtained from high intensity laser-plasma experiments. Experimental measurements made via the use of optical diagnostics and cameras, to sample light during an interaction, are typically temporally integrated. Simulations are then employed to help understand the physical processes that occur during the interaction, due to the possibility of interrogating the dynamics over a time interval equal to the laser period, and length scales shorter than the Debye length. For example, results presented in Refs. [52, 53, 237] have highlighted that the collective dynamics within the plasma change drastically during the course of an interaction, with different physical processes driving the acceleration of charged particles at different times. Experimentally, it is only possible to infer these complex dynamics from the macroscopic quantities which can be measured, for example, the time integrated proton energy spectrum and spatial distribution. By employing numerical simulations however, it is possible to observe these dynamics and then compare with the experimental measurements. In addition, there is a large parameter space which could be probed experimentally but which often is not possible due to time constraints. Numerical simulations enable the parameter space to be sampled before the experiment, to isolate the most promising regions, and to therefore guide the experiment. It is important to note that these numerical modelling techniques have limitations of their own, and so the development of the field of laser-plasma interactions relies on a combination of these two approaches.

In this section, one specific approach to the numerical modelling of plasmas will be described, the Particle-In-Cell (PIC) approach [238]. The general principles underpinning this scheme will be explored, as well as the implementation of novel new physics such as QED effects. Whilst the simulations in this thesis were run using a specific code, EPOCH, the overall discussion is general to many PIC codes.

4.3.1 The numerical approach

The most complete description of a plasma, in principle, is obtained by solving the coupled equations of motion for every particle within the plasma [166]. There are two main obstacles associated with this approach. The first is that since the particles are charged, their motion results in the generation of currents and associated electromagnetic fields. The motion of the one particle then generates fields which influence the motion of the other particles, such that it is difficult to obtain a self-consistent description of the particle trajectories and fields. The second obstacle is the number of particles involved. A solid density foil, for example, when fully ionised produces a plasma with $\sim 10^{27}$ electrons per cubic metre. Even with access to a supercomputer it not possible to solve the set of equations numerically on a feasible timescale. Typically, the solution is to employ the kinetic description of a plasma, which was introduced in section 3.1.2. Rather than describing the particles within a plasma in terms of their individual equations of motion, the phase space occupied by the particles is discretised in terms of a distribution function. This is a function of position and velocity, and describes the probability, at a given time, of locating a particle within a certain volume of phase space. The evolution of the distribution function, in the absence of collisions, is described by the Vlasov equation (Eqn. (3.11)). However, given that the distribution function is a 6D quantity (it has three position and three velocity co-ordinates) solving the Vlasov equation is also computationally expensive. In addition, the distribution function is typically localised to a small region of phase space, such that much of the computational power is wasted on regions of low density plasma, or vacuum.

PIC codes address this problem by sampling the distribution function into finite elements, called macro-particles [238]. Each macro-particle represents a collection of particles, and behaves in the same way; their motion is still governed by the Lorentz force, and they have the same charge-to-mass ratio as the particles they represent. The macro-particles have no internal degrees of freedom, they cannot rotate and they cannot change shape. In the absence of collisions, it is also possible for the macro-particles to move through each other and occupy the same volume in space. The shape with which the macro-particles are initialised has an influence on how accurate the simulation results are; generally the smoother the distribution, the better the results. The number of macro-particles used in the simulation must be chosen to closely approximate the distribution function. The distribution of macro-particles is determined by the initial conditions, which are expressed in the form of fluid moments, such as density and pressure [238, 239].

The system of equations which describes the motion of the macro-particles and the associated fields is defined as follows;

$$\frac{d\mathbf{r}}{dt} = \mathbf{v} \tag{4.7}$$

$$\frac{d\mathbf{u}}{dt} = \frac{q}{m}(\mathbf{E} + \mathbf{v} \times \mathbf{B}) \tag{4.8}$$

where $\mathbf{u} = \gamma\mathbf{v}$, such that $\gamma = \left(1 + (\frac{u}{c})^2\right)^{1/2}$, and:

$$\frac{\partial\mathbf{B}}{\partial t} = -\nabla \times \mathbf{E} \tag{4.9}$$

$$\frac{\partial\mathbf{E}}{\partial t} = c^2\nabla \times \mathbf{B} - \frac{\mathbf{j}}{\epsilon_0} \tag{4.10}$$

Note that it is only necessary to include two of Maxwell's equations; provided that $\nabla \cdot \mathbf{B}$=0 at the start of the simulation, this condition will be satisfied at all subsequent times, and charge will be conserved, provided that Gauss' law is satisfied [239].

To determine the current density, $\mathbf{j}$, the positions of the particles are interpolated onto a grid. The shape (or weight) of the macro-particle describes the fraction of the particle located at a given position of the grid. The flux of particles across the grid determines the current density, from which the electric and magnetic fields are calculated. These are obtained using the Finite Difference Time Domain (FDTD) method, which enables both the electric and magnetic fields to be determined at the same time step. Starting at time step n, the fields are defined as:

$$\frac{\mathbf{E}^{n+1/2} - \mathbf{E}^n}{\Delta t/2} = c^2\nabla \times \mathbf{B}^n - \frac{\mathbf{j}^n}{\epsilon_0} \tag{4.11}$$

$$\frac{\mathbf{B}^{n+1/2} - \mathbf{B}^n}{\Delta t/2} = -\nabla \times \mathbf{E}^{n+1/2} \tag{4.12}$$

where Δt is the size of the time step. These fields are then interpolated to the particle positions, and re-injected into the equation of motion to push the particles to their new positions. By interpolating the new positions onto the grid, the current density at the next time step, $\mathbf{j}^{n+1}$, is determined. This process repeats iteratively, as illustrated in the flow diagram presented in Fig. 4.6.

The components of the electric and magnetic fields are stored on the vertices and

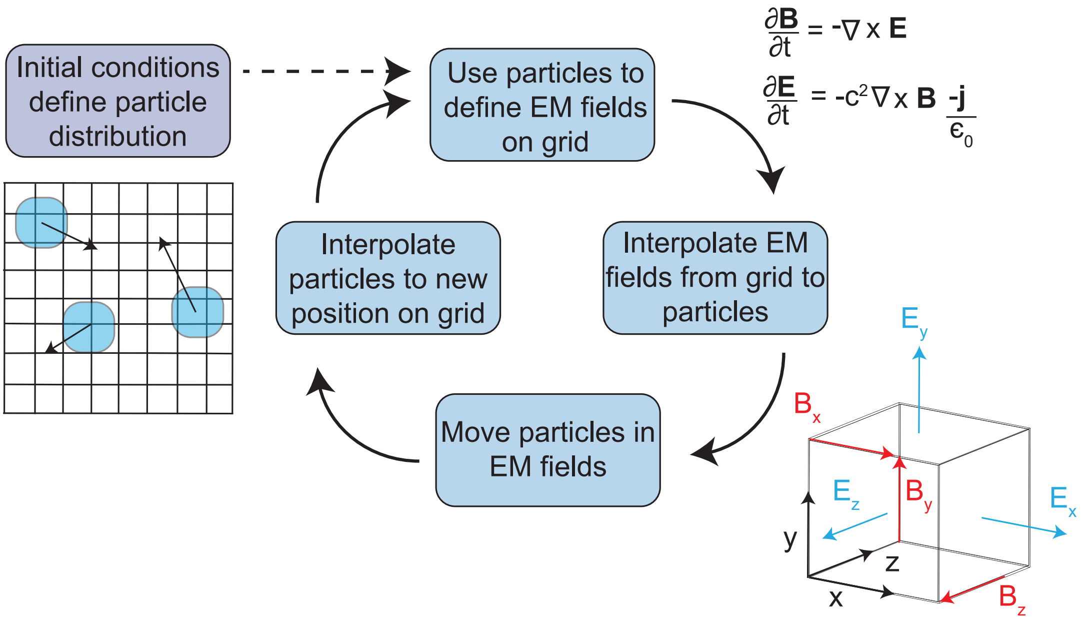

Figure 4.6: A flow diagram demonstrating the PIC numerical technique. On the left, the initial conditions define the particle distribution function, which is sub-sampled into macro-particles. The EM fields are defined based on the position of the macro-particles on the grid, these fields are then interpolated onto the particle positions and used to update their positions. The field positions are calculated on the Yee grid, which is illustrated on the right of the figure.

edges of a Yee grid (illustrated in Fig. 4.6) [240], as opposed to being defined in the centre of the grid elements. This ensures second order accuracy of the algorithm in space, meaning that the magnitude of the errors scales with the square of the time step size.

Finally, the equations of motion for the particles are updated using the leapfrog algorithm. Since the EM fields are calculated at half time steps, the particle positions and the current density on the grid are obtained at integer time steps. The Boris algorithm, described in detail in Ref. [241], is then used to centre the velocity.

4.3.2 Limitations of the PIC approach

Whilst PIC codes can be employed to great effect in numerical studies of laser-plasma interactions, it is important that they are not treated as a 'black box', and that their limitations are taken into account when analysing results.

A well-reported issue which arises in PIC simulations is numerical heating [238, 242]. This is an artificial effect, which arises when the spatial resolution of the simulations is not sufficient to resolve the Debye length. In this case, the electric fields are aliased over adjacent cells, causing the plasma to heat up until the Debye length is resolved.

One way to minimise the amplitude of this effect is to use smoother shaping functions to initialise the macro-particles [242], for example, third order interpolating splines.

Before running PIC simulations, it is also important to understand the spatial and temporal scales which must be resolved in order to obtain meaningful results. In terms of the temporal resolution, it is necessary to resolve the highest frequency in the system; as a rule of thumb the size of the time step is related to the spatial resolution of the grid as follows, $\Delta t_c \leq \Delta x/c$ [239, 243]. In laser-solid interactions, the frequency which is typically resolved is the plasma frequency, such that the time step restriction is $\Delta t_p \leq \omega_{p,e}^{-1}$. It is important to note that if strong magnetic fields are present in the interaction, the gyro-frequency of the particles must also be temporally resolved.

PIC simulations are also susceptible to numerical noise, which scales inversely to the square of the number of macro-particles per cell in the system. This noise arises from aliasing of the fields within the cells of the grid, which introduces fluctuations in the measurement of these fields. This problem can therefore be reduced by using a sufficiently high number of particles per cell, however it is often difficult to gauge when this condition is satisfied. One way this can be addressed is through convergence testing. For a given simulation a gridded quantity, such as the sum of the cell-averaged kinetic energy for a given species, can be calculated as a function of time. The simulation is then re-run with a different number of particles per cell, for example, doubling this number. If the summed kinetic energy is comparable to the previous simulation (say, to within 20%), then a sufficient degree of convergence has been achieved. It is also important to note that the EPOCH PIC code used in this thesis conserves momentum, rather than energy. Whilst in many applications energy will be conserved to a sufficient degree, this condition should not be assumed, and again depends on the simulation being initialised with a high enough number of macro-particles per cell.

Finally it is worth noting that, in general, PIC codes ignore collisions, which may lead to unphysical behaviour when modelling dissipative mechanisms. Recent developments to EPOCH have enabled collisions to be accounted for by replacing the right hand side of the Vlasov equation with a Fokker-Planck collision operator, however running the simulations with this modification included leads to a significant increase in computation time.

4.3.3 Implementing QED effects

The simulations presented in this thesis are obtained using EPOCH [239], an open source, fully-relativistic QED-PIC code. In this section, the implementation of QED effects within the code is described. A full description of the EPOCH QED module can be found in Refs. [58, 120, 239].

The first step in the implementation of QED effects in the PIC code is the decoupling of the radiation and the laser fields, which is achieved by separating the electromagnetic fields into low and high frequency components. The low frequency fields are associated with the low energy photons of the laser, which describe a classical, coherent state. The high frequency radiation is associated with the high energy, synchrotron-like radiation produced by the accelerating charges. This radiation is incoherent such that the photons do not interact with each other. It is important to note that this assumption of incoherent photons means that certain physical processes cannot currently be implemented in EPOCH. These include photon-photon scattering and self amplified spontaneous emission, a process by which a radiating electron interacts with its radiation and which is crucial for the operation of X-ray free electron lasers [244, 245].

Having separated the laser fields from those of the high energy radiation, the motion of the electrons (and positrons) is described by the method of Baier and Katkov [246]. These charged particles follow classical trajectories, and move according to the Lorentz force in the laser fields. At points along their trajectory, the electrons and positrons experience QED processes, such as photon emission. The momentum of an emitted photon is assumed to be in the same direction as that of the radiating electron, and is subsequently subtracted from the electron momentum. This assumption neglects the fact that the photon is emitted into a narrow forwards facing cone, with a divergence half-angle of $1/\gamma_e$. For the laser intensities at which QED effects become important (i.e. $\geq 10^{23}$ Wcm^{-2}), the radiating electons typically have $\gamma \geq$100, such that the divergence half-angle becomes negligibly small. In addition, the implemented QED routine neglects the energy transferred from the radiating electron to the laser field. This provides an estimate of the error in the QED-PIC code, and is estimated in Ref. [116] to be of the order $\mathcal{O} \sim 1/\gamma_i\gamma_y$, where γ_i and γ_f are the electron Lorentz factor, before and after photon emission. The electron and positron trajectories are then recalculated using the classical equation of motion, whilst the photon follows a ballistic trajectory.

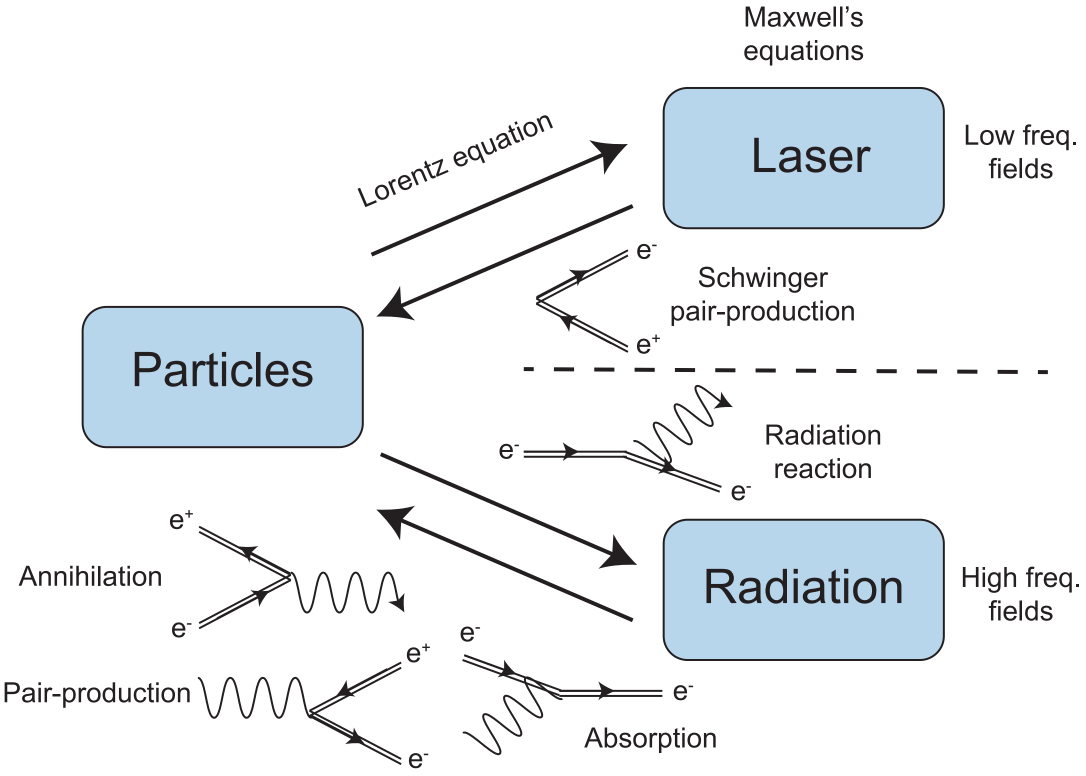

Figure 4.7: A schematic demonstrating the key QED processes which may be implemented in PIC codes. The high and low frequency field components of the electromagnetic fields are separated, such that the particles only move in the coherent fields of the laser. The particles and radiation interact via the processes of photon emission and pair-production, which are illustrated with first order Feynman diagrams. The double lines indicate that the charged particles are dressed by the background (laser) fields.

The QED module includes two fundamental high-field processes; photon emission from an accelerating electron (and the associated radiation reaction force) and the production of electron-positron pairs. In order to calculate the probabilities of these processes it is necessary to introduce a number of assumptions. The first is that the photon formation length (the region of space over which photon formation occurs, given by $\ell_{photon} = \lambda_L/a_0$) is much shorter than the laser wavelength [120]. In this case, the laser can be treated as a constant background field over the time scale of a given QED process, whose probability then depends on the constant, local values of the field. This assumption is typically valid for relativistic interactions, in which $a_0 \gg 1$. Another key assumption is that when the magnitude of the laser field is much less than that of the Schwinger field, then the probability of a given process depends only on χ_e and χ_γ (see Eqn. (2.84) and (2.85)), such that the background fields are interchangeable with any other configuration with the same values of these quantum parameters. In this case, the rates of photon emission and pair production are calculated for a constant background magnetic field, a configuration for which the rates are well known. Note that this is why the radiation produced in QED-PIC codes is referred to as synchrotron-like radiation; the radiation produced by the accelerating charged species is calculated as if it were arising from the motion of that species in a constant magnetic field, i.e. synchrotron radiation.

The rate of synchrotron emission from a charged particle in a constant magnetic field is given in Eqn. (4.13) [65, 98, 113], below. It is important to note that this rate is averaged over the photon spin and polarisation, an approximation which will be addressed later in this chapter.

$$\frac{dN_\gamma}{dt} = \frac{\sqrt{3}\alpha c}{\lambda_c}\frac{\chi_e}{\gamma}\mathcal{H}(\chi_e) \tag{4.13}$$

In the above equation, α is the fine structure constant, λ_c is the Compton wavelength, and $\mathcal{H} = \int_0^{\chi_e/2} \mathcal{F}(\chi_e, \chi_\gamma)\chi_\gamma d\chi_\gamma$, where $\mathcal{F}$ is the quantum synchrotron function (as described in section 2.2.2). The rate of pair-production from a photon in a constant magnetic field is expressed as:

$$\frac{dN_\pm}{dt} = \frac{2\pi\alpha c}{\lambda_c}\frac{m_e c^2}{h\nu_\gamma}\chi_\gamma T_\pm(\chi_\gamma) \tag{4.14}$$

where $T_\pm \sim 0.16\frac{K^2_{1/3}(2/3\chi_\gamma)}{\chi_\gamma}$ is a function which controls the pair-production rate [58], and $K_{1/3}$ is a Bessel function of the second kind [65, 98, 113].

As discussed in the previous section, PIC codes deal with having to simulate a large number of particles by sampling the distribution function into macro-particles, where the evolution of the distribution function is described by the Vlasov equation. In the QED module, two further kinetic equations are introduced, which describe the evolution of the electron-positron distribution function (described by $f_\pm$) and the photon distribution function (described by f_γ), in the presence of emission processes. These equations are written:

$$\frac{\partial f_\pm}{\partial t} + \mathbf{v}\cdot\nabla f_\pm + \mathbf{F}_{L,e}\cdot\nabla_p f_\pm = \left(\frac{\partial f_\pm}{\partial t}\right)_{\text{QED}} \tag{4.15}$$

$$\frac{\partial f_\gamma}{\partial t} + c\hat{\mathbf{v}}\cdot\nabla f_\gamma = \left(\frac{\partial f_\gamma}{\partial t}\right)_{\text{QED}} \tag{4.16}$$

where $\mathbf{F}_{L,e}$ is the Lorentz force and $\hat{\mathbf{v}}$ is the direction of the photon velocity. The QED rates on the right hand side of the above equations act as sources and sinks of particles in the distribution function, as opposed to the Vlasov equation which assumes the distribution function of a given species occupies a constant volume in phase space (in the absence of collisions). The distribution of macro-particles then samples the kinetic equations described above.

Stochastic photon emission

In EPOCH, photon emission and radiation reaction are implemented using a semi-classical approach, in which the stochastic nature of photon emission is approximated via a Monte-Carlo algorithm. This treatment of photon emission as a stochastic, rather than a continuous, process accounts for the effect of straggling, described in section 2.3.2. Straggling enables electrons to penetrate into regions of high-fields which they could not reach classically. In turn, this leads to the emission of higher energy photons and an enhancement of the pair-production rate relative to the classical predictions [116, 121].

The Monte-Carlo emission process is described in Refs. [116, 120], and summarised here as follows. At the start of the simulation, each macro-particle is given a final optical depth associated with one of the described QED processes. For example, the electrons are given a final optical depth against photon emission, and photons are given a final optical depth against pair-production. The initial optical depth for each macro-particle, $\tau(t)$, is set to zero and at every time step is re-calculated by solving the differential equation: $\tau(t) = \int_0^t \lambda_{\mathrm{QED}}(\chi_e(t'))dt'$, where λ_{QED} is the rate of the relevant process [117]. When the optical depth for a given species reaches its pre-assigned final value, the relevant emission process occurs. The photons, electrons and positrons generated by the emission process are then added to the simulation as additional macro-particles [239].

The energy of an emitted photon is defined in terms of its χ_γ value, which also depends on the χ_e of the radiating electron. The cumulative probability, which describes the probability that the emitted photon has an energy greater than χ_γ, is randomly assigned a value between 0 and 1. This probability is defined as $P_{\chi_\gamma} = \int_0^{\chi_\gamma} \frac{F(\chi_e,\chi_\gamma)}{\chi_\gamma \mathcal{H}} d\chi'_\gamma$, such that the associated χ_γ value is obtained by looking up a cumulative probability table. The momentum of the photon is then subtracted from the radiating electron, such that the equation of motion for the electron, which is solved at the next time step, begins with this reduced value of the momentum. Similarly, for pair-production, the fraction of the initial photon energy which goes to each particle is defined by first randomly assigning the cumulative probability of one of the species obtaining a given fraction of the total energy, then interpolating back to a specific χ_e.

It is important to take the process of straggling into account, particularly for laser intensities $\leq 4 \times 10^{23}$ Wcm^{-2} [65, 113, 116]. Above this threshold, the radiated photons tend to have high enough energy to produce electron-positron pairs in the intense background field of the laser, without the need for straggling to enhance the pair-production rate. It has been demonstrated in Ref. [116] that the number of pairs can be boosted by a factor of five compared to a non-stochastic description, for intensities below the aforementioned threshold. Given that these photons may then trigger cascade pair-production, accounting for straggling is extremely important.

Limitations of the QED-PIC approach

It is necessary to understand the limitations of the QED-PIC approach and to determine the relevant time scales which must be resolved when running simulations. In contrast to regular PIC simulations, the time scale which must now be resolved is that of the highest frequency QED process, typically taken as the inverse of the pair-production rate [239]. The production of copious electron-positron pairs leads to another problem, the volume of data generated during a simulation. A sufficient number of macro-particles must be initialised in order to resolve the dynamics of the system and to eliminate statistical noise, however, throughout the interaction, the production of large numbers of electron-positron pairs means that the size of the output files will grow accordingly. A potential solution is to introduce a minimum photon energy of ∼1 MeV, such that photons below this threshold are included in computations but are not written to the output files.

It is also important to note that EPOCH does not account for spin polarisation effects, which are described in Refs. [66, 96, 124, 125]. These spin polarisation effects can cause a reduction in the magnitude of the electron radiated power, and a subsequent decrease in the rate of pair-production, by as much as 30% [66]. In addition, EPOCH only accounts for the lowest order QED processes of photon emission and pair-production (via the non-linear Breit-Wheeler and trident processes). Whilst these are sufficient for the laser and target parameters utilised in this thesis, there are additional effects which are not included, such as Bremstrahlung emission, which is important during the interaction of accelerated electrons and high-Z materials at intermediate intensities $\leq 10^{22}$ Wcm^{-2}.

A final consideration is that QED-PIC codes typically apply the constant crossed fields approximation (CCFA) [97, 247], for example in the calculation of the amplitude of non-linear Compton scattering. This approximation enables the laser field to be treated as a constant background field on the time scale of any relevant QED processes, and is generally regarded to hold in the case where $a_0 \gg 1$. The CCFA may not apply when the laser fields have rapidly varying temporal profiles, for example, when employing ultra-short pulses. The validity of the CCFA has been questioned recently due to the lack of agreement between high-field experiments and QED-PIC simulations [131]. Whilst alternatives to this approach are under development [97, 247], it is important to keep this limitation in mind when analysing simulations of pair-production, and putting these in context with experimental results.

Chapter 5

Relativistic transparency and mode conversion

5.1 Introduction

The aim of this thesis is to investigate the generation of radiation via ultra-intense laser-solid interactions. The properties of the radiation will provide vital information about the QED-plasma regime, in which classical plasma physics is strongly intertwined with QED effects. As discussed in the introduction, signatures of QED have been observed during the collision of ultra-intense laser pulses ($\sim 10^{20}$ Wcm^{-2}) with counter-propagating, relativistic electron beams, produced via the process of laser wakefield acceleration (LFWA). However, much higher laser intensities ($\geq 10^{23}$ Wcm^{-2}) are required to induce QED effects in laser-solid interactions, since the electrons accelerated within the target acquire lower energies than those produced via LWFA. The QED processes which occur at these ultra-high intensities are predicted to impact key plasma physics processes which occur during laser-solid interactions, such as the onset of RSIT (as described in section 3.2.2). For example, in Ref. [54] it is reported that RR will slow the onset of RSIT, whilst the production of a dense electron-positron plasma will prevent the transmission of laser light through targets which would otherwise be transparent. In this chapter, the process of RSIT will be investigated using currently available laser intensities ($\sim 10^{20}$ Wcm^{-2}). This process is of great importance at current intensities, given its role in ion acceleration mechanisms [51–53, 171], but it will become even more important at upcoming laser facilities, where the process will be influenced by QED effects.

The interaction of a relativistically intense laser pulse with ultra-thin ($\sim$ 10 nm) foils leads to the generation of a so-called 'plasma aperture', as described in detail in Refs. [49, 248–250]. The intense laser fields drive relativistic electron oscillations, such that the plasma within the most intense region of the laser focal spot undergoes RSIT, enabling the laser light to propagate through. It was found in Ref. [49, 248] that the resulting diffraction pattern in laser light transmitted through the aperture causes the formation of dense lobes of electrons which escape the target, and whose dynamics may be controlled via the polarisation of the incident laser pulse. The generation of a relativistic plasma aperture will also play an important role during ultra-intense laser-solid interactions. Rather than just the most intense region within the focal spot undergoing transparency, it will be possible for a large area of the target plasma, which is initially overdense, to undergo RSIT as a result of enhanced target heating and expansion. The heating of the electrons via interaction with a relativistically intense laser pulse can, in itself, lead to interesting plasma physics effects. For example, it has recently been demonstrated that temperature anisotropy within the plasma can lead to shifts in the polarisation of the light which it interacts with. This temperature anisotropy is driven by differences in the degree of electron heating caused by employing different laser polarisations. This results in temperature gradients in the plasma, in the plane perpendicular to the laser propagation direction. The plasma then becomes birefringent, as will be described in section 5.2, such that it behaves in a manner analogous to an optical polariser or wave plate. The plasma wave plate effect has been demonstrated via numerical simulations in Refs. [159, 160]. It has also been demonstrated experimentally during the interaction of an intense laser pulse with a gas-jet, in Ref. [161].

The plasma polariser and wave plate effects described above represent important developments in the field of plasma photonics. This is concerned with controlling the properties of light as it interacts with a plasma. Notable developments in this field include the amplification [251–253] and compression [254] of intense laser light propagating through a plasma, which could potentially lead to the generation of ultra-high power Exawatt laser pulses [225]. For example, the amplification of laser light can occur via the process of stimulated Raman backscattering, where a long-duration laser pulse resonantly transfers energy to a short probe pulse by exciting a plasma wave [253]. Another significant development is the so-called 'plasma mirror', which is now commonly utilised in high power laser systems to enhance the temporal intensity contrast of laser pulses generated via CPA [212, 214]. This idea has led, in recent years, to the concept of the ellipsoidal plasma mirror, which in addition to the aforementioned temporal intensity contrast enhancement, enables tight focusing of laser pulses without the need to change the solid state optics in the system [215, 216]. The advantage of using plasma photonics, as opposed to solid state optics, is that they can handle a much higher energy fluence. As discussed in section 4.1.1, the damage threshold of conventional optics is a major limitation in the development of high energy laser systems, thus plasma photonics will be key in the development of future systems. In addition, plasma photonics enables smaller optics to be employed (since the size of the optic is no longer determined by the damage threshold), leading to the realisation of more compact experimental geometries.

Looking forward, a key aim of the field is to develop plasma photonics effects which will enable control over the polarisation state of high intensity laser light [180, 181, 255, 256], in addition to the generation of transverse electromagnetic (TEM) modes of higher order than the Gaussian modes which are typically produced at the focus of these laser pulses [257]. An example is the radially polarised mode, which has been predicted to enhance the trapping of particles within the strong gradients in the field structure [258–263]. The ability to achieve such trapping may lead to more efficient acceleration of electrons and positrons, and therefore has applications for the production of high energy radiation sources [264]. In addition, beams of electrons trapped within ultra-intense, radially polarised pulses may be collided to trigger cascade pair-production (using the dual pulse interaction scheme proposed in chapter 7), and strong radiative cooling of the trapped electrons may enable quantum RR to be observed [265, 266]. Thus these higher order TEM modes have applications in the experimental observation of QED effects.

The aim of this chapter is to investigate relativistic laser-plasma phenomena, which are predicted to become even more important at upcoming multi-PW facilities, due to the influence of high-field physics effects. It is discovered that the interaction of an intense laser pulse with a relativistic plasma aperture, formed via interaction with an initially overdense solid target, leads to the self-generation of light at both the laser frequency (ω_L) and the second harmonic frequency ($2\omega_L$). This light takes the form of higher order TEM modes, namely a TEM$_{02}$ in the E_y field, and a TEM$_{11}$ in the E_z

field. At the target rear, both the self-generated modes and the laser fields are detected, such that a superposition state is formed. The polarisation of this superposition state appears to be rotated with respect to the input polarisation. This leads to an effective polarisation shift, which is demonstrated both experimentally and numerically. In addition, when the self-generated mode and the transmitted laser field are of the same magnitude, the superposition state takes the form of a high intensity, radially polarised mode at $2\omega_L$. The conversion efficiency of laser light into various higher order TEMs is demonstrated to depend on the target and laser parameters, such that the proposed mode conversion mechanism is highly tunable.

5.2 Review of relevant literature: polarisation shifts in anisotropic plasmas

In this section, a brief review is provided of relevant experimental and numerical investigations into effects related to RSIT. An interesting starting point is the result presented in Stark *et al* [160], which demonstrates that temperature anisotropy within a layer of plasma ∼8 μm thick (which is thick relative to the ∼10 nm targets presented in this chapter) can be used to alter the polarisation state of the light which it interacts with. In that study, 3D numerical simulations were utilised to demonstrate that a weakly overdense plasma can, under certain conditions, act as either a polariser or a wave plate. First, a circularly polarised, relativistically intense laser pulse was used to irradiate a thick slab of plasma, in which the electron distribution was initialised with an anisotropy (in this case a temperature gradient) along one axis in the laser polarisation plane. This temperature anisotropy leads to changes in the refractive index of the plasma along the different directions in the polarisation plane, therefore inducing birefringence. The two orthogonal components of the incident circular polarisation then experience different refractive indices, to the point where one component can be completely suppressed. The resulting transmitted pulse is then linearly polarised, indicating that the plasma has behaved analogously to an optical polariser. The so-called ‘plasma polariser’ effect is a special case, in which the electron temperature anisotropy is chosen to completely suppress one of the polarisation components. The plasma wave plate effect can be thought of as a generalisation of this idea. It was further demonstrated in Stark *et al* [160] that if a plasma containing temperature anisotropy is irradiated with light which is linearly polarised at 45°, then the induced birefringence will again affect the propagation of the orthogonal polarisation components. The transmitted polarisation in this case is elliptical, since both components experience different refractive indices, but neither one is completely suppressed. Since the incident linear polarisation is converted into elliptical, this is hence referred to as the plasma wave plate effect.

Another plasma based scheme to control the polarisation of light propagating through low density plasma was proposed theoretically in Michel *et al* [159], and subsequently demonstrated experimentally in Turnbull *et al* [161]. Here, the anisotropy results from density perturbations within the plasma, which are controlled by self-phase modulation. In this scheme, a probe pulse and a driving pulse are overlapped in a low density plasma, produced via interaction with a gas jet, which drives density perturbations at the beat frequency of the waves. This enables a high degree of control over the anisotropy within the plasma; in the case of Turnbull *et al* [161] it was demonstrated that it is possible to convert initially elliptical polarisation into nearly perfect circular polarisation by employing this plasma wave plate scheme.

The aforementioned studies have demonstrated that the plasma polariser and wave plate effects can be used as a diagnostic for anisotropy within a relativistic plasma. This idea will be developed further in this chapter, with the aim of employing the plasma wave plate effect to diagnose relativistic effects in thin layers of plasma (produced via the interaction of an ultra-intense laser pulse with ultra-thin foils). In contrast to the study presented in Stark *et al* [160], the plasma is initially overdense, and generally does not have a uniform density profile, due to enhanced heating in the polarisation direction. It will also be investigated whether the polarisation state of the light detected at the rear of the target can be controlled, via the plasma wave plate effect, by varying the laser and target parameters (such as pulse duration and target thickness). Finally, the effect of self-generated light within the plasma on the polarisation state of the light detected at the target rear will be investigated. The work presented in this chapter will examine whether there are polarisation changes in this light, at ω_L and $2\omega_L$, as well as probing its spatial structure.

5.3 Methodology

5.3.1 Experimental set-up

The experimental results presented in this chapter were obtained during an experimental campaign which aimed to measure polarisation shifts in laser light propagating through ultra-thin foil targets. A schematic diagram of the experimental set-up which was employed is provided in Fig. 5.1, with additional photos of the set-up provided in Fig. 5.2. The experiment was conducted using the Astra-Gemini laser system at the Rutherford Appleton Laboratory (described in section 4.1.2). This system delivered short pulses of linearly p polarised light, with a central wavelength λ_L=800 nm (with a bandwidth of 35 nm) and a maximum energy of (3.1 ± 0.2) J on target (after reflecting off a double plasma mirror). These laser pulses were focused, using an F/2 off-axis parabola (OAP), to a focal spot of diameter (3.9 ± 0.7) μm (FWHM) and enclosed energy $\sim$30%, which then interacted with the targets at near normal incidence. The calculated peak intensity for this experiment was $(2.8 \pm 0.4) \times 10^{20}$ Wcm^{-2}, corresponding to an a_0 of approximately 10.

Three parameters were varied during the experiment, these were; target thickness, pulse duration and input polarisation. For the first of these scans, the targets were ultra-thin aluminium foils with thickness, ℓ, varied in the range 16-100 nm. The light transmitted through the target, and generated within it (propagating in the same direction as the laser), was collected and re-collimated using a secondary F/2 OAP. This light was then reflected off two wedged mirrors, each with approximately 4% reflectivity at 800 nm. Reflection off the non-parallel surfaces of the wedged mirrors reduced the energy of the laser light, such that it could propagate out of the target chamber to the external diagnostics (i.e. the reduction in energy suppresses non-linear optical effects, and the possibility of damaging optics). For the second parameter scan, the pulse duration was varied in the range τ_L=40-200 fs. This was achieved using a Dazzler, an opto-acoustic device which enables control over the spectral phase of the pulse. The energy on target was maintained in the aforementioned range throughout this scan, such that stretching the pulse duration resulted in a reduction of the intensity on target. Finally, control over the polarisation state irradiating the target was achieved via the addition of a half ($\lambda_L/2$) and quarter ($\lambda_L/4$) wave plate, which were placed in the collimated beam path, prior to the first OAP.

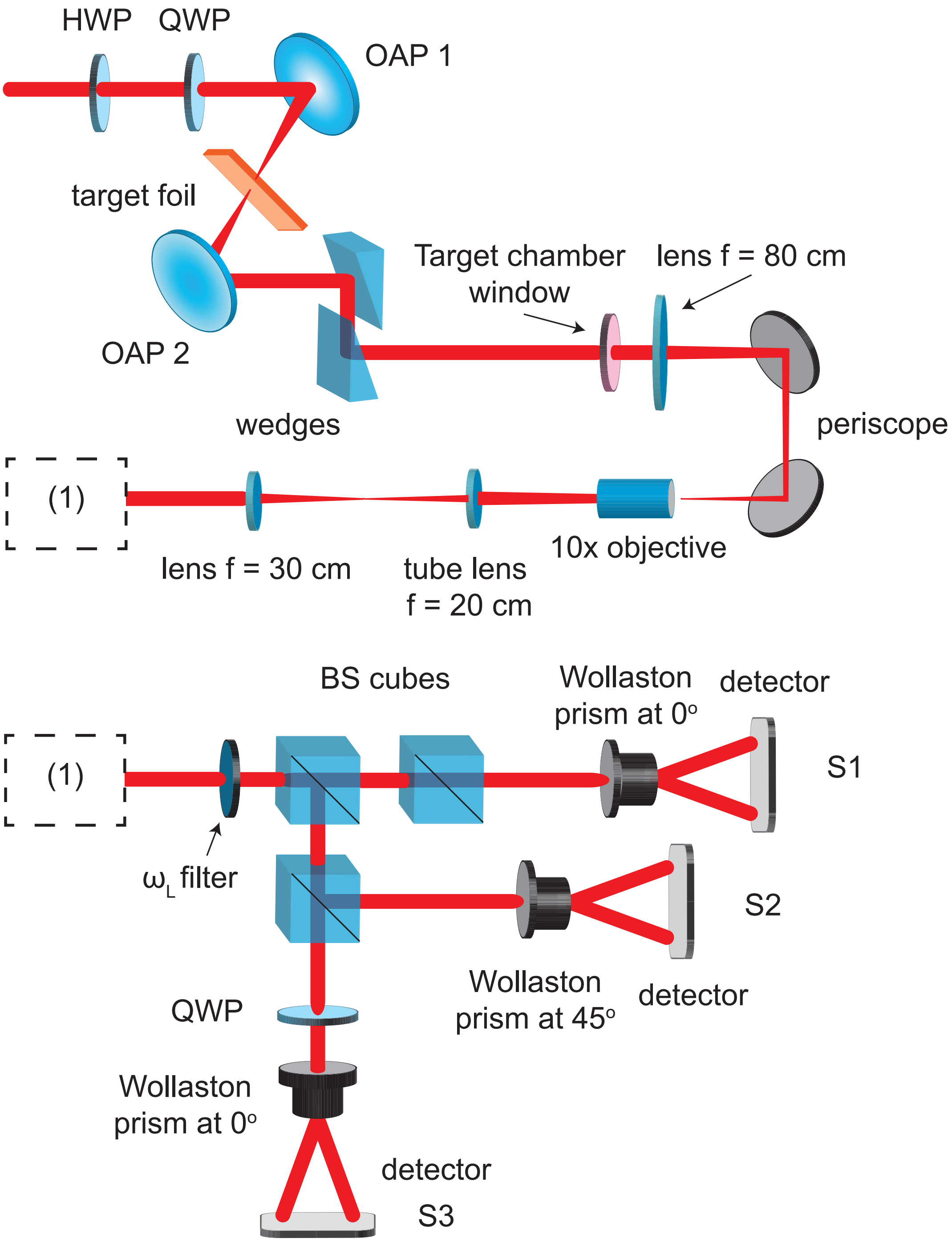

Figure 5.1: A schematic of the experimental set-up employed in this chapter. The top panel illustrates the in-chamber set-up, which includes an OAP to focus the laser pulse onto the target, and a second OAP to collect the light at the target rear. This is reflected off two wedged mirrors, and directed out to the external Stokes polarimeter diagnostic, as shown in the bottom panel.

After exiting the target chamber, the collimated light was focused using a lens with an 80 cm focal length, and periscoped down to the level of the optical bench on which the external diagnostics were set-up. This light was then passed through a 10× microscope objective, and focused using a tube lens with a 20 cm focal length. This formed the object for a final lens, with a focal length of 30 cm, such that the light could then be passed into the Stokes polarimeter and subsequently imaged.

The Stokes polarimeter first split the propagating light into three paths, such that the Stokes parameters could be measured. The first component in this diagnostic was an interference filter, allowing transmission of light at the laser wavelength λ_L, with a bandwidth of ±35 nm. The light was then split into three paths by a series of non-polarising beam-splitter cubes, with 50:50 transmission:reflection for light at λ_L. A Wollaston prism was inserted along each of the paths in order to separate the light into two orthogonal polarisation states. For each of the three paths, the Wollaston angles were set to 0°, 45°and 0°, with respect to their fast axes, whilst the final path (along which the Wollaston was set to 0°) also included an additional $\lambda_L/4$ wave plate after the Wollaston, in order to separate the left and right handed circular polarisation states. The Wollaston angles were set using an external rig, composed of a green He:Ne laser, a linear polariser, a Wollaston prism, and a camera to record the spots. Consider the case where the Wollastons are set to 0°. The light from the He:Ne was first polarised to 0°, then the Wollaston was rotated until one of the spots attained its maximum brightness, whilst the other vanished (where each spot is an orthogonal component of the polarisation state). This condition is met when the angle on the polariser matches the angle on the Wollaston, and is therefore used to set the angles.

Within the Stokes polarimeter, the orthogonal states which emerged from the Wollaston prisms were in the form of two spots of light, which were recorded using an Andor-Neo camera. These cameras have a chip size of 16.6×14 mm, containing 2560×2160 pixels, and a dynamic range of 3×10^4. This Stokes polarimeter enables a time-integrated measurement of the polarisation state of the light transmitted through (and generated within) the target, at the laser fundamental frequency, ω_L. In principle this experimental set-up also enables the spatial distribution of the collected light to be determined, however the resolution of the Stokes polarimeter employed on this campaign was too low to make such a measurement (as demonstrated by the quality of the images presented in Fig. 5.2 (c) and (d)).

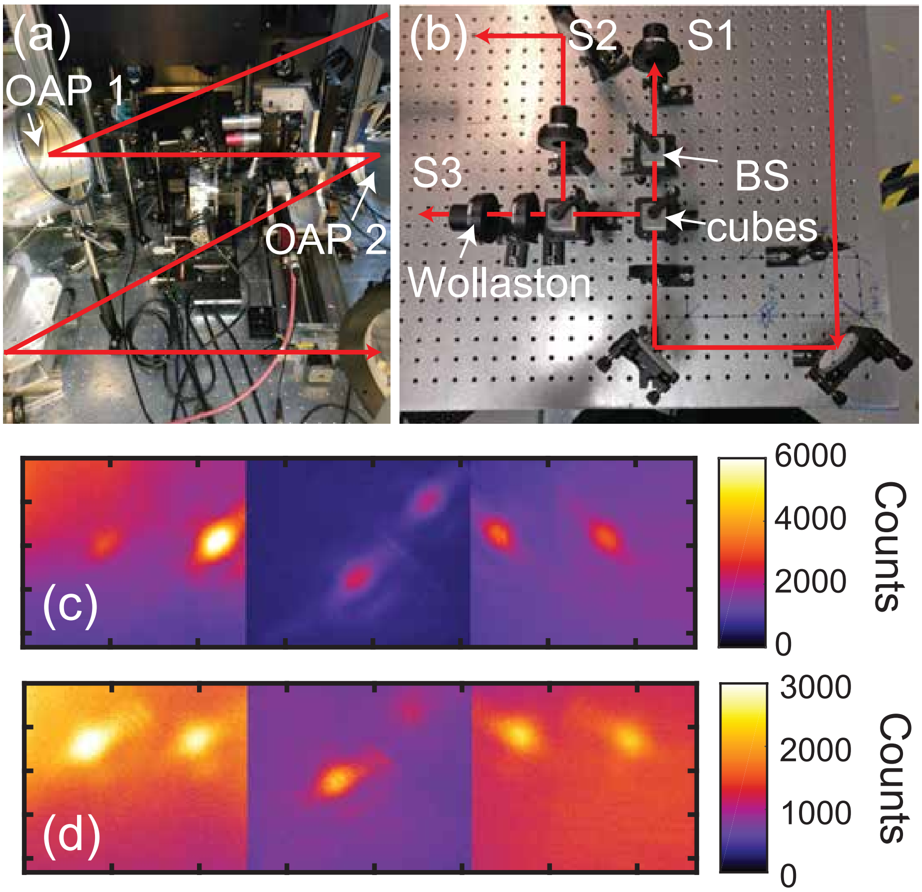

Figure 5.2: Photos of the experimental set-up. (a) An in-chamber photo of the OAPs used to focus the laser pulse on to the target and to re-collimate the light which appears at the target rear. (b) A close up of the Stokes polarimeter, showing the beam paths used to measure the Stokes parameters. (c) Sample images of the raw data obtained on each of the cameras in the Stokes polarimeter, for a 16 nm target. The colormap value indicates the background subtracted number of counts. (d) Images recorded on the Stokes polarimeter cameras for a 35 nm target.

5.3.2 Modelling the Stokes polarimeter

In order to understand how specific polarisation states propagate through the Stokes polarimeter, it was necessary to model the diagnostic analytically. To achieve this, the Stokes representation introduced in section 4.2.1 can be extended to describe the propagation of polarised light through a system of optical components. Each component can be described by a 4×4 matrix, a so-called 'Mueller matrix'. Whilst these matrices can be easily obtained for common optical components, such as wave plates, Wollaston prisms and polarisers, this is not the case for many of the other optics within the Stokes polarimeter. These include, for example, the wedged mirrors and target chamber window, which may modify the polarisation state of the propagating light. The reason this occurs is that the optics act as polarisation dependent attenuators; their reflectivity changes due to the fact that they are positioned at an angle with respect to different input polarisations. In principle, Mueller matrices could be derived for these components if they are first characterised using a spectro-photometer, a device which measures the relative intensity of light transmitted through (or reflected by) an optic over a range of wavelengths and incidence angles with respect to the optical surface. This method is time consuming, as every optical component in the system must be isolated and analysed. It is also impractical, given that some of the optics are too large for the available spectro-photometer. In any case, it may not provide complete characterisation of the components since such a technique does not account for non-linear effects, which may subsequently change the phase of the light during full power shots.

Rather than modelling the system by combining the Mueller matrices for each component, the matrices which describe the general effects these components have on the propagating light are combined. This method accounts for the effects of attenuation, rotation and retardation, which are described by the matrices, M_{att}, M_{rot} and M_{ret}, as follows:

$$M_{att} = \begin{pmatrix} p_x^2 + p_y^2 & p_x^2 - p_y^2 & 0 & 0 \\ p_x^2 - p_y^2 & p_x^2 + p_y^2 & 0 & 0 \\ 0 & 0 & 2p_xp_y & 0 \\ 0 & 0 & 0 & 2p_xp_y \end{pmatrix}$$

$$M_{rot}(2\theta) = \begin{pmatrix} 1 & 0 & 0 & 0 \\ 0 & \cos 2\theta & \sin 2\theta & 0 \\ 0 & -\sin 2\theta & \cos 2\theta & 0 \\ 0 & 0 & 0 & 1 \end{pmatrix}$$

$$M_{ret} = \begin{pmatrix} 1 & 0 & 0 & 0 \\ 0 & 1 & 0 & 0 \\ 0 & 0 & \cos\phi & \sin\phi \\ 0 & 0 & -\sin\phi & \cos\phi \end{pmatrix}$$

where 0$\leq p_{x,y} \leq$1 is the degree of attenuation of the electric field components in the polarisation plane, ϕ is the angle associated with a phase delay, and θ is the angle of rotation of the electric field compared to the input direction. Combining these effects produces a composite (or system) matrix which describes the attenuation, rotation and retardation of light propagating through the Stokes polarimeter. This is opposed to having to isolate each optical component and describe its effect in terms of a Mueller matrix. The resulting system matrix has a number of free parameters, which are then determined via a Monte-Carlo fitting routine, which is described in the next section.

5.3.3 Calibrating the Stokes polarimeter

To fit the free parameters in the system matrix, and calibrate the Stokes polarimeter, it was necessary to measure the response of the diagnostic over a range of known input polarisation states. Control of the input polarisation state was achieved via a combination of a $\lambda_L/4$ and a $\lambda_L/2$ wave plate, placed in the collimated beam path. There was no target in place for this calibration, which was performed using the Astra-Gemini laser in low power (continuous wave) mode, which produces linearly p polarised light by default. One of the wave plates was fixed in place whilst the other was rotated in 5° increments, in the range 0°-180°, enabling the polarisation state to be tuned. The brightness of the resulting two spots on each of the three polarimeter cameras was recorded for each position of the wave plate. To satisfy the normalisation condition for the Stokes parameters (described in section 4.2.1), $S_0 = \sqrt{S_1^2 + S_2^2 + S_3^2}$, the number of counts within the spots on each of the three cameras was normalised to the total number of counts on that camera. Henceforth this is referred to as the relative brightness of the spots. The process was then repeated, swapping the fixed and rotating wave plates.

On a technical note, it is important to mention that this calibration procedure does not generate linearly independent polarisation states. This is due to the fact that whilst one wave plate is rotating, the other is kept in the system. Consider the case where the $\lambda_L/2$ wave plate, which the propagating light encounters first, rotates whilst the $\lambda_L/4$ wave plate is fixed. As the light passes through the $\lambda_L/2$ wave plate, it becomes

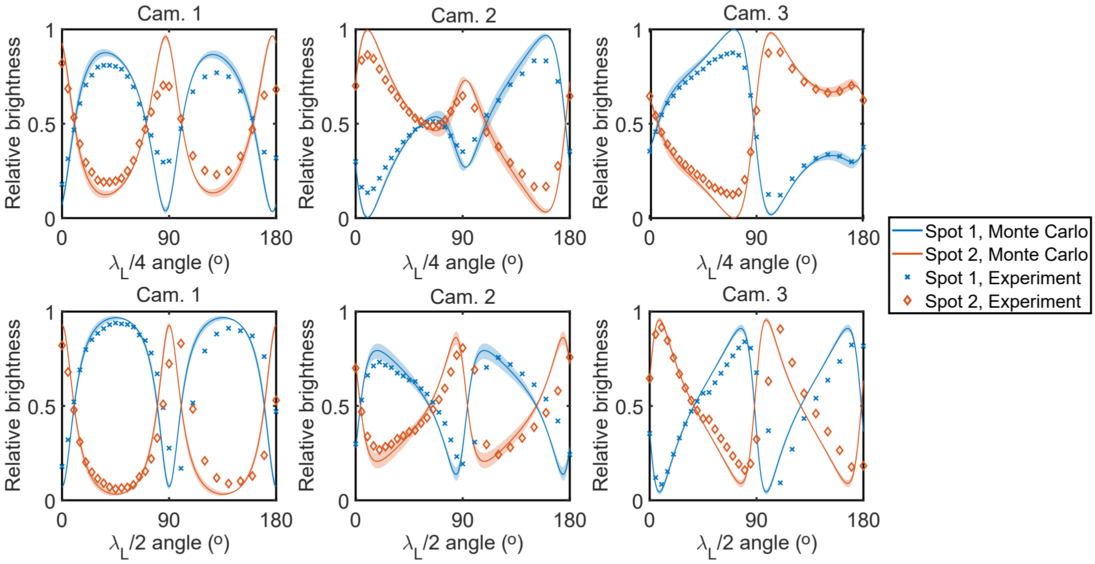

Figure 5.3: Stokes polarimeter response to different known input polarisations. Each column corresponds to one of the three cameras, with the top row describing the effect of rotating the $\lambda_L/4$ wave plate, with the $\lambda_L/2$ wave plate fixed, and vice versa for the bottom row. The orange diamonds and blue crosses correspond to the experimentally obtained values for the relative brightness of the first and second spots of each camera, respectively. The solid orange and blue curves are the best fits obtained using the Monte-Carlo algorithm, for the same spots. The shaded regions indicate the 3σ confidence limits of the fitted curves.

linearly polarised at an angle. It then interacts with the $\lambda_L/4$ wave plate at a non-zero angle of incidence, inducing some degree of circular polarisation. This does not have a significant bearing on the following analysis, as the $\lambda_L/4$ and $\lambda_L/2$ wave plate values are only used to label the various polarisation states. The aim of the analysis is to compare the results of full power shots to known polarisation states; whilst some states will be missing from the 'library' of final states, there is sufficient data from the calibration shots to accurately determine the measured polarisation state via interpolation.

From this calibration procedure, twelve response curves are generated, as follows. The brightness of each of the six spots in the Stokes polarimeter is recorded as the $\lambda_L/4$ wave plate is rotated from 0°-180°, producing the first six curves. The process is then repeated, this time rotating the $\lambda_L/2$ wave plate in order to generate the next six curves. These response curves are plotted in Fig. 5.3, where each of the three columns corresponds to results obtained on one of the three polarimetry cameras, whilst the top and bottom rows correspond to results obtained by rotating the $\lambda_L/4$ and $\lambda_L/2$ wave plates, respectively.

The experimentally obtained response curves in Fig. 5.3 were then used to determine the free parameters in the system matrix, via a Monte-Carlo fitting routine.

The steps involved in this routine are as follows; first, the set of free parameters are chosen quasi-randomly, subject to certain constraints such as $0 \leq p_{x,y} \leq 1$ and $\theta, \phi \in [-180°, 180°]$. These parameters are inserted into the system matrix, and linearly p polarised light is then propagated though the system, with the relative brightness in each of the six spots recorded. The input polarisation state is then varied by passing the Stokes vector for the input light through the Mueller matrices for the $\lambda_L/2$ and $\lambda_L/4$ wave plates, before it enters the system matrix. One of these wave plates is rotated through a range of input angles, with the relative brightness of the spots again recorded at every position, in order to generate a response curve. This process is then repeated, swapping the fixed and rotating wave plates, and varying the rotating wave plate through the same range of input angles. This generates a set of twelve 'simulated' response curves. Each one of these simulated curves is then subtracted from the corresponding experimentally measured response curve, and the residual value is calculated. If the residual value falls below a pre-determined threshold value, obtained by calculating the residual for a known good fit, then the set of fitting parameters is saved. For the next iteration of the routine, the initial parameters are sampled from a normal distribution, centered on the good fitting parameters from the previous run. If the residual value is greater than the pre-determined threshold, then the fitting parameters for the next run are randomly generated, as per the first step. The Monte-Carlo fitting routine was run iteratively until good agreement was obtained between the experimental and simulated response curves (i.e. until the residuals were minimised).

The uncertainty in the best fit parameters was calculated by running the Monte-Carlo algorithm for 15,000 iterations and analysing the distribution of the accepted values of each parameter (these are plotted in the appendix, Fig. A2). For each parameter, the values follow an approximately normal distribution, centered on the mean (or best fit value). The 3σ confidence limits were then calculated, which means that these limits enclose ∼99.7% of the fitting parameter values. These limits indicate the uncertainty in the response curves generated by the Monte-Carlo algorithm.

The results of this Monte-Carlo parameter fitting are plotted in Fig. 5.3, where the solid orange and blue lines represent the best fit response curves for spots one and two, respectively, on each of the three cameras. The shaded regions indicate the uncertainty in the fitted response curves, and are generated using the upper and lower limits of the fitting parameters, as detailed in Table 5.1. The fitted curves are compared to

Fit parameter	Lower limit	Median	Upper limit	Confidence level
1	0.8085	0.8313	0.8563	3σ
2	0.4790	0.4959	0.5134	3σ
3	-146.1	-142.9	-138.7	3σ
4	-32.6	-35.8	-31.3	3σ
5	0.1321	0.1363	0.1402	3σ
6	0.5790	0.5906	0.6117	3σ
7	9.59	9.83	10.27	3σ
8	-184.9	-178.6	-173.7	3σ

Table 5.1: Table containing the best fit parameters obtained from the Monte-Carlo algorithm. The parameters are expressed with a confidence level of 3σ, meaning that ∼99.7% of the fitting parameters accepted by the algorithm fall within 3 standard deviations of the mean value.

the experimentally obtained values, which are denoted by orange diamonds and blue crosses. The response curves generated by the Monte-Carlo routine agree well with the experimental curves, in that they follow the same trends and have the same crossing points. As is particularly clear for the $\lambda_L/4$ wave plate however, there are points where the peaks in the Monte-Carlo curves have a greater magnitude than the experimental curves. This means that when comparing the experimentally measured spot brightness to the Monte-Carlo curves, there will be a larger number of possible states which can describe the experimental data. This ambiguity in the final state is used to determine the uncertainty in the Stokes parameters calculated using the analysis code.

As the response curves were generated by fixing the angle of one wave plate whilst rotating the other, they represent only a subset of all the possible polarisation states. To completely characterise the system, it is necessary to extrapolate these results, and determine the relative brightness of the six spots for all possible combinations of angles on the $\lambda_L/4$ and $\lambda_L/2$ wave plates. This process generates a so-called ‘polarisation map’, as illustrated in Fig. 5.4. Each of the six spots has a corresponding polarisation map; for the pair of spots associated with each camera (i.e. looking at each of the three columns in Fig. 5.4 in turn), the colourmap value for a given spot represents its brightness with respect to the other spot on the corresponding camera. For any combination of $\lambda_L/4$ and $\lambda_L/2$ wave plate angles, it is thus possible to determine the relative brightness of the pair of spots on each of the polarimetry cameras. It is important to note that taking line outs of the polarisation maps, along the lines $\lambda_L/2=0°$, and $\lambda_L/4=0°$, reproduces the response curves plotted in Fig. 5.3.

The process for measuring the polarisation state of light detected at the rear of the

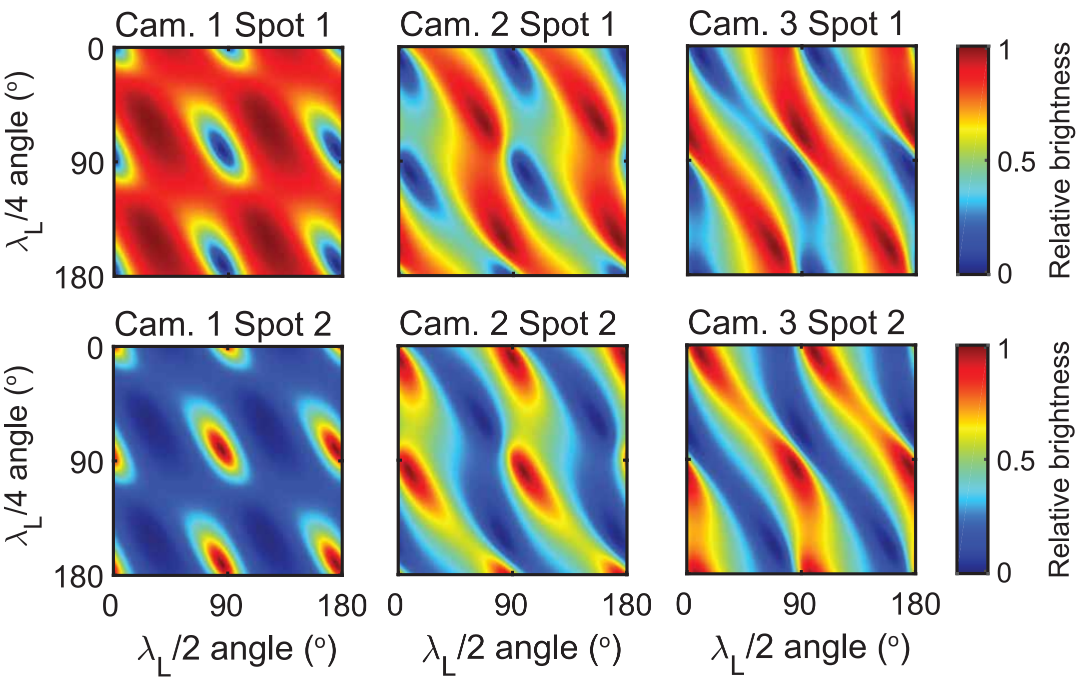

Figure 5.4: Polarisation maps, indicating the relative brightness of the spots on the Stokes polarimeter cameras, for any combination of $\lambda_L/2$ and $\lambda_L/4$ wave plate angles.

target, for full power shots, is as follows. The raw experimental data yields images on each of the three polarimeter cameras, each containing two spots. The integrated counts within each of the spots is measured, enabling the relative brightness to be determined. To make this measurement, the centre of each spot is located, then the total number of counts are recorded, within a circular area which encloses the entire spot. The radius of the circle is increased in five increments, and the relative brightness at each radius is determined by comparing with the number of counts in the second spot, at the corresponding radius. The average relative brightness across the five measurements is used, so that the results are not skewed if, for example, one spot is asymmetric. The relative brightness of the spot is then located in the corresponding polarisation map, giving the 'effective' $\lambda_L/4$ and $\lambda_L/2$ wave plate values of the plasma, and the corresponding Stokes parameters. Even when the code is run with a high resolution (i.e. a large number of input $\lambda_L/2$ and $\lambda_L/4$ wave plate angles, $\geq$10 data points per degree), the polarisation map is made of discrete values, and so it is unlikely that the exact value of the relative brightness calculated from the experimental data can be located within the map. For this reason, it is typically not possible to find a specific state in the polarisation map, rather a region containing multiple states, all of which satisfy the experimental data within a margin of uncertainty. The degree of uncertainty in the

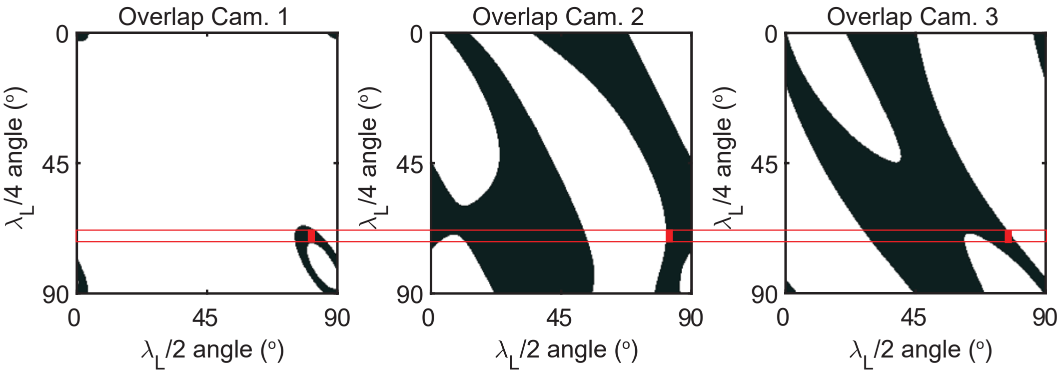

Figure 5.5: Diagram illustrating how the final polarisation state is determined. Each of the three panels corresponds to one of the polarimetry cameras, with the black shaded region denoting the points in the polarisation map which satisfy the experimental measurement of the relative spot brightness for that camera. The set of final states must satisfy all three cameras simultaneously, and is denoted by a red box.

final polarisation state is then related to the standard deviation in the measurement of the Stokes parameters, across the set of states which satisfy the experimental data. This method also takes into account the fact that the spot size may vary shot to shot, or become aberrated due to misalignments in the optical path.

The set of effective wave plate values which satisfy all six polarisation maps simultaneously defines the final polarisation state of the detected light. In reality, there may be multiple states which satisfy the experimental data, in which case the final state is the average of the set of possible states. This process of determining the final polarisation state is further illustrated in Fig. 5.5, for an example shot in which a polarisation shift was measured. Each panel in this figure corresponds to one of the polarimetry cameras, with the black region indicating the range of effective $\lambda_L/2$ and $\lambda_L/4$ wave plate values which satisfy the experimental measurements (i.e. the region of the polarisation map in which the relative brightness of the spots are equal to those measured experimentally, within the limit of uncertainty). Note that here the map is zoomed into a region of 0°-90° to show the overlap more clearly, but the results are symmetric over the entire range of angles. The final polarisation state must then satisfy all three cameras simultaneously. The region which satisfies all these constraints is indicated by a red box. This contains the set of final states which describe the experimental data.

5.3.4 Simulation parameters

The experimental results presented in this chapter are supported by 3D PIC simulations, performed using the fully-relativistic EPOCH code [239]. These enable temporal resolution of the collective electron dynamics, whilst also providing information about the spatial distribution of the detected light, which was not achieved experimentally. In addition, the light can be decomposed into the first and second harmonics of the laser frequency.

The simulation grid was composed of 1,000 × 720 × 720 computational mesh cells, corresponding to a volume of 20 μm × 20 μm × 20 μm. The laser enters the grid from the left boundary, where all of the other boundaries are set to be free space. The laser parameters were chosen to match those of the experiment as closely as possible; the laser wavelength was set to $\lambda_L = 800$ nm, and the pulse had a FHWM duration of 40 fs. This pulse was focused to a Gaussian focal spot, with a FWHM diameter of 3 μm. The peak intensity was varied in the range I_L = (6-15)$\times 10^{20}$ Wcm^{-2}, with the level of light transmitted through the target matching the experimental results most accurately for an intensity of 6×10^{20} Wcm^{-2}. Whilst this peak intensity is higher than that obtained experimentally, this may be due to the fact that the temporal intensity contrast of the laser is different in the simulations. As will be explained later, the target is pre-expanded in order to account for its interaction with the rising edge of the laser pulse. The degree of pre-expansion matches that of the simulations described in Refs. [49, 248, 249], which closely reproduced the results of the aforementioned experimental campaigns.

The targets in the simulations are constructed of a layer of Al^{13+} ions, with thickness in the range 5-40 nm, with a 6 nm thick layer of mixed C^{6+} and H^{+} ions on the front and rear sides. This accounts for the hydrocarbon contaminants which are present in experiments. To account for the effects of the laser temporal intensity contrast in the numerical modelling, the target electron density was pre-expanded to a Gaussian profile, with a FHWM related to the initial target thickness (whilst the areal density was maintained, using solid density aluminium; $n_e = 444 n_c$ for λ_L=800 nm, which is also relativistically overdense, i.e. $n_e > \gamma_e n_c$). The electron temperature is initially set to 100 keV, whilst the ions are initialised with a relatively low temperature of 10 eV. This choice of electron temperature approximates the interaction of the target plasma with the rising edge of the laser pulse, whilst ensuring that the corresponding Debye length is spatially resolved within the mesh size of the computational grid.

5.4 Experimental results

5.4.1 Correlation between the amount of transmitted light and the magnitude of the effective polarisation shift

In this section, experimental results are presented for an investigation of effective polarisation shifts in the ω_L light detected at the rear of ultra-thin foil targets. As described in section 5.3.1, the targets were aluminium foils, with thickness in the range ℓ=16-100 nm. To measure an effective polarisation shift in the transmitted light, it is necessary that the targets undergo transparency at some point during the interaction, hence the requirement of ultra-thin foils.

The objective of this experiment was to measure the influence of the degree of target transparency on the polarisation of the light detected at the target rear. Initially, it is assumed that there is some correlation between these quantities, since the mechanism behind any such effective polarisation shift will in some way depend on the duration of the interaction between the laser pulse and the target plasma. The late onset transparency (for example, through the choice of a thicker target) enables the interaction to proceed for longer, possibly leading to a larger effective polarisation shift. It is therefore proposed that the largest polarisation shift should occur for the target thickness which just about goes transparent.

It is important to note that the experimentally measured quantity is referred to as an ‘effective’ polarisation shift; the reasons for this terminology will become clear later in the chapter. For now, it is stated that the term ‘effective’ shift alludes to the fact that during the laser-solid interaction, additional light may be self-generated by the plasma, for example via transition radiation produced as electrons transition across the target-vacuum boundary. This self-generated light (at ω_L) is also detected at the target rear by the Stokes polarimeter, and so the superposition of this light with the transmitted laser light leads to the possibility of measuring a state whose polarisation appears to be shifted with respect to the input state. In reality, this shift is simply the result of adding a new source of self-generated light to the diagnostic, hence the terminology of an ‘effective’ polarisation shift.

Since the amount of light detected at the rear of the target is expected to play a

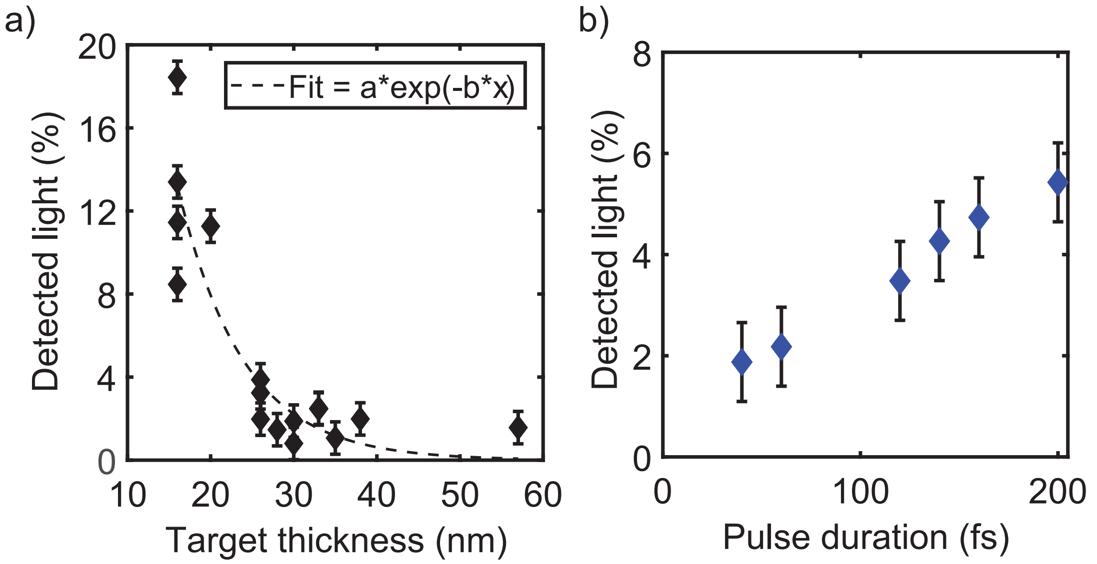

Figure 5.6: Experimental results investigating the degree of target transparency. (a) A plot of the detected light as a function of target thickness for τ_L*=40 fs, and as a function of* τ_L *for* ℓ*=30 nm in panel (b). In both cases, the energy of the transmitted light is normalised to the energy on target. The black dashed line in (a) is an exponential decay curve fitted to the data, illustrating the non-linear decrease in the transmission with increasing target thickness, as described in Refs. [49, 248–250].*

large role in the magnitude of the effective polarisation shift, the degree of transmission was varied. This was achieved in two ways; by varying the target thickness and the pulse duration, separately. The results of these scans are presented in Fig. 5.6 (a) and (b), respectively. The targets employed in the thickness scan varied in the range 16-100 nm. However the level of light transmitted through targets with thickness ℓ>57 nm was sufficiently low (<0.5%) that these targets were generally considered to remain opaque throughout the interaction, and are therefore omitted from Fig. 5.6 (a).

The experimentally measured transmission values in panels (a) and (b) are stated as a percentage, indicating the amount of transmitted laser energy is normalised to the laser energy delivered on target. First, the transmitted energy was obtained from full power shots, without a target; the Stokes polarimeter recorded the total number of counts, for calibration shots of known energy, which then enabled a calibration curve to be generated such that the number of counts could be converted to an energy in Joules. The energy on target was obtained by scaling the laser energy after compressor by the throughput of the system, and accounting for the reflectivity of the double plasma mirror (which was measured to be 48%). Whilst the laser parameters (focal spot size and energy on target) were maintained within the aforementioned range, fluctuations in these parameters lead to variation in the level of transmitted light, for a fixed target thickness. The error bars in Fig. 5.6 therefore correspond to the standard deviation in the set of transmission measurements, obtained for a fixed target thickness of 30 nm (the most commonly employed thickness during the experiment).

Figure 5.6 (a) shows that the level of transmission decreases non-linearly with increasing target thickness, ranging from ~20% transmission measured using a ℓ=16 nm target, down to ~2% for a ℓ=57 nm target. As previously discussed, the transmission through the 100 nm targets was <0.5%. However, since such targets do not undergo transparency, they serve as an indication of the level of light associated with coherent transition radiation, compared to the level of transmitted laser light. The line fitted to this data is an exponential decay curve, which illustrates the rapid decline in transmission levels with increasing target thickness. These results are in excellent agreement with those presented in Refs. [49, 248–250], in which transmission measurements were made for similar targets using the same laser system.

Panel (b) in Fig. 5.6 shows how the level of transmission varies with the laser pulse duration, which was varied in the range τ_L=40-200 fs. The total energy of the pulse was kept consistent, as was the spot size, such that the variation in τ_L gave rise to intensity values in the range $I_L = (3.8 \pm 1.5) \times 10^{19}$ Wcm^{-2} (for the longest pulses, with duration 200 fs) to $(1.7 \pm 0.4) \times 10^{20}$ Wcm^{-2} (for the shortest pulses, with duration 40 fs). Again, varying I_L enables an alternative approach to controlling the degree of target transparency, however, the largest factor in the pulse duration scan is the duration of the interaction between the target plasma and the rising edge of the laser pulse. The amount of detected light in Fig. 5.6 (b) is seen to increase approximately linearly with the pulse duration. This increased transparency is driven by enhanced target expansion, due to the longer interaction time between the target plasma and the laser pulse. Whilst there appear to be no non-linear effects in the level of transmission across the range of pulse durations considered in this study, the level of transmission should decrease again as the pulse duration increases beyond $\tau_L \geq 200$ fs. This is because the intensity will decrease to below the threshold at which RSIT can occur.

Having investigated how the degree of transmitted light depends on both the target thickness and pulse duration, further experimental results are presented which describe how the level of transmission is correlated with the magnitude of the effective polarisation shift. In the results which follow, the magnitude of the polarisation shift is

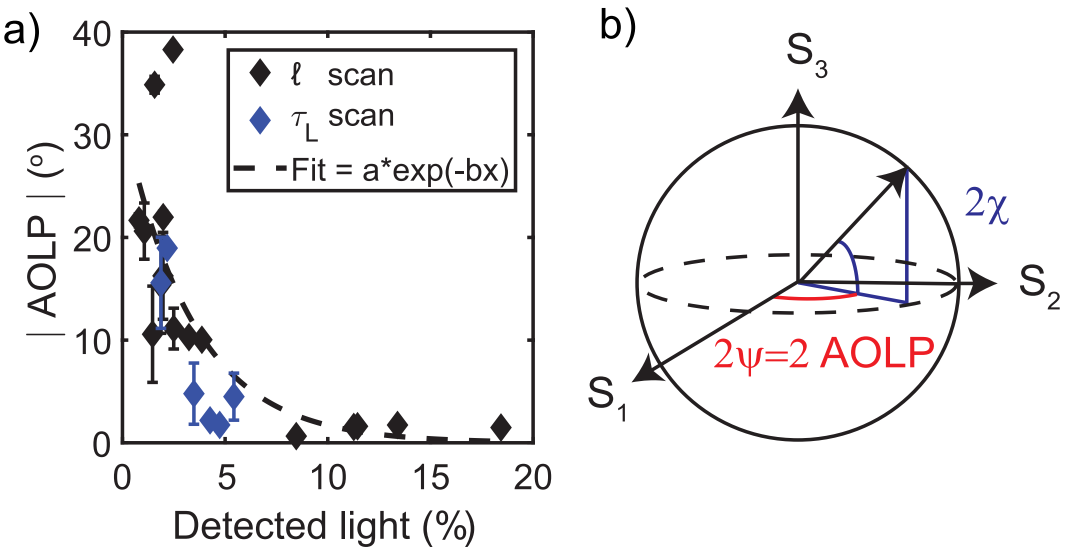

Figure 5.7: An investigation of the degree of transmission on the magnitude of the effective polarisation shift. (a) The magnitude of the AOLP (in degrees) is plotted as a function of the amount of detected light, for the target thickness and pulse duration scans (black and blue diamonds, respectively). The black dashed line is an exponential decay curve, fitted to the data within the target thickness and pulse duration scans. (b) An illustration of the AOLP parameter in the Poincaré sphere.

characterised by a single parameter, the angle of linear polarisation (AOLP). This parameter was described in detail in section 4.2.1, so here it is simply reiterated that this angle is proportional to the ratio of the magnitudes of the measured S_1 and S_2 parameters, such that it measures shifts in the linear polarisation state. In the Poincaré sphere this is interpreted as a rotation of the Stokes vector along the equator, i.e. a rotation in the plane of S_1-S_2, as illustrated in Fig. 5.7. This parameter accurately quantifies the effective polarisation shift as there were no significant changes measured in the S_3 parameter (as demonstrated in Fig. 5.8).

Experimental measurements of the magnitude of the AOLP as a function of the amount of detected light are presented in Fig. 5.7. The black and blue diamonds correspond to data points in the target thickness and pulse duration scans, respectively. The uncertainty in the measurements of the AOLP account for the fact that the analysis technique applied here can find multiple polarisation states which satisfy the experimental data. These uncertainties then correspond to the standard deviation in the set of all possible final states. Both scans demonstrate the same inverse relationship between the magnitude of the AOLP and the amount of detected light. The black dashed line is an exponential decay curve fit to the experimental data, which raises two interesting points. The first is that the ℓ and τ_L scans can be fitted with the

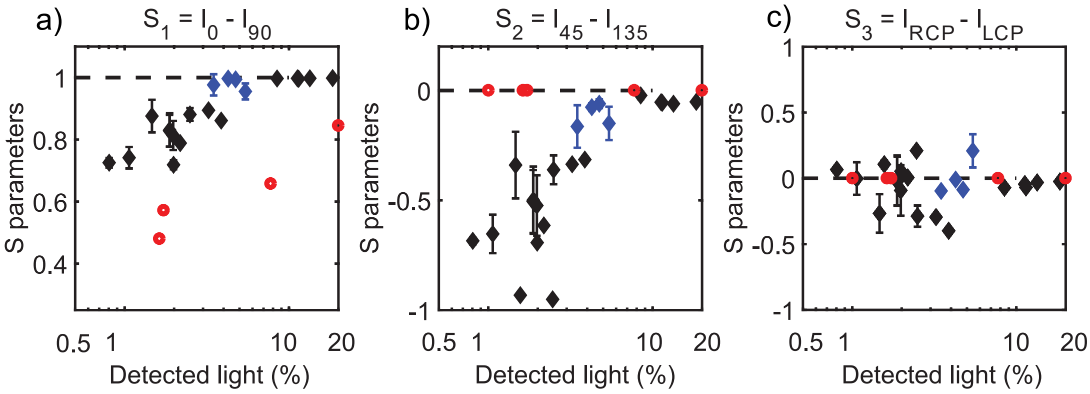

Figure 5.8: Plot of the experimentally measured Stokes parameters as a function of the % of detected light, with the black and blue diamonds corresponding to data points in the target thickness and pulse duration scans, respectively. The black dashed lines indicate the corresponding Stokes parameters for the p polarised input state. The red circles indicate the values of the Stokes parameters determined from the simulations, again as a function of the amount of detected light.

same best fit curve, indicating that the effective polarisation shift is correlated with the degree of transmission, but does not depend on how this parameter is varied. The second interesting aspect is that there is a threshold beyond which there is no measured polarisation shift. The experimental data suggests that for transmission >5%, the measured AOLP decreases to $\leq 1°$, which is within the level of uncertainty in the diagnostic. Even within the threshold for detecting effective polarisation shifts, it is clear that the measured AOLP decreases rapidly, from a peak of $(40 \pm 3)°$ down to $(5 \pm 2)°$ whilst the detected light varies by only 5%. Figure 5.7, demonstrates that the largest measurements of the AOLP, and therefore the largest effective polarisation shifts, occur for the targets with the lowest transmission. These correspond to thicker targets, in which the process of transparency occurs late in the interaction. In terms of pulse duration, the largest measurements of the AOLP occur for the shortest pulses, through which the transmission of laser light is low.

Whilst the AOLP is a convenient parameter to use to characterise the total effective polarisation shift, more information is obtained via calculation of the three Stokes parameters (or S parameters). In Fig. 5.8, each of the three Stokes parameters are presented as a function of the amount of detected light, using data in both the target thickness and pulse duration scans (denoted by black and blue diamonds, respectively). The data is plotted with a logarithmic x axis, since the magnitude of the AOLP varies non-linearly with the degree of detected light, over a narrow range of 1-5%. The data points in the pulse duration scan show less of a spread compared to the target thickness scan, since for the τ_L scan the detected light fell within the range 2-6%, whereas for the ℓ scan this varied in the range 0.5-20%. The red circles on this plot are the S parameters calculated from the 3D PIC simulations, over a similar range of transmission values as for the experimental data (see Fig. 5.6). The black dashed lines in each panel indicate the reference value of the associated Stokes parameter, for an input p polarisation, i.e. the case of no polarisation shift.

First, looking at the S_1 parameter (Fig. 5.8 (a)), it is observed that for levels of detected light >5%, the experimentally measured S_1 parameter is equal to the reference value, indicating that no effective polarisation shift has occurred. For relatively low transmission levels of <5% however, the S_1 parameter decreases approximately linearly as the transmission decreases. For transmission of ~1%, S_1 is reduced to ~70% of the reference value, indicating a large shift in the measured effective polarisation state. This is a demonstration of the same inverse relation between the amount of detected light and the magnitude of the polarisation shift, which was observed experimentally. The rate of decrease in S_1, with decreasing transmission (i.e. the gradient of the best fit line) for the simulations and the experimental results are approximately equal, however the simulations slightly overestimate the level of transmission.

Experimentally, the same trend is observed in S_2, as demonstrated in Fig. 5.8 (b). When the level of detected light exceeds 5%, there is effectively no polarisation shift and the measured S_2 value is equal to the reference value. For low transmission, S_2 deviates strongly from the reference value, exhibiting a much larger shift than the S_1 parameter over a similar range of transmission values. In fact, the S_2 value shifts from 0-1, indicating that the polarisation is nearly entirely oriented along the S_2 axis in the Poincaré sphere, and that the AOLP will take its maximum allowed value of 45°. Interestingly, this trend in the experimental data is not reflected in the simulations, which predict no change in the S_2 parameter. The reason for the discrepancy between the experiment and simulations, which arises only for the S_2 parameter, will be discussed later.

Finally, Fig. 5.8 (c) shows that there is approximately no change in the measured S_3 values as a function of the amount of detected light. The experimental results are scattered around the reference value of S_3=0. This is in agreement with the simulation results, which also predict there should be no change in this parameter. This is the first indication that the mechanism of the polarisation change is not driven by temperature anisotropy, and is therefore different to the physics explored in Stark *et al* [160], as will be discussed in section 5.5.2. To alter S_3, and therefore change the degree of circular polarisation, it is necessary to induce a phase change in the propagating light. The experimental and simulation data show no such shift in the circular polarisation state, with any measured changes occurring only in the linear polarisation state. The fact that S_3 does not change also justifies the use of the AOLP as the figure of merit for interpreting the experimental results.

5.4.2 Interpreting the discrepancies between the experiment and simulation results

The fact that the experimental measurements of the S_2 parameter do not match the predictions of the simulations again indicates that the effective polarisation shifts are not driven by anisotropy within the plasma. Instead, it is proposed that the polarisation shift is caused by the superposition of the transmitted laser light with the self-generated light produced during the interaction. The polarisation state which is detected at the rear of the target then appears to be shifted with respect to the input state. If this is the case, then the discrepancy between the experiment and simulation results can be explained in terms of limitations of the Stokes polarimetry technique.

To cause an effective polarisation shift, the self-generated light must appear in the form of a strong E_z field. By adding light to the Stokes polarimeter, the previous assumption that the degree of polarisation is constant is now violated, and the normalisation $\sqrt{S_1^2 + S_2^2 + S_3^2}/S_0 = 1$ no longer holds. To investigate the impact this has on measurements of the AOLP, we consider the case of a linearly p polarised input state. The addition of an E_z field results in a superposition state which is now linearly polarised, but at an angle. This will cause a shift in the measurement of S_2, and the AOLP will subsequently increase towards its maximum value of 45°. The fact that there is no change in the S_3 parameter is a consequence of the fact that the self-generated E_z field is in phase with the transmitted laser fields. Again this suggests that the polarisation shifts are not driven by temperature anisotropy, since the resulting birefringence should lead to a phase change, and the detection of an elliptical polarisation state.

Further evidence of self-generated light is demonstrated by the fact that the rate of change of S_1 and S_2, with respect to the amount of light detected at the target rear, are not equal. Given that there is no observed change in the S_3 parameter, if the total degree of polarisation were maintained it would be expected that S_1 and S_2 change by equal amounts. This is not the case, with the simulation results indicating that the rate of change of S_2 is higher than that of S_1. This again suggests that there is light being added to the S_2 channel, via the self-generation of a strong E_z field.

It is reasonable to ask whether the analysis could be modified in such a way that it could account for a varying degree of polarisation (which is equivalent to the addition of the self-generated field). Whilst this is in principle possible, it no longer makes sense to interpret the data in this way. The analysis technique was adopted under the hypothesis that the measured polarisation shifts would be driven by temperature anisotropy, in which case the polarisation detected at the rear of the target is a simple rotation of the input state. The simulation results (which will be further explored in section 5.6.1) suggest that the light detected at the rear of the target contains more than simply the light transmitted through it. It does not make sense to compare the input state to the input state plus self-generated light, since these are not comparable quantities. In addition, it has been discussed in Ref. [230] that Stokes analysis does not apply to superposition states of light. As a final point, when the magnitude of the laser E_y and self-generated E_z fields are approximately equal, it will be demonstrated (in section 5.6.2) that the superposition state is a radially polarised mode. The Stokes parameters for such a mode are all equal to zero [267], and so developing this analysis further will not provide any more useful information about the final state. The key point of this section is that the Stokes analysis does indeed predict that large shifts in the polarisation state occur for targets in which the level of detected light is low (in agreement with the simulations) and suggests that these shifts are driven by self-generated light within the plasma. It will be demonstrated that this light arises from the deceleration of electron bunches ejected from the edge of the relativistic plasma aperture. This leads to the generation of radiation, analogously to Larmour radiation, which takes the form of higher order Transverse ElectroMagnetic modes (TEMs). To develop this idea further, 3D PIC simulations are employed to provide the missing information in terms of the spatial distribution of the light detected at the rear of the target.

5.5 Ruling out temperature anisotropy

5.5.1 The influence of the input polarisation on the magnitude of the effective polarisation shift

To further demonstrate that the experimentally measured polarisation shifts are not a result of temperature anisotropy within the plasma, additional experimental data is presented, in which the input polarisation state was varied. This data should enable the plasma polariser and wave plate effects, predicted in Stark *et al* [160] to be detected. These effects are evidenced by a rotation of the input polarisation state; for example, an input circular state will become linearly or elliptically polarised (polariser effect), and an input linear polarisation at an angle will become elliptically polarised (wave plate effect).

First, the plasma polariser effect is investigated. In the simulations presented in Stark *et al* [160], a circularly polarised pulse interacts with a low density plasma, in which temperature anisotropy is artificially induced via modifications to the electron distribution. The degree of anisotropy is chosen such that one of the orthogonal components of the polarisation is completely suppressed, and nearly pure linear polarisation is detected at the rear of the target. To test this prediction experimentally, the $\lambda_L/4$ wave plate was employed to generate a circularly polarised input laser pulse. Note that because the $\lambda_L/2$ wave plate (set to 0°) is located first in the beam path, this does not affect the polarisation. This circularly polarised laser pulse then interacts with ultra-thin foil targets, this time with thickness in the range ℓ=26-35 nm. These were selected due to the fact that, in the experimental data presented in the previous sections, this approximate target thickness range gave rise to the largest polarisation shifts. In contrast to Stark *et al* [160], it is not possible to control the temperature anisotropy within the plasma, so neither of the orthogonal components of the circular polarisation will be completely suppressed. There will however be some degree of anisotropy within the plasma, for example, laser driven density perturbations associated with the propagation of a plasma wave, or temperature anisotropy driven by absorption mechanisms. This may induce birefringence and lead to the laser pulse becoming elliptically polarised. For the experimental conditions under investigation, it is expected that the input circular polarisation should be converted into an elliptical polarisation state, resulting in a change in the S_3 parameter. The results of this data set are presented in Fig. 5.9,

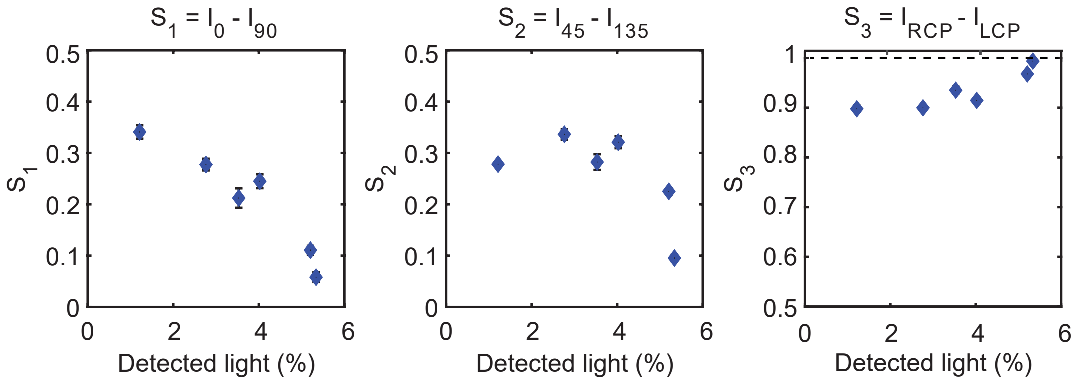

Figure 5.9: Measurements of the Stokes parameters, for light detected at the rear of the target, from a data set in which a circularly polarised pulse interacts with targets in the thickness range ℓ=26-35 nm. The plasma polariser effect should lead to conversion of the input circular polarisation into elliptical polarisation.

in which each of the S parameters are plotted as a function of the amount of light detected at the target rear (compared to the level of light incident on the target). It is interesting to note that the level of detected light is lower here than for the results obtained using linear polarisation (see Fig. 5.8), interacting with the same target thickness. This is due to the fact that electron heating is suppressed for the case of circular polarisation, which is therefore associated with the later onset of transparency. Given that the input polarisation is now circular, the reference values of the S parameters under consideration are (0,0,1). Hence Fig. 5.9 shows the same trend as was observed previously, which is that as the degree of detected light increases, the Stokes parameters tend towards the reference values, indicating no shift in the polarisation state.

For low levels of detected light, the S_1 and S_2 parameters indicate a moderate polarisation shift, both having deviated from the reference values by the same amount. This indicates a rotation of the polarisation within the linear plane, which was described in section 5.4.2 as arising due to self-generated light. It is expected that the largest shift occurs in the S_3 parameter, however Fig. 5.9 indicates that this is not the case. Whilst there is evidence of a moderate shift in the S_3 parameter for low levels of detected light, the change in the S_3 parameter is much less that that of the S_1 and S_2 parameters.

Whilst it is tempting to rule out temperature anisotropy effects based on this data set, it is important to discuss some of the limitations of this study. The first is that, due to the choice of circular polarisation, the level of transmission is low compared to the case of linear polarisation (because of the late onset of transparency). As a result, the low level of detected light is comparable to the level of coherent transition radiation

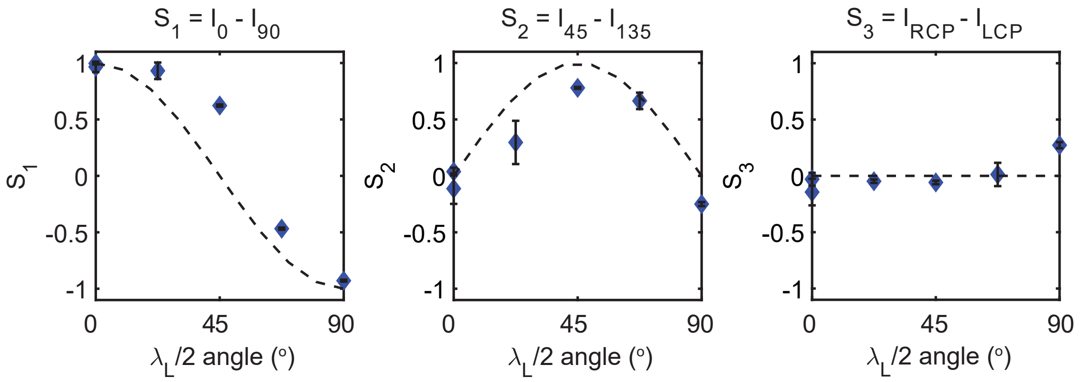

Figure 5.10: Measurement of the Stokes parameters of light detected at the rear of 35 nm thick aluminium targets. The angle of linear polarisation of the input pulse is varied between 0°-90°. The blue diamonds are the experimentally measured values, whilst the black dashed lines are the theoretical values associated with linearly polarised light at the corresponding angle, which serve as a reference.

detected in the linear polarisation thickness scan, so the signal-to-noise ratio will be low.

To test the plasma wave plate effect, the input linear polarisation state was rotated through a range of angles (between 0°-90°) via rotation of the $\lambda_L/2$ wave plate. For this particular data set, the $\lambda_L/4$ wave plate was removed, so the input polarisation is purely linear at an angle, as opposed to having any circular character (which would be the case if the $\lambda_L/4$ plate was kept in place). The targets used here were ℓ=35 nm aluminium foils. By varying the angle of linear polarisation, it is expected that for a particular input angle, the polarisation direction will be aligned with the temperature anisotropy direction within the plasma, causing the light to become elliptically polarised (according to Stark *et al* [160]).

The results of this scan are shown in Fig. 5.10, in which the experimentally measured Stokes parameters are plotted a as function of the input linear polarisation angle (which is equal to the $\lambda_L/2$ wave plate angle). The blue diamonds correspond to the experimentally measured values, whilst the black dashed lines indicate the predicted Stokes parameters, associated with linear polarisation at the corresponding angle. These lines act as reference values for the Stokes parameters, such that deviation away from these lines suggests a polarisation shift. The key result to note from Fig. 5.10 is that the S_3 parameter does not change significantly throughout the scan. Again, this indicates there is no degree of circular polarisation, such that any shifts that do occur result in a change in the degree of linear polarisation.

The interpretation of the S_1 and S_2 parameters is rather more difficult. In general, these follow the theoretically predicted trends. In the previous sections the effective polarisation shifts are described in terms of the self-generation of a strong E_z field. Later in this chapter it will be demonstrated that this E_z field arises from the interaction of the laser pulse with the edge of the plasma aperture, an interaction which is symmetric for any angle of input linear polarisation. The magnitude of the effective polarisation shift should therefore be independent of the input polarisation angle. It is difficult to conclude whether this is the case from Fig. 5.10, since it appears that the biggest shifts occur at angles $\sim 45°$.

The conclusion from these additional data sets is that it is unlikely the experimentally measured polarisation shifts are driven by anisotropy (or, at the very least, the anisotropy effect is small compared to the mode conversion effect presented in this chapter). This is based on the fact that the plasma polariser and wave plate effects could not be replicated. Instead the results are more consistent with the idea of self-generated light being measured at the rear of the target. It is important to note that anisotropic heating may still be the dominant mechanism driving polarisation shifts in other target regimes, such as in the use of near critical density targets with uniform density profiles, as investigated in Stark *et al* [160].

5.5.2 Investigating the degree of anisotropy using PIC simulations

To further rule out temperature anisotropy as the cause of the polarisation shifts, the degree of anisotropy is investigated in the electron distributions from 3D PIC simulations. In Stark *et al* [160], the degree of anisotropy within the plasma is characterised by the parameter $\alpha = \sqrt{\langle p_y^2 \rangle / \langle p_z^2 \rangle}$. This quantity is proportional to the ratio of the effective Lorentz parameter in the orthogonal directions within the polarisation plane, and therefore gives an indication of the degree of temperature anisotropy [268]. For the plasma polariser case, in which the authors completely suppressed one of the orthogonal components of the input circularly polarised light, the anisotropy was calculated to have a peak magnitude of $\alpha \sim 1.35$. A relatively simple test, to see if the same degree of anisotropy is present in this study, is to calculate the parameter α as a function of time from the simulations.

In Fig. 5.11, the parameter α is plotted for a 10 nm (solid blue line) and 30 nm (solid orange line) target, as a function of time, each with the same laser parameters.

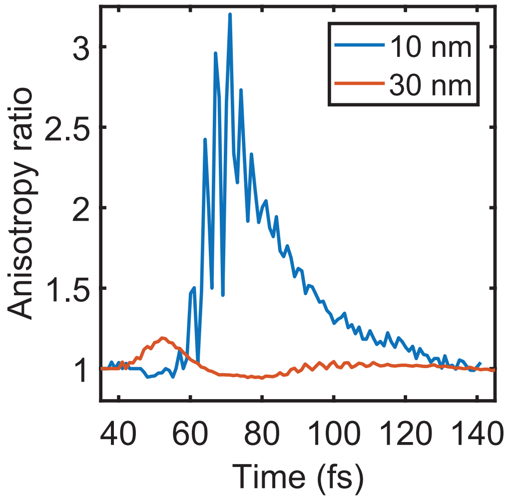

Figure 5.11: A plot of the degree of temperature anisotropy within the 3D PIC simulations. The anisotropy is quantified by the ratio $\alpha = \sqrt{\langle p_y^2\rangle/\langle p_z^2\rangle}$*, which is plotted as function of time for a 10 nm (blue solid line) and 30 nm (orange solid line) target.*

Here, the rising edge of the laser begins to interact with the target at ∼30 fs. The electrons are sub-sampled, such that only those contained approximately within the FWHM diameter of the laser focal spot are considered (i.e. electrons with positions in the range -2.5 μm<x,y,z <2.5 μm).

There are two interesting results in Fig. 5.11. The first is that the degree of temperature anisotropy within the 10 nm target is much larger than that of the 30 nm target, with a peak α ∼ 3× larger. This is the opposite of the experimental and simulation results, in which the largest effective polarisation shifts occur for thick targets. This then indicates that temperature anisotropy is not correlated to the results of the experiment and simulations. In addition, the peak anisotropy value measured in the 30 nm target is similar to that of Stark *et al* [160], however our simulations do not show the same wave plate or polariser effects. The conclusion here is that the aforementioned study considers only a very idealised case, in which the target is near critical density, and the density profile is approximately uniform. If more realistic conditions are investigated, for example a target with a Gaussian density profile, there may still be some aspect of the polarisation shift related to anisotropy however other effects, such as self-generated light, may play a more significant role.

It is also interesting to note that in the 30 nm case, the anisotropy follows the temporal profile of the laser, with a FWHM approximately equal to the pulse duration. This suggests that the low degree of anisotropy occurs due to electron oscillations within the laser field, which then decrease in amplitude as the laser light is reflected from the overdense target surface. This is in contrast to being a plasma driven process, which could continue after the peak of the pulse. For the 10 nm case, the degree of anisotropy remains high after the peak of the pulse. This may be caused by early onset transparency; the laser penetrates through the target and continues to interact with the escaping electrons which are emitted from the rear of the target. This is evidenced by the fact that the peaks in the anisotropy ratio, for the 10 nm target, are separated by approximately a laser period. The temperature anisotropy is still driven by the laser pulse, but the effect is now larger since the laser interacts with the electrons over the full thickness of the target. This is contrary to the surface dominated interaction in the 30 nm target case. Whilst the degree of anisotropy within the simulations presented in this chapter is similar in magnitude to that of Stark *et al* [160], here it is driven by oscillations of electrons in the laser field, as opposed to being a collective effect within the plasma. As such, temperature anisotropy does not explain the experimentally measured polarisation shifts, in which the largest shifts occur for targets which become transparent late in the interaction.

5.6 Simulation results

5.6.1 Role of spatial modes on the effective polarisation shift

The analysis of the 3D PIC simulations is now extended, to provide information about the spatial structure of the light detected at the rear of the targets. Such simulations, for similar laser and target parameters, have provided excellent agreement with experimental results in previously reported studies [49, 248–250], all of which involve investigations of the properties of light transmitted through ultra-thin foil targets, and under similar experimental conditions to those described in this chapter. This enables confidence in the extrapolation of the simulation results to infer information about the spatial structure of the detected light, which could not be made during the experimental campaign detailed in this chapter.

To interpret the experimental results presented in section 5.4, the idea of the ‘plasma mode converter’ is introduced, in which laser light incident on an ultra-thin layer of relativistic plasma is converted into higher order Transverse Electromagnetic (TEM) modes. This is an extension of the idea of self-generated E_z fields which was discussed

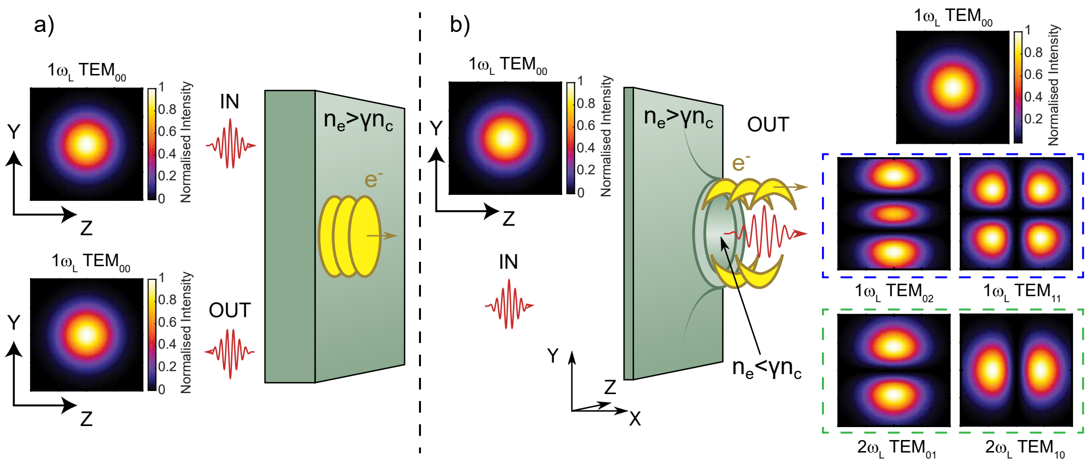

Figure 5.12: Schematic diagram demonstrating the principle of the plasma mode converter. (a) A laser pulse reflects off the surface of a thick, overdense target, generating electron bunches at ω_L or $2\omega_L$, depending on the absorption mechanism. (b) When the laser interacts with an ultra-thin plasma layer, a relativistic aperture is generated, and electron bunches are accelerated from the aperture edge. This leads to the formation of higher order TEM modes, both at ω_L and $2\omega_L$, associated with radiation emitted from the electron bunches as they decelerate in the target sheath field.

in section 5.4.2, since the E_y and E_z fields detected at the rear of the target are in the form of TEM_{02} and TEM_{11} modes, respectively (as illustrated in the appendix A.2). Whilst both of these TEMs are produced at the laser fundamental frequency (ω_L), evidence will also be presented of the formation of a high intensity, radially polarised mode at $2\omega_L$.

The first stage in the plasma mode converter is the formation of a relativistic aperture in the ultra-thin foil target. As described in section 3.2.2, the plasma located within the most intense region of the incident Gaussian laser pulse undergoes RSIT. This results in the formation of a relativistic aperture with a diameter close to the FWHM diameter of the laser pulse [49, 248]. The concept of the relativistic aperture, and the transmission of higher order TEM modes is further illustrated in Fig. 5.12. The interaction of the incident linearly polarised laser pulse (i.e. p polarised such that the electric field points along the y direction) with the edges of the relativistic plasma aperture leads to the generation of TEM modes. As the laser propagates, it accelerates electrons from the edge of the aperture, leading to the emission of dense ($n_e \sim n_c$), crescent shaped bunches of electrons which travel along the direction of laser propagation. There are two forces which contribute to the generation of these bunches; the $\mathbf{j} \times \mathbf{B}$ force and the force exerted by the longitudinal field of the laser, E_x. The $\mathbf{j} \times \mathbf{B}$ force has two components, which drive electrons along the laser propagation direction at frequencies of ω_L and $2\omega_L$, respectively. The second force which accelerates electrons from the aperture edge is associated with the laser E_x field. Whilst the laser is completely polarised in the y direction, the E_x field arises in order to satisfy Gauss' law. The electron number density within the aperture is so low that this region can be considered to be vacuum. In the absence of a current, Gauss' law yields $\nabla \cdot \mathbf{E}=0$, a condition which must then be met within the aperture. Given that the incident laser E_y field has a spatial structure, there must also be a self-generated, spatially varying E_x, such that the total electric field has no divergence. Electron bunches are then accelerated from the edge of the aperture when these two forces point in the same direction.

Considering either the top or bottom edge of the aperture, the ω_L component of the laser ponderomotive force always points in the same direction, whilst the self-generated E_x field reverses direction every half laser period. Since the electron bunches are emitted when these forces are in the same direction, a bunch will be emitted from the top and bottom edge of the aperture at a frequency of ω_L. Overall, the aperture then emits bunches at a frequency of $2\omega_L$, with consecutive bunches emitted at each pole separated by a distance of λ_L. As these structures emerge from the target rear, they are decelerated by the strong electrostatic sheath fields. Although by this stage in the interaction, a region of plasma within the laser focal spot has already undergone RSIT, the sheath fields arise due to the expansion of the plasma around the aperture edge into the vacuum [173]. As the electron bunches are decelerated in the sheath field of the target, they emit Larmor radiation (see section 2.2) via a process analogous to coherent transition radiation [269–271]. This is due to the change in permittivity experienced by the electrons as they transition from plasma into vacuum. The fact that the bunches are emitted from both the top and bottom edges of the aperture (i.e. a bipolar spatial distribution) means that the associated radiation is in the form of a higher order TEM$_{02}$ mode, as can be seen in Fig. 5.12.

Further analysis of the fields detected at the rear of the target leads to two interesting results. The first is that there is a strong self-generated E_z field, which in the case of a relatively thick, 30 nm target, is of the same order of magnitude as the transmitted laser E_y field. The second important point is that the spatial structure of the self-generated E_z field is that of a TEM$_{11}$ mode. The superposition of the transmitted E_y field of the laser with the self-generated E_z field, leads to the detection of a polarisation state which appears to be rotated relative to the input p polarisation, as discussed previously. The presence of the strong E_z field again indicates that the mechanism of the polarisation shift is different to Stark *et al* [160], since if such shifts were driven purely by temperature anisotropy within the plasma, there would be no such self-generated field.

The generation of a TEM_{11} mode is found to be the result of a two stage process. First, a TEM_{02} mode is produced in the E_y field, via the deceleration of the electron bunches emitted from the edge of the aperture. The spatial distribution of this light is in the form of a TEM_{02} mode due to the bipolar spatial distribution of the emitted electron bunches. Spatial gradients in the E_y field (the TEM_{02} mode) then drive electron motion in the y-z plane, which leads to an electron current, j_z. This current produces an associated E_z field in the form of a TEM_{11} mode. This hypothesis could potentially be tested experimentally via measurements of the angular distribution of the electrons which escape the target, by employing the wrap-around stack detector employed in Ref. [272].

To demonstrate this process, the first step is to write the expression for the absolute value of the E_y field, which is a combination of the laser TEM_{00} mode, and the TEM_{02} mode associated with radiation from the decelerating electrons (i.e. the bipolar electron structure decelerating in the sheath field). The E_y field is expressed as follows:

$$E_y = E_0\left(\frac{w_0}{w(x)}\right)\exp\left(-\frac{r^2}{w^2(x)}\right)\left[H_2\left(\frac{\sqrt{2}z}{w(x)}\right)+1\right] \tag{5.1}$$

where E_0 is the amplitude of the electric field, w_0 is the Rayleigh range, $w(x)$ is the beam waist, $r^2 = x^2 + y^2 + z^2$, and H_m is the m^{th} Hermite polynomial. Projecting the Maxwell-Faraday equation along the laser propagation direction (i.e. the x-axis) yields:

$$\frac{\partial E_z}{\partial y} = \frac{\partial E_y}{\partial z} \tag{5.2}$$

$$E_z = \int \frac{\partial E_y}{\partial z} dy \tag{5.3}$$

The integral above can be evaluated by exploiting the properties of the Hermite polynomials, namely $\frac{\partial H_m(u)}{\partial u} = 2mH_{m-1}(u)$. This leads to the following expression for the

E_z field:

$$E_z \sim 2\text{TEM}_{11} - \frac{z}{\sqrt{2}w(x)}[\text{TEM}_{12} + \text{TEM}_{10}] \tag{5.4}$$

$$\sim 2\text{TEM}_{11} + \mathcal{O}\left(\frac{z}{w(x)}\right) \tag{5.5}$$

The important point from the above analysis is that the TEM_{11} mode arises directly from the TEM_{02} mode, produced via the deceleration of the bipolar electron structure in the sheath fields. For small $z/w(x)$, the z component of the electric field behaves as a TEM_{11} mode, in agreement with the simulation results.

It is important to note that this mode conversion process offers a number of advantages over conventional optics, such as phase mirrors, which are typically used to obtain higher order TEMs. As previously discussed, a major restriction in employing these conventional optics is their damage threshold. This issue may be partially resolved by placing the phase plate before the amplification stages, however this can lead to back reflections in the laser chain and subsequent damage to sensitive optics. In addition, a conventional optic only enables one TEM mode to be produced. The plasma mode conversion process described in this chapter enables various modes to be produced. In particular, it will be shown in section that the spatial structure of the mode varies throughout the interaction, demonstrating that this is a highly tunable mechanism.

These concepts are tied together in Fig. 5.13 (a) and (b), which demonstrate the plasma mode converter effect in a 10 nm and 30 nm target, respectively. The panels to the left of (a) and (b) show the spatial distribution of the E_y (top) and E_z (bottom) fields, averaged over a laser period. It is clear that the input pulse is set to a fundamental Gaussian TEM_{00} mode, and there is no initial E_z field. The middle panel shows the spatial distribution of the electron density, normalised to the critical value and measured 40 fs after the peak of the pulse (at which point the target has undergone RSIT). For the 10 nm case in panel (a), a sharply defined plasma aperture forms in the region of the focal spot, enabling a high level of transmission. In contrast, the 30 nm target in panel (b) does not undergo a significant degree of transparency until relatively late in the interaction, and is driven by target expansion. Although the target appears to remain opaque to the laser in Fig. 5.13 (b), there will still be some fraction of light transmitted due to the late onset of transparency. The plots on the right of (a) and (b) show the spatial distributions of the E_y and E_z fields in the

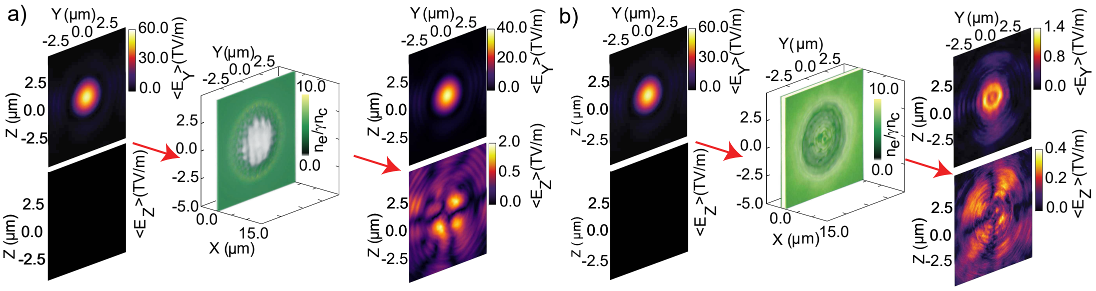

Figure 5.13: 3D PIC simulation results demonstrating the plasma mode converter concept. (a) A linearly polarised Gaussian pulse, with a peak intensity of 6×10^{20} Wcm^{-2} interacts with a 10 nm thick aluminium foil. The panels on the left show the spatial distributions of the E_y (top) and E_z (bottom) fields, in the polarisation plane. The panels on the right show the same distributions for the light detected 10 μm behind the target rear, at a time equal to 40 fs after the peak of the pulse. The fields are averaged over one laser period. The panel in the middle shows the spatial distribution of the electron number density (normalised to the critical value), in this case illustrating the formation of the relativistic plasma aperture. (b) The same quantities are plotted, this time for a 30 nm thick foil.

polarisation plane, measured at a distance of 10 μm behind the rear of the target. At this distance it is the far field distribution of the light which is sampled, and so the diffraction effects discussed in Refs. [49, 248, 249] are not important. Again, these plots are averaged over a laser period, and measured 40 fs after the peak of the pulse. They are also filtered so that only ω_L light is considered, to be consistent with the experimental measurements.

In comparing panels (a) and (b), it is both the structure of the detected fields, and the ratio of the magnitude of the E_y field to that of the E_z field, which are of interest. For the 10 nm target in panel (a), the output E_z field demonstrates a clear TEM$_{11}$ structure, as evidenced by the four symmetric lobes which appear around the laser propagation axis. In the E_y field however, the only structure visible is the TEM$_{00}$ mode of the laser, which has a magnitude ∼40 times greater than that of the peak E_z field. This exceptionally high transmission is the result of early onset transparency. In order for the TEM$_{11}$ to appear in E_z, there must be some TEM$_{02}$ structure in the E_y field, however this signal is suppressed by the much stronger fundamental laser mode. It is important to note again that this 10 nm case also gives rise to the smallest effective polarisation shift. This is due to the fact that the self-generated field is much weaker than that of the laser, thus the superposition state measured at the rear of the target is essentially the same as the input state.

In Fig. 5.13 (b) however, there is much stronger evidence of the TEM$_{02}$ mode in the distribution of the E_y field. This is clear from the fact the distribution is

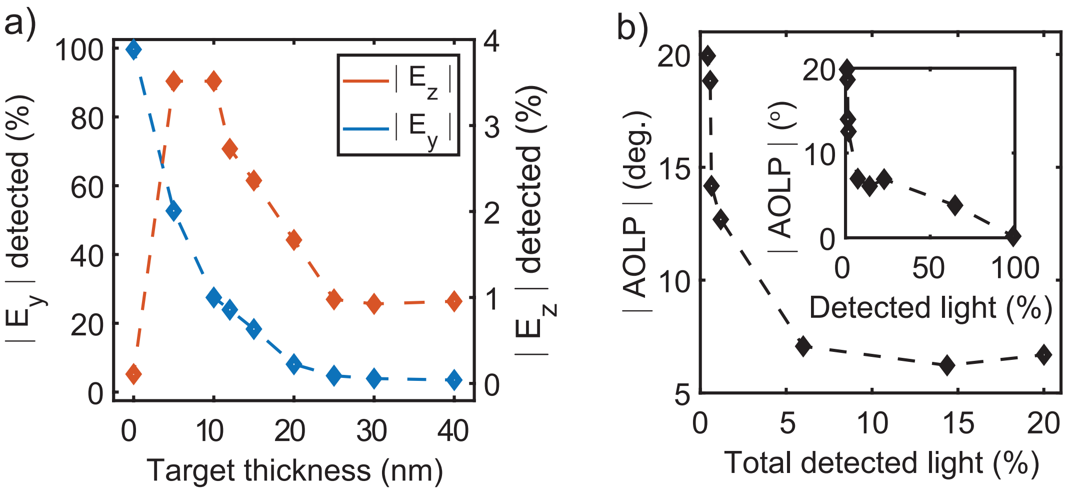

Figure 5.14: (a) The amount of E_y (blue) and E_z (orange) light detected at the fundamental frequency, ω_L, at the rear of the target. These magnitudes are normalised to the total amount of light detected at ω_L. The case of zero target thickness refers to a simulation run without a target in place, where it is shown that there is no E_z present. (b) A plot of the AOLP as a function of the total detected light (normalised to the input laser pulse). The large plot shows how the AOLP varies over the range of detected light levels which were observed experimentally, whilst the inset shows the variation of the AOLP over a wider range of transmission values.

elongated compared to the 10 nm case, with the structure translating into the bipolar distribution of the accelerated electron bunches. In the E_z field, there is some TEM$_{11}$ structure, however the distribution has a lower signal-to-noise ratio, given the low levels of transmitted light. The key result here is that, for this 30 nm target, the ratio of the peak E_y/E_z ∼3 and so these fields are of the same order of magnitude. The presence of a strong, self-generated E_z field means that the polarisation of the superposition state which is measured at the rear of the target will appear to be rotated with respect to the input state, and the resulting AOLP will be large.

The link between the ratio E_y/E_z and the magnitude of the polarisation shift (i.e. the magnitude of the AOLP) is further demonstrated in Fig. 5.14. Here, the percentage of detected light contained within the E_y and E_z fields, compared to the total amount of light detected, is plotted as a function of the target thickness within the range ℓ=10-40 nm. The case ℓ=0 nm corresponds to a simulation with no target, in which it is clear that there is no self-generated E_z. Panel (a) shows that the largest magnitude E_z field is produced by the 10 nm target, however this also transmits the most E_y, and so the overall effect is a weak shift in the effective polarisation state. As the target thickness increases, the level of transmitted E_y light decreases, as does the level of self-generated E_z light, albeit at a slower rate. The magnitudes of E_y and E_z are now comparable, meaning that a larger polarisation shift is observed by measuring the superposition state. This is corroborated by Fig. 5.14 (b), in which the AOLP is plotted as a function of the amount of detected light. Again the thinnest targets, which give rise to the highest levels of detected light, also correspond to the smallest shift in the measured AOLP, in excellent agreement with the experimental results (see Fig. 5.7). The main plot in panel (b) spans the transmission levels observed in the experiment, whilst the inset shows the variation in the AOLP as a function of transmission over a wider range of values.

To demonstrate that the emission of accelerated electron bunches (with a bipolar spatial distribution), is purely an aperture driven effect, the results of a 3D PIC simulation, in which the laser pulse interacts with a pre-formed aperture, are presented in Fig. 5.15. In this simulation, the target is a 1 μm thick, overdense ($n_e = 10n_c$) slab of plasma, from which a circular area with a diameter of 5 μm has been removed from the center. Panel (a) shows the acceleration of electron bunches from the aperture edge, where the red lines denote contours of density $n_e = n_c$. As described earlier, these bunches are emitted at ω_L from the top and bottom of the aperture, and move towards the laser propagation axis as they decelerate in the electrostatic sheath field. The magnitude of this sheath field is denoted in Fig. 5.15 (a) with a green colour scale. In panels (b) and (c), the spatial distributions of the E_y and E_z fields in the polarisation plane are plotted, at a distance 10 μm behind the target and averaged over a laser period. Again, the TEM$_{00}$ mode of the laser dominates the E_y field which is detected at the target rear, and the magnitude of the peak E_y field is ~16 times greater than that of the E_z field. However, in this case, there is a very clear TEM$_{11}$ mode in the E_z field. This mode is visible due to the higher signal-to-noise ratio associated with a pre-defined plasma aperture, compared to Fig. 5.13, in which the aperture forms during the interaction. Whilst there must be some TEM$_{02}$ structure in the detected E_y field, in order to induce the TEM$_{11}$ in the E_z field, it is not visible in Fig. 5.15 (b) due to the dominant TEM$_{00}$ mode associated with the transmitted laser light. The key point of Fig. 5.15 is that by simplifying the simulation via the introduction of a pre-defined aperture, the generation of the electron bunches is clearly seen during the interaction of the laser with the edges of the aperture.

It is possible to simplify the simulations further, and to demonstrate the generation of the TEM$_{02}$ mode via the deceleration of the emitted electron bunches in the

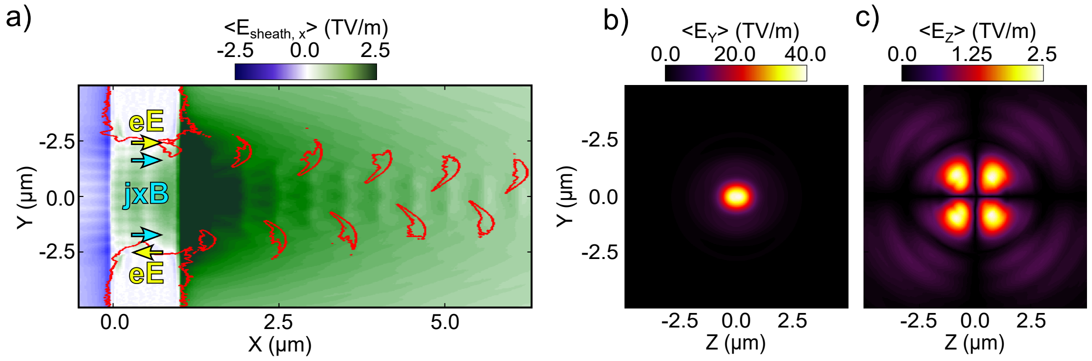

Figure 5.15: 3D PIC simulations demonstrating that the electron bunches arise from the interaction of the laser pulse with the plasma aperture. (a) The laser propagates in the positive X direction, along the Y=0 axis (since the laser is normally incident on the target). It then interacts with a μm thick slab of plasma, in which an aperture with a diameter of 5 μm has been pre-defined in the polarisation plane, to match the focal spot size of the laser pulse. Accelerated electron bunches are emitted when the laser $\mathbf{j} \times \mathbf{B}$ *force and the force exerted by the laser* E_x *field, point in the same direction. The colormap indicates the magnitude of the sheath fields at the target rear, whilst the red lines denote contours in the electron number density, such that* $n_e = n_c$*. (b) The spatial distribution of the laser* E_y *field in the polarisation plane, averaged over a laser period. (c) The spatial distribution of the* E_z *field in the same plane.*

electrostatic sheath field at the target rear. In Fig. 5.16, 3D PIC simulation results are presented in which there is no target, rather the electrons are initialised in crescent shaped bunches, with density $n_e = n_c$. These bunches have a drift velocity in the positive x direction, and are decelerated by an electric field applied across the grid (with a magnitude of 10 TVm^{-1}), which is analogous to the electrostatic sheath field at the target rear, as measured from the simulations presented in Fig. 5.13. Here it is possible to spatially separate the emitted radiation and the electron bunches, since the radiation propagates along the positive x axis, whilst the electron bunches are decelerated and reverse direction. In addition, there is no incident laser pulse in these simulations, such that the detected E_y field will not be dominated by either the fundamental laser mode or transition radiation associated with laser accelerated electrons passing through the target rear.

The plots on the top and bottom right of Fig. 5.16 (a) show the spatial distributions of the E_y and E_z fields in the polarisation plane, 10 μm behind the target rear, and averaged over a laser period. In the E_y distribution, it is clear that there is a TEM$_{02}$ mode, as indicated by the elongated lobe structure, which follows the bipolar spatial distribution of the accelerated electron bunches. The presence of this TEM$_{02}$ mode then leads to the generation of the TEM$_{11}$ in the E_z field, via the conversion mechanism described earlier. Indeed the TEM$_{11}$ mode is clearly visible in the lower plot in panel

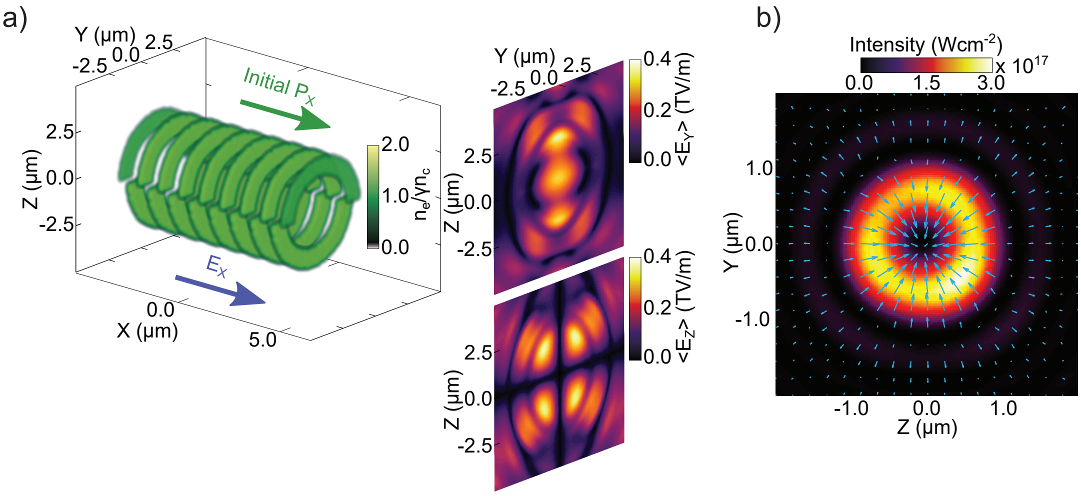

Figure 5.16: 3D PIC simulations demonstrating the generation of the TEM_{02} mode in the E_y field, and the TEM_{11} mode in the E_z field, as a result of the decelerating electron bunches. Panel (a) shows the initialised bunches decelerating in a strong longitudinal electric field. This leads to the formation of a TEM_{02} mode in the E_y field, and a TEM_{11} mode in the E_z field. (b) The spatial intensity distribution of the $2\omega_L$ light, which is observed in a high intensity, radially polarised mode.

(a).

Thus far, only the light detected at ω_L has been considered, however the simulations also indicate that mode structure is present in the second harmonic, $2\omega_L$. The spatial intensity distribution of the light detected at the target rear, at a frequency of $2\omega_L$ (and averaged over a laser period), is presented in Fig. 5.16 (b) for the simulation with the pre-defined electron bunches. The arrow heads indicate the direction in which the electric field vector points, and thus indicate the polarisation of the detected light. Here, there is clear evidence of a radially polarised mode. This arises from the superposition of the modes present in the E_y and E_z fields, when they are of the same order of magnitude. In addition, the mode is polarised and has a peak intensity of 3×10^{17} Wcm^{-2}. This $2\omega_L$ light is sufficiently intense that spatial gradients in the intensity distribution may be exploited to trap and accelerate electrons at the target rear. The polarised mode is also generated at $2\omega_L$ in the full target simulations, however the signal-to-noise ratio is lower than that presented in Fig. 5.16. It is important to note that despite the high intensity of the $2\omega_L$ light, it does not drive electron motion at the target rear; the simulations are run without the QED module for this study, meaning that the electrons cannot interact with their self-generated fields.

5.6.2 Generation of high intensity radially polarised modes at $2\omega_L$

The generation of these radially polarised modes is further investigated in Fig. 5.17, in which the spatial intensity profile of the $2\omega_L$ light is investigated as a function of target thickness, along with the temporal evolution of the produced mode. Each of the plots is taken at the same position in space, located 10 μm behind the target rear, with the light averaged over a laser period. In each panel, the blue arrows indicate the direction of the electric field vector. Each row corresponds to a different target thickness; in panels (a)-(c), (d)-(f) and (g)-(i), the target thickness is ℓ=5, 20 and 30 nm, respectively. The columns indicate different times during the interaction. Panels (a), (d) and (g) are compared at a time of 28 fs after the peak of the pulse, panels (b), (e) and (h) are compared 40 fs after the peak of the pulse (which is the time at which the 20 nm target undergoes transparency), and panels (c), (f) and (i) are compared 52 fs after the peak of the pulse.

First, comparing different target thicknesses (i.e. rows of Fig. 5.17), it is clear that for the 5 nm target, the structure in the intensity spatial distribution is dominated by the TEM_{02} mode in the E_y field. This mode is associated with the deceleration of the emitted electron bunches in the sheath fields at the rear of the target. The magnitude of the self-generated E_z field in this case is much lower than that of the E_y field, and so the spatial intensity distribution closely follows the distribution of radiation from the decelerating electron bunches. As the target thickness increases to 20 nm, a radial mode appears in the spatial intensity distribution. This indicates that the $2\omega_L$ light in both E_y and E_z are approximately equal in magnitude, such that the superposition of these fields results in the generation of a near perfect radial mode. For a target thickness of 30 nm, the radial mode is still present, however it appears modulated due to the reduced signal-to-noise ratio associated with late onset transparency. Figure 5.17 indicates that different target thicknesses give rise to different spatial modes. This is due to the varying ratio of E_y/E_z as a function of target thickness, which impacts the modes which can be generated. The mode conversion process described in this chapter is therefore tunable, via the target thickness. This is not possible with conventional optics, which can only generate a single mode. In addition, Fig. 5.17 shows that, in the case of a 20 nm thick target, the radial mode is produced with an intensity of $\sim 5 \times 10^{18}$ Wcm^{-2}. It is not currently possible to generate modes at this intensity using conventional optics, given their relatively low damage thresholds.

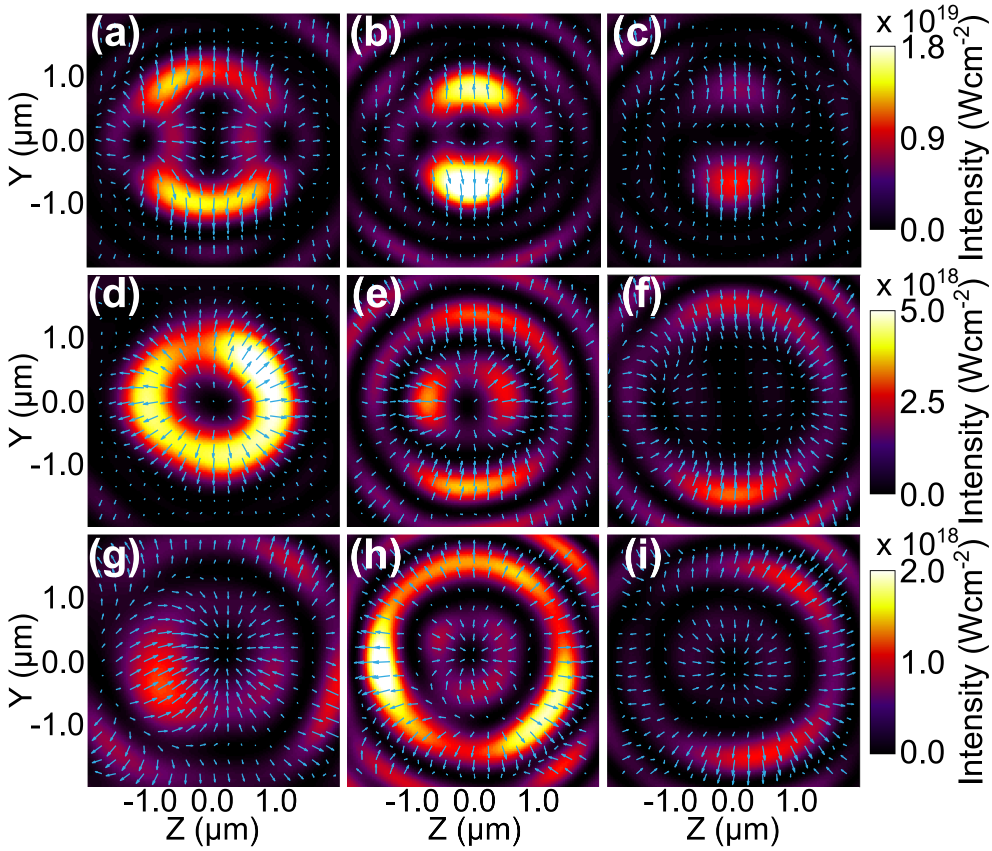

Figure 5.17: Spatial intensity distributions and electric field vectors (blue arrows) for $2\omega_L$ *light, from the full laser-foil simulations, measured 10 μm behind the target rear. Three values of target thickness are compared; (a)-(c) 5 nm, (d)-(f) 20 nm and (g)-(i) 30 nm. The spatial intensity distributions evolve temporally; panels (a),(d) and (g) are compared 28 fs after the peak of the pulse, (b), (e) and (h) are compared 40 fs after the peak of the pulse, and finally (c), (f) and (i) are compared 52 fs after the peak of the pulse.*

Figure 5.17 also demonstrates that the spatial distribution of the TEM modes vary temporally during the interaction. This is due to the ratio of E_y/E_z, which has a temporal dependence due to the varying degree of target transparency. The fact that different spatial structures, and therefore modes, appear at different times in the interaction demonstrates that this is a dynamic mode conversion process. Again, temporal variation of the generated mode is not possible using conventional optics. This raises the possibility of varying the intensity at which an interaction with a given mode occurs, or investigating the influence of 'spot size' effects, purely by varying the distance from the target rear.

It is important to note that the radial modes produced in Fig. 5.17 do not carry angular orbital momentum (OAM). In order to generate OAM, the light must have a helical wavefront. This is not the case in these simulations, since the electrons are emitted in discrete bunches at a frequency of ω_L (from either the top or bottom edge of the relativistic aperture). These bunches do not rotate within the polarisation plane, but instead move along the laser propagation direction. This is also evident when examining the electric field vectors; the field does not change direction as a function of time, again suggesting that the electron bunches are not rotating and therefore do not carry OAM. The case may be different if the incident laser is circularly polarised, since the electrons will be emitted from the aperture edge in a helical bunch, as opposed to the bipolar structure which arises from the interaction of a linearly polarised laser pulse with the aperture.

Finally, it is worth briefly commenting on possible applications of the high intensity radially polarised modes presented in this chapter. For example, the ponderomotive force associated with the steep spatial gradients in such a mode could be used to enhance electron and positron trapping within the beam, during laser driven wakefield experiments [273, 274]. The interaction of an ultra high intensity, radially polarised mode with a high energy electron source could additionally be used to experimentally investigate radiation reaction. For example, the electrons may become trapped within the spatial gradients in the electric field associated with the mode, radiating away a significant fraction of their energy. In addition, if the trapped electrons are collided with another high intensity laser pulse, the set-up could be used to trigger pair-production cascades. This could be achieved by employing radially polarised modes in the dual pulse interaction scheme which is presented in chapter 7. A possible method by which these prospective experiments could be performed is by introducing a system of two OAPs; one would be positioned at the focus of the radially polarised mode, to collect the light, which could then be focused onto a gas/solid target using the second OAP.

5.7 Conclusions

In this chapter, the polarisation state of light detected at the rear of ultra-thin foil targets was investigated, both experimentally and via 3D PIC simulations. The predictions of Refs. [159–161] suggested that laser-induced birefringence within the resulting plasma should lead to useful plasma photonics effects, such as polariser and wave plate-like behaviour. Experimentally, an effective polarisation shift was measured, which was found to be greatest when the level of light detected at the rear of the target was relatively low. In addition, this shift was seen to affect only the degree of linear polarisation, whilst the circular polarisation state remained unchanged. Upon further investigation, with different input polarisation states, it was not possible to detect a significant change in the circular polarisation state. This suggests that for the laser and target parameters employed in this chapter, the polarisation shifts cannot be explained in terms of temperature anisotropy within the plasma, as is the case in Stark *et al* [160].

Further analysis with 3D PIC simulations revealed that the interaction of the laser pulse with the relativistic plasma aperture led to the acceleration of crescent shaped electron bunches with a bipolar spatial distribution from the target, and subsequently generated a strong E_z field at the rear of the target. This field is not predicted in Stark *et al* [160], and hinted towards a different mechanism driving the polarisation shift. The structure of the E_z field was found to be a TEM_{11} mode, such that the superposition of this mode with the transmitted laser field leads to the experimental measurement of an effective polarisation shift. The shift is largest when the magnitude of the self-generated E_z field is comparable to that of the E_y field, explaining why the magnitude of the shift was experimentally observed to depend on the level of detected light.

It was demonstrated that the mode structure is also present in the $2\omega_L$ light generated during the interaction, and when the magnitude of the transmitted laser field is approximately equal to that of the self-generated field, that the superposition results in a radially polarised mode. This mode is formed at high intensity $\sim 10^{18}$ Wcm^{-2}, and is also tunable, given that the conversion efficiency to a given mode depends on the target thickness. This is, to our knowledge, the first demonstration of a method by which high intensity radially polarised modes can be generated via laser-solid interactions. This application of plasma photonics may enable the properties of ultra-intense laser pulses to be tailored to experiments, without the use of expensive solid-state optics. In addition, the generated modes may be applied to enhance the degree of control possible over laser-driven particle and radiation sources.

The mode conversion process described in this chapter may be enhanced at multi-PW laser facilities, in terms of the intensity of the modes which can be generated and the degree of control which is possible over their spatial and temporal profiles. In this chapter it is demonstrated that optimal mode conversion occurs when the transmitted light is comparable in magnitude to the self-generated light. The immediate concern is that, in moving to ultra-high laser intensities, the transmitted laser light will dominate over the self-generated light such that no mode conversion is observed. However, it is predicted in Ref. [54] that the onset of transparency may be delayed due to RR. This could enable the level of transmitted light to be reduced such that mode conversion can still be observed from thin foil targets. In addition, the dynamics of the accelerated electron bunches in the transmitted laser fields will be influenced by RR. This could lead to more intense self-generated light via strong radiative cooling of the electron bunches. This cooling leads to contraction of the electron phase space, producing more dense and spatially compact bunches of electrons (compared to a case where RR is weak). Thus different modes could be produced at multi-PW laser facilities compared to the results presented in this chapter. In addition, RR will affect the electron dynamics temporally, therefore it is likely the mode structure will vary throughout the interaction. It is demonstrated in chapter 6 that the magnitude of the RR effects can be controlled via the laser and target parameters employed during laser-solid interactions, therefore it may be possible to gain enhanced control over the spatial and temporal properties of the modes generated at multi-PW laser facilities. The ability to vary the spatial structure of the mode offers a new degree of control over the collective electron dynamics, since this is not possible using conventional solid-state optics. Varying the spatial structure of the mode throughout the interaction will enable steep acceleration gradients to be achieved, which can be employed to investigate QED effects (such as RR and subsequent radiative trapping).

Chapter 6

Modelling the effects of the radiation reaction force on the interaction of ultra-intense laser pulses with thin foils

6.1 Introduction

With the next generation of laser facilities, such as the Extreme Light Infrastructure (ELI) [220] and APOLLON [218], it will be possible to reach focused laser intensities exceeding 10^{23} Wcm^{-2}. Among the first experiments at these facilities will be investigations of laser driven acceleration of thin foils. As the laser light reflects off these targets, they are accelerated to high velocities through the process of radiation pressure acceleration (RPA) [43, 186, 188, 275]. This process generates bunches of ions, with high peak energies and a narrow energy spread [178, 276, 277]. Such ions have applications in oncology, proton radiography and the fast ignition approach to inertial confinement fusion [39, 154, 278].

Utilising laser-solid interactions to generate the high energy ions has a number of advantages over conventional methods, such as radio-frequency (RF) particle accelerators. RF accelerators are restricted to acceleration gradients of ∼TVm^{-1}, beyond which they suffer electrical breakdown. Plasma-based acceleration schemes are not limited by this breakdown condition, and can instead produce acceleration gradients of ∼GVm^{-1}.

This enables high energy electrons to be produced over scales of centimeters, such that more compact experimental geometries may be achieved at a comparatively lower cost. For these reasons, laser-driven ion acceleration is an extremely active reasearch area.

Recent studies have focused on ions generated during the interaction of ultra-intense laser pulses with thin foils (whose thickness is comparable to the plasma skin depth, $\ell \sim \ell_s$). In this so-called 'light sail' regime of RPA, it is predicted that the maximum ion energy scales with the square of the laser intensity ($\epsilon_i \propto I_L^2$) [38, 170, 185, 279]. However when ultra-high intensities (i.e. $\gtrsim 10^{22}$ Wcm^{-2}) are involved, these models neglect the radiation reaction (RR) force and QED effects, which could limit the maximum ion energies which can be achieved. The RR force, in particular, has been demonstrated to modify the collective electron dynamics within (micron) thick foil targets, causing a notable reduction in the target velocity and subsequent ion energies [62, 63, 66, 280]. There is currently no model to account for such an effect in the 'light sail' (LS) regime, which occurs during the acceleration of thin foils (with thickness just greater than the plasma skin depth, $\ell \gtrsim \ell_s$, described in Eqn. (3.2.1)).

In this chapter, an analytical model is presented which, for the first time, accounts for the effect of the RR force on the target velocity within the LS regime. This model is achieved by adding a classical radiation friction term to the existing equation of motion for a thin foil undergoing RPA. Such an approach guarantees energy conservation within the system, accounting for the radiation losses in a self-consistent manner by relating these to the fraction of laser energy converted into synchrotron-like radiation. The model depends on two key parameters which are estimated using a series of 1D QED-PIC code simulations, performed using the EPOCH code [239]. These parameters are the spatial extent of the region from which radiation is emitted and the angular distribution of the electron radiated power.

QED-PIC code simulations are also used to verify the predictions of the analytical model, by investigating the target dynamics, the distribution of the emitted radiation, and the energy partition between plasma species. The predictions of the model and the simulations are demonstrated to be in good agreement. Specifically, the simulations reveal that the magnitude of the RR force in the LS regime is strongly sensitive to the target thickness, implying that the properties of the emitted radiation (such as the photon energy and angular distributions) and the accelerated species could be controlled during experiments at upcoming laser facilities.

A concise summary of this work can be found in Duff *et al* [61], however the aim of this chapter is to provide the reader with a more detailed description of the underlying physics and the development of the analytical model.

6.1.1 Literature review: Effects of the RR force on thin foil acceleration

As described in section 2.3, the RR force is related to the emission of high energy, synchrotron-like radiation from electrons accelerated within ultra-intense laser fields [86, 100, 101]. Investigations into the effects of the RR force have demonstrated that it opens additional channels by which laser energy can be coupled to plasma species [58, 59, 120, 281], enhances the magnitude of magnetic fields generated in laser-solid interactions [282], and reduces the maximum energy achievable by laser-accelerated ions [62, 63, 66, 280]. These RR effects become significant for laser intensities $\gtrsim 10^{23}$ Wcm^{-2} [129], at which point ion acceleration predominantly occurs via the process of RPA. As discussed in chapter 3, there are two main regimes of RPA; hole boring and light sail. Research into RR effects during RPA have, to-date, focused on the hole boring regime. This is due to the fact that thick targets are required to access this regime, which are less likely to undergo relativistic self-induced transparency (RSIT) during the interaction. The dynamics are then comparatively easier to model than for the LS regime, in which case either RSIT must be accounted for (see, for example, Ref. [38]), or the analysis must be restricted up until the time at which the target goes transparent (which is the case in this chapter). Regardless, there have been a small number of studies into RR effects within the LS regime, which will be briefly reviewed in this section.

In general, RR effects are considered to be weak within the LS regime, due to the assumption that the high velocity acquired by the target results in strong Doppler downshifting of the laser intensity in its reference frame, and a suppression of QED effects [60, 62, 63, 66, 243, 280, 283–286]. However, these high velocities are only obtained for targets which remain opaque to the laser throughout the entire interaction, and which can therefore be treated as perfectly reflecting relativistic mirrors. To access the LS regime, it is necessary to use thin foil targets which subsequently undergo transparency during the interaction with an ultra-intense laser pulse. This may occur via the process of RSIT or via skin depth transparency, in which case the target is compressed to a thickness less than the plasma skin depth, allowing laser light to propagate through. It has been indicated in several studies [60, 62, 283] that the onset of (skin depth) transparency leads to significant RR effects, even within the LS regime. In this case, the electrons accelerated by charge separation fields within the plasma can interact directly with the laser pulse, therefore experiencing strong radiative cooling.

The magnitude of the RR effects in the LS regime are strongly dependent on the laser polarisation. Using linear polarisation, Tamburini *et al* [60] demonstrated that the laser penetrates up to a distance of $\lambda_L/4$ through the target, due to skin depth transparency, enabling the onset of RR effects. When the same authors switched to circular polarisation, the skin depth was reduced to $\lambda_L/20$, in which case the magnitude of the RR effects were negligible. When the target thickness was reduced such that it was able to undergo RSIT, it was reported that circular polarisation led to a slight boost in the peak ion energies, however this came at the cost of a non-monoenergetic ion spectrum.

A RR effect which has been reported in Refs. [60, 62, 283, 286] is the enhancement of the charge separation field within the target. As the laser penetrates into the region of the target which undergoes skin depth transparency, it interacts with counter-propagating electrons which are accelerated across the charge separation field. Due to the geometry of the interaction these electrons experience strong radiative cooling, emitting energy in the form of synchrotron-like radiation. If the electrons radiate a sufficient amount of energy, they can no longer propagate against the laser pulse and are instead reflected. For the electrons to be reflected by the laser pulse, they must satisfy the condition $\gamma_e \geq a_0/2$ [107, 129], which is typically satisfied by electrons within the charge depletion zone. These are then bunched up at the laser-plasma interface, leading to an enhancement of the local charge separation field. This effect has been shown to shift peaks in the ion spectra to higher energies [283]. However, as indicated in Tamburini *et al* [60], the $\mathbf{j}_e \times \mathbf{B}$ force of the intense laser pulse drives hot electron populations, leading to a greater degree of target expansion and therefore increasing the ion energy spread.

It has been demonstrated in Refs. [60, 283] that RR effects in the LS regime lead to a substantial fraction of the laser energy being converted into radiation. In Ref. [283] the authors report a photon conversion efficiency of ∼10% during the interaction of an ultra-intense pulse with an overdense, 300 nm thick aluminium foil. In Tamburini *et al*

[60] a photon conversion efficiency of 20% was obtained using a similar intensity pulse interacting with a micron thick target. Interestingly, the ion conversion efficiency in Tamburini *et al* [60] was observed to decrease by a value equal to the photon conversion efficiency. This indicates that the RR force significantly impacts the energy partition in thin foil interactions, coupling more energy to the radiation whilst reducing the efficiency of ion acceleration.

Whilst these studies indicate that RR effects occur within the LS regime, there is scope for this research to be continued. For example, there is currently no model to describe the target dynamics under the influence of the RR force, which could subsequently describe the decrease in ion conversion efficiency reported in Tamburini *et al* [60]. Another aspect of this research which is currently missing is an investigation of the radiation distribution from thin foil targets, and how the properties of the emitted radiation are related to the target dynamics. The work presented in this chapter addresses these gaps in the literature, by investigating the distribution of radiation from targets undergoing acceleration in the LS regime, which is subsequently related to the collective electron dynamics under the influence of the RR force.

6.2 Modelling radiation losses in the LS regime

In this section, the development of an analytical model which details the effects of the RR force on the collective electron dynamics, and the target velocity within the LS regime, is presented. Intuitively, the target velocity is related to the magnitude of the total radiated power, and therefore on the magnitude of the RR force acting on it. RR enables more laser energy to be converted into radiation, reducing the efficiency of RPA. To describe this effect, an existing LS equation of motion is modified to account for the coupling of laser energy to synchrotron-like radiation through the absorption coefficient. By re-injecting this coefficient into the equation of motion for the thin foil, the target velocity and the photon conversion efficiency may be calculated, under the influence of the RR force. These predictions will be tested against simulation results later in the chapter.

6.2.1 Angular distribution of the emitted radiation

As demonstrated in Eqn. (2.64), the magnitude of the RR force is related to the power radiated from a single electron. To obtain an expression for the RR force, the radiated power is first expressed in terms of the Lorentz force, $\mathbf{F}_{L,e}$, such that:

$$P_\gamma = \frac{\tau_r \gamma_e^2}{m_e} \mathbf{F}_{L,e}^2 (1 - \beta_e^2 \cos^2 \psi) g(\chi_e) \tag{6.1}$$

where ψ is the angle between the electron velocity and the perpendicular component of the Lorentz force. The function $g(\chi_e)$ is the stochastic scaling factor, previously given in Eqn. (2.86).

The Lorentz force is then calculated by making assumptions about the direction of the electromagnetic fields and the subsequent electron motion. The laser is treated as a plane wave, propagating along the x axis, and linearly polarised in the y direction. It is then assumed that that the laser electric field is much stronger than the local charge separation field, such that $E_y \gg E_x$. Following from these assumptions, the Lorentz force is written:

$$\mathbf{F}_{L,e}^2 = e^2 (\mathbf{E} + \mathbf{v}_e \times \mathbf{B})^2 \tag{6.2}$$

$$\mathbf{F}_{L,e}^2 = e^2 (E_y - v_e \cos\theta B_z)^2 \tag{6.3}$$

Using that, $B_z = \frac{E_y}{c}$ and $a_0 = \frac{eE_y}{m_e c \omega_L}$, the Lorentz force may be written:

$$\mathbf{F}_{L,e}^2 = a_0^2 (m_e c \omega_L)^2 (1 - \beta_e \cos\theta)^2 \tag{6.4}$$

By re-injecting the Lorentz force term into Eqn. (6.1), an expression for the electron radiated power is obtained which depends on two characteristic angles. The first angle, θ, is the projection angle of the electron velocity along the laser axis, whilst ψ is defined in Eqn. (6.1). These angles are not independent of each other, as they both depend on the electron momentum, $\mathbf{p}_e$. The relation between the angles is obtained from the definition of ψ, as shown below.

$$\cos\psi = \frac{\mathbf{v}_e \cdot \mathbf{E}}{|\mathbf{v}_e||\mathbf{E}|} \tag{6.5}$$

Re-writing Eqn. (6.5) in terms of the electron momentum, $\mathbf{p}_e = |\mathbf{p}_e| \cos\theta\, \hat{\mathbf{x}} + |\mathbf{p}_e| \sin\theta\, \hat{\mathbf{y}}$, yields:

$$\cos\psi = \frac{E_x\cos\theta + E_y\sin\theta}{\sqrt{E_x^2+E_y^2}} \equiv \frac{\alpha\cos\theta+\sin\theta}{\sqrt{\alpha^2+1}} \tag{6.6}$$

The last expression on the right is obtained by defining $\alpha = E_x/E_y$, the ratio of the magnitude of the charge separation field, to that of the laser field. In the case where the charge separation field is weak, such that $\alpha \ll 1$, the characteristic angles are related by $\psi = \pi/2 - \theta$.

Combining Eqns. (6.1) and (6.4), gives an expression which describes both the magnitude and angular distribution of the electron radiated power. It is helpful at this point to define a function which gathers all the terms with an angular dependence, $\mathcal{G}(\theta)$. This function is written:

$$P_\gamma = \frac{\tau_r\gamma_e^2}{m_e}a_0^2(m_e c\omega_L)^2\left[(1-\beta_e\cos\theta)^2(1-\beta_e^2\cos^2\psi)\right]g(\chi_e) \tag{6.7}$$

$$P_\gamma \equiv \frac{\tau_r\gamma_e^2}{m_e}a_0^2(m_e c\omega_L)^2\mathcal{G}(\theta)g(\chi_e) \tag{6.8}$$

where

$$\mathcal{G}(\theta) = \frac{(1-\cos\theta)^2}{1+\alpha^2}\left(1+\alpha^2-(\alpha\cos\theta+\sin\theta)^2\right) \tag{6.9}$$

Eqn. (6.9) shows that the angular distribution of the electron radiated power depends on both the orientation of the electron velocity with respect to the laser propagation direction and the relative magnitude of the charge separation field, described by the parameter α. Since α strongly depends on the target thickness, it follows that the function $\mathcal{G}(\theta)$ also has a target thickness dependence.

The variation of the function $\mathcal{G}(\theta)$ with the characteristic angle θ is plotted in Fig. 6.1, for different values of α. This figure indicates that for the magnitudes of the charge separation field typically obtained in the simulations presented in this chapter ($\alpha \sim 0.15$), that the distribution of the radiated power is not substantially changed from the case where $\alpha = 0$. This verifies the assumption that $E_y \gg E_x$ which was used to obtain Eqn. (6.9). When $\alpha = 0.5$ however, the function $\mathcal{G}(\theta)$ becomes highly asymmetric around the line $\theta = 0°$, due to the dominance of the $(1-\cos\theta)^2$ term. This demonstrates that the most significant contribution to the magnitude of the electron radiated power comes from the backwards moving electrons (where $\theta<0°$). Indeed,

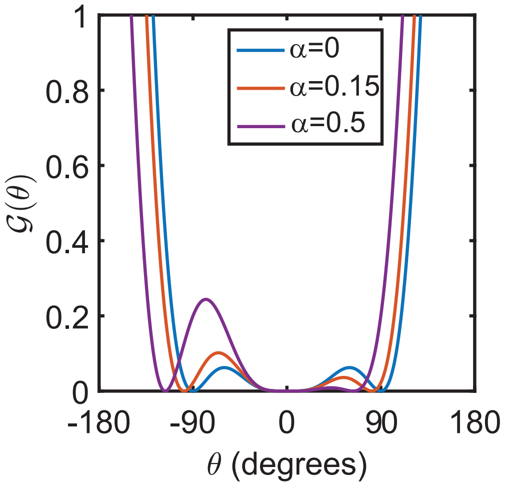

Figure 6.1: Angular dependence of the radiated power for a single electron, for $\alpha = 0$ (blue line), $\alpha = 0.15$ (orange line) and $\alpha = 0.5$ (purple line), corresponding to different magnitudes of the charge separation field. As α increases, the peak electron radiated power is emitted in the backwards direction.

the function $\mathcal{G}(\theta)$ is maximised for the electrons which directly counter-propagate with respect to the laser, such that $|\theta| = 180°$.

Finally, the corresponding RR force can be recast as:

$$\mathbf{F}_{rad} = \tau_r \omega_L \gamma_e^2 a_0^2 m_e c \omega_L g(\chi_e) \mathcal{G}(\theta) \boldsymbol{\beta}_e \tag{6.10}$$

To determine the total radiated power, the next step is to average the radiated power for a single electron over the electron distribution function and to multiply by the number of radiating electrons.

6.2.2 Accounting for the RR force in the equation of motion of the thin foil

To account for RR effects, an existing thin foil equation of motion (derived in Macchi *et al* [38] and previously described in section 3.4.1) is modified, such that the conversion of laser energy into synchrotron-like radiation is accounted for within the absorption coefficient. Again, it is assumed that the target does not act like a perfectly reflecting mirror, and the enhanced coupling of laser energy into radiation leads to less efficient acceleration of the target.

During the interaction with the (initially relativistically overdense) target, the laser light can be reflected, absorbed or transmitted. The relative probability of these processes are described by the coefficients $\mathcal{R}, \mathcal{A}$ and $\mathcal{T}$ respectively, which are related via the normalisation $\mathcal{R} + \mathcal{A} + \mathcal{T} \equiv 1$. In the case where there is no transmission, the reflection coefficient can be expressed as a unique function of the absorption. This assumption that $\mathcal{T} = 0$ is reasonable provided that the analysis of the collective electron dynamics is restricted up until the time at which the target goes transparent. The reflection coefficient is then $\mathcal{R} = 1 - \mathcal{A}$, which is substituted into the thin foil equation of motion (Eqn (3.43)). This leads to an adapted equation of motion, shown below, which accounts for the influence of the RR force on the acceleration of the thin foil.

$$\frac{d}{dt}(\gamma_t \beta_t) = \frac{I_L}{\rho \ell c^2}(2 - \mathcal{A})\frac{1 - \beta_t}{1 + \beta_t} \tag{6.11}$$

Here, β_t is the target velocity normalised to the speed of light, $\gamma_t = (1 - \beta_t^2)^{-1/2}$ is the target Lorentz factor and $\rho\ell$ is the target areal density. The absorption term in Eqn. (6.11) is obtained by normalising the total intensity of radiation emitted by the electrons, up until the time of transparency ($t = t_{tr}$), to the laser intensity. The absorption coefficient, which is equivalent to the photon conversion efficiency, is given by:

$$\mathcal{A} = \frac{N_{rad} \int_0^{t_{tr}} \langle P_\gamma \rangle dt}{\int_0^{t_{tr}} I_L dt} \tag{6.12}$$

where

$$\langle P_\gamma \rangle \equiv \frac{\int_{\mathbb{R}^3} f_e P_\gamma \mathbf{dp}_e}{\int_{\mathbb{R}^3} f_e \mathbf{dp}_e} \tag{6.13}$$

The absorption coefficient is seen to depend on the number of radiating electrons per unit surface, N_{rad}, and the average electron radiated power, $\langle P_\gamma \rangle$. Integrating the average radiated power over time, and scaling by the total number of radiating electrons, gives an estimate of the total energy radiated by the electrons during the interaction.

Eqn. (6.11) shows that the effect of the RR force is to reduce the efficiency of the RPA process. As more synchrotron radiation is produced, the absorption coefficient increases, leading to a reduction in the radiation pressure exerted on the target. The target velocity is then obtained by integrating the equation of motion, however this first requires knowledge of N_{rad} and $\langle P_\gamma \rangle$. Deriving these quantities will be the focus of the next sections.

6.2.3 The average electron radiated power

The average radiated power, $\langle P_\gamma \rangle$ is obtained by integrating the expression for the power radiated by a single electron over the entire electron distribution. As described previously, the distribution function, $f_e = f_e(\mathbf{x}, \mathbf{p}_e, t)$, is the probability of finding an electron with momentum $\mathbf{dp}_e$ in a volume $\mathbf{dx}$, per unit time, and is used to define the electron number density $n_e = n_e(\mathbf{x}, t)$, as follows:

$$n_e \equiv \int_{\mathbb{R}^3} f_e \mathbf{dp}_e \tag{6.14}$$

To proceed with the calculation, it is necessary to assume the form of the distribution function. For the ultra-intense laser-plasma interactions presented in this chapter, a Maxwell-Juttner (or relativistic Maxwell) distribution may be assumed to describe the electron population. In general, the distribution function may begin with some degree of anisotropy, for example, caused by heating of electrons in the direction of the laser polarisation. It is then assumed that this tends towards a Maxwell-Juttner distribution at equilibrium. However, the interaction between the laser and the electrons in the plasma is collisionless (i.e. field driven), and so it is not immediately clear which process drives the relaxation of the electron population. It is assumed in this chapter that it is the RR force which drives the distribution towards equilibrium. Further justification of the use of the Maxwell-Juttner distribution is provided later in this chapter, by fitting the electron temperature from sample simulation spectra. The Maxwell-Juttner distribution function is defined as follows:

$$f_e(\gamma_e) = \mathcal{N} \exp\left(- \frac{(\gamma_e - 1)}{\Theta} \right) \tag{6.15}$$

where $\mathcal{N}$ is a normalisation factor, such that

$$\mathcal{N} = \frac{n_e}{4\pi (m_e c)^3 K_2(1/\Theta)\Theta} \tag{6.16}$$

In the above equation, $\Theta = k_B T_e / m_e c^2$, and $K_2(1/\Theta)$ is a Bessel function of the second kind. In the case where $\Theta \gg 1$, which is typical of ultra-intense laser plasma interactions, it can be assumed that $K_2 \simeq 2\Theta^2$.

Substituting the radiated power from a single electron (Eqn. (6.8)) into the integral in Eqn. (6.13), yields an expression for the average electron radiated power as an integral over the distribution function.

$$\langle P_\gamma \rangle = \frac{g(\chi_e)\mathcal{G}(\theta)\omega_L\tau_r\omega_L a_0^2 m_e c^2}{8\pi(m_e c)^3}\int_{\mathbb{R}^3}\frac{\gamma_e^2}{\Theta^3}\exp\left(-\frac{(\gamma_e-1)}{\Theta}\right)\mathbf{dp}_e \tag{6.17}$$

This integral is evaluated by writing the momentum in polar coordinates, where the Jacobian is defined as $\mathbf{dp}_e = p^2 dp_{e,x}dp_{e,y}d\Psi$, with Ψ the polar angle such that $\Psi \in [0, 2\pi]$. Since the Lorentz factor is a function of the electron momentum, it is possible to change variable from $\mathbf{p}_e$ to γ_e, which implicitly assumes that the distribution function is isotropic (i.e. $f_e = f_e(|p_e|)$). This change of variable leads to the following integral:

$$\langle P_\gamma \rangle = \frac{1}{4}g(\chi_e)\mathcal{G}(\theta)\omega_L\tau_r\omega_L a_0^2 m_e c^2\int_1^\infty\frac{\gamma_e^4}{\Theta^3}\exp\left(-\frac{(\gamma_e-1)}{\Theta}\right)d\gamma_e \tag{6.18}$$

To proceed, it is necessary to undergo another variable change to $X = \gamma_e/\Theta$. The resulting integral can be solved analytically, with the solution given in Eqn. (6.20).

$$\langle P_\gamma \rangle = \frac{1}{4}g(\chi_e)\mathcal{G}(\theta)\omega_L\tau_r\omega_L a_0^2 m_e c^2\Theta^2\int_{1/\Theta}^\infty X^4\exp(-X)dX \tag{6.19}$$

$$\int_{1/\Theta}^\infty X^4\exp(-X)dX = (\Theta^{-4}+4\Theta^{-3}+12\Theta^{-2}+24\Theta^{-1})\exp(\Theta^{-1}) \simeq 24+\mathcal{O}\Theta^{-1} \tag{6.20}$$

Assuming that the electrons are ultra-relativistic, Θ will be large, meaning any terms which are inversely proportional to Θ in the above equation are negligibly small, and the exponential tends to 1. In addition, it can be approximated that $T_e \simeq (\sqrt{1+a_0^2/2})m_e c^2$ [268], such that $\Theta \simeq a_0$, leading to the expression for the average electron radiated power below.

$$\langle P_\gamma \rangle = 6a_0^4 g(\chi_e)\mathcal{G}(\theta)\omega_L\tau_r\omega_L m_e c^2 \tag{6.21}$$

Eqn. (6.21) describes the average radiated power from a single electron and its angular dependence. It is then possible to estimate $\langle P_\gamma \rangle$ over a range of laser intensities and target thicknesses (due to the $\mathcal{G}(\theta)$ dependence on the target thickness). The total radiated power is obtained by multiplying the average radiated power by the number of radiating electrons.

6.2.4 The number of radiating electrons

An expression for the number of radiating electrons per unit surface has been derived, for the hole boring regime, in Ref. [282]. In this model, the radiating electrons are those which counter-propagate against the laser pulse as they accelerate through the charge separation field. As discussed in section 3.4, laser radiation pressure drives a dense layer of electrons in front of the laser pulse, leaving a charge depletion zone behind it. This leads to the formation of a strong electrostatic field, which subsequently accelerates the ions. These are accelerated from the bulk of the target, and (partially) neutralise the charge imbalance induced by ponderomotive acceleration of the electrons. At this point, a fraction of electrons within the compressed layer can then move back into the charge depletion zone, where they counter-propagate against the laser pulse and experience strong RR [243]. The model presented in Ref. [282] is derived for the case where $a_0 n_c/n_e > 1$, which is not the case for the simulations presented in this chapter due to the fact that the target is initially highly overdense ($n_e = 777n_c$).

In the LS regime, the physics of the radiating electrons is quantitatively similar, except that the number of radiating electrons will have a dependence on the target thickness. In the hole-boring regime, the target is assumed to be semi-infinite ($\ell \gg \lambda_L$), such that a sufficiently large number of ions can be drawn to restore charge balance. For the thin targets considered here, the finite target thickness means that this may not be the case, leading to a reduction in the number of radiating electrons.

The first step in deriving an expression for the number of radiating electrons in the LS regime is to balance the laser radiation pressure with the electrostatic pressure, following the method outlined in Ref. [282]. However in this chapter, the skin depth is eliminated from the set of equations, leaving the expression for N_{rad} in terms of d (the spatial extent of the depletion zone) which has a target thickness dependence. This leads to the following set of equations:

$$\frac{eEn_0\ell_s}{2} = \frac{2I_L}{c} \qquad \text{pressure balance} \tag{6.22}$$

$$n_0\ell_s = n_e(d+\ell_s) \qquad \text{charge conservation} \tag{6.23}$$

$$N_{rad} = (n_0 - n_e)\ell_s \tag{6.24}$$

Here, $E = 4\pi n_0 d$ is the peak electric field strength, and ℓ_s is the target skin depth. The laser intensity is expressed in terms of the target critical density, through the relation

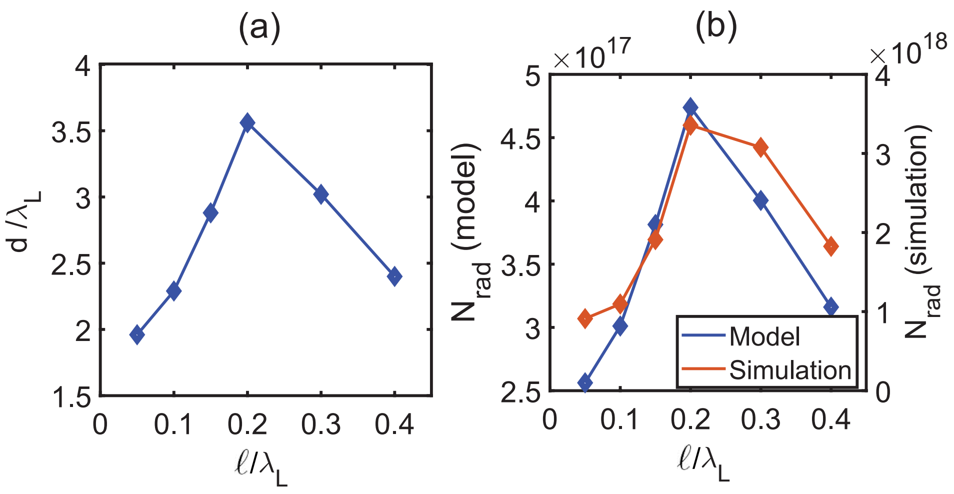

Figure 6.2: (a) Plot of the spatial extent of the charge depletion zone, d, as a function of the target thickness, obtained from simulations. (b) The number of radiating electrons for each of the target thickness values, calculated using the analytical model (blue diamonds) is compared to the corresponding values from the simulations (orange diamonds).

$I_L = m_e c^3 a_0^2 n_c$. Finally, n_0 is the peak electron number density during the compression phase and n_e is the electron number density after the ion acceleration time, i.e. when charge balance is restored.

In order to express N_{rad} in terms of the spatial extent of the charge depletion zone, d, the charge conservation equation is rewritten as follows:

$$\frac{n_0}{n_e} = \frac{d}{\ell_s} + 1 \tag{6.25}$$

Rearranging the pressure balance equation then enables the skin depth to be determined, and substituted into the above equation. This leads to a quadratic expression for the ratio (n_0/n_e), with a physical root shown below in Eqn. (6.26).

$$\left(\frac{n_0}{n_e}\right) = \left(\frac{1}{2} \pm \sqrt{\frac{1}{4} + \frac{1}{4}\left(\frac{\omega_L d n_0}{n_c c a_0}\right)^2}\right) \tag{6.26}$$

Finally, this leads to an expression for the number of radiating electrons per unit surface, N_{rad}:

$$N_{rad} = \frac{a_0^2}{\pi}\frac{n_c}{n_0}\frac{1}{r_c d}\left[\left(\frac{1}{4} + \frac{1}{4}\left(\frac{\omega_L d n_0}{n_c c a_0}\right)^2\right)^{1/2} - \frac{1}{2}\right] \tag{6.27}$$

where the electron classical radius, $r_c = \frac{1}{4\pi\epsilon_0}\frac{e^2}{m_e c^2}$, has been introduced as a normalisation. It is important to note that the expression for N_{rad} provided in Ref. [282] is recovered by setting $a_0 n_c/n_e > 1$ in the above equation.

In Fig. 6.2, Eqn. (6.27) is used to estimate the number of radiating electrons from measurements of the spatial extent of the charge depletion zone, d, obtained from simulations. This corresponds to a measure of the distance over which the electron radiated power decays to $1/e$ of its peak value, at the time of maximum synchrotron emission. Panel (a) shows that the largest charge depletion zone is observed in the 200 nm target. Since this distance is related to the skin depth, it is likely that this target produces the electrons with the highest average γ_e at the time of transparency. In panel (b), the estimates of N_{rad} using Eqn. (6.27) are plotted in blue, indicating that the greatest number of radiating electrons comes from the 200 nm target, which has the largest charge depletion zone. The values from (6.27) are compared to estimates from the simulations, plotted in orange. These estimates are obtained by multiplying the peak electron number density within the charge depletion zone by its spatial extent. The simulations show the same trend as Eqn. (6.27), but overestimate the value of N_{rad}, most likely due to the fact that the peak electron number density was used in the estimate.

6.2.5 Calculating the absorption and target velocity

Using the expressions for N_{rad} and $\langle P_\gamma \rangle$ it is now possible to obtain an estimate for the laser energy absorption into synchrotron-like radiation (which is equivalent to the photon conversion efficiency). This is an important quantity to evaluate for next generation laser facilities, as previous simulation based studies have indicated that a significant fraction of the laser energy will be converted into synchrotron-like radiation [58, 59]. Understanding the parameter regimes in which radiation production is maximised or minimised may enable control over fundamental properties of laser-solid interactions.

In Ref. [282], the photon absorption in the hole boring regime is given by $\mathcal{A} = a_0^3 r_c/\lambda_L$, and is independent of the target thickness. For ELI-like laser parameters ($a_0 = 300, \lambda_L = 800$ nm), this suggests the absorption will be $\sim 10\%$, in line with previous estimates [60, 283]. In this chapter, an expression was derived for the number of radiating electrons, which retained the target thickness dependence which was seen in the simulations (see Eqn. (6.27)). The expression for the absorption in this case is rather more complicated, obtained by substituting Eqns. (6.21) and (6.27) into Eqn. (6.12). This estimate of the laser absorption still scales quickly with the laser intensity, predicting a peak in the absorption for the target in which the spatial extent of the charge depletion zone, and therefore the number of radiating electrons, is maximized.

Having estimated the absorption coefficient, the equation of motion (Eqn. (6.11)) can be solved to determine the target velocity under the influence of the RR force. Following the method outlined in Ref. [177], the first step is to switch variable to the retarded time (corresponding to the phase $\phi = \omega_L t - kx$) and integrate up to the time at which the target goes transparent. This leads to the following expression for the target velocity:

$$\beta_t = \frac{(\varepsilon(\phi) - \kappa(\phi) + 1)^2 - 1}{(\varepsilon(\phi) - \kappa(\phi) + 1)^2 + 1} \tag{6.28}$$

where $\varepsilon(\phi) = (\int_{-\infty}^{\phi} I(\phi')d\phi')/\rho l c^2$ is the normalised laser fluence. This expression is similar in form to the solution of the light sail equation of motion presented in Macchi [38], but with an additional term. This term, $\kappa(\phi)$, describes the radiative correction, which acts to reduce the target velocity as a result of the RR force. The radiative correction is written as follows:

$$\kappa(\phi = \phi_{tp}) = 12\mathcal{G}(\theta)g(\chi_e)\frac{\omega_L^2 \tau_r m_e c^2 \int_0^{\phi_{tp}} a_0^5(\phi')d\phi'}{r_c \lambda_L \rho \ell c^2} \tag{6.29}$$

with ϕ_{tp} denoting the phase at the point of transparency. This model can be adapted for any arbitrary pulse shape by introducing a temporally varying a_0 in the integral. The predictions of this model will be compared to simulation results in the next section, using a Gaussian temporal laser profile. It is important to note that the target velocity depends on the distribution of the emitted radiation through the $\mathcal{G}(\theta)$ term. To determine the target dynamics, it is therefore necessary to know the distribution of the radiation emitted from the target so that the characteristic angle, θ, can be determined.

6.2.6 Summary of the analytical model

The first half of this chapter has been devoted to developing an analytical model to describe the effects of the RR force on the acceleration of thin foil targets within the LS regime. This model describes the electron dynamics up until the target undergoes transparency. First, the radiated power from a single electron was evaluated, limiting this analysis to a regime in which the laser field is dominant over the charge separation field within the target. The angular distribution of the electron radiated power was then described in terms of a function, $\mathcal{G}(\theta)$, which importantly depends on the magnitude of the charge separation field and a characteristic angle, θ. The most appropriate choice for this angle, which gives the best agreement between the model and simulation results, will be discussed in detail in the next section.

Finally, it is important to stress that the model presented here offers a self-consistent method of calculating the absorption and the target velocity (i.e. macroscopic properties of the laser-solid interaction which can, in principle, be measured experimentally) from the collective electron dynamics (i.e. from the microscopic properties). This model holds in the semi-classical regime of RR, in which quantum effects, such as pair-production and stochastic photon emission [58, 114, 116, 118], are negligible.

6.3 Numerical simulations

6.3.1 Simulation parameters

In order to investigate the influence of the RR force on the collective electron dynamics, and to verify the predictions of the absorption and the target velocity obtained from the analytical model, a series of simulations were run using the fully relativistic QED-PIC code, EPOCH [239]. 1D simulations have been used to scan over a wide range of parameters with high spatial and temporal resolution. The targets used here are solid density ($777n_c$) aluminium (Al) in a charge state of 13^+, which is known to be a common charge state of Al during interaction with the laser intensities used in this study. These targets interact with an ultra-intense laser pulse, with a peak intensity of 2×10^{23} Wcm^{-2}. At this intensity, the RR force plays an important role in the electron dynamics, whilst the process of pair-production can be neglected. As discussed in section 4.3.3, effects associated with stochastic photon emission are handled by a Monte-Carlo algorithm in the QED-PIC code [58, 116, 120].

The targets are varied in thickness in the range ℓ=50-400 nm, such that during the interaction they are accelerated in the LS-like regime. To be rigorous, this regime is referred to as ‘light sail like’, given that some of the assumptions used in the derivation of the target velocity in Macchi [38] are violated. The key difference here is that the target does not act as a perfectly reflecting mirror. The simulations have a spatial resolution of 2 nm (100,000 cells across a grid size of 2 μm), in order to fully resolve the Debye length and prevent numerical heating. Dynamic load balancing was also used, a process which redistributes the load on the processors such that each handles approximately the same number of particles. This makes the computation less demanding and ensures convergence of the simulation results, with at least 1000 particles per cell used throughout. There is also a condition on the temporal resolution of the simulations, arising from the fact that EPOCH assumes that the electron follows an arc-like trajectory between time steps. This imposes a condition on the size of the time step, such that it must be less than the time defined by the inverse of the electron oscillation frequency, $\omega_r =\mid \mathbf{p}_e \times \mathbf{F}_{Le} \mid /p_e^2$. The time step, $\triangle t$, must then satisfy the following condition, detailed in Ref. [243]:

$$\triangle t = \frac{\triangle x}{c} \leq \frac{T_L}{a_0} \tag{6.30}$$

Here, T_L is the laser period, a_0 is the normalised laser intensity and $\triangle x$ is the spatial resolution.

The laser has a Gaussian temporal profile, with a FWHM pulse duration of 60 fs and a peak intensity of 2×10^{23} Wcm^{-2} (corresponding to a peak dimensionless laser intensity of a_0=382). The laser wavelength is 1 μm, with simulation outputs produced every laser period. The laser strikes the target at time $t = 0$, with the interaction proceeding for 350 fs ($105T_L$); this time scale is sufficiently long that the ion and photon energies saturate at the end of the simulation, indicating that the interaction has reached equilibrium.

Both linear and circular laser polarisations have been considered for this study, however it is linear polarisation (LP) which gives the most noticeable differences between the cases with and without RR. For circular polarisation (CP), the oscillating component of the ponderomotive force, responsible for generating the fast electron population at $2\omega_L$, is suppressed. This means that in the linear polarisation case, the electron heating, and thus the magnitude of the RR force, is enhanced. The choice of linear polarisation also makes the results more experimentally relevant. Whilst CP is typically used in ion acceleration experiments in the current intensity regime, to maximise the achievable ion energies during RPA [180, 181, 255, 256], work presented in Ref. [43] has shown linear polarisation can also drive efficient RPA at ultra-high laser intensities. Future experiments can therefore generate high energy ions whilst employing LP. In addition, the first experiments on ELI-NP will use LP, as only one of the 2×10 PW beams will initially be commissioned with control over the laser polarisation

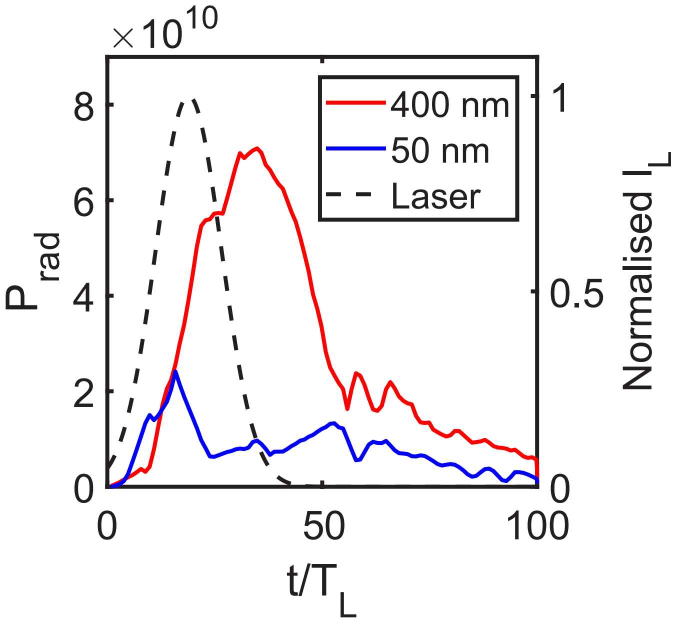

Figure 6.3: Temporal profile of the total electron radiated power, for a 50 nm and 400 nm target (blue and red solid lines, respectively). The total radiated power peaks at the so-called 'maximum synchrotron emission time'. The black dashed line indicates the laser intensity temporal profile, normalised to its maximum value.

[287].

6.3.2 Relevant timescales in the interaction

The simulations presented in this chapter enable temporal resolution of the collective electron dynamics under the influence of the RR force. It is then necessary to define important timescales within the interaction at which key properties of the particles can be compared. Temporally integrated measurements are more meaningful for comparison with experiment, since it is generally not possible to obtain temporally resolved experimental measurements of the particle dynamics on the time scale of the laser pulse. In this chapter, measurements are generally made at two characteristic times: the maximum synchrotron emission time, t_{rad}, and the time at which the target goes transparent, t_{tp}. In the simulations, the onset of transparency is marked by the appearance of the laser fields behind the electron critical density surface, and a rapid decrease in the level of laser light reflected from the target.

The maximum synchrotron emission time is defined when the total electron radiated power peaks. This indicates when the electrons will experience the largest RR force, therefore it is a relevant time to measure the magnitude of RR effects, by comparing simulations with and without RR. It is important to note the simulations without RR are unphysical; these do not conserve energy since the electrons radiate but do not experience recoil. These simulations are, however, useful for identifying effects which arise purely due to the RR force.

In Fig. 6.3, the temporal profile of the total electron radiated power is compared for two cases, a 50 nm and a 400 nm target. The laser intensity temporal profile (normalised to its maximum value), is also plotted, with a dashed black line. The thin 50 nm target goes transparent early in the interaction, meaning that the plasma electrons oscillate at relativistic velocities within the laser fields, producing copious amounts of radiation. For this thin target case, the temporal profile of the electron radiated power follows that of the laser, such that t_{rad} corresponds to the time at which the laser intensity is maximised.

For the thicker 400 nm target, t_{rad} occurs later in the interaction, after the peak of the laser pulse has arrived. For this case, the target does not go transparent during the interaction, and so radiation production arises from the motion of the plasma electrons within the self-generated charge separation field. For thick targets, t_{rad} occurs after the peak of the pulse, since the electrons emit radiation over a longer timescale (i.e. the time it takes them to traverse the charge separation field), compared to the case where the target goes transparent [243, 288].

In Fig. 6.3, it is clear that the magnitude of the electron radiated power is ∼3 times higher for the 400 nm target compared to the 50 nm. The radiation in the 50 nm case originates from electron oscillations in the laser fields, however these electrons are also subjected to the ponderomotive force, which pushes them away from the regions of highest intensity. This reduces the magnitude of RR effects, and so the radiating electrons are less likely to produce high energy photons. For the 400 nm case, the radiation comes from the electrons which propagate through the charge separation field, against the laser pulse. In this case, the counter-propagating geometry maximises the magnitude of the RR force, leading to a higher radiated power.

From the above discussion, it is deduced that the onset of transparency drastically impacts the collective electron dynamics, as well as the magnitude of the RR effects. It is therefore important to determine whether transparency occurs during the interaction, and at what time. In Fig. 6.4, two methods are demonstrated for probing the onset of

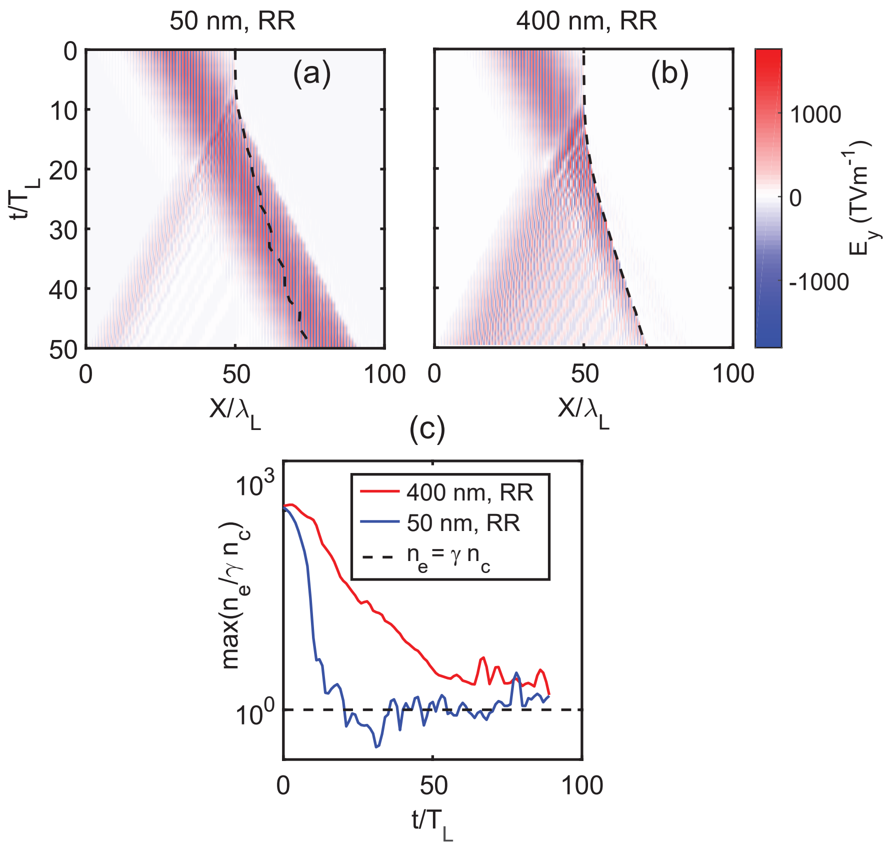

Figure 6.4: Onset of transparency as a function of time. Panels (a) and (b) show the space-time evolution of the laser electric field, interacting with a 50 nm and 400 nm target. The black dashed line indicates the position of the maximum electron number density. Panel (c) plots the relativistically corrected electron number density as a function of time for the 50 nm and 400 nm targets.

transparency. Panels (a) and (b) show the evolution of the laser E_y field in both space and time, for the 50 nm and 400 nm targets. In both cases, the rising edge of the laser strikes the target at a position $X = 50$ μm at time $t = 0$. The black dashed line in these plots shows the position of the maximum electron number density; by tracking this position it is possible to obtain the target velocity. In panel (a), the 50 nm target is observed to go transparent after 10 laser periods, as indicated by the presence of the laser field beyond the maximum electron density surface. In contrast, panel (b) shows that the 400 nm target does not undergo RSIT during the interaction. Panel (c) plots the maximum value of the relativistically corrected electron density as a function of time, where the electron Lorentz factor is obtained from the cell-averaged kinetic energy. Transparency occurs when the electron density drops below the relativistically corrected critical value, marked with a dashed black line. Again, it is immediately clear that the 50 nm target goes transparent, whilst the 400 nm target does not.

6.3.3 Properties of the radiation emitted from the plasma

A key aspect of the analytical model developed in section 6.2.1 is that the angular distribution of the electron radiated power, described by the function $\mathcal{G}(\theta)$ (Eqn. 6.9), depends on a characteristic angle, which itself varies with target thickness. The angular distribution of the emitted radiation is investigated in this section, such that the characteristic angle, θ, can be determined. The photon angular distributions will be presented as a function of target thickness, and compared with and without RR. By averaging over the entire distribution of photons, it is possible to determine the average angle of the photon angular distribution, which can then be used in conjunction with the analytical model to make predictions about the collective electron dynamics.

For a given system of electrons, the average emission angle, $\langle\theta_\gamma\rangle$, is defined as follows:

$$\langle\theta_\gamma\rangle = \frac{\int_{\mathbb{R}^3} |\theta_\gamma| f_e \mathbf{dp}_e}{\int_{\mathbb{R}^3} f_e \mathbf{dp}_e} \tag{6.31}$$

$$\theta_\gamma = \arctan(p_{e,y}/p_{e,x}) \tag{6.32}$$

where $p_{e,x}, p_{e,y}$ are the electron longitudinal and transverse momenta, respectively, and f_e is the electron distribution function. The outputs from this function lie in the range $\theta_\gamma \in [-180^\circ, 180^\circ]$, with 90° indicating emission parallel to the target surface. Forwards directed radiation is then emitted at 0° whilst backwards emitted radiation corresponds to emission angles in the range $|\theta_\gamma| \in [90^\circ, 180^\circ]$. The average emission angle (Eqn. 6.31) is expressed in terms of $|\theta_\gamma|$, due to the fact that the radiation distributions are typically symmetric.

In the above definitions, the electron momenta are used to determine the properties of the photon angular distributions. The assumption that the electron and photon momenta can be used interchangeably is valid for ultra-relativistic electrons. This is due to the fact that emitted photons propagate along the direction of the electron momentum, and are localised within a forwards facing cone with an opening angle $\sim 1/\gamma_e$. The average emission angle is plotted as a function of target thickness, with and without RR, in Fig. 6.5. Each point in this plot is evaluated at t_{rad} for the corresponding target thickness. As stated previously, the simulations without RR do not conserve energy, however these are presented in order to isolate effects which arise purely due to the influence of the RR force.

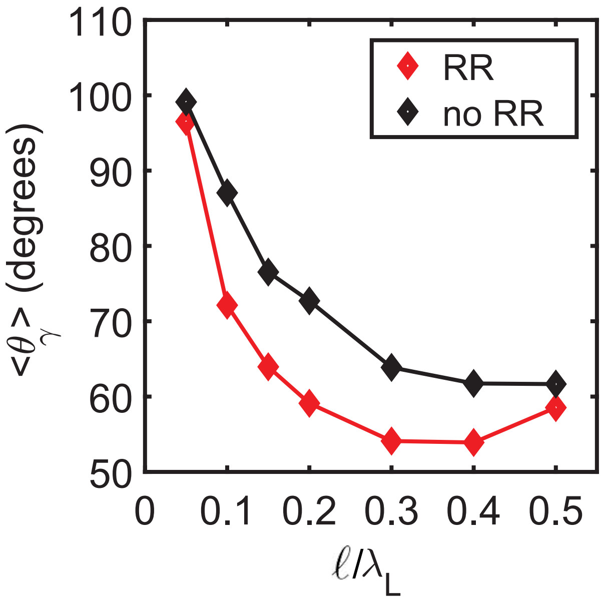

Figure 6.5: The first average emission angle, $\langle\theta_\gamma\rangle$, as a function of target thickness. The red and black diamonds correspond to the cases with and without RR, respectively.

An important observation in Fig. 6.5 is that the average emission angle is strongly dependent on the target thickness and therefore the magnitude of the RR force must also be sensitive to the target thickness. For the thinnest targets, transparency occurs early in the interaction and RR effects are subsequently suppressed. At the point of transparency, the laser can directly interact with the electrons in the bulk of the target. These electrons are ejected from the focal spot of the laser by the transverse ponderomotive force. In this case there is no significant difference in the value of the average emission angle, with or without RR.

As the target thickness increases, transparency occurs later in the interaction, or in the case of ℓ=400 nm, is completely suppressed over the time scale of the interaction. There is therefore sufficient time for a charge separation field to build up, such that the electrons radiating within the field significantly impact both the distribution of the emitted radiation and the collective dynamics of the plasma. It has been demonstrated in section 6.2.4 that the intermediate target thicknesses (ℓ=100-300 nm) produce the largest number of radiating electrons. This is, in turn, due to the fact that in the thicker targets there are sufficient numbers of ions in the target bulk to restore charge balance in the compressed electron layer. The electrons which then return to the charge depletion zone are subsequently reflected by the laser pulse, due to the RR force, such that they primarily contribute radiation in the forwards direction. This causes a reduction in the average emission angle relative to the case with no RR. It is clear that if there is no RR, the counter-propagating electrons are not deflected and instead mostly contribute radiation in the backwards direction. The strong radiative cooling tends to cause the electrons to bunch together at the laser plasma interface, enhancing the magnitude of the charge separation field. The electrons accelerated across this boosted field obtain large longitudinal momenta, which from Eqn. (6.31) is seen to cause a reduction in the average emission angle.

There is a substantial amount of information about the magnitude of the RR force which can be obtained from measurements of the average photon emission angle. Since this value is averaged over the entire electron population, it is a macroscopic variable which may be measured experimentally. One way in which this could be realised is through the application of a wrap-around stack [272]. This is a detector constructed of layers of image plate (which is sensitive to ionising radiation), curved such that it samples a wide angle around the equator of the interaction plane. This would enable the photon angular distribution, and subsequently the average emission angle, to be measured over a range of target thicknesses. The difficulty in making such a measurement is likely to be in the separation of the synchrotron radiation from that of Bremstrahlung. If the experiment were conducted using a low-Z material, such as cryogenic hydrogen, then the Bremstrahlung contribution would be drastically diminished, and changes in the emitted synchrotron radiation could be readily detected.

The wrap-around stack provides a spatially and spectrally resolved measurement of the angular distribution, which is also time integrated. The simulation results thus far suggest that in order to detect the changes in the angular distribution as a function of target thickness, it is a requirement that t_{rad} occurs before the onset of transparency. If this is the case, then the RR effects are imprinted into the angular distribution. If the converse is true, and transparency occurs early in the interaction, then any changes in the angular distribution (due to variation of the magnitude of the RR force) are masked by the approximately isotropic radiation produced by electron oscillations in the laser fields. In order to demonstrate this effect, the photon angular distributions are plotted for two target thicknesses in Fig. 6.6, with and without RR.

First considering the 50 nm target with RR, the angular distribution is nearly isotropic, with the average emission value $\sim 90^\circ$. The distribution is approximately flat, with a null region around 0°; this corresponds to an unphysical emission angle,

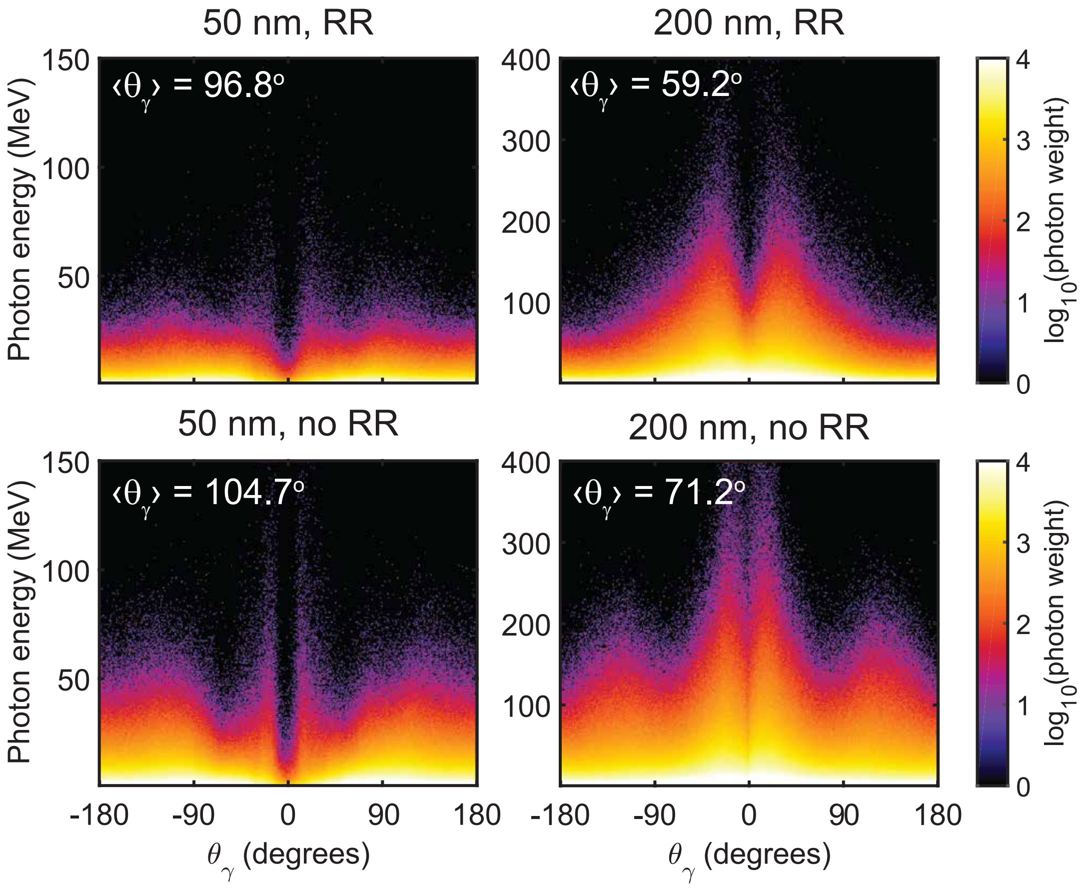

Figure 6.6: Photon angular distributions from the 50 nm and 200 nm targets (left and right columns, respectively), with and without RR (top and bottom rows, respectively). Each distribution is calculated at time t_{rad}, with the average emission angle, $\langle\theta_\gamma\rangle$, for each case displayed in the top left corner.

since in order for $\theta_\gamma = 0°$ the transverse momentum would also need to be zero. The cause of this isotropic distribution is the early onset of transparency. This also explains the fact that the angular distributions from the 50 nm target, with and without RR, are nearly identical. The only difference between these is that for the case with RR off, the photon energies are higher. The radiation from the thin 50 nm target is therefore relatively uninteresting, and indistinguishable from any other target thickness which undergoes transparency before the maximum radiation emission has occurred.

Interesting features appear in the angular distribution for the 200 nm target, considering first the case with no RR. Here there is evidence of radiation emission in both the forwards and backwards directions. There are also two distinct lobes of forwards directed radiation. These arise from electrons accelerated into the target by the $\mathbf{j}_e \times \mathbf{B}$ component of the ponderomotive force. The electrons are accelerated along the laser propagation direction, beyond the target critical surface. Here, the laser fields decay in amplitude exponentially and the $\mathbf{v}_e \times \mathbf{B}$ term becomes important. This subsequently leads to non-negligible values of the Lorentz invariant quantum parameter, χ_e (see Eqn. (2.85)), and a significant contribution to the forwards directed radiation.

The striking difference between the angular distributions from the 200 nm target, with and without RR, is that with RR, the lobes of backwards directed radiation vanish. It is also interesting to note that the forwards directed radiation has a larger opening angle for the case with RR on, compared to the case without, which gives an indication of the target velocity. The electrons within the target have some distribution of velocities; assuming that the electrons are relativistic, each will emit radiation into a narrow cone pointing along its propagation direction, with an opening angle inversely proportional to the Lorentz factor. For the simulations with RR, the opening angle is larger, which suggests that the angular distribution of radiation from the target is wider than for the case without RR. This immediately suggests the target velocity is lower in the case with RR.

It is possible to define a second average emission angle which provides information about the direction in which the RR force acts, i.e. whether it is stronger in the longitudinal or transverse direction. This second angle, $\delta\theta$, is defined as follows:

$$\delta\theta = \arctan\left(\frac{\langle \delta p_y \rangle}{\langle \delta p_x \rangle}\right) \tag{6.33}$$

where,

$$\langle \delta p_x \rangle \equiv p_{x,\mathrm{RR\ on}} - p_{x,\mathrm{RR\ off}} = \int_0^t F_{\mathrm{rad},x}(t')dt' \tag{6.34}$$

$$\langle \delta p_y \rangle \equiv p_{y,\mathrm{RR\ on}} - p_{y,\mathrm{RR\ off}} = \int_0^t F_{\mathrm{rad},y}(t')dt' \tag{6.35}$$

such that;

$$\delta\theta = \arctan\left(\frac{\int_0^t a_0(t')\beta_{e,y}(t')\mathcal{G}(\theta)dt'}{\int_0^t a_0(t')\beta_{e,x}(t')\mathcal{G}(\theta)dt'}\right) \tag{6.36}$$

The brackets, $\langle\rangle$, in the above equations indicate that the entire distribution with no RR is subtracted from that with RR. In the longitudinal and transverse directions, the change in momentum between the cases with and without RR is equal to the impulse exerted by the RR force.

Another way of interpreting this angle is through the contraction of electron phase space volume. The RR force causes radiative cooling of the electrons: they lose momentum through the emission of photons, such that they then occupy a smaller volume in phase space [284]. The first average emission angle, $\langle\theta_\gamma\rangle$, is proportional to this decrease in phase space volume, since it describes effects which depend on the magnitude of the RR force, but provides no information about the direction in which the force acts. The second average emission angle, $\delta\theta$, is more specific and describes the ratio of phase space volume contraction in the longitudinal and transverse directions. Large values of $\delta\theta$ indicate that the change in momentum due to the RR force is greatest in the transverse direction, whilst $\delta\theta \to 45°$ suggests that the RR force acts with equal amplitude in both directions. Note that in the case where the RR force is very weak, but in both directions, then $\langle\delta p_x\rangle \approx \langle\delta p_y\rangle$ such that $\delta\theta$ again tends towards 45°.

An extremely interesting feature of $\delta\theta$ is that it is a deterministic rather than a stochastic variable. As described in section 2.3.2, the term ‘stochastic’ refers to the fact that there is a probability of photon emission at each point along the electron trajectory, rather than this emission being a continuous process [118, 120]. The probabilistic nature of the photon emission means that it is only sensible to consider quantities which are averaged over many measurements. The fact that $\delta\theta$ is deterministic can be seen in Eqn. (6.36), given that this angle depends on the integral of the quantities a_0, β_e and $\mathcal{G}(\theta)$ over time, rather than the evaluation of these at a given time. Characterising the emitted radiation in terms of a deterministic variable is favourable over, for example, the first average emission angle, which oscillates throughout the interaction and therefore depends on the time at which it is measured. Whilst it is justified to measure such a variable at t_{rad}, where the cases with and without RR will show the largest differences, there may be fluctuations in this measurement if it was repeated over many simulations or prospective experiments. The deterministic value, $\delta\theta$, is not subject to such fluctuations.

The variation of $\delta\theta$ as a function of the target thickness is plotted in Fig. 6.7. The results presented here are in good agreement with previous discussions, in that the intermediate target thicknesses give rise to the largest RR effects, with the magnitude of such effects decreasing for the thicker targets. For the thinnest targets, transparency occurs early in the interaction, such that electrons interact directly with the laser and are driven out of the focal spot by the ponderomotive force. Whilst these electrons are ejected in both the transverse and longitudinal directions, the oscillations of the electrons in the transverse direction are responsible for photon emission. The RR

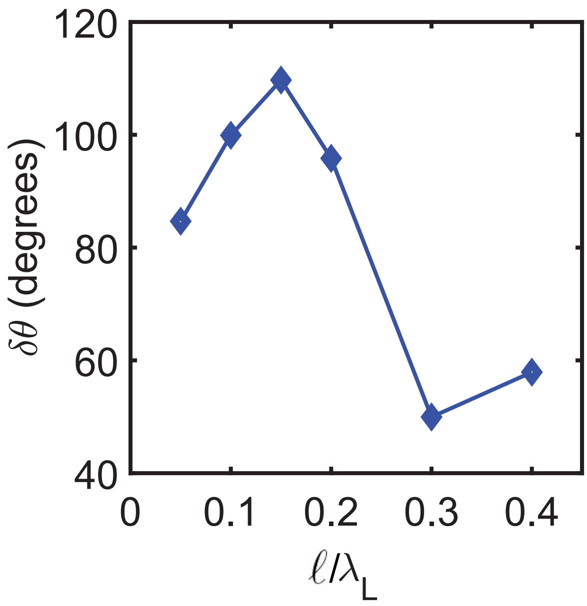

Figure 6.7: Plot of the second average emission angle, $\delta\theta$, as a function of target thickness. This angle provides information about the partition of the RR force into the longitudinal and transverse directions.

force is therefore greatest in this direction and the second average emission angle, $\delta\theta$, peaks. As the target thickness increases, the self-generated electrostatic fields within the target give rise to strong RR effects in the longitudinal direction, such that the ratio $\langle \delta p_y \rangle / \langle \delta p_x \rangle$ decreases compared to the thin target cases, as does the value of $\delta\theta$. If the target thickness were increased further, a transition occurs into a regime in which efficient RPA drives the targets to high velocities, decreasing the magnitude of RR effects.

So far it has been demonstrated that the magnitude of the RR force on the collective electron dynamics is strongly dependent on the target thickness, and that the effects of the RR force can be quantified in terms of an appropriate choice of average emission angle. The first average emission angle is an experimentally measurable quantity, which describes the effect of the charge separation field on the radiating electrons. The second average emission angle describes the partition of the RR force into the longitudinal and transverse directions. This angle directly compares differences in the distribution of electron momenta, with and without RR, and importantly it is a deterministic quantity. It is therefore the angle $\delta\theta$ which links the analytical model with the simulation results.

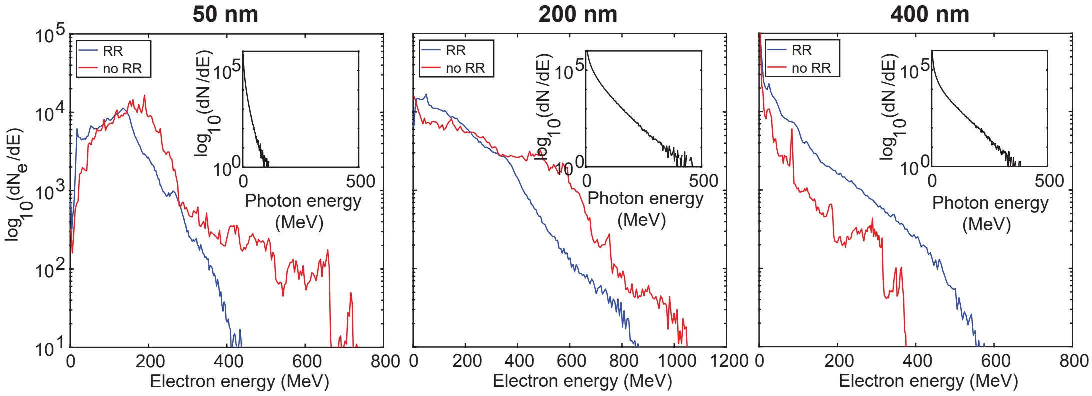

Figure 6.8: Electron energy spectra from the 50, 200 and 400 nm targets. The cases with and without RR are compared (blue and red lines, respectively) and the insets show the corresponding photon energy spectra.

6.3.4 Properties of the electron and photon energy spectra

So far in this chapter, two key assumptions have been made about the electron and photon distributions. First, due to the fact that the radiating electrons are relativistic, it was assumed that the photons are emitted along the direction of the electron momentum, therefore correlating the electron and photon distributions. Secondly, it was assumed that the electron distribution could be fitted with a Maxwell-Juttner function. In this section, these assumptions will be tested via an investigation of the electron and photon energy spectra.

Figure 6.8 compares the electron energy spectra for three different target thicknesses: 50, 200 and 400 nm. Each energy spectrum is compared at t_{rad}, and spatially integrated over the entire simulation grid. The cases with and without RR are denoted using blue and red lines respectively. For each target thickness, the photon energy spectrum is plotted as an inset.

From Fig. 6.8, it is evident that there are multiple electron populations, indicated by the fact there a is non-constant gradient across the spectrum. Assuming in these ultra-intense laser-plasma interactions that the RR force quickly drives the electron distribution towards equilibrium, it may be assumed that the spectra can be fitted with a Maxwell-Juttner distribution, as per Eqn. (6.15). In this case, the temperature of a given population is inversely proportional to the gradient; thus the plateau in the spectrum, which is particularly visible in the 200 nm target case, corresponds to a high temperature electron population. This population is likely driven by an electrostatic shock propagating through the target.

Transparency is seen to play an important role in the electron energy spectra. In the 50 nm target case, the early onset of transparency enables the plasma electrons to interact directly with the laser fields, therefore undergoing strong radiative cooling on a short time scale. This is seen clearly in Fig. 6.8, where the cut-off electron energy is reduced compared to the thicker targets, and a large region of the spectrum can be approximated with a single gradient, indicating the electrons are close to equilibrium. As the target thickness increases to 200 nm, the hot electron population is produced by an electrostatic shock. In this case, the electrons in the bulk of the target are accelerated down stream of the laser, such that there is a spatial separation between the intense laser fields and the electrons. This leads to a less significant difference in the electron temperatures, with and without RR, compared to the 50 nm case. For the 400 nm target, the electrons acquire higher energies with RR. This is as a result of radiative trapping: the RR force causes a reduction in the target velocity such that the electrons interact with the laser for longer, absorbing more energy through, for example, the process of resonance absorption.

It is interesting to note that in all cases, the electron energy spectra with RR are smoother than those without. This indicates that the RR force acts to equilibrate the electron energies, driving the initially anisotropic distribution towards a Maxwell-Juttner distribution. Evidence of this is the fact that the electron energy spectra from the simulations with RR may be approximated by a single gradient.

Further insight is gained by comparing the electron energy spectra to those of the photons (inset, black solid lines). For the 50 nm target, the cut-off energy in the photon spectrum is low, at approximately 100 MeV, compared to ∼400 MeV from the 200 and 400 nm targets. For thicker targets, the photons are predominantly produced by electrons in the strong charge separation fields within the target. These highly relativistic electrons radiate a significant fraction of their kinetic energy in the form of high energy photons, as indicated by the spectra. For the 50 nm target, which goes transparent early in the interaction, the laser ponderomotive force directly accelerates the electrons away from the regions of highest laser intensity, resulting in the production of lower photon energies.

In all cases with RR, the cut-off energies in the photon spectra are lower than those of the electrons. This indicates that quantum RR effects are not significant for the target and laser parameters considered in this study. It is only when the electrons

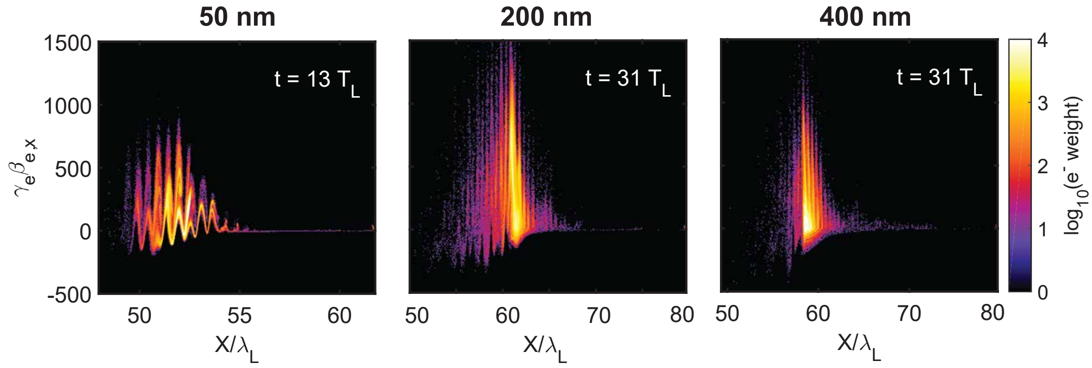

Figure 6.9: Longitudinal phase space plots for the 50, 200 and 400 nm targets, with each plot measured at the corresponding t_{rad}.

radiate photons with energy comparable to their kinetic energy that the interaction enters the radiation dominated regime, described in Refs. [129, 289]. In this chapter, it is possible to describe the electron dynamics using classical RR, in which quantum effects are neglected.

To validate the claim that the hot electron population observed in the thick target simulations are driven by an electrostatic shock, the electron longitudinal phase space is plotted in Fig. 6.9. From the 50 nm target, it is observed that the peaks in the longitudinal momenta occur twice per laser period (i.e. the peaks are separated by a distance of $0.5\lambda_L$). This is indicative of electron acceleration via the oscillating component of the ponderomotive force. As discussed, the RR effects are weaker in this case. In the 200 nm target, there is a localised region of electrons with a large longitudinal momentum. This suggests acceleration via an electrostatic shock, since the electrons with high momenta are localised to the shock front, whilst the electrons located within the bulk of the target, which is down stream of the shock, remain unperturbed. For the 400 nm target case, the longitudinal phase space is calculated at the same time as for the 200 nm target, however, here the region of high momenta is located over a larger distance, and has not propagated as far as in the 200 nm case. Given that the LS velocity decreases with increasing areal density, this suggests that rather than being shock driven, the electrons are predominantly driven by RPA at this point in the interaction.

The analysis presented so far has only examined the spectral properties at the time t_{rad}. In Fig. 6.10 the electron energy spectra from the 400 nm target are presented as a function of time, for the cases with and without RR. The spectra are compared at three times (40, 45 and 50 laser periods), all of which occur after t_{rad}. Immediately it is clear

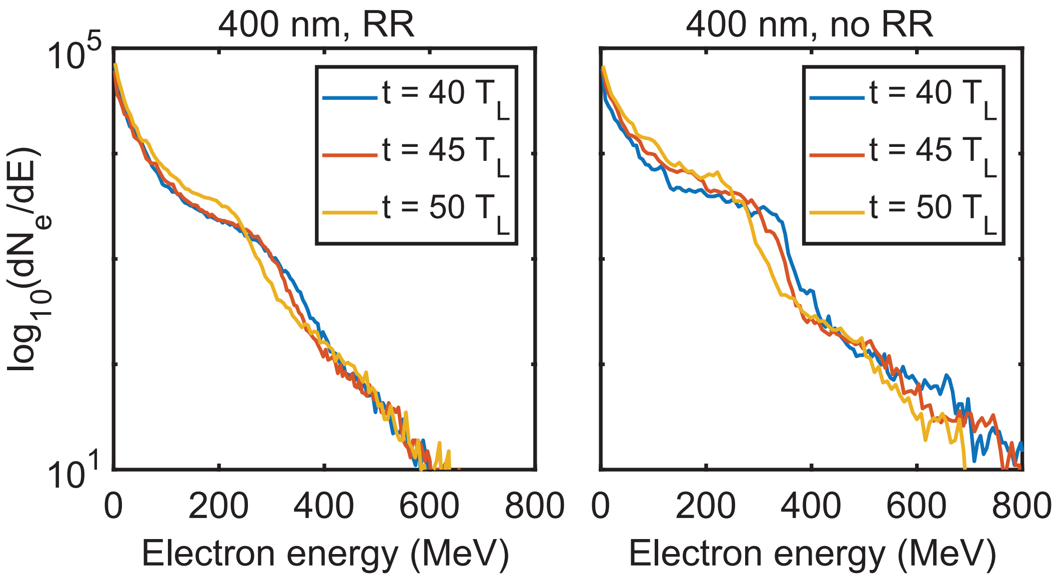

Figure 6.10: Temporal evolution of the electron energy spectra from the 400 nm target, with and without RR. The spectra are obtained at 40, 45 and 50T_L, i.e. after the time of maximum synchrotron emission.

that the RR force causes cooling of the entire electron energy spectrum, and pushes it towards an equilibrium distribution, such as a Maxwell-Juttner distribution. With increasing time, the edge of the 'hard shoulder', which is indicative of a hot electron population, moves to lower energies. For the case with RR, the cut-off energy for this population has reached $\sim$ 200 MeV by a time of $50T_L$, whereas at the equivalent time, this population has a cut-off energy of $\sim$ 300 MeV for the case without RR.

The key result obtained from analysis of the electron and photon energy spectra is that the RR force acts to cool the electron population, driving it towards an equilibrium distribution. It is therefore reasonable to model the electron distribution using a Maxwell-Juttner distribution. Finally, it is important to note that the photon energy spectra indicate the energies of the emitted photons are significantly less than those of the radiating electrons, and therefore stochastic photon emission is justifiably excluded from this analysis.

6.3.5 Energy partition

In this section the partition of laser energy into plasma electrons, ions and photons will be investigated as a function of target thickness. Although it is beyond the scope of this chapter, it is important to note that it is also possible for the laser energy to be channeled into electron-positron pair-production [54, 59, 66, 280, 290]. The conversion

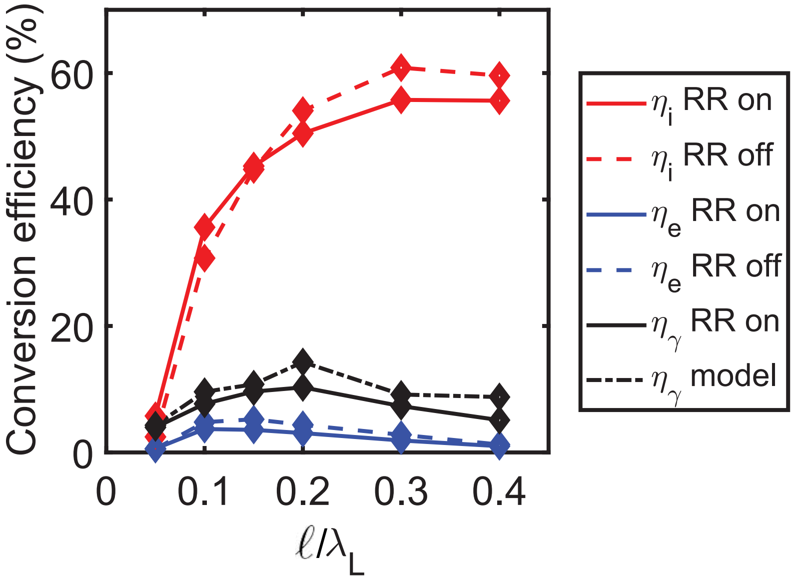

Figure 6.11: Partition of the laser energy into plasma species, as a function of target thickness, with and without RR. The photon conversion efficiency from the PIC simulations (solid black line) is in good agreement with the predictions of the analytical model (dashed black line).

efficiency of laser energy into plasma species is plotted as a function of target thickness in Fig. 6.11. The solid red, black and blue lines represent the conversion efficiency to ions, photons and electrons, respectively, with RR in each case. The dashed red and blue lines show the conversion efficiency to ions and electrons from simulations without RR. The photon conversion efficiency without RR is not considered, since energy is not conserved in this case. Instead, the dot dashed black line in Fig. 6.11 is the photon conversion efficiency calculated from the analytical model presented in section 6.2.5.

In Fig. 6.11, the conversion efficiency is calculated by integrating the total energy for each species up to the end of the simulation, and normalising to the laser energy. The conversion efficiency may then be expressed as $\eta_k = E_k/E_{laser}$, where $k \in [i, e, \gamma]$ represents the plasma species under consideration. The results presented in this section are bench-marked against a similar study conducted in Tamburini *et al* [60], in which the conversion efficiency was investigated as a function of time for a fixed target thickness of 800 nm. In Tamburini *et al* [60], the target was also an overdense Al foil ($n_e = 100n_c$), interacting with a linearly polarised laser pulse with a peak intensity 2.33×10^{23} Wcm^{-2}. Comparing to the existing literature then enables confidence in the extrapolation of the conversion efficiencies over a wider range of target thicknesses in this study.

An interesting feature of Fig. 6.11 is that the electron conversion efficiency is relatively unchanged, with and without RR. Given that the RR force has been demonstrated to radiatively cool the electrons (see, for example Fig. 6.10), the conversion efficiency should subsequently decrease, in particular for the intermediate target thickness in which the number of radiating electrons is highest. It is proposed here that the radiatively cooled electrons, which are deflected by the laser pulse and become trapped at the laser plasma interface, are able to continue absorbing laser energy. The energy losses of these electrons to synchrotron radiation approximately balance the gain in energy due to prolonged interaction with the laser, leaving the electron conversion efficiency unchanged with and without RR.

The ion conversion efficiency varies significantly over the range of target thicknesses considered. The thinnest targets, which go transparent early in the interaction, experience inefficient RPA and so are unable to acquire high ion energies. As the target thickness increases, the target remains overdense throughout the interaction and more energy can be coupled to the ions. For both cases, with and without RR, the ion conversion efficiency is high, peaking for the cases without RR at around 60%. This is due to the 1D nature of the simulations, in which the conversion efficiency is overestimated. This is because the ions are pushed predominantly along the laser propagation direction without allowing for transverse expansion of the target. The high conversion efficiency also demonstrates that the ions are accelerated to high energies by strong electrostatic fields within the target. Whilst the ion conversion efficiencies presented here are higher than would be predicted experimentally, they are in excellent agreement with the results presented in Tamburini *et al* [60].

Comparing the ion conversion efficiency with and without RR, it is observed that for the thinnest targets there are no significant RR effects, again due to the early onset of transparency. As the target thickness increases, the increasing strength of the charge separation field enhances the amount of laser energy converted into high energy radiation [243], which subsequently leads to a reduction in the target velocity. Given that the electron energy conversion efficiency remains effectively unchanged, with or without RR, the increased coupling of laser energy to high energy radiation must subsequently lead to a reduction in the ion energy conversion efficiency.

The photon conversion efficiency from the simulations with RR on is plotted in Fig. 6.11 with a solid black line. This is found to be of the order $\sim 10\%$, in agreement with Tamburini *et al* [60]. It is also encouraging that the photon conversion efficiency is approximately equal to the magnitude of the decrease in the ion conversion efficiency, with RR on (compared to the case with no RR). This demonstrates that the reduction in ion energy with RR on is a direct consequence of enhanced conversion of laser energy into radiation. The dot dashed line in Fig. 6.11 is the analytical estimate of the photon conversion efficiency using the analytical model presented in section 6.2.5. This model shows the same peak in the photon conversion efficiency, for a target thickness of 200 nm, as is observed in the simulations, and predicted by Eqn. (6.27). The values of the photon conversion efficiency are also in good agreement; the conversion efficiency calculated from the simulation peaks at 10.3%, whilst the model predicts a peak of 14.3%. Again, the simulations and the model are in agreement that the thinnest target, with $\ell = 50$ nm, gives rise to the lowest photon conversion efficiency, predicting values of 4% and 4.3%, respectively. The model slightly overestimates the conversion efficiencies, due to the fact that it does not account for RSIT effects.

6.3.6 The effect of the RR force on the target dynamics

Finally, the analytical estimates for the target velocity can be verified using the simulations. The target velocity is obtained by tracking the position of the maximum electron density as a function of time, which is assumed to indicate the interface at which RPA occurs. The evolution of the maximum density surface is plotted with a solid black line in Fig. 6.4. The gradient of this curve provides an estimate of the target velocity as a function of time.

The prediction of the target velocity in Eqn. (6.28) is then tested via comparison with the simulation results. These values are also compared to the predictions of an existing LS model, developed in Macchi *et al* [38], in which the target is assumed to remain perfectly reflective throughout the interaction. It is worth noting that the same authors have proposed an additional model which accounts for transparency during the interaction, in Ref. [170], however this model only differs substantially from the perfectly reflective case when the target thickness is ~ 1 nm for typical laser parameters.

The target velocity is plotted as function of time for the 400 nm target in Fig. 6.12 (c). First, comparing the results of Eqn. (6.28) (solid black line) to Macchi *et al* (solid red line), the target velocities both follow the same trend in time. For early times, when the laser intensity is low and the RR force is weak, the two models are identical. After t_{rad}, the velocity saturates as the RR effects decrease in magnitude. For the 400

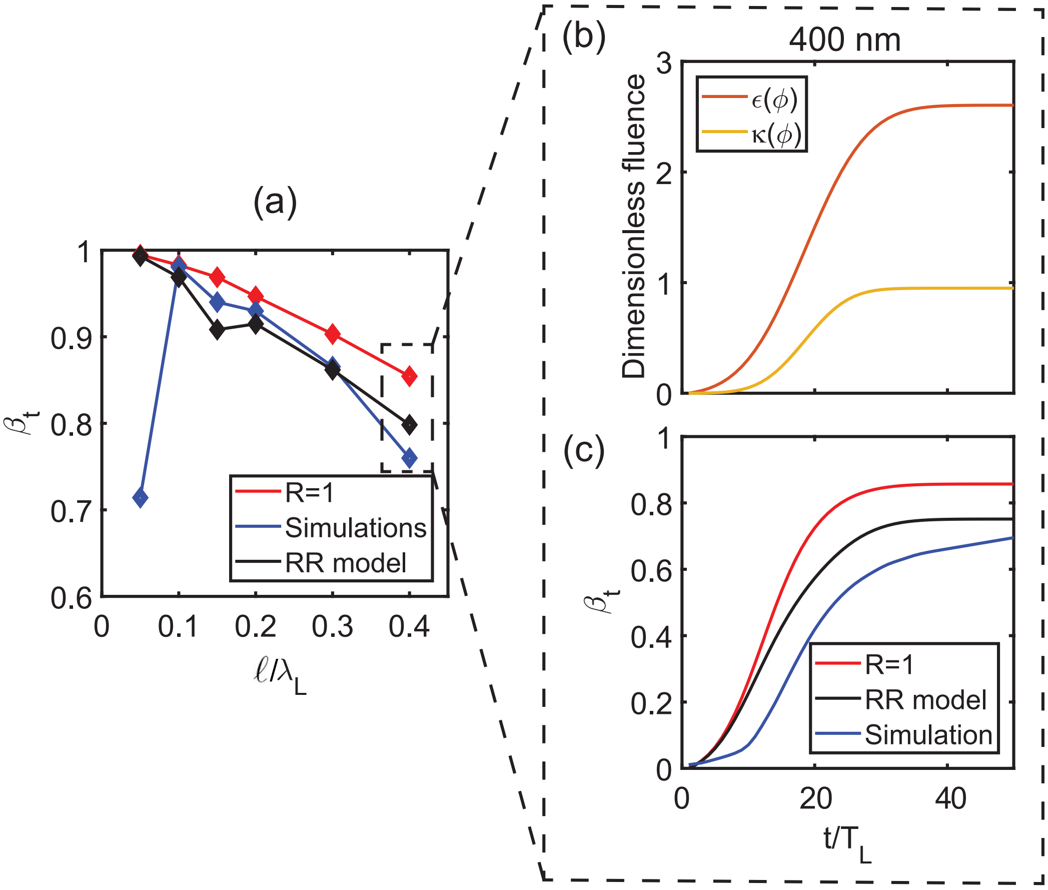

Figure 6.12: (a) Plot of the target velocity as a function of thickness, comparing the target velocity predicted by Eqn. (6.28) (black solid line) to Macchi et al (red solid line), and simulation results (blue solid line) (b) The normalised fluence and radiative correction are plotted as a function of time for the 400 nm target. In panel (c) the target velocity from the analytical model is again compared to the simulation results and an existing model, this time as a function of time for the 400 nm target.

nm target, a ∼12% decrease in the final target velocity is predicted using Eqn. (6.28), compared to the study of Macchi *et al.*

The velocities predicted by Eqn. (6.28) are closer to the simulation results (blue solid line) than those of Macchi *et al* [38]. It is interesting to note that in the simulations, the target velocity increases more slowly than in either of the models. This is caused by heating mechanisms, such as $\mathbf{j}_e \times \mathbf{B}$ heating, which are important early in the interaction and which complicate the dynamics of the RPA process. The key point here is that the target velocity in the simulation approximates the predictions of Eqn. (6.28) later in the interaction, when the velocity tends towards a constant final value. Figure 6.12 also demonstrates that, even for a target thickness of 400 nm, the target velocity exceeds the values predicted by the hole boring model (see Refs. [179, 190]) after approximately

$15T_L$, and thus it is definitely the LS equation of motion which should be modified in this regime of target and laser parameters.

To calculate the target velocity via Eqn. 6.28, it necessary to know the normalised fluence ($\varepsilon(\phi)$) and the magnitude of the radiative correction ($\kappa(\phi)$), as a function of time. These parameters are plotted in Fig. 6.12 (b) for the 400 nm target. This particular case was chosen as it does not go transparent during the interaction, and so the model is valid over a longer time range compared to the thinner targets. The target velocity is related to the difference between the normalised fluence and the radiative correction, such that the model in Macchi *et al* [38] can be recovered by setting $\kappa(\phi)$=0.

For the targets in which the electron radiated power is high ($\ell \approx 150 - 200$ nm), the magnitude of the radiative correction can exceed the normalised fluence. This is due to the fact that Eqn. (6.28) assumes the electron temperature scales with the ponderomotive potential. To account for the fact that this is not always the case, the radiative correction is scaled by the factor $T_e(\phi_{rad})/T_e(\phi_0)$, where $T_e(\phi_{rad})$ is the electron temperature evaluated at the value of the phase associated with t_{rad}, and $T_e(\phi_0)$ is the temperature associated with the peak laser a_0 at this same time [291].

In Fig. 6.12 (a), the target velocity is plotted as a function of target thickness, again comparing the results of Eqn. (6.28) to those of Macchi *et al* [38], and the simulations. It is clear that the existing LS model overestimates the target velocity in all cases, since it does not account for the onset of transparency or RR effects, both of which reduce the efficiency of RPA. The predictions of Eqn. (6.28) demonstrate relatively good agreement with the simulations. The agreement is better for thicker targets ($\xi > a_0$), where transparency has less impact on the target dynamics. Eqn. (6.28) describes the target dynamics up until the point of transparency; for the 50 nm target this occurs within $12T_L$ and so it is not surprising that the predictions of the target velocity do not match the simulation results as closely in this case. As the target thickness extends to 150-200 nm, Eqn. (6.28) predicts the same sharp decrease in the target velocity as is observed in the numerical simulations. This is due to the large electron radiated power in these cases, with the function $\mathcal{G}(\theta)$ (Eqn. 6.9) maximised for the case of a 150 nm target. Here, Eqn. (6.28) slightly overestimates the decrease in the velocity, again because it does not account for the onset of transparency which tends to weaken the RR effects. The possibility remains that a model could be developed which produces better agreement for ultra-thin targets (<100 nm) by accounting for both RR and transparency effects.

Finally, the reduction in target velocity leads to an associated reduction in the peak ion energies which can be produced in the LS regime. Whilst the RR force leads to only moderate effects on the target dynamics for the laser and target parameters used in this study, it is likely that with higher laser intensities, or higher mass targets such as gold foils (which will have stronger self-generated electrostatic fields), that the effects will become more pronounced. This study is part of a growing area of research, suggesting that the QED effects in ultra-intense laser-plasma interactions will place a limit on the maximum attainable ion energies which can be produced at multi-PW facilities [62, 63, 66, 280].

6.3.7 Conclusions

In this chapter an analytical model was developed which, for the first time, describes the effect of the RR force on the collective electron dynamics in the LS regime. This model describes a reduction in the target velocity due to the increased coupling of laser energy into synchrotron-like radiation. This effect is accounted for by including the emitted radiation in the target absorption coefficient, implying that the target is no longer considered to be a perfectly reflecting mirror. The absorption coefficient crucially depends on the magnitude of the electron radiated power, which is expressed in terms of the average emission angle. This model enables macroscopic quantities, such as the number of radiating electrons, the photon conversion efficiency and the target velocity, to be calculated from the collective dynamics of the system.

The predictions of the analytical model have been tested via 1D QED-PIC simulations, using the EPOCH code [239]. From these simulations, further information was obtained about the effects of the RR force on the distribution of the emitted radiation. The photon angular distributions were characterised in terms of an average emission angle, which provides the link between the simulation results and the analytical model. The predictions of the photon conversion efficiency and the target velocity from the model are in good agreement with the simulation results, especially in the case of thicker targets in which transparency does not play a key role in the dynamics.

The predictions of the model that could be tested experimentally at multi-PW laser facilities have also been outlined. For example, changes in the distribution of the emitted radiation as a function of target thickness could be measured. This provides information about the magnitude of the RR force, and may additionally indicate the transition from a surface dominated interaction between the laser and the plasma, to a volumetric based interaction, as the process of RSIT occurs. This study indicates that the distribution of radiation from thin foil targets in ultra-intense laser-solid interactions will provide fundamental insights into high-field plasma physics, where the collective plasma physics effects are intertwined with strong field QED effects.

Chapter 7

Multi-stage scheme for non-linear Breit-Wheeler pair-production utilising ultra-intense laser-solid interactions

7.1 Introduction

The exploration of QED effects at high power laser facilities (via beam-beam collisions) is an active research area which has been facilitated in recent years, due to an increase in the achievable intensity of focused laser pulses, and the capability to accelerate electrons to ultra-relativistic energies. Multi-PW laser facilities, such as APOLLON [218] and ELI-NP [221, 222], are expected to deliver peak intensities exceeding 10^{23} Wcm^{-2}. At such intensities, there are two key QED processes which are predicted to influence the laser-plasma interaction; high energy (synchrotron-like) radiation generation from accelerating electrons, accompanied by radiation reaction (RR), and the production of electron-positron pairs [86, 100, 101]. In this chapter, an investigation of the properties of electron-positron pairs produced during laser-solid interactions is presented. A two-stage interaction scheme is proposed, in which a beam of γ-ray photons is produced via an initial laser-solid interaction. The γ-ray beam then interacts with dual counter-propagating laser pulses, inducing pair-production via the non-linear (or multi-photon) Breit-Wheeler process [136, 148, 292] (see section 2.4).

There are many reasons why laser-induced pair-production has become an active area of research in recent years. The first is that this a fundamental process in QED, which has become experimentally testable with the advent of ultra high intensity laser pulses [65, 73, 113, 293, 294]. For the first time, it has become experimentally possible to generate complex states of matter, containing a significantly high density of electrons and positrons that collective behaviour can be observed. [295–297]. These electron-positron pair-plasmas are exotic states of matter, known to occur in extreme astrophysical environments such as pulsars and active galactic nuclei [91]. Laser induced electron-positron plasmas may therefore enable these astrophysical environments to be studied in the laboratory. There are alternative processes by which electron-positron pairs can be generated in the laboratory, for example, in the collision of electron and positron beams in particle accelerators, and at the focus of a quantum free-electron laser (QFEL) [298–300]. Relative to laser-induced processes however, these produce a smaller number of positrons. In the context of laser-plasma interactions, pair-production is of great interest given that it is predicted to deplete the energy of ultra-intense laser pulses [67, 151, 153, 301]. This may place a fundamental limit on the maximum laser intensities that can be generated (estimated to be $\sim 10^{26}$ Wcm^{-2} for colliding circularly polarised laser pulses in Ref. [67]); such a limit will then impact other key areas of ultra-intense laser solid interactions, such as limiting the efficiency of ion acceleration mechanisms [66, 280]. Theoretical studies of such high-field effects may be facilitated by numerical simulations, which compute the pair-production rates based on a number of limiting assumptions, which were discussed in section 4.3.3. By experimentally measuring the pair-production rates, it will be possible to investigate whether these assumptions are indeed valid, and to test the limits of QED. For example, the process of pair-production at ultra-high intensities may eventually lead to experimental probing of the structure of the quantum vacuum, a topic which is at the forefront of theoretical physics [302–305].

The QED plasma physics effects alluded to above become significant when the magnitude of the laser electric field, experienced in the rest frame of a relativistic electron within the plasma, becomes comparable to the Schwinger limit (as described in Eqn. (1.1)). The magnitude of the electric fields produced at the highest intensities achievable (at multi-PW laser facilities currently under development) will still be three orders of magnitude below the Schwinger limit. QED processes can, however, be observed at current laser intensities via the head-on collision of a focused laser pulse with an ultra-relativistic electron beam. The field strength in the rest frame of the electron is boosted by the Doppler effect, enhancing the magnitude of the electric field, and therefore the probability of QED effects. For this reason, laser-induced pair-production studies typically use the process of laser wakefield acceleration (LWFA) to generate GeV electron beams, which subsequently interact with a counter-propagating laser pulse, in order to produce electron-positron pairs [117, 133, 306].

The head-on collision of intense laser pulses with ultra-relativistic electron beams has thus provided the first glimpse of QED effects. For example, this experimental geometry has already led to the first observations of RR [130, 131]. As discussed in section 2.3.3, these experiments demonstrated a decrease in the cut-off energy of the electron spectrum which was correlated with a strong γ-ray signal, implying that RR occurred. Both of the aforementioned studies suggested that there were quantum aspects of the detected RR, since the magnitude of the electron energy loss was less than the classical prediction. At upcoming multi-PW laser facilities, it will be possible to probe quantum RR via the collision of GeV electron beams with even higher laser intensities than in the aforementioned studies [117, 127]. It is important to note that this scheme can be employed to induce pair-production without the need for the initial LWFA stage. For example, a highly cited example of laser-induced pair-production is the SLAC E144 experiment, which utilised a 46.6 GeV electron beam generated via a linear accelerator. This electron beam was collided with a relativistic laser pulse, producing a relatively small number of positrons ($\sim$100) via the non-linear Breit-Wheeler process [139, 146]. In this chapter, an alternative interaction scheme is introduced, which may also enable the measurement of quantum RR, and boost the number of electron-positron pairs produced relative to the previously discussed experimental configuration.

7.1.1 The two-stage interaction scheme

The two-stage interaction scheme introduced in this chapter can be used to verify the results obtained from LWFA experiments, and to extend these investigations into the highly non-linear regime. Whilst this is not the first proposed scheme for generating electron-positron pairs utilising laser solid-interactions [147, 150] (see section 2.4), it is the first to exploit a γ-ray beam, produced via an ultra-intense laser interaction with an overdense solid target, to induce multi-photon pair production.

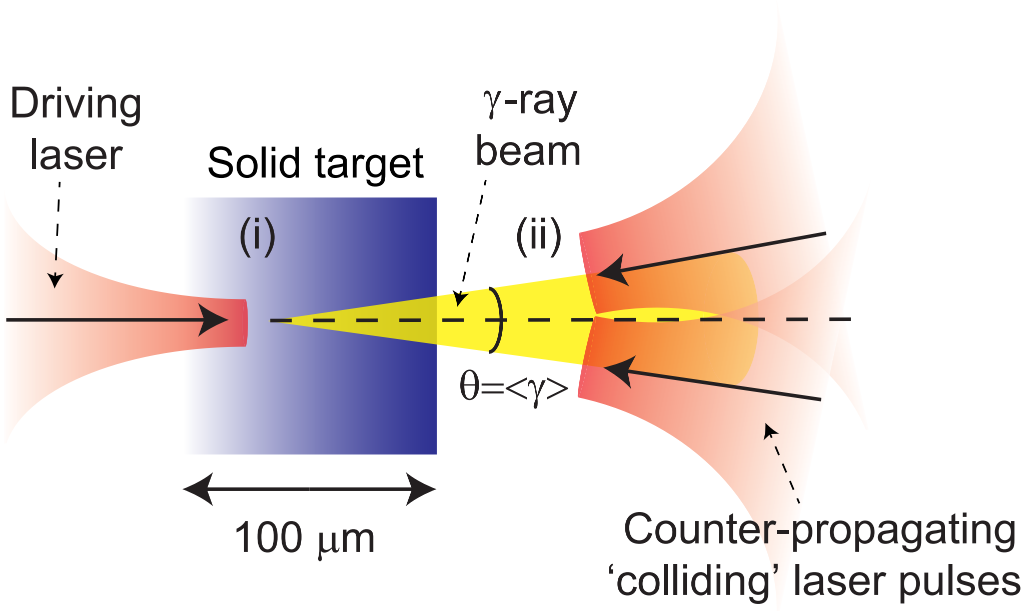

Figure 7.1: A schematic diagram illustrating the two-stage interaction geometry.

The two-stage interaction scheme is illustrated in Fig. 7.1. In the first stage, an ultra-intense driver pulse interacts with a thick, solid target to generate a γ-ray beam. This beam is optimised in terms of the average photon energy and divergence angle. Both of these parameters are demonstrated in this chapter to depend on the electron dynamics, thus enabling some degree of control over the properties of the γ-ray beam. In the second stage of this scheme, the γ-ray beam then interacts with dual laser pulses in a counter-propagating geometry. It is important to note that in this chapter, counter-propagating does not refer to a head-on collision (at 180° incidence with respect to the propagation direction of the γ-ray beam). Instead, 'counter-propagating' refers to the fact that the dual lasers are incident at a fixed angle either side of a central propagation axis, which is directly opposite the central axis of the γ-ray beam. The angle of incidence is chosen to be equal to the divergence half-angle of the γ-ray beam, such that the spatial and temporal overlap with the dual laser pulses is maximised. It will be demonstrated in this chapter that this interaction geometry not only enhances the number and energy of the produced positrons, relative to a head-on interaction, but that the energy-angle distribution of the produced positrons is highly anisotropic, making it suitable for laboratory astrophysics experiments [295].

The results of this investigation have been published in the second high fields special edition of the journal of Plasma Physics and Controlled Fusion [307]. This chapter builds upon the research presented in that paper to provide the reader with more detail on the development of the two-stage interaction geometry, and to discuss the feasibility of future experiments to verify the predictions made.

7.1.2 Literature review: Formation of the γ-ray beam

In this section, a brief review of the physics underpinning the generation and optimisation of the γ-ray beam is provided. As has been described in earlier chapters, during the interaction with ultra-intense laser pulses, overdense targets may be driven to high velocities via the process of radiation pressure acceleration (RPA). For targets which are significantly thicker than the plasma skin depth, radiation pressure accelerates a double-layered structure of electrons and ions, in the laser-piston regime [190].

Due to the high laser intensities involved in this study, electrons accelerating within this regime can lose a substantial fraction of their energy in the form of high energy, synchrotron-like radiation. The process by which these electrons produce radiation is described in Refs. [61, 282] and summarised in section 6.2.4. The key point is that electrons are accelerated through the charge separation field within the target, where they propagate against the laser field and experience strong RR. It is possible for these electrons to radiate so strongly that they are reflected by the laser pulse, therefore contributing to the forward-directed radiation, which forms the desired γ-ray beam.

Another significant contribution to the forward-directed radiation comes from electrons that are driven along the laser axis, beyond the plasma critical surface. In this region the magnitude of the laser electric field decays exponentially, such that $c\boldsymbol{\beta}_e \times \mathbf{B} \gg \mathbf{E}_\perp$, and the χ_e parameter for electrons accelerated within the target bulk becomes non-negligible [58]. This produces a significant contribution to the γ-ray beam. This source of radiation is confirmed via simulations, in which the average χ_e for electrons within the target bulk was found to be $\sim$0.18.

The strong radiation emission from electrons in the laser-piston regime leads to a reduction in the piston velocity, as described in Refs. [62, 63, 66, 280]. Theoretical models that do not account for the RR force during RPA, tend to assume that the target acts like a perfect relativistic mirror. Within the context of semi-classical RR, it is possible to account for RR effects through the reflection coefficient, $\mathcal{R}$. In this approach, RR causes a reduction in $\mathcal{R}$, such that the efficiency of RPA decreases. This leads to a subsequent reduction in the target velocity, equivalent to the effect of strong radiation friction. An expression for the non-linear reflection coefficient, under the influence of the RR force, is derived in Ref. [62] and given as:

$$\mathcal{R} = \frac{1-\beta_p}{1+\beta_p} - \frac{\langle\varepsilon_\gamma\rangle(1-\cos\langle\theta_\gamma\rangle)}{2(1-\beta_p)} \leq \frac{1-\beta_p}{1+\beta_p} \tag{7.1}$$

where β_p is the target (piston) velocity, $\langle\varepsilon_\gamma\rangle$ is the conversion efficiency of laser energy to synchrotron-like radiation and θ_γ is the average radiation emission angle, averaged over all space. The equality on the right indicates that in the case of no RR, the classical expression for the reflection coefficient is obtained. Through substitution of the above expression for $\mathcal{R}$ into the equations for momentum and energy conservation (see section 3.4.2), an expression is obtained for the target velocity in the laser-piston regime, under the influence of the RR force. Again this is derived in Ref. [62], yielding:

$$\beta_p = \frac{B}{B+1}\mathcal{F}(\langle\varepsilon_\gamma\rangle, B, \langle\theta_\gamma\rangle) \tag{7.2}$$

where $B = a_0\sqrt{\frac{n_c}{n_i}\frac{m_e}{Zm_e+m_i}}$ is a dimensionless parameter, and $\mathcal{F}$ is a decreasing function in B and $\langle\varepsilon_\gamma\rangle$. From the definition of B, it is clear that a higher target velocity can be achieved by employing a low target density (n_i/n_c). An explicit form of the function $\mathcal{F}$, in the case where the average emission angle of the radiation is 90°, is provided in Ref. [62].

From Eqn. (7.2) it is clear that the target velocity depends on the average emission angle of the synchrotron-like radiation, $\langle\theta_\gamma\rangle$. It is demonstrated in Ref. [62, 243] that, in the hole-boring regime, the angular distribution of this radiation is a function of the ion mass. Moving from a proton plasma to a deuterium plasma, for example, leads to an enhancement in the amplitude of the charge separation field. This result is due to the increased mass of the ions, meaning that they take longer to respond to the charge imbalance within the plasma. The strong charge separation field then results in a greater number of electrons counter-propagating against the laser field within the charge depletion zone, leading to radiation in the backwards direction. This is in addition to the forward-directed radiation produced by electrons which are reflected by the laser. In the case of a proton plasma, the charge separation field is weaker compared to the higher mass cases, and radiation is produced predominantly in the forwards direction by electrons accelerated into the target directly by the laser field. The emission of radiation along the laser propagation direction leads to a reduction in the magnitude of RR effects. For this reason, a proton plasma slab was selected as the target for this study, since the predominantly forward-directed radiation from this case leads to weaker RR, and therefore a higher target velocity.

The high target velocities which can be achieved in this study enable an enhancement in the average photon energy within the γ-ray beam via the relativistic Doppler effect. This effect is detailed in Ref. [68], in which the forward-directed radiation emitted via the interaction of an ultra-intense laser pulse with a thin plasma slab (ℓ=800 nm, n_e=40n_c) is shown to be boosted by the Doppler factor, $\mathcal{D}$;

$$\mathcal{D} \equiv \mathcal{D}(\langle\beta\rangle, \theta) = \frac{1 - \langle\beta\rangle^2}{1 - \langle\beta\rangle \cos\theta} \tag{7.3}$$

where θ is the angle between the emitted radiation and the laser propagation axis, and $\langle\beta\rangle$ is the average velocity of electrons within the target. In the hole-boring regime, this average velocity may be approximated as $\langle\beta\rangle \sim \beta_p$. For the laser and target parameters used in this chapter, the factor $\mathcal{D}$ is ~2.

The spatial properties of the γ-ray beam can also be optimised, by applying a strong magnetic field to reduce the divergence of the electrons accelerating through the target, and therefore the divergence of the emitted radiation [308]. Recently this idea was discussed in Ref. [72], in which a high energy, low divergence γ-ray beam was generated during the interaction of an ultra-intense laser pulse with a micro-channel target. This target contained a near critical density channel, which guides the laser pulse, generating a current of fast electrons as it propagates. This produces an axial magnetic field, which reduces the divergence of the propagating electrons, and therefore of the emitted radiation. The magnitude of this self-generated field was of the order 10^5 T. In this chapter, an external magnetic field is applied across the target, similarly to reduce the divergence of the radiating electrons. This field is directed along the laser propagation axis, and has a dimensionless amplitude in the range $\hat{B}_x$=0-1a_0 (where $\hat{B}_x = e/m_e\omega_L$ and the peak magnitude corresponds to 10^5 T).

It is important to stress that the magnetic fields employed in these simulations have a magnitude which is much greater than can currently be achieved using either permanent or superconducting magnets, which are limited to strengths ~10 T. However, fields of this magnitude can be generated in laser-solid interactions. Kilotesla magnetic fields have been demonstrated in the implosion of metal tubes, plasma targets and capacitive coils [309]. Ultra-intense laser-solid interactions generate populations of fast electrons, which in turn give rise to 10^4 T fields [310], which have been measured experimentally in Ref. [311]. The generation of 10^5 T fields (the maximum magnitude explored in this chapter) have been predicted in Ref. [312], as a result of strong electron currents driven by the ponderomotive force. Similar magnetic field strengths have been demonstrated to be self-generated in ultra-intense laser-plasma interactions in Refs. [68, 72]. Importantly, it has been demonstrated in Ref. [282] that a longitudinal magnetic field, of the magnitude employed in this chapter, may be generated via the inverse Faraday effect, and enhanced by RR. Reference [282] employs similar laser and target parameters to this study (the laser intensity varies in the range $I_L = (1.9-16.7)\times 10^{23}$ Wcm^{-2} and the target is hydrogenic plasma with density $90n_c$), demonstrating the feasibility of generating such strong magnetic fields in numerical simulations of laser-solid interactions.

7.2 Simulation parameters

The simulations are run using the fully-relativistic QED-PIC code, EPOCH [58, 120, 239] which was introduced in chapter 4. The results are presented in two stages; (i) the generation and optimisation of the γ-ray beam, and (ii) the production of electron-positron pairs via the interaction of this γ-ray beam with counter-propagating laser pulses.

For the first stage, a series of 1D simulations were performed, in order to scan over a range of external magnetic field strengths and to determine the conditions necessary for an optimised γ-ray beam. The simulation grid was initialised with 50,000 cells in the x direction (the laser propagation direction), over a grid size of 200 μm, and initialised with 100 macro-particles per cell. The driving laser for the interaction was a circularly polarised pulse (in order to suppress electron heating and enhance the efficiency of RPA, as discussed in section 3.3.1), with a peak intensity of 1×10^{23} Wcm^{-2} and wavelength λ_L=1 μm. This corresponds to a peak $a_0 = \sqrt{2}a_z = \sqrt{2}a_y \sim 282$. The pulse had a Gaussian temporal profile, with a full width half max (FWHM) duration of 10 fs. The target utilised in these simulations was a 100 μm thick slab of pure proton plasma, with a density of n_e=$10n_c$ (where n_c is the classical critical density). This thickness was selected to minimise the number of accelerated electrons escaping the target rear during the interaction. Escaping electrons are undesirable, as these emit hard photons which subsequently produce positrons via interaction with the dual laser pulses; this is as opposed to investigating pair-production only via the interaction of the dual lasers with the γ-ray beam. A thickness of 100 μm was sufficient to prevent a significant number of electrons from traversing the longitudinal extent of the target and escaping through the rear. Following the procedure described in Refs. [72, 308], an external magnetic field was applied across the simulation grid, to reduce the divergence of the radiating electrons and therefore of the produced γ-ray beam. This field was applied along the direction of laser propagation and had a dimensionless magnitude of $\hat{B}_x = eB_x/m_e\omega_L$, in the range 0-1$a_0$.

In the second stage, during which the γ-ray beam interacts with the dual laser pulses, 2D simulations were required in order to capture the angled geometry of the interaction, and the effect of the electric field configuration within the focal spot. The simulation grid had dimensions 200 μm × 28.8 μm, initialised with 9984 × 1440 cells in the x and y directions, respectively. The γ-ray beam was generated using a driving pulse with the same FWHM duration and peak intensity as in stage 1, but now focused to a Gaussian intensity profile on the target front surface, with a FWHM diameter of 5 μm. The target is the same 100 μm thick proton plasma slab as in the previous stage, now extended in the y direction. The γ-ray beam produced by this interaction then interacts with dual laser pulses in various geometric configurations, which enter the grid at an angle equal to the divergence half-angle of the γ-ray beam (as measured at the interaction point from an initial 2D test simulation, with no counter-propagating pulses). To ensure the properties of the γ-ray beam were the same in each simulation, the time step at which the beam escapes the target rear was saved as a restart file, and reloaded for each subsequent configuration. This method significantly speeds up the computation, since the initial hole-boring stage of the interaction does not need to be re-run. The dual counter-propagating lasers were initialised with Gaussian temporal and spatial profiles, with FWHM values of 30 fs and 3 μm, respectively, and peak intensity equal to 4×10^{23} Wcm^{-2} in each pulse. The focal spot size was chosen such that the spatial overlap of the dual laser pulses and the γ-ray beam is maximised at the interaction point. Again, an external magnetic field was applied across the grid to reduce the divergence of the emitted radiation; this field had a dimensionless amplitude $\hat{B}_x$=0.1a_0, which is found in stage 1 to optimise the γ-ray beam. The interaction point is selected to be 10 μm behind the target rear, such that the entire temporal profile of the dual pulses can interact with the γ-ray beam before striking the target rear.

The dual pulse configurations were compared to a conventional case [58, 287], where a single laser with a peak intensity 8×10^{23} Wcm^{-2} (and the same total energy as the dual pulse configurations) strikes the γ-ray beam head-on.

7.3 Results

7.3.1 Stage 1 - Properties of the γ-ray beam

The results of the simulations are presented in this section, starting with an investigation of the generation of the γ-ray beam, as demonstrated in Fig. 7.2. Each panel is obtained at a time t=15T_L, where T_L is the laser period, after the driving laser first strikes the target front surface. The red dashed line indicates the position of the peak laser field. Panels (a) and (b) show the electron and photon number densities, normalised to the critical value. It is clear that a significant number of photons are produced within the charge depletion zone (the region in front of the peak laser field where the magnitude of E_y decays exponentially). In panels (c) and (d), the electron and photon kinetic energy distributions are plotted, with the energy values in units of MeV. Again, the highest energy photons are located in the charge depletion zone, whilst the highest energy electrons propagate just behind the laser pulse, within the dense layer driven by radiation pressure.

The produced γ-ray beam is then optimised (in terms of its divergence half-angle), by variation of the strength of the external magnetic field. To quantify the divergence of the γ-ray beam, the photon angular distributions are plotted in Fig. 7.3. In panels (a) to (f), the magnitude of the dimensionless magnetic field increases from $\hat{B}_x$=0-1a_0. The angular distributions are characterised in terms of the divergence half-angle, $\langle\theta_\gamma\rangle$, defined as follows:

$$\theta_\gamma = \arctan\left(\frac{p_{y,\gamma}}{p_{x,\gamma}}\right) \tag{7.4}$$

$$\langle\theta_\gamma\rangle = \frac{2}{N}\Sigma_N|\theta_\gamma| \tag{7.5}$$

where $p_{y,\gamma}$ and $p_{x,\gamma}$ are the photon transverse and longitudinal momenta, and the N which appears in Eqn. (7.5) refers to the total number of photons in the system. The

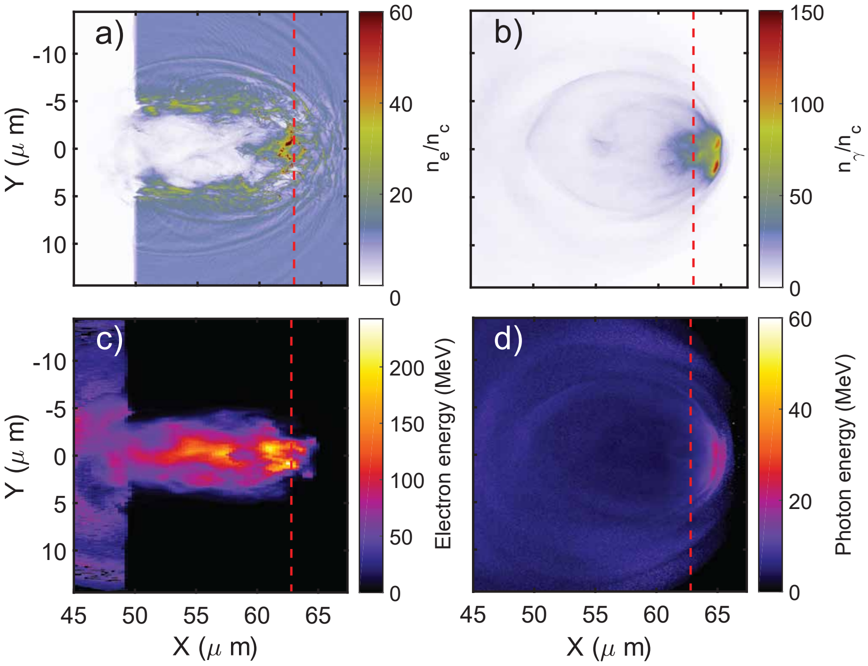

Figure 7.2: Simulation results illustrating the formation of the γ-ray beam. Panels (a) and (b) show the spatial distribution of the electron and photon number densities, normalised to the critical density. Panels (c) and (d) show the spatial distribution of the electron and photon kinetic energies, in units of MeV. All cases are compared $15T_L$ into the interaction, with the red solid line indicating the position of the peak laser field.

parameters defined above are analogous to the definitions of the first average emission angle in section 6.3.3, except that here the photon momenta are explicitly used in the calculation as opposed to inferring properties of the radiation from the electron distributions, and the factor of two enables calculation of the divergence half-angle.

The angular distributions in Fig. 7.3 are obtained by sampling a region located 2 μm behind the target rear, at the time at which the peak photon density crosses the target rear, and using only photons with an energy >1 MeV. This distance of 2 μm corresponds to the approximate distance the photons travel during a laser period, which is equal to the temporal resolution of the simulations. These photon distributions are compared in terms of two key parameters; the FWHM of the strongly forward-directed beam of photons, located around θ_γ ~0° (i.e. the photons emitted around the laser propagation axis), and the average photon emission angle. First, in terms of the central photon population, the FWHM of the distribution decreases as the magnetic field strength increases. The FWHM reduces from ~ 12°, without an external B field, down to ~2° for the case where $\hat{B}_x$=0.5a_0. Beyond this value of $\hat{B}_x$, the central photon population vanishes, and the photon emission occurs at large angles.

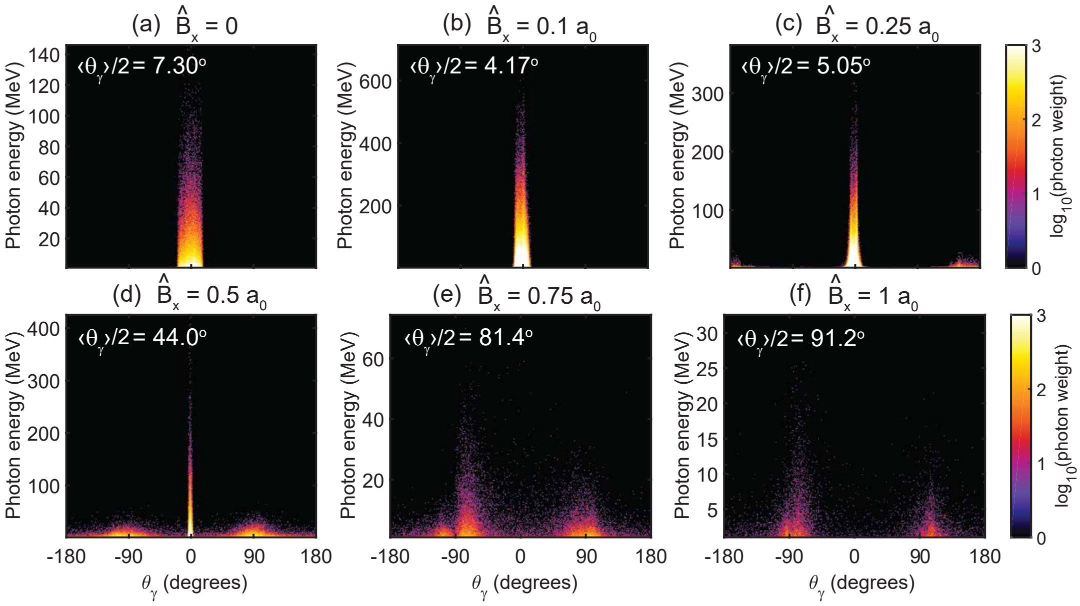

Figure 7.3: Plot of the photon angular distribution as a function of the external magnetic field strength (as stated above each panel), $\hat{B}_x = eB_x/m_e\omega_L$. The distributions sample a region of space located 2 μm behind the target rear, and are calculated at the time at which the peak photon density crosses the rear of the target.

Looking at the divergence half-angle ($\langle\theta_\gamma\rangle/2$, plotted in the top left of each panel in Fig. 7.3) as a function of the magnitude of the magnetic field, this angle initially decreases as $\hat{B}_x$ reaches a value of $0.1a_0$, then subsequently increases for magnetic fields greater than this value. This is due to the emission of photons at large angles ($\sim$90°), which are first observed in the photon distribution when $\hat{B}_x$=$0.25a_0$. These photons are emitted perpendicular to the laser axis, and arise due to the gyro-motion of the electrons around the applied magnetic field. These larger angle emissions (with respect to the on-axis beam) become more significant as $\hat{B}_x$ increases, leading to an increase in the average emission angle and suggesting that the γ-ray beam is also becoming more divergent. This effect is further illustrated in Fig. 7.4, in which the divergence half-angle, and the FWHM of the photon population centered on $\theta_\gamma \sim 0°$ (i.e. excluding the high angle emissions at $\sim$90°) are plotted explicitly as functions of the magnitude of the externally applied magnetic field.

The changes in the divergence half-angle as a function of the magnitude of the $\hat{B}_x$ field can be explained in terms of the dynamics of the radiating electrons. The electrons are predominantly accelerated along the longitudinal direction by the laser ponderomotive force, however there is also a component of electron motion in the plane perpendicular to the direction of the applied external magnetic field, resulting

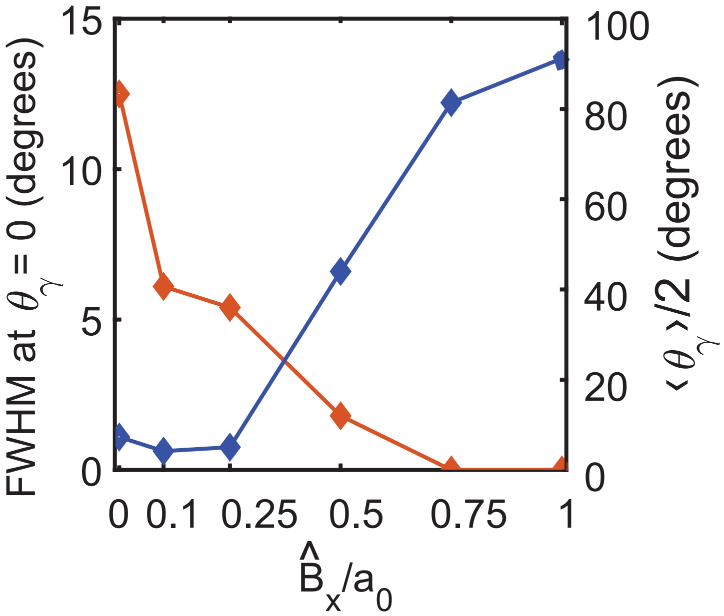

Figure 7.4: Plot of the FWHM of the angular distribution for the photon population centered on θ_γ *∼0° (orange data points), and the photon divergence half-angle (blue data points), as functions of the magnitude of the externally applied magnetic field,* $\hat{B}_x$*. These quantities are calculated for photons located within 2* μ*m of the target rear, at a simulation time corresponding to the peak photon density crossing the target rear.*

in a helical electron trajectory. The radius of the electron orbit in the perpendicular plane is given by the Larmour radius, $r_L = m_e v_\perp/|e|B_x$, where $v_\perp$ is the electron transverse velocity. As the magnitude of $\hat{B}_x$ increases, the Larmour radius decreases and the radiation is emitted into a narrow forward-facing cone. For a magnetic field of magnitude $\hat{B}_x$=0.1a_0, the case which gave rise to the γ-ray with the lowest divergence half-angle in Fig. 7.4, the Larmour radius is equal to $r_L = 0.17\lambda_L$, and the electron helical orbit contracts. As the magnitude of $\hat{B}_x$ increases beyond 0.25a_0, the electron motion is predominantly in the transverse plane and the divergence angle increases towards 90°.

For large external magnetic field amplitudes, it would be expected that the divergence angle reaches a constant value. This is because the electron motion will be confined to the perpendicular plane, in which case $p_{y,\gamma} \gg p_{x,\gamma}$ and the divergence half-angle saturates. The fact that the divergence half-angle continues to increase with the magnitude of the magnetic field strength suggests that kinetic effects are important in the electron dynamics. The magnetic field induces anisotropy in the electron energy distribution [313], presumably leading to the observed changes in the divergence angle. This effect is further illustrated in Eqn. (7.6) below, where the rate of change of the

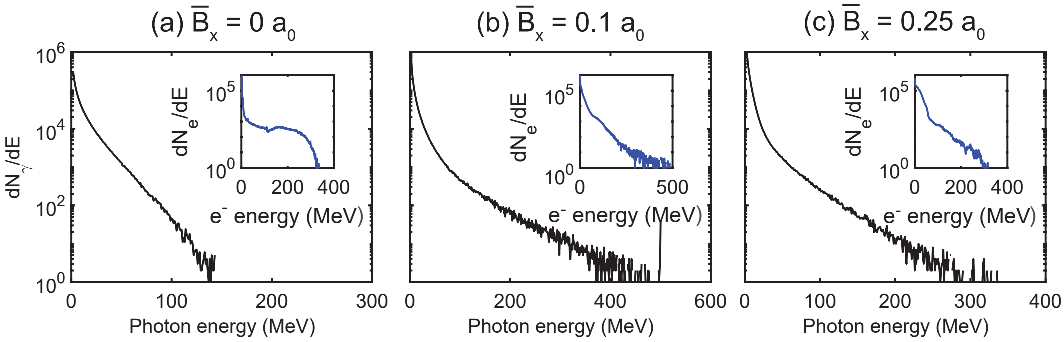

Figure 7.5: Plots comparing the photon energy spectra (solid black lines) and electron energy spectra (solid blue lines, inset), for three different magnitudes of the externally applied magnetic field; $\hat{B}_x = 0, 0.1$ and 0.25 a_0 in panels (a), (b) and (c), respectively. All spectra are compared at the time at which the peak photon density crosses the target rear.

divergence half-angle with respect to the magnitude of the external field, $\frac{d\langle\theta_\gamma\rangle}{d\hat{B}_x}$, is seen to depend on the integral of the distribution function over phase space.

$$\frac{d\langle\theta_\gamma\rangle}{d\hat{B}_x} = \int_{\mathbb{R}^3} \frac{df_\gamma}{d\hat{B}_x}\theta_\gamma \mathbf{dp}_\gamma \tag{7.6}$$

Deriving this effect analytically is beyond the scope of this thesis, since even for a relatively simple choice of electron energy distribution function, such as a Maxwell-Juttner distribution, evaluating the integral in Eqn. (7.6) is a difficult task.

Thus far it has been demonstrated that the application of an external magnetic field, of magnitude $\hat{B}_x$=0.1a_0, can significantly reduce the divergence of the γ-ray beam. The relativistic Doppler effect has also been utilised to boost the average photon energy within the beam. To investigate this effect further, the photon and electron energy spectra are presented in Fig. 7.5. In panels (a)-(c), the external magnetic field has values of $\hat{B}_x = 0, 0.1$ and $0.25a_0$. The photon spectra are denoted with solid black lines, whilst the corresponding electron spectra are represented with solid blue lines in the inset panels. The scale showing the number of counts is kept the same for each panel, however the energy scale (along the x axis) changes for each, in order to illustrate the dramatic changes in the spectrum cut-off energy as a function of the external magnetic field strength.

From Fig. 7.5, it is clear that the highest photon energies are obtained in panel (b), where $\hat{B}_x$=0.1a_0. The cut-off energy for the photon energy spectrum in this case is ∼400 MeV, and corresponds to the case with the least divergent γ-ray beam. Panels (a) and (c) highlight how sensitive the photon energy spectrum is to changes in the external magnetic field strength, since a relatively small change in this parameter leads to a significant reduction in the photon cut-off energy. As the magnetic field strength increases beyond $\hat{B}_x$=0.25a_0, the effect becomes more dramatic; in the case of $\hat{B}_x = a_0$, it was found that the photon cut-off energy dropped significantly, down to 20 MeV. The explanation for such a dramatic effect is that the strong magnetic field orients the electron motion into the plane perpendicular to the laser propagation direction. This geometry leads to a reduction in the magnitude of RR effects, and suppression of the emission of high energy photons. The aim of this stage is to maximise the energy of the γ-ray photons, since this enhances the non-linear aspect of the interaction, and therefore increases the probability of pair-production.

A similar trend is observed in the electron spectra, in that the highest cut-off energy is observed for the case where $\hat{B}_x$=0.1a_0. It is interesting to note that in the case with no magnetic field, the electron energy spectrum indicates that there are multiple electron populations present. If the electron distribution is assumed to take the form of a Maxwell-Juttner distribution, then the average temperature of a given electron population is inversely proportional to the gradient of the spectrum. The fact that there are different gradients in the electron spectrum plotted in panel (a) then suggests that multiple electron populations are present, with the highest temperature corresponding to the least steep gradient. The inset in panel (a) indicates that there is an electron population (the region of the spectrum which extends from 0 to 200 MeV) which may be driven by an electrostatic shock. A shock wave is triggered when the overdense layer of electrons, driven by RPA, propagates through the target at a velocity greater than the local speed of sound. The shock wave drives electrons in the target bulk down stream of the laser, leading to a separation of the peak laser fields and the energetic electrons. This therefore leads to a reduction in the magnitude of the RR effects; this is observed in panel (a), where it is seen that the electrons maintain relatively high energies due to the propagation of the shock wave, whilst the cut-off energy in the emitted photons is lower than the cases in panels (b) and (c). As the magnitude of the external magnetic field increases, the effect of the shock on the electron spectrum is reduced, and the photons reach higher energies compared to the cases without the magnetic field.

An important observation in Fig. 7.5 is that for the case with no externally applied magnetic field, the photon cut-off energy is significantly lower than that of the electrons

(∼300 MeV for the electrons compared to ∼150 MeV for the photons), whereas these cut-off energies are approximately equal in panels (b) and (c), where there is an external magnetic field. The fact that the photon and electron cut-off energies are comparable indicates that the RR force is stochastic in nature; since the electrons emit photons with a significant fraction of their kinetic energy, they experience a strong back reaction force. This stochastic emission is only seen in the presence of the external magnetic field, suggesting that the application of such a field could provide a relatively straightforward means of experimentally observing quantum aspects of RR. For example, a driving pulse could be employed to generate a strong magnetic field within the target, with a secondary pulse then generating the γ-ray beam. Stochastic photon emission effects would manifest themselves in the electron energy spectrum, and the γ-ray spectrum, which could be measured using a scintillator array (such as the one presented in Ref. [132]). These measurements could then be compared to the energy spectra obtained without the first pulse driving the production of a strong magnetic field, to isolate the stochastic effects.

7.3.2 Stage 2 - Counter-propagating laser configurations for pair-production

Having generated a high energy, low divergence γ-ray beam (with maximum photon energy ∼400 MeV and divergence half-angle ∼10°), the next stage is to interact this beam with dual laser pulses, in order to generate electron-positron pairs via the non-linear Breit-Wheeler process.

Typically, laser-induced pair-production studies employ a head-on collision of an ultra-intense laser pulse with a source of highly relativistic electrons (or in this case, a high energy γ-ray beam). The γ-ray beam used in this study has a small but non-negligible divergence half-angle, such that by the time the beam reaches the interaction point, there will be a significant number of photons located off-axis (i.e. at a large radius from the center of the beam). When this interacts with the dual laser pulses, there will be relatively few photons contained within the laser focal spot and therefore a lower cross-section for the non-linear Breit-Wheeler process. One solution to this problem is to focus the laser pulse closer to the electron/γ-ray beam, so that it will have less space to diverge before the interaction, leading to a larger spatial overlap with the counter-propagating beams. However, experimentally it is beneficial to have a significant distance between the source (the target rear) and the interaction point. This enables external diagnostics to have a clear line of sight to the interaction and therefore probe the properties of the produced electron-positron pairs.

In this chapter, it will be demonstrated that a more efficient interaction geometry (in terms of the number and total energy of the produced positrons) can be achieved by interacting the γ-ray beam with dual counter-propagating laser pulses, which are incident at an angle equal to the divergence half-angle of the γ-ray beam. The focal spot size of the dual laser pulses are chosen such that, in their focal plane, the γ-ray beam completely overlaps with the laser pulses. This enhanced spatial overlap, compared to the head-on interaction geometry, then boosts the number of γ-ray photons which the dual laser pulses interact with.

Four different interaction configurations are explored in order to optimise the properties of the emitted positrons. These configurations are shown schematically in Fig. 7.6, and are described as follows; these configurations employ (i) two 4×10^{23} Wcm^{-2} linearly polarised pulses, (ii) two 4×10^{23} Wcm^{-2} circularly polarised pulses, in which the rotation direction of the E_y electric fields are the same, (iii) two 4×10^{23} Wcm^{-2} circularly polarised pulses, with the E_y electric fields rotating in opposite directions, and (iv) one 8×10^{23} Wcm^{-2} pulse which interacts head-on with the γ-ray beam. This final case has the same total energy as configurations (i)-(iii), however the head-on geometry is expected to maximise the electron and photon quantum parameters (see Eqn. (2.84) and (2.85)). The counter-propagating pulses have a FWHM duration of 30 fs, and each one is focused to a Gaussian focal spot with a FWHM diameter of 3 μm, thus matching the area covered by the slowly diverging γ-ray beam at the point of interaction.

The influence of the interaction configuration on the production of positrons

The total number and energy of the positrons produced for each of the four configurations is shown in Fig. 7.7. Panel (a) shows the number of positrons produced, normalised to the initial number of electrons in the system (where the number of positrons and electrons is determined by summing the weight per macro-particle), as a function of time. The time is expressed in units of laser periods (where the temporal resolution of the simulations is $\sim 1T_L$), where $t = 0$ is the time at which the γ-ray beam escapes from the target rear. Positrons are first produced as the forward-directed photons within

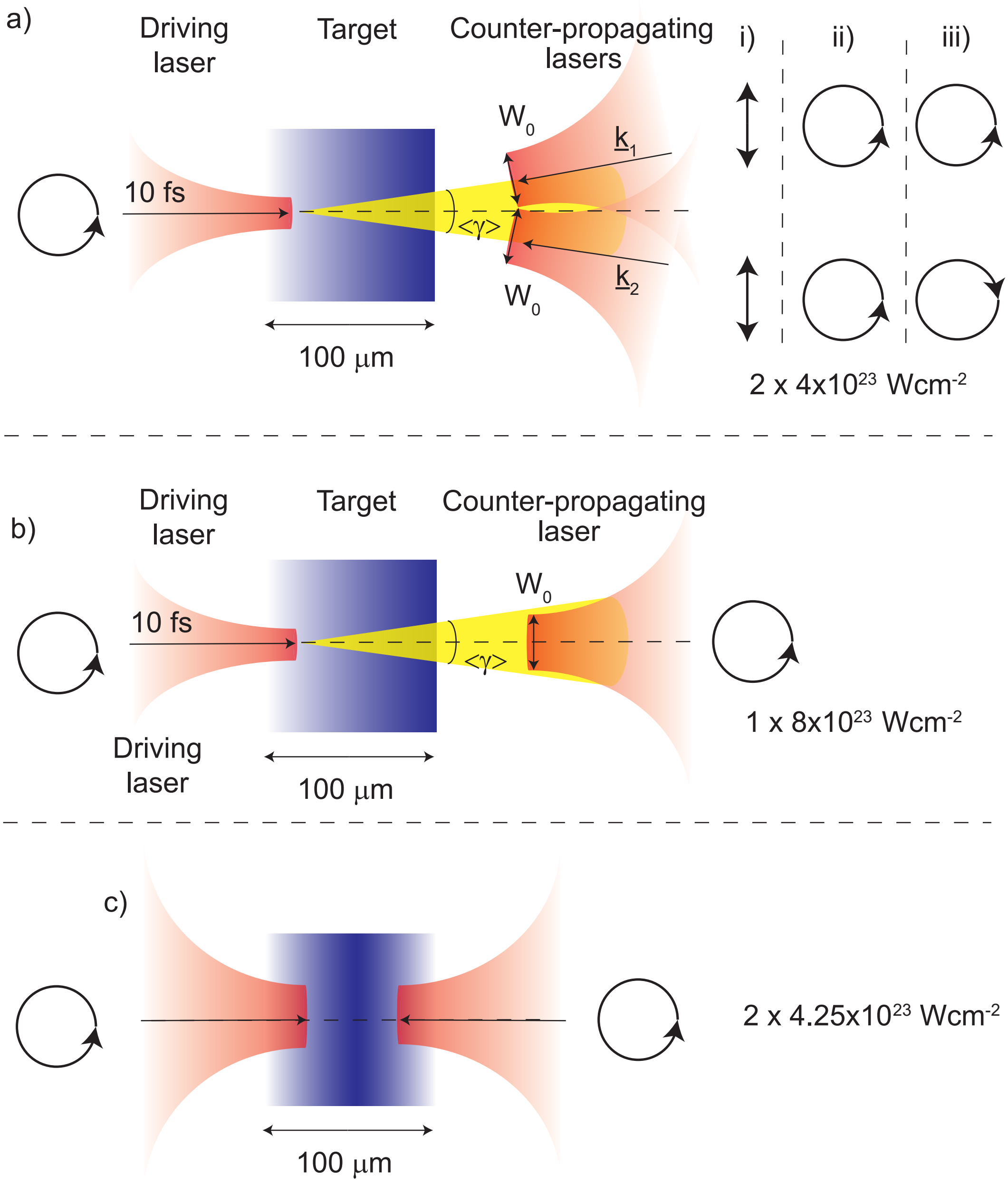

Figure 7.6: Schematic of the different dual pulse interaction configurations. (a) A γ-ray beam is produced via the interaction of a 10 fs duration, 1×10^{23} Wcm^{-2} pulse with a 100 μm slab of pure proton plasma. This then interacts with two lasers, propagating at an angle equal to the divergence half-angle of the γ-ray beam. (i)-(iii) Three different configurations are investigated, corresponding to different polarisations for the counter-propagating pulses. (b) These cases are compared to a single pulse, with the same energy, interacting head-on with the γ-ray beam. (c) The previous cases are additionally compared to a laser-solid interaction in which there is no initial stage of generating the γ-ray beam (in section 7.3.3). The energy content in this case is equal to the energy of the counter-propagating and driver lasers in (a) and (b).

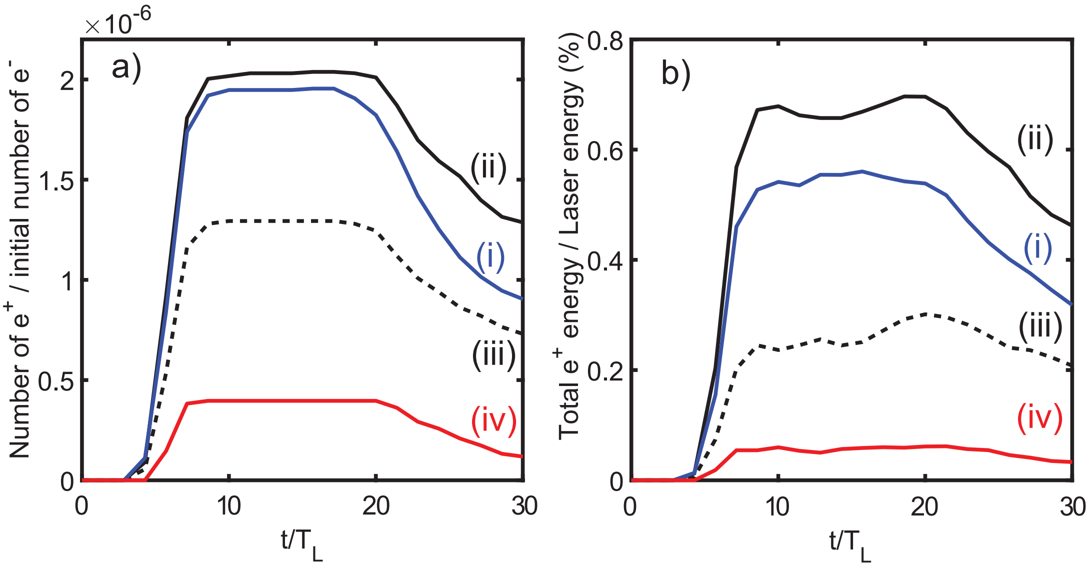

Figure 7.7: Properties of the positrons produced for each of the interaction geometries. These are labelled (i)-(v), and correspond to the configurations presented in Fig. 7.6. (a) A plot of the total number of positrons, normalised to the initial number of electrons in the system, as a function of time. (b) A plot of the total positron energy, normalised to the total energy of both the driving and counter-propagating laser pulses, as a function of time. For both plots, time is given in laser periods, where t=0 corresponds to the time at which the γ-ray beam escapes the target rear.

the γ-ray beam interact with the rising edge of the dual laser pulses. These laser pulses focus at the interaction point (10 μm behind the target rear) at $\sim 10T_L$, at which point the number of positrons saturates. At later times, the number of positrons decreases, as they are accelerated by the laser fields and escape the boundaries of the simulation box. These positrons also emit copious amounts of synchrotron-like radiation, causing the total positron energy to decrease over time.

Figure 7.7 (a) shows that configuration (ii), two circularly polarised pulses with the same rotation direction, produces the largest number of positrons when comparing configurations (i)-(iv). This configuration produces marginally more positrons than the case with two linearly polarised pulses, configuration (i). Interestingly, there is a significant reduction in the number of positrons produced when the two circular polarisations have the opposite rotation direction. Comparing configurations (ii) and (iii), the number of positrons is reduced by a factor of two for the latter case. A similar effect was reported in Ref. [128, 153], for the case of two circularly polarised laser pulses interacting in a head-on geometry. Despite the fact that the total energy of the single pulse head-on interaction is the same as for the dual pulse configurations, the number of positrons produced is lower by approximately a factor of four relative to the best dual pulse case. This result is counter-intuitive, since the head-on interaction is predicted to maximise the electron and photon quantum factors (χ_e and χ_γ), and therefore boost the probability of pair-production. Later in this chapter it will be demonstrated that this drastic difference in the number of positrons is the result of reduced spatial overlap of the γ-ray beam and the counter-propagating laser pulses. At the interaction point, the source has diverged such that there are a significant number of photons located off-axis, which cannot interact with the peak fields of the directly counter-propagating laser pulse. It is therefore beneficial to reduce the divergence half-angle of the γ-ray beam as much as possible such that the overlap is enhanced.

In Fig. 7.7 (b), the total positron energy is plotted as a function of time, normalised to the total energy of the driving laser and the dual counter-propagating lasers. This total positron energy is obtained by summing the product of the positron weight and energy per macro-particle, at each time in the simulation. In terms of total positron energy, configuration (ii) again performs the best. There are drastic differences between the considered configurations when they are compared in terms of energy; the total positron energy is reduced by approximately an order of magnitude for the head-on interaction, compared to the best case dual pulse interaction. The difference between the linear and circularly polarised (with the same rotation directions) cases is also more significant, with the linear case producing $\sim$30% lower total energy. This is in line with the theoretical predictions of Ref. [314], in which it is demonstrated that the radiated energy is significantly higher for electron oscillations in circularly polarised laser fields, compared to linear polarisation (in vacuum).

There are numerous factors which may help elucidate the differences between the presented configurations. Any differences due to the properties of the γ-ray beam can be ruled out; the same source is employed for all simulations and so the average energy of the γ-ray photons, and the divergence half-angle, will remain the same. It has already been alluded to that the degree of spatial and temporal overlap between the dual laser pulses and the γ-ray beam has a significant impact on the number of positrons produced. However, another factor which could influence the number of positrons produced is the electric field configuration at the point of interaction. Due to the fact that the counter-propagating lasers have a relatively small angle of incidence, and a finite spatial extent, they will interfere with each other as they propagate towards the interaction point. This may lead to a beat-like structure in the spatial distribution of the electric field,

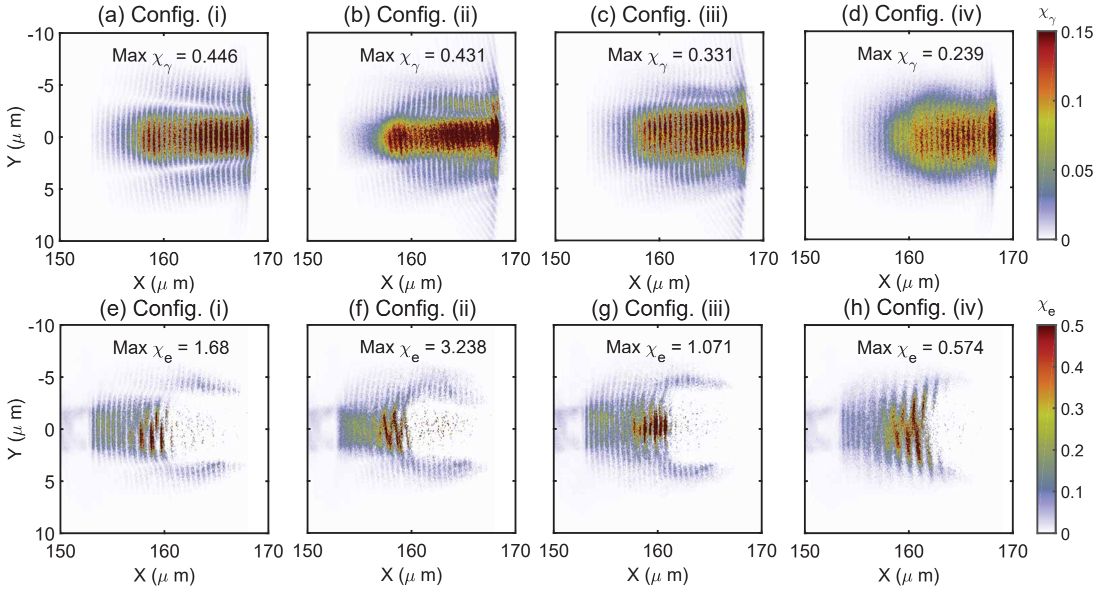

Figure 7.8: (a)-(d) Spatial distribution of the photon quantum parameter, χ_γ, for different interaction configurations, all compared at the time at which the number of positrons in the system is maximised. (e)-(h) Spatial distribution of the electron quantum parameter, χ_e, for the same configurations and at the same time as for χ_γ. The maximum values of the quantum parameters are displayed at the top of the panel.

which could lead to enhanced trapping of radiating electrons [265, 315].

These differences in the electric field structure at the interaction point can be investigated through the spatial distribution of the photon and electron quantum parameters. Figure 7.8 (a)-(d) shows the spatial distribution of χ_γ, for each of the four configurations under consideration. These measurements are made at the time at which the number of positrons is maximised. Panels (e)-(h) show the spatial distribution of χ_e for the same configurations and at the same time. In panels (a)-(h), the target rear is located at X=150 μm; Fig. 7.8 then indicates that the positrons are produced at the interaction point and not from the interaction of the counter-propagating lasers with the rear of the target.

Figure 7.8 demonstrates significant differences in the spatial distribution of the quantum parameters between the various interaction configurations. First, examining configuration (ii), which produced the highest number of positrons, there is clear evidence of a spatially localised structure in the distribution of χ_γ (located $\sim$160 μm in panel (b)). This structure contains a large number of counts of high χ_γ values, such that the peak signal is much higher than for the other configurations. Comparing this to the spatial distribution of χ_e for the same configuration (panel (f)), there is also strong radiative trapping of electrons within this same region (located at X=160 μm).

These trapped electrons are associated with extremely high χ_e values, as indicated by the fact that the maximum value of $\chi_e = 3.28$ is located within the focal spot of the dual laser pulses. In addition, these electrons lead to copious positron production via the interaction of the dual laser pulses with hard photons emitted by the trapped electrons.

Figure 7.8 additionally shows that the linearly polarised interaction geometry produces the highest value of χ_γ, however the spatially localised structure in the χ_γ distribution is not as pronounced as for the best case dual pulse interaction (Fig. 7.8 (b)). In terms of electron trapping (panel (e)), it is seen that linear polarisation produced fewer trapped electrons, and a lower maximum χ_e, compared to the best case circularly polarised interaction. Finally, in panel (d), the head-on interaction, which previously produced the lowest number of positrons, also gives the lowest χ_γ values. In addition, the spatial distribution is relatively wide and shows no indication of the localised structure which was observed in the other configurations. The same trend is seen in the distribution of χ_e, panel (h), in which there are very few trapped electrons. As has been stated previously, this case is associated with the lowest degree of spatial overlap between the γ-ray beam and the counter-propagating laser pulses, which may account for the low χ_γ values.

The degree of electron trapping, and therefore the formation of a spatially localised feature in the distribution of χ_γ, is strongly dependent on the polarisation of the counter-propagating pulses. Fig. 7.8 indicates that the trapping is enhanced by the use of two circularly polarised pulses, with the same rotation directions; it is proposed that this configuration could be applied to boost the probability of pair cascades at higher laser intensities. It may also be possible to use this configuration to induce a pair cascade [153, 301] in the interaction of the dual laser pulses with a LWFA electron beam, provided that the interaction is not dominated by stochastic photon emission effects. If these effects are significant, they can lead to a broadening of electron phase space [58, 114, 120] (relative to classical RR models) and reduced electron trapping.

Determining the pair-production mechanism

There are multiple pair-production mechanisms which are predicted to occur in multi-PW laser-plasma interactions, which have been described previously in section 2.4. Here, the electron-positron pairs are produced via the non-linear Breit-Wheeler (NLBW) process [136, 148, 292]. This process occurs when a photon within the γ-ray beam interacts with n photons of the colliding lasers. The non-linearity in the interaction arises due to both the high flux of photons within the laser focal spot and the high energy of the photons within the γ-ray beam. Whilst there is also a linear Breit-Wheeler process, the cross-section for this process in these simulations is vanishingly small. The Bethe-Heitler [135, 146] and trident [138, 316] processes are similarly negligible in comparison to the NLBW process, due to the choice of a low Z-number target. The trident process may also occur in the laser field, however the cross-section for this process is negligible in comparison to the same process occurring in the Coulomb field of a high Z atom. In any case, these simulations are run with the trident process turned off.

The aim of this part of the study is to distinguish the positrons produced via the interaction of the dual laser pulses with photons of the γ-ray beam, from those produced via the interaction of the laser pulses with hard photons emitted by the trapped electrons. The target and laser parameters were chosen with the aim of minimising the number of electrons which escape the target rear (i.e. a thick, dense plasma slab was used to reduce the degree of transparency, whilst the choice of circular polarisation suppresses electron heating through the oscillating component of the ponderomotive force), however there will always be a small fraction of electrons which escape the target, due to electron heating mechanisms which occur during the laser-solid interaction.

To isolate the positrons produced via the interaction of the dual laser pulses with photons in the γ-ray beam, a modified version of EPOCH was developed, in which the electrons and positrons are unable to radiate after a 'user defined cut-off time'. In EPOCH, the electrons, positrons and photons are randomly assigned an optical depth for emission processes (such as photon emission and pair-production). These optical depths are equal to zero at the start of the simulation and directly after an emission event. At all other times the optical depth for a given process is updated by solving its associated differential equation [58, 65, 117]. The modification to EPOCH presented in this chapter prevents the electron and positron optical depths from updating after a pre-defined time, which is selected to be equal to the time at which the γ-ray beam escapes the target rear. This means that any escaping electrons cannot radiate hard photons, which subsequently contribute to pair-production. It is then assumed that any positrons produced in these simulations arise purely due to the interaction of the dual laser pulses with photons of the γ-ray beam. The results of this investigation are summarised in table 7.1. For each of the four interaction configurations (see Fig. 7.6), the number of positrons produced via the interaction of the dual counter-propagating laser pulses with photons in the γ-ray beam, compared to the total number of positrons, is calculated. The total number of positrons comes from the simulations run with the un-modified version of EPOCH, i.e. those presented in Fig. 7.7. A similar quantity is presented for the total positron energy.

Configuration	**(i)**	**(ii)**	**(iii)**	**(iv)**
Number of e^+ produced via interaction with the γ-ray beam (%)	79	45	60	84
Energy of e^+ produced via interaction with the γ-ray beam (%)	40	14	17	56

Table 7.1: Number and energy of positrons produced via interaction with the γ-ray beam, compared to the total produced for each of the four interaction configurations.

The key result from table 7.1 is that the configuration which previously produced the largest total number of positrons (configuration (ii); two 4×10^{23} Wcm^{-2} circularly polarised pulses with the same rotation direction), now produces the smallest number of positrons via interaction with the γ-ray beam. Given that this configuration also produced the largest amount of radiative electron trapping, it is deduced that the majority of positrons in this case must come from the interaction of the counter-propagating lasers with hard photons emitted by the trapped electrons. The head-on interaction (configuration (iv)), which previously yielded the lowest total number of positrons, now produces the largest percentage of positrons via interaction with the γ-ray beam. These results indicate that the more radiative electron trapping is present in the interaction, the more positrons will be produced, however these will primarily be generated via the interaction of the counter-propagating laser pulses with hard photons emitted by the trapped electrons, as opposed to interaction with photons in the γ-ray beam. This same trend is observed in terms of the total positron energy; in the head-on interaction, over 50% of the total positron energy comes from the interaction of the counter-propagating laser pulse with the γ-ray beam, whereas this drops to only ~14% for the best circular polarisation configuration.

Describing the differences between the interaction configurations

In this section, it is demonstrated that the dual pulse interaction produces an enhanced number of positrons, compared to a head-on collision geometry, due to the increased

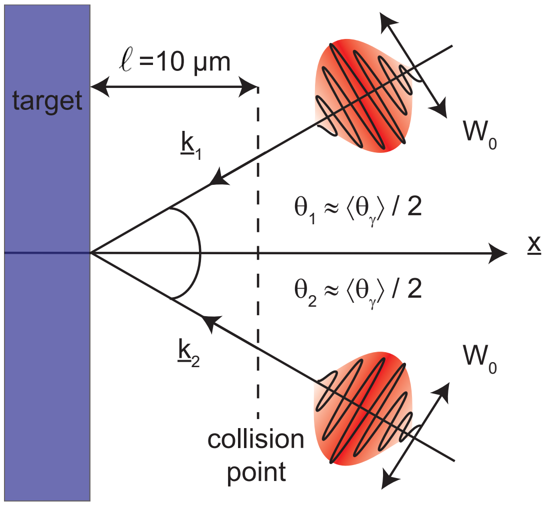

Figure 7.9: Schematic showing the interaction geometry used to model the dual pulse interaction. The laser pulses propagate along the divergence half-angle of the γ*-ray beam, such that* $|\theta_1| = |\theta_2| = \langle\theta_\gamma\rangle/2$ *∼10° . The counter-propagating pulses come into focus at a distance* ℓ*=10* μ*m behind the target rear.*

spatial overlap of the γ-ray beam and the counter-propagating laser pulses. This is achieved via an analytical estimate of the quantity $\sqrt{\bar{\chi}_\gamma^2}$, which is related to the average of χ_γ and can therefore be extrapolated to describe the differences in the number of positrons produced by each of the configurations. To estimate $\sqrt{\bar{\chi}_\gamma^2}$, the laser pulses are modelled as polarised plane waves, interacting with a single photon. This simple approach is sufficient to demonstrate the trends observed in the simulations, although this approach could be extended by expressing the laser pulses in terms of their spatial and temporal profiles, and by averaging the estimated $\sqrt{\bar{\chi}_\gamma^2}$ value over a population of photons, whose energies are sub-sampled from the simulations.

Two laser pulses are considered, propagating with angles θ_1 and θ_2 with respect to the x-axis (which is also the central axis of the γ-ray beam). To match the simulations, these angles are equal to half the divergence half-angle of the γ-ray beam, measured just before the interaction point. A schematic of this interaction geometry is provided in Fig. 7.9. The propagation directions of these two lasers (denoted by α=1,2, respectively) are described by the following wave vectors:

$$\hat{\mathbf{k}}_\alpha = (\cos\theta_\alpha, \mp\sin\theta_\alpha, 0) \tag{7.7}$$

The electric and magnetic fields associated with these lasers are:

$$\frac{e\mathbf{E}_\alpha}{m_e c\omega_L} = a_\alpha(\cos\phi_\alpha\hat{\mathbf{y}}_\alpha + \delta_\alpha\sin\phi_\alpha\hat{\mathbf{z}}) \tag{7.8}$$

$$\frac{e\mathbf{B}_\alpha}{m_e \omega_L} = a_\alpha(-\delta_\alpha\sin\phi_\alpha\hat{\mathbf{y}}_\alpha + \cos\phi_\alpha\hat{\mathbf{z}}) \tag{7.9}$$

where the unit vector $\hat{\mathbf{y}}_\alpha$ describes the projection of the fields from the rotated coordinate frame of the lasers into the standard Cartesian grid, such that $\hat{\mathbf{y}}_\alpha$= $(\pm\sin\theta_\alpha, -\cos\theta_\alpha, 0)$. The parameter δ_α is related to the polarisation of the laser pulses, such that $\delta = 0$ for linear, and $\delta = \pm 1$ for left and right handed circular polarisations. Here, $a_\alpha \sim 380\Omega$ is the normalised vector potential, where $\Omega = \sqrt{2}$ for linear polarisation and $\Omega = 1$ for circular polarisation. Finally, the phase is given by $\phi_\alpha = \mathbf{k}_\alpha\cdot\hat{\mathbf{r}} - \omega_L t$, where $\hat{\mathbf{r}} = \hat{\mathbf{x}} + \hat{\mathbf{y}} + \hat{\mathbf{z}}$ is the Cartesian position vector.

Using the above expressions for the laser fields, the Lorentz force and the projection of the electric field along the direction of the photon velocity can be evaluated. This leads to the following estimate of the photon quantum factor:

$$\chi_\gamma = \gamma_\gamma a_\alpha \mathcal{G}\mathcal{H}\frac{\hbar\omega_L}{m_e c^2} \tag{7.10}$$

where γ_γ is the average photon Lorentz factor. This is estimated by assuming that the frequency of the photon under consideration is equal to the critical frequency of the synchrotron spectrum, such that $\hbar\omega_\gamma \sim \hbar\omega_{cr}$, where the critical frequency is related to the oscillations of the electrons in the laser field, as follows: $\omega_{cr} = \gamma_e^3|\mathbf{p}_e \times \mathbf{F}_{L,e}|/p_e^2$. This leads to $\gamma_\gamma \sim \gamma_e^2 a_0\hbar\omega_L/m_e c^2 \sim$20.

The function, $\mathcal{H}$, accounts for the degree of spatial overlap between the γ-ray beam and the dual laser pulses. This function is defined as follows:

$$\mathcal{H} = \exp\left(-\frac{\ell^2}{w_0^2}\left(\tan\theta - \tan\frac{\langle\theta_\gamma\rangle}{2}\right)^2\right) \tag{7.11}$$

where θ is the angle the photon velocity makes with respect to the central axis of the γ-ray beam, and w_0 is the beam width, given by w_0=FWHM/$\sqrt{2\ln 2}$. Finally, ℓ is the distance from the rear of the target to the interaction point, equal to 10 μm in the simulations, which plays an important role in the interaction. From Eqn. (7.11), it is clear that if the dual laser pulses propagate along the divergence half-angle of the γ-ray beam, then $\theta = \langle\theta_\gamma\rangle/2°$, such that $\mathcal{H}$=1. This is the interaction geometry which maximises the spatial overlap with the counter-propagating lasers. For any other angle of incidence, for example a head-on interaction in which θ=0°, the divergence of the γ-ray beam means that the counter-propagating pulse does not interact with the entire radiation source as it comes into focus. The degree of overlap in such a case depends on ℓ. If this is large, then the γ-ray beam will diverge significantly before the interaction point, thus there are fewer photons on-axis to interact with the laser pulse, i.e. $\mathcal{H}$ <1. The spatial overlap can be improved by moving the interaction point as close as possible to the target rear. Such a configuration is typically not experimentally feasible, since it is not possible to probe the properties of photons and positrons produced so close to the target rear. Equation (7.11) then demonstrates that the maximum spatial overlap is achieved when the dual laser pulses propagate along the divergence half-angle of the γ-ray beam, provided that ℓ >0.

The second function, $\mathcal{G}$, which appears in Eqn. (7.10) is defined by summing the Lorentz force and the projection of the photon velocity along the direction of the laser electric field, for each of the two laser pulses. From inspection, it is clear that this quantity is $\propto \chi_\gamma^2$ (see Eqn. (2.85)). This leads to the following definition:

$$\mathcal{G}^2 = \Sigma_{\alpha=1}^{\alpha=2} \frac{1}{a_\alpha^2} \left(\mathbf{F}_{L,\alpha}^2 - e^2 (\mathbf{v}_\gamma \cdot \mathbf{E}_\alpha)^2 \right) \tag{7.12}$$

where the magnitude of the photon velocity is $v_\gamma = \hbar k_\gamma / m_e c$. The quantity $\mathcal{G}^2$ contains terms which oscillate within a laser period. The simulation results, however, are output every laser period; in order to get a comparable quantity, the function $\mathcal{G}^2$ is averaged over the phase of each of the dual laser pulses, as follows:

$$\bar{\mathcal{G}^2} = \frac{1}{(2\pi)^2} \int_0^{2\pi} \int_0^{2\pi} \mathcal{G}^2 d\phi_1 d\phi_2 \tag{7.13}$$

Here, the quantity $\mathcal{G}^2$ is averaged, as opposed to $\mathcal{G}$, as the presence of the square root means that Eqn. (7.13) is extremely difficult to evaluate. Substituting $\sqrt{\bar{\mathcal{G}^2}}$ into Eqn. (7.10) yields a quantity $\sqrt{\bar{\chi_\gamma^2}}$, which is related to the average χ_γ through the variance, σ^2, as follows: $\sigma^2 = \bar{\chi_\gamma^2} - (\bar{\chi_\gamma})^2$. Performing the average leads to the expression for $\mathcal{G}$ given in Eqn. (7.14), below.

$$\begin{aligned} \bar{\mathcal{G}^2} =& 2 + \Delta + 2\beta_x \cos\theta (1+\delta) + \beta_x^2 (\Delta \cos^2\theta - \sin^2\theta) \\ &+ \beta_y^2 (\Delta \sin^2\theta - \cos^2\theta) \end{aligned} \tag{7.14}$$

where $\beta_{\gamma,x} = \cos\frac{\langle\theta\rangle}{2}$ and $\beta_{\gamma,y} = \sin\frac{\langle\theta\rangle}{2}$ are the projections of the photon velocity in the x and y directions, respectively. Here, $\delta = \frac{1}{2}(\delta_1 + \delta_2)$ and $\Delta = \frac{1}{2}(\delta_1^2 + \delta_2^2)$, are defined by the sum of the polarisation states of the dual laser pulses, corresponding to different interaction configurations; as per Fig. 7.6. Evaluating the above equation for the head-on (θ=0), and the dual pulse interaction ($|\theta| = |\theta_1| = |\theta_2| = |\langle\theta_\gamma\rangle|/2$), yields the following expressions for $\bar{\mathcal{G}}^2$.

$$\begin{aligned}\bar{\mathcal{G}}^2(\theta = \langle\theta_\gamma\rangle/2) =& 2 + \Delta + 2(1+\delta)\cos^2\frac{\langle\theta_\gamma\rangle}{2}\\ &\Delta\left[\cos^4\frac{\langle\theta_\gamma\rangle}{2} + \sin^4\frac{\langle\theta_\gamma\rangle}{2}\right] - \frac{1}{2}\sin^2\langle\theta_\gamma\rangle\end{aligned} \tag{7.15}$$

and

$$\bar{\mathcal{G}}^2(\theta = 0) = 2(1+\Delta) + 2(1+\delta)\cos\frac{\langle\theta_\gamma\rangle}{2} - (\Delta+1)\sin^2\frac{\langle\theta_\gamma\rangle}{2} \tag{7.16}$$

By examining Eqn. (7.15), which corresponds to the different interaction configurations, it is observed that for the linear case, where $\delta = \Delta = 0$, the first term on the second line of the equation vanishes, such that the value of $\bar{\mathcal{G}}^2$ decreases relative to the circularly polarised cases. For the circularly polarised cases, the magnitude of $\bar{\mathcal{G}}^2$ then depends on the sign of δ.

For a circularly polarised laser pulse interacting head-on with the γ-ray beam (Eqn. (7.16)), it is necessary to account for the finite spot size effect (i.e. including the factor $\mathcal{H}$). The analytical estimate then predicts the lowest $\bar{\mathcal{G}}^2$ for this configuration. By calculating $\bar{\mathcal{G}}^2$ for each configuration, and substituting into Eqn. (7.10), the following estimates of $\sqrt{\bar{\chi}_\gamma^2}$ are obtained:

$$\sqrt{\bar{\chi}_\gamma^2} = \begin{cases} 0.0425 & : \text{config. (i)}\\ 0.0426 & : \text{config. (ii)}\\ 0.0366 & : \text{config. (iii)}\\ 0.0299 & : \text{config. (iv)}\end{cases}$$

The above values indicate the analytical estimate recovers the trends observed in the simulations. All of the interaction configurations produce higher $\sqrt{\bar{\chi}_\gamma^2}$ values than the head-on interaction (i.e.config (iv)). It is also observed that $\sqrt{\bar{\chi}_\gamma^2}$ is higher for the circular cases when the polarisation vectors rotate in the same direction, i.e. in the comparison of configurations (ii) and (iii).

The above estimates recover the trend that $\sqrt{\bar{\chi_\gamma^2}}$ is higher for the best case circularly polarised configuration, compared to linear polarisation. In terms of the analytical estimate, the results are in agreement with those of Ref. [314], in which it is demonstrated that the radiated power from an electron oscillating in a linearly polarised laser pulse is a factor of γ_e^2 lower compared to oscillations in a circularly polarised pulse. This difference is demonstrated by expressing χ_e as follows [314]:

$$\chi_e^2 = \left(\gamma_e \frac{\mathbf{E}}{E_{Sch}} + \frac{\mathbf{p} \times \mathbf{B}}{m_e c E_{Sch}}\right) - \left(\frac{\mathbf{p} \cdot \mathbf{E}}{m_e c E_{Sch}}\right)^2 \tag{7.17}$$

The above equation demonstrates that for linear polarisation, the second term on the right is maximised, due to the fact that the electron momentum is oriented along the electric field direction. This leads to a significant reduction in χ_e. For circular polarisation, the electric field direction rotates during a laser period, such that the second term on the right is lower on average, compared to the linear case. The result in Ref. [314] is derived for an electron located at the focus of two directly counter-propagating laser pulses, and therefore describes a situation in which the degree of electron trapping is high. The simulation results demonstrate that there is a lower degree of electron trapping for the linearly polarised case compared to the circular case, thus the difference in the χ_e values may not be as drastic as theoretically predicted.

Finally, whilst the analytical estimate of $\sqrt{\bar{\chi_\gamma^2}}$ exhibits the same trend as the simulations, the values are lower than the maximum χ_γ (see Fig. 7.8) by an order of magnitude. This suggests that it is more relevant to compare the analytical estimate with the average χ_γ value from the simulations. To illustrate this quantity, the χ_γ spectrum is plotted in Fig. 7.10, for each of the four interaction geometries. It is clear that the spectrum is skewed by a high number of counts of χ_γ <0.01, such that the average value is low. The average χ_γ for configuration (iv) for example is 0.002, an order of magnitude below the analytical estimate. The reason for this difference is again that the analytical estimate is for the quantity $\sqrt{\bar{\chi_\gamma^2}}$, which is related to the $\bar{\chi_\gamma}$ of the simulations, as follows: $\bar{\chi_\gamma} = \sqrt{\bar{\chi_\gamma^2} - \sigma^2}$. To compare these quantities it is then necessary to measure the variance of the spectrum. This is a non-trivial task when the spectrum cannot be fitted with a Gaussian distribution as in this case, and is therefore beyond the scope of this thesis. The important point here is that the analytical estimate, and

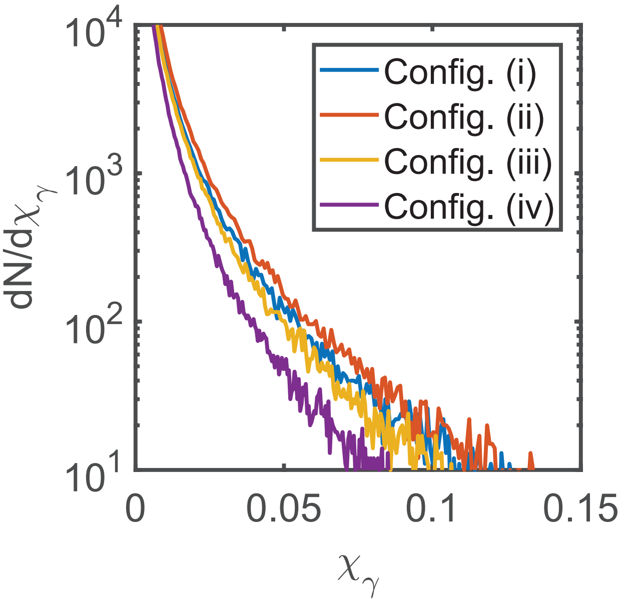

Figure 7.10: Plot of the χ_γ spectrum for each of the four interaction configurations. The analytical estimates produce a quantity which is related to the average χ_γ, and which shows the same trend observed in Fig. 7.8.

the $\bar{\chi_\gamma}$ and maximum χ_γ from the simulations, all agree that the head-on interaction should produce fewer positrons compared to the dual pulse configurations.

7.3.3 Comparison with ‘conventional’ collider configurations

So far, it has been demonstrated that the dual pulse interaction geometry, in which the counter-propagating pulses are circularly polarised and rotate with the same direction, produces the largest total number of positrons; henceforth this is referred to as the best case dual pulse interaction. This result is now compared to two configurations in which there is no initial step of generating the γ-ray beam, instead the ultra-intense laser pulse impacts the solid target directly. These configurations are described as follows; (v) is the interaction of one ultra-intense laser pulse, with total energy equal to the sum of the driving pulse and the dual counter-propagating pulses (in configurations (i)-(iv)), and (vi) is the interaction of two directly counter-propagating pulses, each with half the total energy of configuration (v), incident on either side of a solid target. This target is the same 100 μm-thick proton plasma slab described in the previous configurations. A schematic of this set up is provided in Fig. 7.6 (c). The ‘conventional’ configurations are relatively easy to implement experimentally, and are therefore likely to be among the first investigations conducted at multi-PW laser facilities. The proposed dual pulse interaction geometry will be compared with the ‘conventional’ configurations in terms of the total number, energy, and energy-angle distribution of the emitted positrons. These are three important quantities to compare, given that applications such as laboratory astrophysics experiments will require large numbers of positrons produced in a low divergence source, in order to make statistically valid measurements, and to apply the positron source for additional applications such as a collisions with secondary positron or radiation beams.

First, in terms of the total number of positrons, configuration (v) performed the best, producing an order of magnitude more positrons than the best case dual pulse interaction. This same trend was observed in terms of the total positron energy. The best case dual pulse interaction did however perform better than configuration (vi), in which the two directly counter-propagating laser pulses irradiate the target on both sides. The dual pulse interaction produced ∼66% more positrons, with ∼40% higher total energy.

This result leads to important experimental considerations. The highest number of positrons in this comparison was produced by the direct interaction of one ultra-intense pulse (8.5×10^{23} Wcm^{-2}) with a thick, dense target. Producing such an ultra-high intensity in a single pulse is beyond the normal operational capability of upcoming laser facilities (unless the intensity of the system can be enhanced by moving from a relatively long F number (i.e. $>F/3$), to $\sim F/1$ focusing, via the application of an ellipsoidal plasma mirror [215, 216]). It is therefore more likely that experiments will utilise two lower intensity pulses (for example, two 10 PW beams in the case of ELI-NP), interacting with a target in a directly counter-propagating geometry. However, it has been demonstrated that this configuration is less efficient than the dual pulse interaction geometry.

It is also important to compare the photon and positron angular distributions from the various interaction geometries. The photon angular distribution gives an indication of the direction in which the positrons are most likely to be emitted. This is useful in terms of guiding experimental measurements, since the number of produced positrons will be significantly lower than those of the photons and therefore more difficult to detect.

In Fig. 7.11, the best case dual pulse interaction is compared to the two conventional schemes (configurations (v) and (vi)), in terms of the photon and positron angular

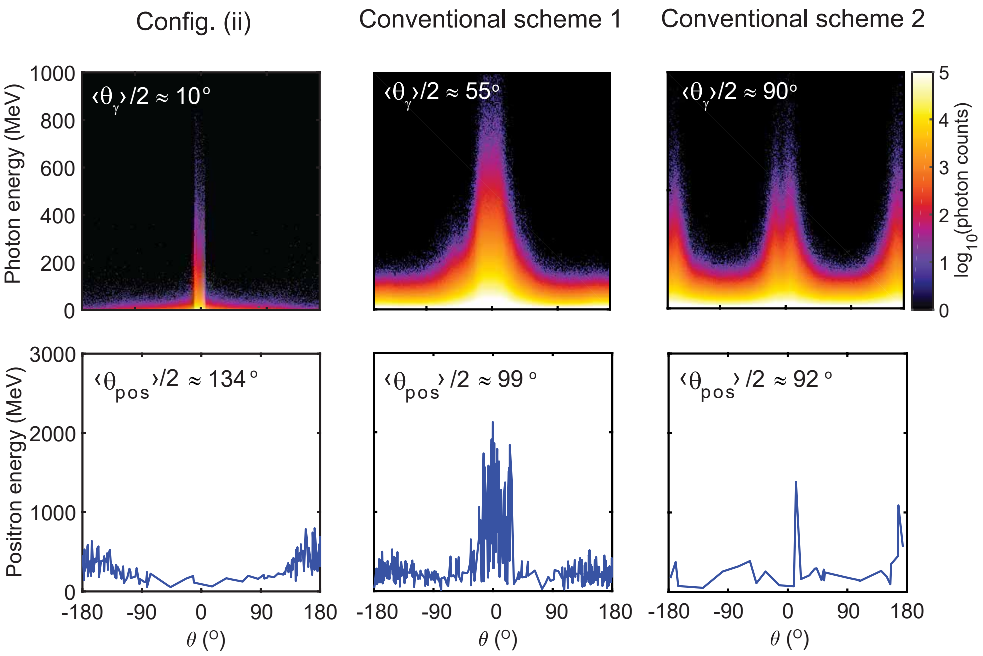

Figure 7.11: Plots comparing the best case dual pulse interaction with two conventional schemes. Conventional scheme 1 is the direct interaction of a 8.5×10^{23} *Wcm*$^{-2}$ *pulse with a solid target, whilst conventional scheme 2 is the interaction of two directly counter-propagating pulses, each with an intensity of* 4.25×10^{23} *Wcm*$^{-2}$*, incident on either side of the same solid target. The top panels compare the photon angular distributions, whilst the bottom panels compare the positron energy-angle distributions. The divergence half-angle is displayed in the top left of each panel, and all are compared at the time at which the number of positrons in the system is maximised.*

distributions. All of these distributions are computed at the time at which the number of positrons in the system is maximised. First, comparing the photon distributions (top row of Fig. 7.11), it is clear that for the best case dual pulse interaction, the γ-ray beam maintains its low divergence angle, even after the interaction. The divergence half-angle in this case is $\sim 10°$. The photons produced in configuration (v) are highly divergent, with a half-angle $\sim 55°$, whilst for configuration (vi) the radiation is emitted isotropically, as indicated by the fact that $\langle\theta_\gamma\rangle/2 \sim 90°$. For these two conventional cases, a substantial amount of the radiation comes from electron motion along the target surface, which is driven by the laser ponderomotive force.

Comparing the positron energy-angle distributions in Fig. 7.11 for the two conventional schemes, these generally follow the shape of the photon distributions. Again, configuration (vi) produces a nearly isotropic positron energy-angle distribution, with a large number emitted on-axis. This is not particularly useful for experiments, since it is generally not possible to measure the positrons over all of the 4π in which they are emitted, and sampling only a small solid angle may result in a significant reduction in the number of counts observed. However it should be noted that employing a single spectrometer, with multiple slits, may enable some degree of spatial resolution in the positron energy spectrum, even when sampling over a small solid angle. Secondly, it is impractical to use an isotropic energy-angle distribution for interactions with counter-propagating lasers or relativistic particle beams, since the energy and number of positrons will be approximately evenly spread over the full solid angle. The best case dual pulse interaction, however, demonstrates a highly anisotropic energy-angle distribution, with a divergence half-angle $\langle\theta_{pos}\rangle/2$=134° . This distribution is favourable for experiments, since the positron source can be easily collided with counter-propagating lasers.

Upcoming laser facilities, such as ELI-NP, will utilize two 10 PW laser pulses [287], in which case the interaction geometry is likely to be similar to configuration (vi). The results presented in this chapter predict that higher positron numbers and energies can be achieved using a dual pulse interaction geometry, if this set up can be realised experimentally. One way in which this configuration could be achieved is by using one of the 10 PW beams to drive the γ-ray beam, whilst splitting the second into two high intensity laser pulses. The advantage offered by this dual pulse interaction geometry is that the distribution of produced positrons has a higher degree of anisotropy than any of the conventional schemes which have been explored in this section, and therefore provide a useful experimental tool. However, when laser intensities of the order 10^{24} Wcm^{-2} become available, it will be possible to obtain higher positron numbers and energies via the direct interaction of an ultra-intense laser pulse with a solid target, albeit producing a more isotropic positron energy-angle distribution compared to the dual pulse interaction geometry.

7.4 Conclusions

In this chapter, pair-production via the non-linear Breit-Wheeler process has been investigated, using a dual pulse interaction geometry which could be realised at multi-PW laser facilities. The first stage in this interaction is the generation of a high energy, low divergence γ-ray beam (with average photon energy ∼10 MeV and a divergence half-angle ∼10°), via an ultra-intense laser-solid interaction. The parameters of the γ-ray beam were found to be dependent on the electron dynamics, and thus it is possible to reduce the divergence of this beam via the application of a strong, externally applied magnetic field. In addition, the application of the magnetic field was demonstrated to enhance the stochastic nature of the photon emission, which could enable quantum RR effects to be investigated in ultra-intense laser-solid interactions.

In the second stage of the interaction, the optimised γ-ray beam interacts with dual laser pulses, to induce non-linear pair-production. The polarisation of these laser pulses was varied in order to determine the configuration which performs best in terms of the total positron number and energy. These dual pulse configurations were compared to a head-on interaction with a single laser pulse, with the same total energy. It was found that using two circularly polarised pulses with the same rotation direction produced the best results, and that all of the dual pulse configurations were more efficient than the single head-on interaction.

Whilst the circularly polarised interaction geometry produced the largest number of positrons, it was found that these were predominantly generated via the interaction of the counter-propagating laser pulses with electrons trapped at the interaction point. The conclusion from this study is that the higher the degree of radiative electron trapping, the more positrons will be produced, however these mostly come from the interaction of the counter-propagating laser pulses with hard photons emitted by the trapped electrons. To experimentally investigate positrons which originate from the interaction of the counter-propagating laser pulses and the γ-ray beam, it is necessary to reduce the number of trapped electrons, for example through the application of a strong magnet at the target rear, or by varying the target thickness.

The results obtained in this study have important implications for the future of ultra-intense laser-plasma interactions. The dual pulse interaction geometry offers a means of enhancing the number of positrons observed at next generation facilities, compared to previously proposed schemes. This will contribute to the study of pair-production via the non-linear Breit-Wheeler process since, to-date, it has not been possible to produce a large number of positrons utilising this process experimentally. The dual pulse interaction geometry may therefore contribute greatly to the investigation of fundamental physics processes, by providing insight into the energy partition and internal dynamics of a plasma dominated by pair-production. The predictions made in this chapter using the dual pulse interaction geometry, such as the total number and energy of produced positrons, can then be compared to experiments at upcoming laser facilities. This will enable the assumptions which are routinely used in modelling ultra-intense laser-solid interactions, such as the CCFA (described in section 4.3.3), to be tested in detail, given that this assumption in particular is important in determining the number of electron-positron pairs produced in QED-PIC simulations. In addition, it was demonstrated in this chapter that an optimised γ-ray beam can be produced via an ultra-intense laser-solid interaction. By colliding two such γ-ray beams, it may be possible to induce pair-production via the linear Breit-Wheeler process, which to-date has never been observed. Such an application would again boost our understanding of fundamental physics processes, by enabling the physics which occurs in the most extreme astrophysical environments to be replicated in the laboratory.

Chapter 8

Conclusions and Future Work

The results presented in this thesis have focused on the generation of radiation from ultra-intense laser-solid interactions, and the possibility of exploiting this radiation to observe high-field QED phenomena. The key results will be summarised in this final chapter, along with a discussion of the ways in which the work presented in this thesis could be developed further and potentially tested at upcoming laser facilities.

8.1 Relativistic transparency and mode conversion in intense laser-foil interactions

The aim of chapter 5 was to experimentally investigate the process of RSIT during the interaction of intense laser pulses with thin, dense foils. In the context of this thesis, relativistic laser-plasma phenomena are predicted to be strongly influenced by QED effects at ultra-high intensities ($\geq 10^{23}$ Wcm^{-2}). It is important to first gain understanding of these plasma physics processes by conducting experiments using currently available laser intensities. A key goal of chapter 5 was to measure the polarisation state of light detected at the rear of thin foil targets which undergo transparency. It was predicted in Stark *et al* [160] that temperature anisotropy within the plasma enables it to act analogously to an optical polariser or wave plate. This temperature anisotropy is driven by differences in the degree of electron heating, as a result of employing different laser polarisations. The resulting polarisation shifts have previously been measured in the context of low density plasmas with uniform density profiles, interacting with weakly relativistic laser pulses, in Stark *et al* [160]. Thus it has been demonstrated that temperature anisotropy can be used to manipulate the properties of light interacting with the plasma. A key aspect of chapter 5 is that it was not possible to re-create this effect for the laser and target parameters explored in this study. For the range of parameters employed experimentally, effective polarisation shifts were detected, however these were the result of an entirely new mechanism. With the assistance of 3D-PIC simulations, it was discovered that the acceleration of electrons from the edge of the relativistic plasma aperture led to the self-generation of light in the polarisation plane, at both the laser frequency and its second harmonic. This light is produced in the form of higher order TEM modes, generating a TEM_{11} mode in the E_z field and a TEM_{02} mode in the E_y field, at a frequency of ω_L. The superposition of these modes with the transmitted laser field leads to the generation of a superposition state whose polarisation angle appears to be rotated with respect to the input laser pulse. This demonstrates a novel process by which effective polarisation shifts may be induced, and which is referred to in this thesis as plasma mode conversion.

The key result of this chapter is that for an optimal target thickness, a radially polarised mode can be generated. This radial mode is produced at a frequency of $2\omega_L$ and at high intensity ($\sim 10^{18}$ Wcm^{-2}). Such modes have important applications including efficient electron and positron acceleration, and the generation of bright radiation sources. However, they are currently difficult to generate given the damage thresholds of the solid state optics required. The results of chapter 5 demonstrate a method by which these modes can be generated at high intensity, via laser-solid interactions. In addition, it was discovered that the degree of mode conversion could be controlled through target parameters, such as the target thickness, and that the spatial structure of the mode also varied temporally. Thus the mode conversion effect described in this chapter is highly tunable, and may enable dynamic control over the polarisation state, and spatial structure, of laser light interacting with a thin layer of plasma.

8.1.1 Future work

Whilst the experimental campaign described in chapter 5 enabled effective polarisation shifts to be measured, it fell short of the objective of measuring the spatial distribution of the light detected at the target rear. Thus, the work presented in this chapter may be developed on future experimental campaigns by designing and implementing a spatially resolved Stokes polarimeter. This would enable experimental confirmation of the mode conversion process, as opposed to inferring it from numerical simulations. With an appropriate polarimetry set-up, it may be possible to measure the near and far-field distributions of the light detected at the target rear, simultaneously. For example, a beam-splitter cube may be positioned behind the target, splitting the light into two paths. The first path can be directed onto a PTFE scatter screen, and imaged with two cameras, filtered appropriately to record the light detected at ω_L and $2\omega_L$. Imaging the screen in this way enables a spatially resolved measurement of the near field distribution of the light detected at the rear of the target. The second path is then directed into the Stokes polarimeter, such that the polarisation state of the light can be measured, as described in the experimental set-up in chapter 5. For future work, optics with sufficiently high quality will be employed to enable spatially resolved measurements. In addition, the light entering the Stokes polarimeter could be separated into two paths, one filtered at ω_L and the other at $2\omega_L$, such that the polarisation state of the second harmonic light can also be measured. This would enable experimental confirmation of the radially polarised mode which is predicted at $2\omega_L$.

In addition, the results presented in chapter 5 highlight the need to characterise the level of transition radiation, emitted from targets which do not go transparent. During the previously detailed experimental campaign, the energy of the transition radiation was measured to be $\leq 1\%$ of the laser energy incident on the target. However, the light entering the Stokes polarimeter was heavily attenuated using neutral density filters (of magnitude ND 5) to protect the cameras from damage. To completely characterise the radiation it would be necessary to repeat the measurement, using a thick target ($\geq$57 nm), and gradually decreasing the level of attenuation. This will enable more accurate determination of the target thickness which just goes transparent to the laser pulse, as well as providing information about the spatial structure and polarisation of the transition radiation (i.e. when there is no transmitted laser light at the target rear).

The simulations presented in chapter 5 indicate that the interaction of the laser pulse with the relativistic plasma aperture is key to the mode conversion process. Another aspect of this work that could be developed further is to vary the spatial structure of the input laser pulse, therefore changing the shape of the aperture and likely driving different mode structures. This may enable an alternative means of tuning the modes which are produced during the interaction (as opposed to tuning via the target thickness, as demonstrated in chapter 5). There are multiple ways in which the spatial structure of the pulse could be varied. The first could be via the application of a deformable optic, which would enable for example, an elliptical focal spot to be generated. The second method could be through the application of a spiral wave plate, such that laser pulses with optical angular momentum could be generated. These laser pulses may influence the shape of the aperture, as well as imparting angular momentum to the accelerated electron bunches, which will again have interesting effects on the generated modes.

8.2 Modelling the effects of the radiation reaction force on the interaction of ultra-intense laser pulses with thin foils

In chapter 6, the effects of RSIT and the RR force were investigated during the interaction of an ultra-intense (10^{23} Wcm^{-2}) laser pulse with thin foil targets in the light sail regime of RPA. This study was conducted by employing numerical simulations and theoretical modelling. Previous studies in this regime had indicated that a significant fraction of the laser energy is converted into high energy radiation, however none of these studies had made the link between the properties of the emitted radiation and the target dynamics. These previous studies also addressed the impact of target transparency on the magnitude of the RR effects, but again had not demonstrated that these effects manifest themselves in the properties of the emitted radiation. Thus, the results presented in chapter 6 are the first to make explicit the link between the properties of the emitted synchrotron-like radiation and the target dynamics within the light sail regime.

Using numerical simulations, it was demonstrated that the magnitude of the RR force in this regime is highly sensitive to the target thickness. These RR effects are realised in the distribution of the emitted radiation, the energy partition, and the target dynamics. It is therefore possible that control over these properties may be achieved at upcoming laser facilities. In particular, the magnitude of the RR force was characterised in terms of an average emission angle, which may be measured experimentally. For target thicknesses in which the magnitude of the RR force was weak, it was found that the radiation angular distribution was approximately isotropic, whereas for strong RR, distinct lobes were present. The RR effects are weak for cases in which RSIT occurs early in the laser-solid interaction, therefore the onset of RSIT can be diagnosed via the aforementioned changes in the properties of the photon angular distribution.

An analytical model was then developed which has enabled, for the first time, the calculation of the target velocity in the light sail regime under the influence of the RR force. In this model, the emission of synchrotron-like radiation was accounted for in the absorption co-efficient, implying that the target no longer acts as a perfectly reflecting relativistic mirror. The model enabled the target velocity and photon conversion efficiency to be calculated, both of which were found to be in good agreement with the simulation results.

8.2.1 Future work

Whilst this study was driven by numerical and theoretical modelling, the predictions of chapter 6 will be testable at upcoming laser facilities. The most substantial development to this work would then be to experimentally test key aspects of the developed model. One key test would be to measure the angular distribution of the radiation emitted from a range of target thicknesses. This measurement would be made by employing the wrap-around stack detector or an array of scintillator detectors. It is predicted that characteristic lobes in the radiation distribution will appear for targets in which the RR force has a strong influence. In addition, the RR force is predicted to impact the electron dynamics via changes in the electrostatic field within the target. The changes in the radiation angular distribution could then be correlated with the electrostatic field strength, for example, via measurements of the energy spectrum for electrons escaping the target.

In addition, this work could be extended by developing the numerical simulations further. It was commented in chapter 6 that the electron conversion efficiency remains relatively constant, with and without RR, over the range of target thickness employed. This is an interesting result, given that the magnitude of the RR force is known to vary over the same target thickness range. It is predicted that this result arises due to the fact that the energy radiated by electrons trapped at the laser-plasma interface, is in equilibrium with the energy they gain from the laser. This same result was observed in Ref. [60], but without explanation. Further investigations may employ circular or elliptical polarisations (as opposed to the linear polarisation previously utilised), to vary the degree of electron heating and to determine whether this saturation of the electron conversion efficiency (with and without RR) occurs for other incident laser polarisation states.

8.3 Multi-stage scheme for non-linear Breit-Wheeler pair-production utilising ultra-intense laser-solid interactions

In chapter 7, a dual pulse interaction scheme was proposed to investigate non-linear pair-production. Whilst this is not the first pair-production study to propose a dual pulse interaction, it is the first, to our knowledge, which utilises an optimised γ-ray beam to induce non-linear pair-production. The employed γ-ray beam was generated via an ultra-intense ($\sim 10^{23}$ Wcm^{-2}) laser-solid interaction, and it was demonstrated in chapter 7 that its properties are highly tunable. For example, the divergence half-angle of the γ-ray beam was reduced via the application of an externally applied magnetic field, whilst the average energy of the photons within the beam was boosted via the relativistic Doppler effect.

The optimised γ-ray beam then interacted with dual laser pulses, which propagate in the direction opposite, off-set from the central axis by a characteristic angle. It was demonstrated that setting this angle equal to the divergence half-angle of the γ-ray beam enhances the degree of spatial and temporal overlap, therefore enhancing the number of positrons produced compared to a head-on interaction with the same total energy. In addition, the polarisation state of the dual beams was varied, to determine the optimum configuration in terms of the number and energy of the produced pairs. Here it was demonstrated that two circularly polarised laser pulses, with the same rotation direction, give rise to the best case dual pulse interaction.

The dual pulse interaction geometry was additionally compared with ‘conventional’ configurations, which are likely to be employed at upcoming laser facilities. It was discovered that the dual pulse interaction geometry performs better, in terms of the total number and energy of positrons produced, than a conventional scheme in which two laser pulses (with the same total energy) irradiate a thick, solid target on both sides. The key result obtained by employing the dual pulse interaction geometry is that the resulting positron angular-energy distribution is highly anisotropic. Such a source of positrons is useful for laboratory astrophysics experiments, since it can be easily collided with ultra-intense laser pulses, or secondary particle beams. This could enable extreme astrophysical phenomena, such as shock propagation in pair-plasmas, and the mechanisms by which cosmic rays are generated, to be explored for the first time in the laboratory. Not only do the results of chapter 7 have practical applications, but the key predictions (such as the positron energy-angle distribution) can be tested experimentally, as will be described in the future work section.

8.3.1 Future work

As with the results of chapter 6, the most substantial way to develop the work presented in chapter 7 would be to test the predictions at upcoming laser facilities. The first obstacle in an experimental set-up to test these results would be the application of the external magnetic field used to collimate the emitted radiation. Whilst the required strength of 10^5 T is beyond the reach of conventional superconducting magnets, field strengths of this order have been measured in ultra-intense laser-plasma interactions. Therefore, a driver pulse could be used to generate the magnetic field, whilst a second pulse drives the hole boring phase and generates the γ-ray beam. It is predicted that the application of the magnetic field enhances the stochastic nature of photon emission, a prediction which could be tested by measuring the electron and photon spectra in subsequent experiments, with and without the driver pulse to generate the magnetic field. By conducting such an experiment, the predictions of classical RR models (such as those described in section 2.3.1) could finally be tested against experiment, as well as the assumptions which drive QED-PIC simulations, such as the CCFA approximation. If the numerical and experimental results are not in agreement, they may indicate a means by which the approximations can be improved, and therefore enhance our understanding of QED within the context of laser-plasma physics.

Another aspect of this work that could be tested is the efficiency of the dual pulse interaction geometry, compared to a head-on interaction. Upcoming systems such as ELI-NP will be designed with dual pulse configurations in mind. It will then be possible to use one pulse to drive the generation of the γ-ray beam, whilst splitting the second to produce high intensity, counter-propagating pulses. The yield of positrons can then be compared to the head-on interaction, and the conventional set-up (without the initial step of generating a γ-ray beam) to determine the validity of the results presented in this chapter.

Finally, the predicted anisotropy of the positron energy-angle distribution could also be measured at upcoming laser facilities. The positrons are predicted to be generated primarily off-axis, and so an appropriately positioned spectrometer could sample a fraction of the positron distribution, perhaps at a variety of angles around the laser axis. If each spectrometer is fitted with an array of pinholes, it will be possible to measure some degree of the spatial and energy distribution, thus enabling the anisotropy in the positron emission profile to be compared between the dual pulse and conventional configurations.

8.4 Conclusions

In conclusion, this thesis presents a number of important results which will contribute to the advancement of the field of laser-solid interactions. In chapter 5, the process of RSIT was investigated at current laser intensities. This led to the discovery of the plasma mode conversion effect, which enables high intensity, radially polarised modes to be generated via the interaction of an intense laser pulse with a thin, dense layer of plasma. This represents the first step towards tunable and dynamic control over the light transmitted through thin foil targets, and has important implications for aspects of electron and ion acceleration, and radiation production. At ultra-high intensities, it is predicted that the mode conversion process will be influenced by RR, in which case it may be possible to gain enhanced control over the temporal and spatial properties of the modes. The process of RSIT was further investigated in the context of ultra-intense laser-solid interactions in chapter 6. The magnitude of the RR force was demonstrated to depend strongly on the target thickness, and therefore the degree of transparency of the targets. The predictions of this chapter, such as the properties of the emitted radiation, may be tested at upcoming laser facilities. In addition, these results have implications for ion acceleration and energy partition within the context of QED plasmas. Finally, non-linear pair-production was explored via a dual pulse interaction geometry in chapter 7. The results of this study will contribute to the field of laboratory astrophysics, by providing a means of enhancing the number and energy of the produced positrons, and may also lead to the development of applications of QED effects, such as high energy, compact γ-ray sources.

Appendix A

Appendix

A.1 Relativistic electrodynamics

The covariant formulation of electrodynamics is used in chapter 2 to describe the equation of motion of a radiating electron. It is therefore useful to describe some of the relevant quantities here for clarity. The covariant formulation ensures that the fundamental laws governing the motion of a charged particle remain the same in all reference frames, i.e. the form of the equations are Lorentz invariant. It is important that the overall structure of the equations remains the same, since observers in different reference frames will confuse the definitions of charge and current densities, and electric and magnetic fields. More detail can be found, for example, in Refs. [86, 92, 101, 317].

In the covariant formulation, the position, velocity and acceleration of a charged particle are defined by the following 4-vectors;

$$x^\mu = (ct, x, y, z) = (ct, \mathbf{x}) \tag{A.1}$$

$$u^\mu = \frac{d}{d\tau}(ct, \mathbf{x}) = \gamma(c, \mathbf{u}) \tag{A.2}$$

$$a^\mu = \frac{d}{d\tau}(\gamma c, \gamma \mathbf{u}) = \left[\left(\frac{\mathbf{v}\cdot\mathbf{a}}{c^2}\right)\gamma^4, \gamma^2\mathbf{a} + \left(\frac{\mathbf{v}\cdot\mathbf{a}}{c^2}\right)\gamma^4\mathbf{v}\right] \tag{A.3}$$

where $\tau = t/\gamma$ is the proper time, defined in the rest frame of the particle, and all quantities in bold represent 3-vectors. The 4-gradient is defined as:

$$\partial_\mu = \frac{\partial}{\partial x^\mu} = \left(\frac{1}{c}\frac{\partial}{\partial t}, \nabla\right) \tag{A.4}$$

where the convention used for the metric tensor is $\eta^{\mu\nu}$ = diag(1,-1,-1,-1), which is used to lower and raise indices. Electromagnetic fields can be defined in terms of the 4-potential, $A^\mu = (\phi/c, \mathbf{A})$, where the derivative of the 4-potential is the electromagnetic tensor, $F^{\mu\nu}$:

$$F_{\mu\nu} = \partial_\mu A_\nu - \partial_\nu A_\mu \tag{A.5}$$

$$F_{\mu\nu} = \begin{pmatrix} 0 & E_x/c & E_y/c & E_z/c \\ -E_x/c & 0 & -B_z & B_y \\ -E_y/c & B_z & 0 & -B_x \\ -E_z/c & B_y & B_x & 0 \end{pmatrix} \tag{A.6}$$

The motion of a charged particle in an electromagnetic field is described by the set of Maxwell's equations and the Lorentz force equation, which are expressed as follows [101, 317]:

$$\partial_\mu F^{\mu\nu} = \mu_0 j^\nu \tag{A.7}$$

$$\partial_\mu \tilde{F}^{\mu\nu} = 0 \tag{A.8}$$

$$\frac{dp^\mu}{d\tau} = qF^{\mu\nu}u_\nu \tag{A.9}$$

where $p^\mu = mu^\mu$ is the 4-momentum, and $\tilde{F}^{\mu\nu} = \epsilon^{\mu\nu\gamma\delta}F_{\gamma\delta}$ is the electromagnetic dual tensor, with $\epsilon^{\mu\nu\gamma\delta}$ the Levi-Civita tensor.

A.2 Transverse ElectroMagnetic (TEM) modes

The solutions of the wave equation which propagate in laser resonators are referred to as Transverse ElectroMagnetic (TEM) modes. This refers to the fact that the electric field only has components in the plane perpendicular to the laser propagation direction. Typically these modes are symmetric, due to the shape of the laser cavity, and exhibit cylindrical or rectangular symmetry. Of particular interest in this thesis are the Hermite-Gaussian modes. These arise as solutions to the paraxial equation in Cartesian co-ordinates. Assuming an electromagnetic wave propagating along the positive z direction, the electric field is written:

$$E(x,y,z) = E_0 \frac{w_0}{w(z)} H_l\left(\frac{\sqrt{2}x}{w(z)}\right) H_m\left(\frac{\sqrt{2}y}{w(z)}\right) \exp\left(\frac{-(x^2+y^2)^2}{w^2(z)}\right) \tag{A.10}$$
$$\times \exp\left(\frac{-ik(x^2+y^2)^2}{2R(z)}\right) \exp(i\psi(x))$$

In the above equation, E_0 is the amplitude of the electric field and w_0 is the size of the mode waist at focus. The $H_{l,m}$ terms refer to the Hermite polynomials, which are functions of $(\sqrt{2}y/w(z))$ and $(\sqrt{2}z/w(z))$ and l, m are integers which characterise the mode. The laser focal spot employed in typical high power laser systems is a fundamental Gaussian mode, characterised by the indices $l = m = 0$. The remaining parameters are written:

$$w(z) = w_0\sqrt{1+(z/z_R)^2} \qquad \text{beam waist} \tag{A.11}$$

$$z_R = \pi w_0^2/\lambda_L \qquad \text{Rayleigh range} \tag{A.12}$$

$$R(z) = z\left(1+\left(\frac{z_R}{z}\right)^2\right) \qquad \text{Radius of curvature} \tag{A.13}$$

$$\psi(z) = (N+1)\arctan(x/x_R) \qquad \text{Guoy phase}$$

where $N = l + m$ in the expression for the Guoy phase. The Rayleigh range defined above is a useful parameter in the context of laser-plasma interactions. At z_R, the width of the Gaussian beam is $\sqrt{2}\times$ larger than at focus, meaning this is the distance at which the peak intensity is halved. This is useful for quantising the reduction in laser intensity induced by misalignments in the focal position. It is also useful to note that the curvature of the wavefronts of the laser pulse are zero at focus, meaning that the radius of curvature is infinite.

The spatial intensity profile of the mode is obtained by multiplying Eqn. A.10 by its complex conjugate. In Fig. A.1, the spatial intensity profiles for four TEM modes, which are referred to in chapter 5, are plotted. These modes appear in chapter 5, as a result of the interaction of an intense laser pulse with a relativistic plasma aperture.

A.3 Monte-Carlo parameter fitting

The results of the Monte-Carlo fitting algorithm, employed in chapter 4 to model the response curves for the Stokes polarimeter, are explored here in more detail. The

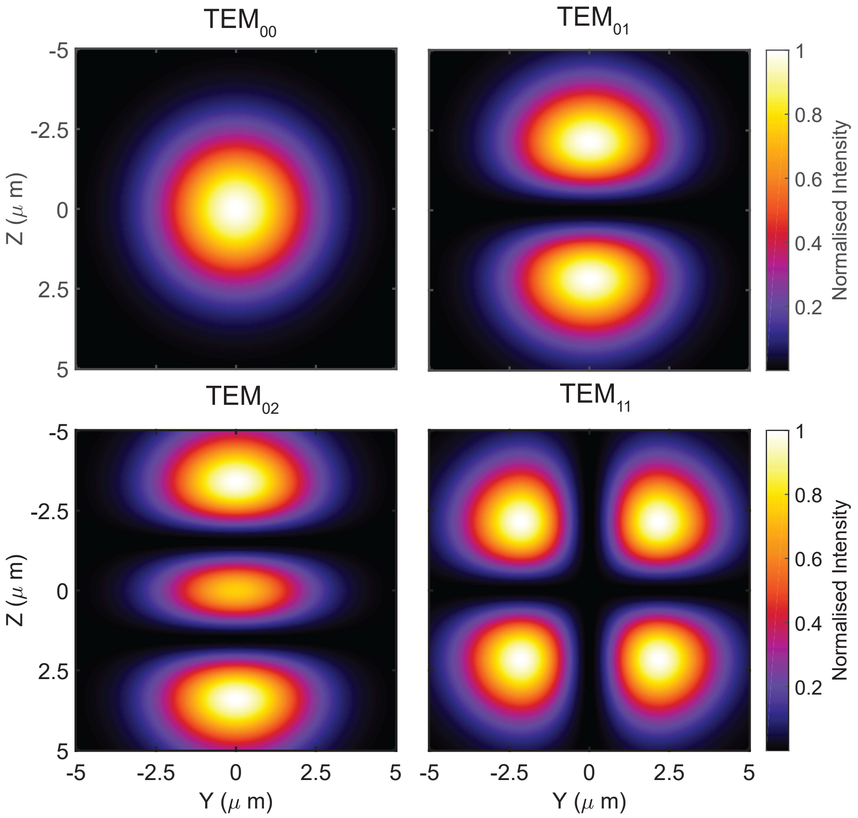

Figure A.1: Plot of the spatial intensity profile (normalised to the maximum value) for four TEM modes which are referred to in this thesis. These are (a) the fundamental TEM$_{00}$ mode, (b) the TEM$_{01}$ mode, (c) the TEM$_{02}$ mode and (d) the TEM$_{11}$ mode.

algorithm was run for 15,000 iterations, saving the values of the fitting parameters which generate a good fit to the experimental data. This means that the residuals for the fitted curves fall below a threshold value, determined from a known good fit. The values of each of the fitting parameters are distributed according to an approximately normal distribution, centered on the mean (or best fit value). These distributions are plotted in Fig. A.2 below. For each parameter, the upper and lower limits enclose 99.7 % of the fitting values, indicating the value of the best fit parameter to the 3σ confidence level. These upper and lower limits are used to determine the uncertainty in the fitting of the response curves in chapter 5.

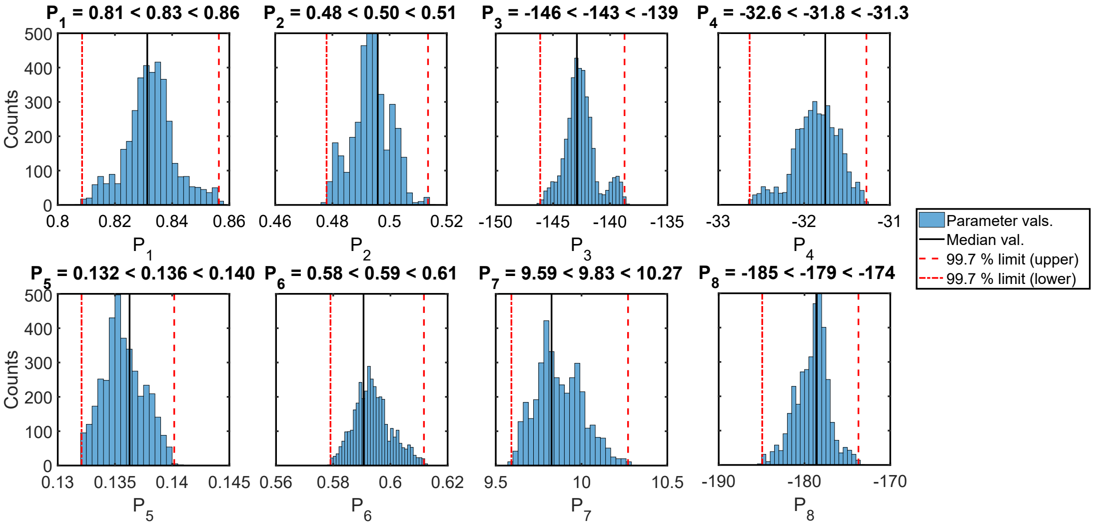

Figure A.2: Distribution of the fitting parameter values obtained after 15,000 iterations of the Monte-Carlo algorithm. The black line indicates the mean value, whilst the dashed red lines indicate the upper and lower limits which enclose 99.7 % of the fitting values.

Bibliography

[1] T. H. Maiman. Optical and microwave-optical experiments in ruby. *Physical Review Letters*, 4(11):564, 1960.

[2] P. R. Drake. *Introduction to High-Energy-Density Physics*. Springer, 2006.

[3] S. W. Bahk, P. Rousseau, T. A. Planchon, V. Chvykov, G. Kalintchenko, A. Maksimchuk, G. A. Mourou, and V. Yanovsky. Generation and characterization of the highest laser intensities. *Optics Letters*, 29(24):2837–2839, 2004.

[4] G. Gregori, A. Ravasio, C. D. Murphy, K. Schaar, A. Baird, A. R. Bell, A. Benuzzi-Mounaix, R. Bingham, C. Constantin, R. P. Drake, et al. Generation of scaled protogalactic seed magnetic fields in laser-produced shock waves. *Nature*, 481(7382):480, 2012.

[5] A. R. Bell. Cosmic ray acceleration. *Astroparticle Physics*, 43:56–70, 2013.

[6] P. Gibbon. *Short pulse laser interactions with matter*. World Scientific Publishing Company Singapore, 2004.

[7] W. Sibbett, A. A. Lagatsky, and C. T. A. Brown. The development and application of femtosecond laser systems. *Optics Express*, 20(7):6989–7001, 2012.

[8] D. E. Spence, P. N. Kean, and W. Sibbett. 60-fsec pulse generation from a self-mode-locked Ti: sapphire laser. *Optics Letters*, 16(1):42–44, 1991.

[9] J. P. Freidberg, R. W. Mitchell, R. L. Morse, and L. Rudsinski. Resonant absorption of laser light by plasma targets. *Physical Review Letters*, 28(13):795, 1972.

[10] E. G. Estabrook, E. J. Valeo, and W. L. Kruer. Two-dimensional relativistic

simulations of resonance absorption. *The Physics of Fluids*, 18(9):1151–1159, 1975.

[11] D. D. Meyerhofer, H. Chen, J. A. Delettrez, B. Soom, S. Uchida, and B. Yaakobi. Resonance absorption in high-intensity contrast, picosecond laser-plasma interactions. *Physics of Fluids B: Plasma Physics*, 5(7):2584–2588, 1993.

[12] S. C. Wilks and W. L. Kruer. Absorption of ultrashort, ultra-intense laser light by solids and overdense plasmas. *IEEE Journal of Quantum Electronics*, 33(11):1954–1968, 1997.

[13] F. N. Beg, A. R. Bell, A. E. Dangor, C. N. Danson, A. P. Fews, M. E. Glinsky, B. A. Hammel, P. Lee, P. A. Norreys, and M. Tatarakis. A study of picosecond laser-solid interactions up to 10^{19} Wcm^{-2}. *Physics of Plasmas*, 4(2):447–457, 1997.

[14] M. Borghesi, J. Fuchs, S. V. Bulanov, A. J. Mackinnon, P. K. Patel, and M. Roth. Fast ion generation by high-intensity laser irradiation of solid targets and applications. *Fusion Science and Technology*, 49(3):412–439, 2006.

[15] M. Roth, A. Blazevic, M. Geissel, T. Schlegel, T. E. Cowan, M. Allen, J. C. Gauthier, P. Audebert, J. Fuchs, J. Meyer ter Vehn, et al. Energetic ions generated by laser pulses: A detailed study on target properties. *Physical Review Special Topics-Accelerators and Beams*, 5(6):061301, 2002.

[16] S. Atzeni, M. Temporal, and J. J. Honrubia. A first analysis of fast ignition of precompressed ICF fuel by laser-accelerated protons. *Nuclear Fusion*, 42(3), 2002.

[17] M. Passoni, L. Bertagna, and A. Zani. Target normal sheath acceleration: theory, comparison with experiments and future perspectives. *New Journal of Physics*, 12(4):045012, 2010.

[18] M. Passoni, C. Perego, A. Sgattoni, and D. Batani. Advances in target normal sheath acceleration theory. *Physics of Plasmas*, 20(6):060701, 2013.

[19] M. Roth and M. Schollmeier. Ion acceleration-target normal sheath acceleration. *arXiv preprint arXiv:1705.10569*, 2017.

[20] S. C. Wilks, A. B. Langdon, T. E. Cowan, M. Roth, M. Singh, S. Hatchett, M. H. Key, D. Pennington, A. MacKinnon, and R. A. Snavely. Energetic proton generation in ultra-intense laser–solid interactions. *Physics of Plasmas*, 8(2):542–549, 2001.

[21] T. E. Cowan, J. Fuchs, H. Ruhl, A. Kemp, P. Audebert, M. Roth, R. Stephens, I. Barton, A. Blazevic, F. Brambrink, et al. Ultralow emittance, multi-MeV proton beams from a laser virtual-cathode plasma accelerator. *Physical Review Letters*, 92(20):204801, 2004.

[22] M. Borghesi, A. J. Mackinnon, D. Campbell, D. G. Hicks, S. Kar, P. Patel, D. Price, L. Romagnani, A. Schiavi, and O. Willi. Multi-MeV proton source investigations in ultraintense laser-foil interactions. *Physical Review Letters*, 92(5):055003, 2004.

[23] L. Romagnani, J. Fuchs, M. Borghesi, P. Antici, P. Audebert, F. Ceccherini, T. Cowan, T. Grismayer, S. Kar, A. Macchi, et al. Dynamics of electric fields driving the laser acceleration of multi-MeV protons. *Physical Review Letters*, 95(19):195001, 2005.

[24] D. C. Carroll, P. McKenna, O. Lundh, F. Lindau, C. G. Wahlström, S. Bandyopadhyay, D. Pepler, D. Neely, S. Kar, P. T. Simpson, et al. Active manipulation of the spatial energy distribution of laser-accelerated proton beams. *Physical Review E*, 76(6):065401, 2007.

[25] S. V. Bulanov, N. M. Naumova, and F. Pegoraro. Interaction of an ultrashort, relativistically strong laser pulse with an overdense plasma. *Physics of Plasmas*, 1(3):745–757, 1994.

[26] B. Dromey, M. Zepf, A. Gopal, K. Lancaster, M. S. Wei, K. Krushelnick, M. Tatarakis, N. Vakakis, S. Moustaizis, R. Kodama, et al. High harmonic generation in the relativistic limit. *Nature Physics*, 2(7):456, 2006.

[27] M. Zepf, B. Dromey, S. Kar, C. Bellei, D. C. Carroll, R. J. Clarke, J. S. Green, S. Kneip, K. Markey, S. R. Nagel, et al. High harmonics from relativistically oscillating plasma surfaces—a high brightness attosecond source at keV photon energies. *Plasma Physics and Controlled Fusion*, 49(12B), 2007.

[28] H. Vincenti, S. Monchocé, S. Kahaly, G. Bonnaud, P. Martin, and F. Quéré. Optical properties of relativistic plasma mirrors. *Nature Communications*, 5:3403, 2014.

[29] P. A. Norreys, M. Zepf, S. Moustaizis, A. P. Fews, J. Zhang, P. Lee, M. Bakarezos, C. N. Danson, A. Dyson, P. Gibbon, et al. Efficient extreme UV harmonics generated from picosecond laser pulse interactions with solid targets. *Physical Review Letters*, 76(11):1832, 1996.

[30] I. Watts, M. Zepf, E. L. Clark, M. Tatarakis, K. Krushelnick, A. E. Dangor, R. M. Allott, R. J. Clarke, D. Neely, and P. A. Norreys. Dynamics of the critical surface in high-intensity laser-solid interactions: Modulation of the XUV harmonic spectra. *Physical Review Letters*, 88(15):155001, 2002.

[31] B. Dromey, S. Rykovanov, M. Yeung, R. Hörlein, D. Jung, D. C. Gautier, T. Dzelzainis, D. Kiefer, S. Palaniyppan, R. Shah, et al. Coherent synchrotron emission from electron nanobunches formed in relativistic laser-plasma interactions. *Nature Physics*, 8(11):804, 2012.

[32] A. Sagisaka, H. Daido, S. Nashima, S. Orimo, K. Ogura, M. Mori, A. Yogo, J. Ma, I. Daito, A. S. Pirozhkov, et al. Simultaneous generation of a proton beam and terahertz radiation in high-intensity laser and thin-foil interaction. *Applied Physics B*, 90(3-4):373–377, 2008.

[33] Y. T. Li, C. Li, M. L. Zhou, W. M. Wang, F. Du, W. J. Ding, X. X. Lin, F. Liu, Z. M. Sheng, X. Y. Peng, et al. Strong terahertz radiation from relativistic laser interaction with solid density plasmas. *Applied Physics Letters*, 100(25):254101, 2012.

[34] H. Hamster, A. Sullivan, S. Gordon, W. White, and R. W. Falcone. Subpicosecond, electromagnetic pulses from intense laser-plasma interaction. *Physical Review Letters*, 71(17):2725, 1993.

[35] W. P. Leemans, C. G. R. Geddes, J. Faure, C. Tóth, J. Van Tilborg, C. B. Schroeder, E. Esarey, G. Fubiani, D. Auerbach, B. Marcelis, et al. Observation of terahertz emission from a laser-plasma accelerated electron bunch crossing a plasma-vacuum boundary. *Physical Review Letters*, 91(7):074802, 2003.

[36] G. Q. Liao, Y. T. Li, Y. H. Zhang, H. Liu, X. L. Ge, S. Yang, W. Q. Wei, X. H. Yuan, Y. Q. Deng, B. J. Zhu, et al. Demonstration of coherent terahertz transition radiation from relativistic laser-solid interactions. *Physical Review Letters*, 116(20):205003, 2016.

[37] G. Marx. Interstellar vehicle propelled by terrestrial laser beam. *Nature*, 211(5044):22, 1966.

[38] A. Macchi, S. Veghini, and F. Pegoraro. Light sail acceleration reexamined. *Physical Review Letters*, 103(8):085003, 2009.

[39] S. V. Bulanov and V. S. Khoroshkov. Feasibility of using laser ion accelerators in proton therapy. *Plasma Physics Reports*, 28(5):453–456, 2002.

[40] M. Borghesi, D. H. Campbell, A. Schiavi, M. G. Haines, O. Willi, A. J. MacKinnon, P. Patel, L. A. Gizzi, M. Galimberti, R. J. Clarke, et al. Electric field detection in laser-plasma interaction experiments via the proton imaging technique. *Physics of Plasmas*, 9(5):2214–2220, 2002.

[41] A. J. Mackinnon, P. K. Patel, R. P. Town, M. J. Edwards, T. Phillips, S. C. Lerner, D. W. Price, D. Hicks, M. H. Key, S. Hatchett, et al. Proton radiography as an electromagnetic field and density perturbation diagnostic. *Review of Scientific Instruments*, 75(10):3531–3536, 2004.

[42] S. Kar, K. F. Kakolee, B. Qiao, A. Macchi, M. Cerchez, D. Doria, M. Geissler, P. McKenna, D. Neely, J. Osterholz, et al. Ion acceleration in multispecies targets driven by intense laser radiation pressure. *Physical Review Letters*, 109(18):185006, 2012.

[43] T. Esirkepov, M. Borghesi, S. V. Bulanov, G. Mourou, and T. Tajima. Highly efficient relativistic-ion generation in the laser-piston regime. *Physical Review Letters*, 92(17):175003, 2004.

[44] E. Lefebvre and G. Bonnaud. Transparency/opacity of a solid target illuminated by an ultrahigh-intensity laser pulse. *Physical Review Letters*, 74(11):2002, 1995.

[45] H. Sakagami and K. Mima. Anomalous penetration mechanisms of very intense laser pulses into overdense plasmas. *Physical Review E*, 54(2):1870, 1996.

[46] S. Guerin, P. Mora, J. C. Adam, A. Héron, and G. Laval. Propagation of ultraintense laser pulses through overdense plasma layers. *Physics of Plasmas*, 3(7):2693–2701, 1996.

[47] V. Vshivkov, M. Naumova, F. Pegoraro, and S. V. Bulanov. Nonlinear electrodynamics of the interaction of ultra-intense laser pulses with a thin foil. *Physics of Plasmas*, 5(7):2727–2741, 1998.

[48] F. Cattani, A. Kim, D. Anderson, and M. Lisak. Threshold of induced transparency in the relativistic interaction of an electromagnetic wave with overdense plasmas. *Physical Review E*, 62(1):1234, 2000.

[49] B. Gonzalez-Izquierdo, R. J. Gray, M. King, R. J. Dance, R. Wilson, J. McCreadie, N. M. H. Butler, R. Capdessus, S. Hawkes, J. S. Green, et al. Optically controlled dense current structures driven by relativistic plasma aperture-induced diffraction. *Nature Physics*, 12(5):505, 2016.

[50] L. Yin, B. Albright, B. M. Hegelich, K. J. Bowers, K. A. Flippo, T. J. T. Kwan, and J. C. Fernández. Monoenergetic and GeV ion acceleration from the laser breakout afterburner using ultrathin targets. *Physics of Plasmas*, 14(5):056706, 2007.

[51] A. Henig, D. Kiefer, K. Markey, D. C. Gautier, K. A. Flippo, S. Letzring, R. P. Johnson, T. Shimada, L. Yin, B. Albright, et al. Enhanced laser-driven ion acceleration in the relativistic transparency regime. *Physical Review Letters*, 103(4):045002, 2009.

[52] H. W. Powell, M. King, R. J. Gray, D. A. MacLellan, B. Gonzalez-Izquierdo, L. C. Stockhausen, G. Hicks, N. P. Dover, D. R. Rusby, D. C. Carroll, et al. Proton acceleration enhanced by a plasma jet in expanding foils undergoing relativistic transparency. *New Journal of Physics*, 17(10):103033, 2015.

[53] A. Higginson, R. J. Gray, M. King, R. J. Dance, S. D. R. Williamson, N. M. H. Butler, R. Wilson, R. Capdessus, C. Armstrong, J. S. Green, et al. Near-100 MeV protons via a laser-driven transparency-enhanced hybrid acceleration scheme. *Nature Communications*, 9(1):724, 2018.

[54] P. Zhang, C. P. Ridgers, and A. G. R. Thomas. The effect of nonlinear quantum electrodynamics on relativistic transparency and laser absorption in ultra-relativistic plasmas. *New Journal of Physics*, 17(4):043051, 2015.

[55] J. Schwinger. On gauge invariance and vacuum polarization. *Physical Review*, 82(5):664, 1951.

[56] T. Tajima and J. M. Dawson. Laser electron accelerator. *Physical Review Letters*, 43(4):267, 1979.

[57] S. P. D. Mangles, C. D. Murphy, Z. Najmudin, A. G. R. Thomas, J. L. Collier, A. E. Dangor, E. J. Divall, P. S. Foster, J. G. Gallacher, C. J. Hooker, et al. Monoenergetic beams of relativistic electrons from intense laser-plasma interactions. *Nature*, 431(7008):535, 2004.

[58] C. P. Ridgers, J. G. Kirk, R. Duclous, T. G. Blackburn, C. S. Brady, K. Bennett, T. D. Arber, and A. R. Bell. Modelling gamma-ray photon emission and pair production in high-intensity laser-matter interactions. *Journal of Computational Physics*, 260:273–285, 2014.

[59] L. L. Ji, A. Pukhov, E. N. Nerush, I. Y. Kostyukov, B. F. Shen, and K. U. Akli. Energy partition, γ-ray emission, and radiation reaction in the near-quantum electrodynamical regime of laser-plasma interaction. *Physics of Plasmas*, 21(2):023109, 2014.

[60] M. Tamburini, F. Pegoraro, A. DiPiazza, C. H. Keitel, and A. Macchi. Radiation reaction effects on radiation pressure acceleration. *New Journal of Physics.*, 12:123005, 2010.

[61] M. J. Duff, R. Capdessus, D. Del Sorbo, C. P. Ridgers, M. King, and P. McKenna. Modelling the effects of the radiation reaction force on the interaction of thin foils with ultra-intense laser fields. *Plasma Physics and Controlled Fusion*, 60(6):064006, 2018.

[62] R. Capdessus and P. McKenna. Influence of radiation reaction force on ultraintense laser-driven ion acceleration. *Physical Review E*, 91(5):053105, 2015.

[63] E. N. Nerush and I. Y. Kostyukov. Laser-driven hole boring and gamma-ray emission in high-density plasmas. *Plasma Physics and Controlled Fusion*, 57(3):035007, 2015.

[64] S. S. Bulanov, A. Brantov, V. Y. Bychenkov, V. Chvykov, G. Kalinchenko, T. Matsuoka, P. Rousseau, S. Reed, V. Yanovsky, K. Krushelnick, et al. Accelerating protons to therapeutic energies with ultraintense, ultraclean, and ultrashort laser pulses. *Medical Physics*, 35(5):1770–1776, 2008.

[65] J. G. Kirk, A. R. Bell, and I. Arka. Pair production in counter-propagating laser beams. *Plasma Physics and Controlled Fusion*, 51(8):085008, 2009.

[66] D. Del Sorbo, D. R. Blackman, R. Capdessus, K. Small, C. Slade-Lowther, W. Luo, M. J. Duff, A. P. L. Robinson, P. McKenna, Z. M. Sheng, et al. Efficient ion acceleration and dense electron-positron plasma creation in ultra-high intensity laser-solid interactions. *New Journal of Physics*, 20(3):033014, 2018.

[67] A. M. Fedotov, N. B. Narozhny, G. Mourou, and G. Korn. Limitations on the attainable intensity of high power lasers. *Physical Review Letters*, 105(8):080402, 2010.

[68] R. Capdessus, M. King, D. Del Sorbo, M. J. Duff, C. P. Ridgers, and P. McKenna. Relativistic Doppler-boosted γ-rays in High Fields. *Scientific Reports*, 8(1):9155, 2018.

[69] H. X. Chang, B. Qiao, T. W. Huang, Z. Xu, C. T. Zhou, Y. Q. Gu, X. Q. Yan, M. Zepf, and X. T. He. Brilliant petawatt gamma-ray pulse generation in quantum electrodynamic laser-plasma interaction. *Scientific Reports*, 7:45031, 2017.

[70] Institute of Physics. Synchrotron light, 2011.

[71] X. Ribeyre, E. d'Humières, O. Jansen, S. Jequier, V. T. Tikhonchuk, and M. Lobet. Pair creation in collision of γ-ray beams produced with high-intensity lasers. *Physical Review E*, 93(1):013201, 2016.

[72] O. Jansen, T. Wang, D. J. Stark, E. d'Humières, T. Toncian, and A. V. Arefiev. Leveraging extreme laser-driven magnetic fields for gamma-ray generation and pair production. *Plasma Physics and Controlled Fusion*, 60(5):054006, 2018.

[73] G. Sarri, K. Poder, J. M. Cole, W. Schumaker, A. Di Piazza, B. Reville, T. Dzelzainis, D. Doria, L. A. Gizzi, G. Grittani, et al. Generation of neutral and high-density electron-positron pair plasmas in the laboratory. *Nature Communications*, 6:6747, 2015.

[74] S. Guha, G. D. Gillen, and K. Gillen. *Light propagation in linear optical media.* CRC Press, 2013.

[75] A. Schluter. Ponderomotive action of light. In *Plasma Physics*, volume 10, page 471. IOP Publishing Ltd., 1968.

[76] H. Hora. Nonlinear confining and deconfining forces associated with the interaction of laser radiation with plasma. *The Physics of Fluids*, 12(1):182–191, 1969.

[77] J. D. Lindl and P. K. Kaw. Ponderomotive Force on Laser-Produced Plasmas. *The Physics of Fluids*, 14(2):371–377, 1971.

[78] P. Sprangle, C. M. Tang, and E. Esarey. Relativistic self-focusing of short-pulse radiation beams in plasmas. *IEEE transactions on plasma science*, 15(2):145–153, 1987.

[79] P. Sprangle, E. Esarey, J. Krall, and A. Ting. Vacuum Laser Acceleration. Technical report, Naval Research Laboratory, 1995.

[80] E. Esarey, C. B. Schroeder, and W. P. Leemans. Physics of laser-driven plasma-based electron accelerators. *Reviews of Modern Physics*, 81(3):1229, 2009.

[81] W. Yu, M. Y. Yu, J. X. Ma, Z. M. Sheng, J. Zhang, H. Daido, S. B. Liu, Z. Z. Xu, and R. X. Li. Ponderomotive acceleration of electrons at the focus of high intensity lasers. *Physical Review E*, 61(3):R2220, 2000.

[82] F. He, W. Yu, P. Lu, H. Xu, L. Qian, B. Shen, X. Yuan, R. Li, and Z. Xu. Ponderomotive acceleration of electrons by a tightly focused intense laser beam. *Physical Review E*, 68(4):046407, 2003.

[83] D. Bauer, P. Mulser, and W. H. Steeb. Relativistic ponderomotive force, uphill acceleration, and transition to chaos. *Physical Review Letters*, 75(25):4622, 1995.

[84] E. A. Startsev and C. J. McKinstrie. Multiple scale derivation of the relativistic ponderomotive force. *Physical Review E*, 55(6):7527, 1997.

[85] W. Kruer. *The physics of laser plasma interactions.* CRC Press, 2018.

[86] J. D. Jackson. *Classical electrodynamics.* John Wiley & Sons, 2007.

[87] J. Schwinger. On the classical radiation of accelerated electrons. *Physical review*, 75(12):1912, 1949.

[88] W. C. Röntgen. On a new kind of rays. *Science*, 3(59):227–231, 1896.

[89] A. Liénard. *Champ électrique et magnétique produit par une charge électrique concentrée en un point et animée d'un mouvement quelconque.* 1898.

[90] E. Wiechert. Elektrodynamische elementargesetze. *Annalen der Physik*, 309(4):667–689, 1901.

[91] M. S. Longair. *High energy astrophysics.* Cambridge university press, 2011.

[92] F. Rohrlich. *Classical charged particles.* World Scientific Publishing Company, 2007.

[93] G. B. Rybicki and A. P. Lightman. *Radiative processes in astrophysics.* John Wiley & Sons, 2008.

[94] N. P. Klepikov. Emission of photons or electron-positron pairs in magnetic fields. 26:19, 1954.

[95] A. Nikishov and V. Ritus. Radiation spectrum of an electron moving in a constant electric field. *Soviet Journal of Theoretical Physics*, 29:1093–1097, 1969.

[96] B. King, N. Elkina, and H. Ruhl. Photon polarization in electron-seeded pair-creation cascades. *Physical Review A*, 87(4):042117, 2013.

[97] A. Ilderton, B. King, and D. Seipt. High-Intensity QED beyond the Locally Constant Field Approximation. *arXiv preprint arXiv:1808.10339*, 2018.

[98] T. Erber. High-energy electromagnetic conversion processes in intense magnetic fields. *Reviews of Modern Physics*, 38(4):626, 1966.

[99] A. A. Sokolov and I. M. Ternov. Synchrotron radiation. 1966.

[100] P. A. M. Dirac. Classical theory of radiating electrons. *Proceedings of the Royal Society of London. Series A. Mathematical and Physical Sciences*, 167(929):148–169, 1938.

[101] L. Landau and E. Lifshitz. *The classical theory of fields*, volume 2. Elsevier, 2013.

[102] R. T. Hammond. Relativistic Particle Motion and Radiation Reaction in Electrodynamics. *Electronic Journal of Theoretical Physics*, 7(23), 2010.

[103] R. T. Hammond. Radiation reaction at ultra-high intensities. *Physical Review A*, 81(6):062104, 2010.

[104] D. A. Burton and A. Noble. Aspects of electromagnetic radiation reaction in strong fields. *Contemporary Physics*, 55(2):110–121, 2014.

[105] R. Capdessus, A. Noble, P. McKenna, and D. A. Jaroszynski. Role of momentum and velocity for radiating electrons. *Physical Review D*, 93(4):045034, 2016.

[106] V. I. Ritus. Quantum effects of the interaction of elementary particles with an intense electromagnetic field. *Journal of Russian Laser Research*, 6(5):497–617, 1985.

[107] A. Di Piazza, K. Z. Hatsagortsyan, and C. H. Keitel. Quantum radiation reaction effects in multiphoton compton scattering. *Physical Review Letters*, 105(22):220403, 2010.

[108] M. Abraham and A. Föppl. *Theorie der Elektrizität: Bd. Elektromagnetische Theorie der Strahlung*, volume 2. BG Teubner, 1905.

[109] H. A. Lorentz. *The theory of electrons and its applications to the phenomena of light and radiant heat.* Teubner, Leipzig, 1909.

[110] V. S. Krivitskii and V. N. Tsytovich. Average radiation-reaction force in quantum electrodynamics. *Soviet Physics Uspekhi*, 34(3):250, 1991.

[111] A. Ilderton and G. Torgrimsson. Radiation reaction in strong field QED. *Physics Letters B*, 725(4-5):481–486, 2013.

[112] H. Spohn. *Dynamics of charged particles and their radiation field.* Cambridge University Press, 2004.

[113] A. R. Bell and J. G. Kirk. Possibility of prolific pair production with high-power lasers. *Physical Review Letters*, 101(20):200403, 2008.

[114] N. Neitz and A. Di Piazza. Stochasticity effects in quantum radiation reaction. *Physical Review Letters*, 111(5):054802, 2013.

[115] V. Dinu, C. Harvey, A. Ilderton, M. Marklund, and G. Torgrimsson. Quantum radiation reaction: from interference to incoherence. *Physical Review Letters*, 116(4):044801, 2016.

[116] R. Duclous, J. G. Kirk, and A. R. Bell. Monte carlo calculations of pair production in high-intensity laser-plasma interactions. *Plasma Physics and Controlled Fusion*, 53(1):015009, 2010.

[117] T. G. Blackburn, C. P. Ridgers, J. G. Kirk, and A. R. Bell. Quantum radiation reaction in laser–electron-beam collisions. *Physical Review letters*, 112(1):015001, 2014.

[118] F. Niel, C. Riconda, F. Amiranoff, R. Duclous, and M. Grech. From quantum to classical modeling of radiation reaction: A focus on stochasticity effects. *Physical Review E*, 97(4):043209, 2018.

[119] V. N. Baier. Processes involved in the motion of high energy particles in a magnetic field. *Soviet Journal of Theoretical Physics*, 26:854, 1968.

[120] C. P. Ridgers, T. G. Blackburn, D. Del Sorbo, L. E. Bradley, C. Slade-Lowther, C. D. Baird, S. P. D. Mangles, P. McKenna, M. Marklund, C. D. Murphy, et al. Signatures of quantum effects on radiation reaction in laser-electron-beam collisions. *Journal of Plasma Physics*, 83(5), 2017.

[121] C. S. Shen and D. White. Energy straggling and radiation reaction for magnetic bremsstrahlung. *Physical Review Letters*, 28(7):455, 1972.

[122] I. V. Sokolov, N. M. Naumova, J. A. Nees, and G. A. Mourou. Pair creation in QED-strong pulsed laser fields interacting with electron beams. *Physical Review Letters*, 105(19):195005, 2010.

[123] N. V. Elkina, A. M. Fedotov, I. Y. Kostyukov, M. V. Legkov, N. B. Narozhny, E. N. Nerush, and H. Ruhl. QED cascades induced by circularly polarized laser fields. *Physical Review Special Topics-Accelerators and Beams*, 14(5):054401, 2011.

[124] D. Seipt, D. Del Sorbo, C. P. Ridgers, and A. G. R. Thomas. Theory of radiative electron polarization in strong laser fields. *Physical Review A*, 98(2):023417, 2018.

[125] D. Del Sorbo, D. Seipt, T. G. Blackburn, A. G. R. Thomas, C. D. Murphy, J. G. Kirk, and C. P. Ridgers. Spin polarization of electrons by ultraintense lasers. *Physical Review A*, 96(4):043407, 2017.

[126] A. G. R. Thomas, C. P. Ridgers, S. S. Bulanov, B. J. Griffin, and S. P. D. Mangles. Strong radiation-damping effects in a gamma-ray source generated by the interaction of a high-intensity laser with a wakefield-accelerated electron beam. *Physical Review X*, 2(4):041004, 2012.

[127] C. Arran, J. M. Cole, E. Gerstmayr, T. G. Blackburn, S. P. D. Mangles, and C. P. Ridgers. Optimal Parameters for Radiation Reaction Experiments. *arXiv preprint arXiv:1901.09015*, 2019.

[128] M. Vranic, T. Grismayer, R. A Fonseca, and L. O. Silva. Electron-positron cascades in multiple-laser optical traps. *Plasma Physics and Controlled Fusion*, 59(1):014040, 2016.

[129] A. Di Piazza, K. Z. Hatsagortsyan, and C. H. Keitel. Strong signatures of radiation reaction below the radiation-dominated regime. *Physical Review Letters*, 102(25):254802, 2009.

[130] J. M. Cole, K. T. Behm, E. Gerstmayr, T. G. Blackburn, J. C. Wood, C. D. Baird, M. J. Duff, C. Harvey, A. Ilderton, A. S. Joglekar, et al. Experimental evidence of radiation reaction in the collision of a high-intensity laser pulse with a laser-wakefield accelerated electron beam. *Physical Review X*, 8(1):011020, 2018.

[131] K. Poder, M. Tamburini, G. Sarri, A. Di Piazza, S. Kuschel, C. D. Baird, K. T. Behm, S. Bohlen, J. M. Cole, D. J. Corvan, et al. Experimental signatures of the quantum nature of radiation reaction in the field of an ultraintense laser. *Physical Review X*, 8(3):031004, 2018.

[132] K. T. Behm, J. M. Cole, A. S. Joglekar, E. Gerstmayr, J. C. Wood, C. D. Baird, T. G. Blackburn, M. J. Duff, C. Harvey, A. Ilderton, et al. A spectrometer for ultrashort gamma-ray pulses with photon energies greater than 10 MeV. *Review of Scientific Instruments*, 89(11):113303, 2018.

[133] G. M. Samarin, M. Zepf, and G. Sarri. Radiation reaction studies in an all-optical set-up: experimental limitations. *Journal of Modern Optics*, 65(11):1362–1369, 2018.

[134] G. V. Dunne, H. Gies, and R. Schützhold. Catalysis of Schwinger vacuum pair production. *Physical Review D*, 80(11):111301, 2009.

[135] H. Bethe and W. Heitler. On the stopping of fast particles and on the creation of positive electrons. *Proceedings of the Royal Society of London. Series A, Containing Papers of a Mathematical and Physical Character*, 146(856):83–112, 1934.

[136] K. Krajewska, C. Müller, and J. Z. Kamiński. Bethe-Heitler pair production in ultrastrong short laser pulses. *Physical Review A*, 87(6):062107, 2013.

[137] H. Chen, S. C. Wilks, J. D. Bonlie, E. Liang, J. Myatt, D. F. Price, D. D. Meyerhofer, and P. Beiersdorfer. Relativistic positron creation using ultra-intense short pulse lasers. *Physical Review Letters*, 102(10):105001, 2009.

[138] A. Ilderton. Trident pair production in strong laser pulses. *Physical Review Letters*, 106:020404, 2011.

[139] C. Bamber, S. J. Boege, T. Koffas, T. Kotseroglou, A. C. Melissinos, D. D. Meyerhofer, D. A. Reis, W. Ragg, C. Bula, K. T. McDonald, et al. Studies of nonlinear QED in collisions of 46.6 GeV electrons with intense laser pulses. *Physical Review D*, 60(9):092004, 1999.

[140] V. Dinu and G. Torgrimsson. Trident pair production in plane waves: Coherence, exchange, and spacetime inhomogeneity. *Physical Review D*, 97(3):036021, 2018.

[141] D. A. Gryaznykh, Y. Z. Kandiev, and V. A. Lykov. Estimates of electron-positron pair production in the interaction of high-power laser radiation with high-Z targets. *Journal of Experimental and Theoretical Physics Letters*, 67(4):257–262, 1998.

[142] G. J. Williams, D. Barnak, G. Fiksel, A. Hazi, S. Kerr, C. Krauland, A. Link, M. E. Manuel, S. R. Nagel, J. Park, et al. Target material dependence of positron generation from high intensity laser-matter interactions. *Physics of Plasmas*, 23(12):123109, 2016.

[143] H. R. Reiss. Absorption of light by light. *Journal of Mathematical Physics*, 3(1):59–67, 1962.

[144] K. Krajewska and J. Z. Kamiński. Breit-Wheeler process in intense short laser pulses. *Physical Review A*, 86(5):052104, 2012.

[145] A. I. Titov, B. Kampfer, H. Takabe, and A. Hosaka. Breit-Wheeler process in very short electromagnetic pulses. *Physical Review A*, 87(4):042106, 2013.

[146] D. L. Burke, F. C. Field, G. Horton-Smith, J. E. Spencer, D. Walz, S. C. Berridge, W. M. Bugg, K. Shmakov, A. W. Weidemann, C. Bula, et al. Positron production in multiphoton light-by-light scattering. *Physical Review Letters*, 79(9):1626, 1997.

[147] H. Z. Li, T. P. Yu, J. J. Liu, Y. Yin, X. L. Zhu, R. Capdessus, F. Pegoraro, Z. M. Sheng, P. McKenna, and F. Q. Shao. Ultra-bright γ-ray emission and dense positron production from two laser-driven colliding foils. *Scientific Reports*, 7(1):17312, 2017.

[148] G. Breit and J. A. Wheeler. Collision of two light quanta. *Physical Review*, 46(12):1087, 1934.

[149] V. B. Berestetskii, L. D. Landau, E. M. Lifshitz, and L. P. Pitaevskii. *Quantum electrodynamics*, volume 4. Butterworth-Heinemann, 1982.

[150] O. J. Pike, F. Mackenroth, E. G. Hill, and S. J. Rose. A photon-photon collider in a vacuum hohlraum. *Nature Photonics*, 8(6):434, 2014.

[151] S. S. Bulanov, C. B. Schroeder, E. Esarey, and W. P. Leemans. Electromagnetic cascade in high-energy electron, positron, and photon interactions with intense laser pulses. *Physical Review A*, 87(6):062110, 2013.

[152] N. B. Narozhny and A. M. Fedotov. Quantum-electrodynamic cascades in intense laser fields. *Physics-Uspekhi*, 58(1):95, 2015.

[153] T. Grismayer, M. Vranic, J. L. Martins, R. A. Fonseca, and L. O. Silva. Laser absorption via quantum electrodynamics cascades in counter propagating laser pulses. *Physics of Plasmas*, 23(5):056706, 2016.

[154] M. Roth, T. E. Cowan, M. H. Key, S. P. Hatchett, C. Brown, W. Fountain, J. Johnson, D. M. Pennington, R. A. Snavely, S. C. Wilks, et al. Fast ignition by intense laser-accelerated proton beams. *Physical Review Letters*, 86(3):436, 2001.

[155] M. Tabak, D. S. Clark, S. P. Hatchett, M. H. Key, B. F. Lasinski, R. A. Snavely, S. C. Wilks, R. P. J. Town, R. Stephens, E. M. Campbell, et al. Review of progress in fast ignition. *Physics of Plasmas*, 12(5):057305, 2005.

[156] E. Ahedo. Plasmas for space propulsion. *Plasma Physics and Controlled Fusion*, 53(12):124037, 2011.

[157] J. W. Coburn and H. F. Winters. Plasma etching-A discussion of mechanisms. *Journal of Vacuum Science and Technology*, 16(2):391–403, 1979.

[158] D. M. Manos and D. L. Flamm. Plasma Etching: an Introduction (Retroactive Coverage). *Academic Press, Inc. (United States)*, page 476, 1989.

[159] P. Michel, L. Divol, D. Turnbull, and J. D. Moody. Dynamic control of the polarization of intense laser beams via optical wave mixing in plasmas. *Physical Review Letters*, 113(20):205001, 2014.

[160] D. J. Stark, C. Bhattacharjee, A. V. Arefiev, T. Toncian, R. D. Hazeltine, and S. Mahajan. Relativistic plasma polarizer: Impact of temperature anisotropy on relativistic transparency. *Physical Review Letters*, 115(2):025002, 2015.

[161] D. Turnbull, P. Michel, T. Chapman, E. Tubman, B. B. Pollock, C. Y. Chen, C. Goyon, J. S. Ross, L. Divol, N. Woolsey, et al. High power dynamic polarization control using plasma photonics. *Physical Review Letters*, 116(20):205001, 2016.

[162] F. F. Chen. *Introduction to Plasma Physics and Controlled Fusion*, volume 1. Springer, 1984.

[163] R. O. Dendy. *Plasma Physics: An Introductory Course*. Cambridge University Press, 1995.

[164] I. P. Shkarofsky, T. W. Johnston, and M. P. Bachynski. *The particle kinetics of plasmas*. Reading, Mass.: Addison-Wesley Publishing Company, 1966.

[165] E. M. Lifschitz and L. P. Pitajewski. *Physical kinetics*. 1983.

[166] Y. L. Klimontovich. Relativistic transport equations for a plasma. *Soviet Journal of Theoretical Physics*, 10(3):524–530, 1960.

[167] D. Grasso. Fluid equations: derivation and simulation. In *Plasma Modeling*, 2053-2563, pages 6–1 to 6–24. IOP Publishing, 2016.

[168] E. S. Weibel. Anomalous skin effect in a plasma. *The Physics of Fluids*, 10(4):741–748, 1967.

[169] Bruno González-Izquierdo. Collective charged particle dynamics in relativistically transparent laser-plasma interactions, 2016.

[170] A. Macchi, S. Veghini, T. V. Liseykina, and F. Pegoraro. Radiation pressure acceleration of ultrathin foils. *New Journal of Physics*, 12(4):045013, 2010.

[171] L. Yin, B. J. Albright, K. J. Bowers, D. Jung, J. C. Fernández, and B. M. Hegelich. Three-dimensional dynamics of breakout afterburner ion acceleration using high-contrast short-pulse laser and nanoscale targets. *Physical Review Letters*, 107(4):045003, 2011.

[172] P. Mora. Theoretical model of absorption of laser light by a plasma. *The Physics of Fluids*, 25(6):1051–1056, 1982.

[173] P. Mora. Plasma expansion into a vacuum. *Physical Review Letters*, 90(18):185002, 2003.

[174] F. Brunel. Not-so-resonant, resonant absorption. *Physical Review Letters*, 59(1):52, 1987.

[175] W. L. Kruer and K. Estabrook. j×B heating by very intense laser light. *The Physics of Fluids*, 28(1):430–432, 1985.

[176] F. A. Zander. (13):15, 1924.

[177] J. F. L. Simmons and C. R. McInnes. Was Marx right? or: How efficient are laser driven interstellar spacecraft? *American Journal of Physics*, 61(3):205–207, 1993.

[178] L. Ji, A. Pukhov, and B. Shen. Ion acceleration in the 'dragging field'of a light-pressure-driven piston. *New Journal of Physics*, 16(6):063047, 2014.

[179] A. P. L. Robinson, P. Gibbon, M. Zepf, S. Kar, R. G. Evans, and C. Bellei. Relativistically correct hole-boring and ion acceleration by circularly polarized laser pulses. *Plasma Physics and Controlled Fusion*, 51(2):024004, 2009.

[180] S. G. Rykovanov, J. Schreiber, J. Meyer ter Vehn, C. Bellei, A. Henig, H. C. Wu, and M. Geissler. Ion acceleration with ultra-thin foils using elliptically polarized laser pulses. *New Journal of Physics*, 10(11):113005, 2008.

[181] A. Henig, S. Steinke, M. Schnurer, T. Sokollik, R. Horlein, D. Kiefer, D. Jung, J. Schreiber, B. M. Hegelich, X. Q. Yan, et al. Radiation-pressure acceleration of ion beams driven by circularly polarized laser pulses. *Physical Review Letters*, 103(24):245003, 2009.

[182] A. Macchi, T. V. Liseikina, S. Tuveri, and S. Veghini. Theory and simulation of ion acceleration with circularly polarized laser pulses. *Comptes Rendus Physique*, 10(2-3):207–215, 2009.

[183] F. Dollar, C. Zulick, A. G. R. Thomas, Y. Chvykov, J. Davis, G. Kalinchenko, T. Matsuoka, C. McGuffey, G. M. Petrov, L. Willingale, et al. Finite spot effects on radiation pressure acceleration from intense high-contrast laser interactions with thin targets. *Physical Review Letters*, 108(17):175005, 2012.

[184] S. Kar, K. F. Kakolee, M. Cerchez, D. Doria, A. Macchi, P. McKenna, D. Neely, J. Osterholz, K. Quinn, B. Ramakrishna, et al. Experimental investigation of hole boring and light sail regimes of RPA by varying laser and target parameters. *Plasma Physics and Controlled Fusion*, 55(12):124030, 2013.

[185] S. Steinke, P. Hilz, M. Schnurer, G. Priebe, J. Branzel, F. Abicht, D. Kiefer, C. Kreuzer, T. Ostermayr, J. Schreiber, et al. Stable laser-ion acceleration in the light sail regime. *Physical Review Special Topics-Accelerators and Beams*, 16(1):011303, 2013.

[186] T. V. Liseykina, M. Borghesi, A. Macchi, and S. Tuveri. Radiation pressure acceleration by ultraintense laser pulses. *Plasma Physics and Controlled Fusion*, 50(12):124033, 2008.

[187] M. Grech, S. Skupin, R. Nuter, L. Gremillet, and E. Lefebvre. High-quality ion

beams by irradiating a nano-structured target with a petawatt laser pulse. *New Journal of Physics*, 11(9):093035, 2009.

[188] B. Qiao, M. Zepf, M. Borghesi, B. Dromey, M. Geissler, A. Karmakar, and P. Gibbon. Radiation-pressure acceleration of ion beams from nanofoil targets: The leaky light-sail regime. *Physical Review Letters*, 105(15):155002, 2010.

[189] A. Macchi, F. Cattani, T. V. Liseykina, and F. Cornolti. Laser acceleration of ion bunches at the front surface of overdense plasmas. *Physical Review Letters*, 94(16):165003, 2005.

[190] T. Schlegel, N. Naumova, V. T. Tikhonchuk, C. Labaune, I. V. Sokolov, and G. Mourou. Relativistic laser piston model: Ponderomotive ion acceleration in dense plasmas using ultraintense laser pulses. *Physics of Plasmas*, 16(8):083103, 2009.

[191] N. Naumova, T. Schlegel, V. T. Tikhonchuk, C. Labaune, I. V. Sokolov, and G. Mourou. Hole boring in a DT pellet and fast-ion ignition with ultraintense laser pulses. *Physical Review Letters*, 102(2):025002, 2009.

[192] A. P. L. Robinson. Production of high energy protons with hole-boring radiation pressure acceleration. *Physics of Plasmas*, 18(5):056701, 2011.

[193] C. Palmer, N. P. Dover, I. Pogorelsky, M. Babzien, G. I. Dudnikova, M. Ispiriyan, M. N. Polyanskiy, J. Schreiber, P. Shkolnikov, V. Yakimenko, et al. Monoenergetic proton beams accelerated by a radiation pressure driven shock. *Physical Review Letters*, 106(1):014801, 2011.

[194] D. W. Forslund and J. P. Freidberg. Theory of laminar collisionless shocks. *Physical Review Letters*, 27(18):1189, 1971.

[195] C. E. Max, J. Arons, and A. B. Langdon. Self-modulation and self-focusing of electromagnetic waves in plasmas. *Physical Review Letters*, 33(4):209, 1974.

[196] P. Monot, T. Auguste, P. Gibbon, F. Jakober, G. Mainfray, A. Dulieu, J. Malka, G. Malka, and J. L. Miquel. Experimental demonstration of relativistic self-channeling of a multi-terawatt laser pulse in an underdense plasma. *Physical Review Letters*, 74(15):2953, 1995.

[197] E. Yablonovitch. Self-phase modulation and short-pulse generation from laser-breakdown plasmas. *Physical Review A*, 10(5):1888, 1974.

[198] D. Strickland and G. Mourou. Compression of amplified chirped optical pulses. *Optics Communications*, 55(6):447–449, 1985.

[199] The Nobel Prize. The Nobel Prize in Physics 2018. https://www.nobelprize.org/prizes/physics/2018/summary/.

[200] I. Jovanovic, J. R. Schmidt, and C. A. Ebbers. Optical parametric chirped-pulse amplification in periodically poled KTiOPO 4 at 1053 nm. *Applied Physics Letters*, 83(20):4125–4127, 2003.

[201] D. Herrmann, L. Veisz, R. Tautz, F. Tavella, K. Schmid, V. Pervak, and F. Krausz. Generation of sub-three-cycle, 16 TW light pulses by using noncollinear optical parametric chirped-pulse amplification. *Optics Letters*, 34(16):2459–2461, 2009.

[202] S. Witte and S. E. Eikema. Ultrafast optical parametric chirped-pulse amplification. *IEEE Journal of Selected Topics in Quantum Electronics*, 18(1):296–307, 2012.

[203] A. Dubietis, G. Jonušauskas, and A. Piskarskas. Powerful femtosecond pulse generation by chirped and stretched pulse parametric amplification in BBO crystal. *Optics Communications*, 88(4-6):437–440, 1992.

[204] D. N. Papadopoulos, P. Ramirez, K. Genevrier, L. Ranc, N. Lebas, A. Pellegrina, C. Le Blanc, P. Monot, L. Martin, J. P. Zou, et al. High-contrast 10 fs OPCPA-based front end for multi-PW laser chains. *Optics Letters*, 42(18):3530–3533, 2017.

[205] C. Hernandez-Gomez, J. L. Collier, D. Canny, O. Chekhlov, R. J. Clarke, M. Dunne, M. Galimberti, S. Hancock, R. Heathcote, P. Holligan, et al. The vulcan 10 PW OPCPA Project. *CLF Annual Report*, 2007:210–1, 2006.

[206] C. J. Hooker, J. L. Collier, O. Chekhlov, R. Clarke, E. Divall, K. Ertel, B. Fell, P. Foster, S. Hancock, A. Langley, et al. The Astra Gemini project-A dual-beam petawatt Ti: Sapphire laser system. In *Journal de Physique IV (Proceedings)*, volume 133, pages 673–677. EDP sciences, 2006.

[207] C. Hooker, S. Blake, O. Chekhlov, R. J. Clarke, J. L. Collier, E. J. Divall, K. Ertel, P. S. Foster, S. J. Hawkes, P. Holligan, et al. Commissioning the Astra Gemini petawatt Ti: sapphire laser system. In *Conference on Lasers and Electro-Optics*. Optical Society of America, 2008.

[208] G. Mourou, G. Korn, W. Sandner, and J. L. Collier. Eli whitebook. *Science and Technology with Ultra-Intense Lasers*, 2011.

[209] G. Mourou and T. Tajima. The extreme light infrastructure: optics' next horizon. *Optics and Photonics News*, 22(7):47–51, 2011.

[210] K. Ertel, S. Banerjee, P. D. Mason, P. J. Phillips, C. Hernandez-Gomez, and J. L. Collier. The DiPOLE project: towards high energy, high repetition rate diode pumped lasers. In *Conference on Lasers and Electro-Optics/Pacific Rim*. Optical Society of America, 2013.

[211] D. N. Papadopoulos, J. P. Zou, C. Le Blanc, G. Chériaux, P. Georges, F. Druon, G. Mennerat, P. Ramirez, L. Martin, A. Fréneaux, et al. The Apollon 10 PW laser: experimental and theoretical investigation of the temporal characteristics. *High Power Laser Science and Engineering*, 4, 2016.

[212] C. Ziener, P. S. Foster, E. J. Divall, C. J. Hooker, M. H. R. Hutchinson, A. J. Langley, and D. Neely. Specular reflectivity of plasma mirrors as a function of intensity, pulse duration, and angle of incidence. *Journal of Applied Physics*, 93(1):768–770, 2003.

[213] B. Dromey, S. Kar, M. Zepf, and P. Foster. The plasma mirror—a subpicosecond optical switch for ultrahigh power lasers. *Review of Scientific Instruments*, 75(3):645–649, 2004.

[214] C. Thaury, F. Quéré, J. P. Geindre, A. Levy, T. Ceccotti, P. Monot, M. Bougeard, F. Réau, P. d'Oliveira, P. Audebert, et al. Plasma mirrors for ultrahigh-intensity optics. *Nature Physics*, 3(6):424, 2007.

[215] M. Nakatsutsumi, A. Kon, S. Buffechoux, P. Audebert, J. Fuchs, and R. Kodama. Fast focusing of short-pulse lasers by innovative plasma optics toward extreme intensity. *Optics Letters*, 35(13):2314–2316, 2010.

[216] R. Wilson, M. King, R. J. Gray, D. C. Carroll, R. J. Dance, C. Armstrong, S. J. Hawkes, R. J. Clarke, D. J. Robertson, D. Neely, et al. Ellipsoidal plasma mirror focusing of high power laser pulses to ultra-high intensities. *Physics of Plasmas*, 23(3):033106, 2016.

[217] E. Liang, T. Clarke, A. Henderson, W. Fu, W. Lo, D. Taylor, P. Chaguine, S. Zhou, Y. Hua, X. Cen, et al. High e+/e- ratio dense pair creation with 10 21 W/cm2 laser irradiating solid targets. *Scientific Reports*, 5:13968, 2015.

[218] J. P. Zou et al. Design and current progress of the Apollon 10 PW project. *High Power Laser Science and Engineering*, 3, 2015.

[219] S. Gales, K. A. Tanaka, D. L. Balabanski, F. Negoita, D. Stutman, O. Tesileanu, C. A. Ur, D. Ursescu, I. Andrei, S. Ataman, et al. The extreme light infrastructure-nuclear physics (ELI-NP) facility: new horizons in physics with 10 PW ultra-intense lasers and 20 MeV brilliant gamma beams. *Reports on Progress in Physics*, 81(9):094301, 2018.

[220] D. Habs, T. Tajima, and V. Zamfir. Extreme light infrastructure: New horizons for photon physics in Europe. *Nuclear Physics News*, 21(1):23–29, 2011.

[221] N. V. Zamfir. Extreme Light Infrastructure-Nuclear Physics (ELI-NP) European Research Centre. In *EPJ Web of Conferences*, volume 66, page 11043. EDP Sciences, 2014.

[222] N. V. Zamfir. Nuclear physics with 10 PW laser beams at extreme light infrastructure-nuclear physics (ELI-NP). *The European Physical Journal Special Topics*, 223(6):1221–1227, 2014.

[223] H. Zhirong et al. Brightness and coherence of synchrotron radiation and FELs. Technical report, SLAC National Accelerator Lab., Menlo Park, CA (United States), 2013.

[224] G. Geloni, E. Saldin, L. Samoylova, E. Schneidmiller, H. Sinn, T. Tschentscher, and M. Yurkov. Coherence properties of the European XFEL. *New Journal of Physics*, 12(3):035021, 2010.

[225] G. A. Mourou, N. J. Fisch, V. M. Malkin, Z. Toroker, E. A. Khazanov, A. M. Sergeev, T. Tajima, and B. Le Garrec. Exawatt-Zettawatt pulse generation and applications. *Optics Communications*, 285(5):720–724, 2012.

[226] T. Tajima and G. Mourou. Zettawatt-exawatt lasers and their applications in ultrastrong-field physics. *Physical Review Special Topics-Accelerators and Beams*, 5(3):031301, 2002.

[227] M. Maier, W. Kaiser, and J. A. Giordmaine. Backward stimulated Raman scattering. *Physical Review*, 177(2):580, 1969.

[228] G. Vieux, S. Cipiccia, D. W. Grant, N. Lemos, P. Grant, C. Ciocarlan, B. Ersfeld, M. S. Hur, P. Lepipas, G. G. Manahan, et al. An ultra-high gain and efficient amplifier based on Raman amplification in plasma. *Scientific Reports*, 7(1):2399, 2017.

[229] V. V. Lozhkarev, G. I. Freidman, V. N. Ginzburg, E. V. Katin, E. A. Khazanov, A. V. Kirsanov, G. A. Luchinin, A. N. Mal'Shakov, M. A. Martyanov, O. V. Palashov, et al. Compact 0.56 petawatt laser system based on optical parametric chirped pulse amplification in KD* P crystals. *Laser Physics Letters*, 4(6):421–427, 2007.

[230] S. E. Segre. A review of plasma polarimetry-theory and methods. *Plasma Physics and Controlled Fusion*, 41(2):R57, 1999.

[231] D. Clarke and J. F. Grainger. Polarized light and optical measurement. *American Journal of Physics*, 40:1055–1056, 1971.

[232] I. H. Hutchinson. Principles of plasma diagnostics. *Cambridge Press*, 1987.

[233] E. Hecht and A. Zajac. Optics, 2002.

[234] T. Mu, C. Zhang, and R. Liang. Demonstration of a snapshot full-Stokes division-of-aperture imaging polarimeter using Wollaston prism array. *Journal of Optics*, 17(12):125708, 2015.

[235] T. Mu, Z. Chen, C. Zhang, and R. Liang. Optimal configurations of full-Stokes polarimeter with immunity to both Poisson and Gaussian noise. *Journal of Optics*, 18(5):055702, 2016.

[236] J. D. Perreault. Triple Wollaston-prism complete-Stokes imaging polarimeter. *Optics Letters*, 38(19):3874–3877, 2013.

[237] H. Padda, M. King, R. J. Gray, H. W. Powell, B. Gonzalez-Izquierdo, L. C. Stockhausen, R. Wilson, D. C. Carroll, R. J. Dance, D. A. MacLellan, et al. Intra-pulse transition between ion acceleration mechanisms in intense laser-foil interactions. *Physics of Plasmas*, 23(6):063116, 2016.

[238] C. K. Birdsall and B. A. Langdon. *Plasma physics via computer simulation.* CRC press, 2004.

[239] T. D. Arber, K. Bennett, C. S. Brady, A. Lawrence-Douglas, M. G. Ramsay, N. J. Sircombe, P. Gillies, R. G. Evans, H. Schmitz, A. R. Bell, et al. Contemporary particle-in-cell approach to laser-plasma modelling. *Plasma Physics and Controlled Fusion*, 57(11):113001, 2015.

[240] K. Yee. Numerical solution of initial boundary value problems involving Maxwell's equations in isotropic media. *IEEE Transactions on antennas and propagation*, 14(3):302–307, 1966.

[241] J. P. Boris. Relativistic plasma simulation-optimization of a hybrid code. In *Proceedings of the 4th Conference on Numerical Simulations of Plasmas*, pages 3–67, 1970.

[242] R. W. Hockney. Measurements of collision and heating times in a two-dimensional thermal computer plasma. *Journal of Computational Physics*, 8(1):19–44, 1971.

[243] R. Capdessus, M. Lobet, E. d'Humieres, and V. T. Tikhonchuk. γ-ray generation enhancement by the charge separation field in laser-target interaction in the radiation dominated regime. *Physics of Plasmas*, 21(12):123120, 2014.

[244] R. Pantell, G. Soncini, and H. Puthoff. Stimulated photon-electron scattering. *IEEE Journal of Quantum Electronics*, 4(11):905–907, 1968.

[245] M. J. Madey. Stimulated emission of bremsstrahlung in a periodic magnetic field. *Journal of Applied Physics*, 42(5):1906–1913, 1971.

[246] V. N. Baier, V. M. Katkov, A. I. Milstein, and V. M. Strakhovenko. On the Theory of Quantum Processes in the Field of an Intense Electromagnetic Wave. *Soviet Journal of Theoretical Physics*, 42:400, 1976.

[247] A. Di Piazza, M. Tamburini, S. Meuren, and C. H. Keitel. Improved local-constant-field approximation for strong-field QED codes. *arXiv preprint arXiv:1811.05834*, 2018.

[248] B. Gonzalez-Izquierdo, R. J. Gray, M. King, R. Wilson, R. J. Dance, H. Powell, D. A. MacLellan, J. McCreadie, N. M. H. Butler, S. Hawkes, et al. Influence of laser polarization on collective electron dynamics in ultraintense laser-foil interactions. *High Power Laser Science and Engineering*, 4, 2016.

[249] B. Gonzalez-Izquierdo, M. King, R. J. Gray, R. Wilson, R. J. Dance, H. Powell, D. A. Maclellan, J. McCreadie, N. M. H. Butler, S. Hawkes, et al. Towards optical polarization control of laser-driven proton acceleration in foils undergoing relativistic transparency. *Nature Communications*, 7:12891, 2016.

[250] B. Gonzalez-Izquierdo, R. Capdessus, M. King, R. J. Gray, R. Wilson, R. J. Dance, J. McCreadie, N. M. H. Butler, S. Hawkes, J. Green, et al. Radiation Pressure-Driven Plasma Surface Dynamics in Ultra-Intense Laser Pulse Interactions with Ultra-Thin Foils. *Applied Sciences*, 8(3):336, 2018.

[251] G. Shvets, N. J. Fisch, A. J. Pukhov, and J. Meyer ter Vehn. Superradiant amplification of an ultrashort laser pulse in a plasma by a counterpropagating pump. *Physical Review Letters*, 81(22):4879, 1998.

[252] J. Ren, W. Cheng, S. Li, and S. Suckewer. A new method for generating ultraintense and ultrashort laser pulses. *Nature Physics*, 3(10):732, 2007.

[253] R. Trines, F. Fiuza, R. Bingham, R. A. Fonseca, L. O. Silva, R. A. Cairns, and P. A. Norreys. Simulations of efficient Raman amplification into the multi-petawatt regime. *Nature Physics*, 7(1):87, 2011.

[254] V. M. Malkin, G. Shvets, and N. J. Fisch. Fast compression of laser beams to highly overcritical powers. *Physical Review Letters*, 82(22):4448, 1999.

[255] A. P. L. Robinson, M. Zepf, S. Kar, R. G. Evans, and C. Bellei. Radiation pressure acceleration of thin foils with circularly polarized laser pulses. *New Journal of Physics*, 10(1):013021, 2008.

[256] T. V. Liseikina and A. Macchi. Features of ion acceleration by circularly polarized laser pulses. *Applied Physics Letters*, 91(17):171502, 2007.

[257] E. Cormier-Michel, E. Esarey, C. G. R. Geddes, C. B. Schroeder, K. Paul, P. J. Mullowney, J. R. Cary, and W. P. Leemans. Control of focusing fields in laser-plasma accelerators using higher-order modes. *Physical Review Special Topics-Accelerators and Beams*, 14(3):031303, 2011.

[258] J. Vieira and J. T. Mendonça. Nonlinear laser driven donut wakefields for positron and electron acceleration. *Physical Review Letters*, 112(21):215001, 2014.

[259] J. Vieira, J. T. Mendonça, and F. Quéré. Optical control of the topology of laser-plasma accelerators. *Physical Review Letters*, 121(5):054801, 2018.

[260] G. B. Zhang, M. Chen, J. Luo, M. Zeng, T. Yuan, J. Y. Yu, Y. Y. Ma, T. P. Yu, L. L. Yu, S. M. Weng, et al. Acceleration of on-axis and ring-shaped electron beams in wakefields driven by Laguerre-Gaussian pulses. *Journal of Applied Physics*, 119(10):103101, 2016.

[261] W. Wang, B. Shen, X. Zhang, L. Zhang, Y. Shi, and Z. Xu. Hollow screw-like drill in plasma using an intense Laguerre-Gaussian laser. *Scientific Reports*, 5:8274, 2015.

[262] C. Baumann and A. M. Pukhov. Generation of attosecond electron packets in the interaction of ultraintense Laguerre-Gaussian laser beams with plasma. *Quantum Electronics*, 47(3):194, 2017.

[263] A. S. Firouzjaei and B. Shokri. Trapping and acceleration of hollow electron and positron bunch in a quasi-linear donut wakefield. *Physics of Plasmas*, 24(1):013107, 2017.

[264] J. W. Wang, C. B. Schroeder, R. Li, M. Zepf, and S. G. Rykovanov. Plasma channel undulator excited by high-order laser modes. *Scientific Reports*, 7(1):16884, 2017.

[265] A. Gonoskov, A. Bashinov, I. Gonoskov, C. Harvey, A. Ilderton, A. Kim, M. Marklund, G. Mourou, and A. Sergeev. Anomalous radiative trapping in laser fields of extreme intensity. *Physical Review Letters*, 113(1):014801, 2014.

[266] C. Harvey and M. Marklund. Radiation damping in pulsed Gaussian beams. *Physical Review A*, 85(1):013412, 2012.

[267] R. Espinosa-Luna, G. López-Morales, V. M. Rico-Botero, and E. Aguilar-Fernández. Spatial average symmetry associated to unconventional polarization. *Revista Mexicana de Física*, 63(2):205–210, 2017.

[268] S. C. Wilks, W. L. Kruer, M. Tabak, and A. B. Langdon. Absorption of ultra-intense laser pulses. *Physical Review Letters*, 69(9):1383, 1992.

[269] V. L. Ginsburg. Radiation of a uniformly moving electron due to its transition from one medium into another. *Soviet Journal of Theoretical Physics*, 16:15–28, 1946.

[270] V. L. Ginzburg. Transition radiation and transition scattering. *Physica Scripta*, 1982(T2A):182, 1982.

[271] B. M. Bolotovskii, V. A. Davydov, and V. E. Rok. The emission of electromagnetic waves in the case of a smooth variation of parameters of a radiating system. *Soviet Physics Uspekhi*, 25(3):167, 1982.

[272] R. J. Gray, X. H. Yuan, D. C. Carroll, C. M. Brenner, M. Coury, M. N. Quinn, O. Tresca, B. Zielbauer, B. Aurand, V. Bagnoud, et al. Surface transport of energetic electrons in intense picosecond laser-foil interactions. *Applied Physics Letters*, 99(17):171502, 2011.

[273] Q. Kong, S. Miyazaki, S. Kawata, K. Miyauchi, K. Nakajima, S. Masuda, N. Miyanaga, and Y. K. Ho. Electron bunch acceleration and trapping by the ponderomotive force of an intense short-pulse laser. *Physics of Plasmas*, 10(12):4605–4608, 2003.

[274] H. S. Ghotra and N. Kant. TEM modes influenced electron acceleration by Hermite-Gaussian laser beam in plasma. *Laser and Particle Beams*, 34(3):385–393, 2016.

[275] A. Macchi, M. Borghesi, and M. Passoni. Ion acceleration by superintense laser-plasma interaction. *Reviews of Modern Physics*, 85(2):751, 2013.

[276] B. M. Hegelich, B. J. Albright, J. Cobble, K. Flippo, S. Letzring, M. Paffett, H. Ruhl, J. Schreiber, R. K. Schulze, and J. C. Fernandez. Laser acceleration of quasi-monoenergetic MeV ion beams. *Nature*, 439(7075):441, 2006.

[277] S. M. Weng, M. Liu, Z. M. Sheng, M. Murakami, M. Chen, L. L. Yu, and J. Zhang. Dense blocks of energetic ions driven by multi-petawatt lasers. *Scientific Reports*, 6:22150, 2016.

[278] A. Pukhov. Strong field interaction of laser radiation. *Reports on Progress in Physics*, 66(1):47, 2002.

[279] A. Macchi. Theory of light sail acceleration by intense lasers: An overview. *High Power Laser Science and Engineering*, 2, 2014.

[280] J. G. Kirk, A. R. Bell, and C. P. Ridgers. Pair plasma cushions in the hole-boring scenario. *Plasma Physics and Controlled Fusion*, 55(9):095016, 2013.

[281] C. S. Brady, C. P. Ridgers, T. D. Arber, A. R. Bell, and J. G. Kirk. Laser absorption in relativistically underdense plasmas by synchrotron radiation. *Physical Review Letters*, 109(24):245006, 2012.

[282] T. V. Liseykina, S. V. Popruzhenko, and A. Macchi. Inverse Faraday effect driven by radiation friction. *New Journal of Physics*, 18(7):072001, 2016.

[283] M. Chen, A. Pukhov, T. P. Yu, and Z. M. Sheng. Radiation reaction effects on ion acceleration in laser foil interaction. *Plasma Physics and Controlled Fusion*, 53(1):014004, 2010.

[284] M. Tamburini, F. Pegoraro, A. Di Piazza, C. H. Keitel, T. V. Liseykina, and A. Macchi. Radiation reaction effects on electron nonlinear dynamics and ion acceleration in laser–solid interaction. *Nuclear Instruments and Methods in Physics Research Section A: Accelerators, Spectrometers, Detectors and Associated Equipment*, 653(1):181–185, 2011.

[285] M. Tamburini, T. V. Liseykina, F. Pegoraro, and A. Macchi. Radiation-pressure-dominant acceleration: Polarization and radiation reaction effects and energy increase in three-dimensional simulations. *Physical Review E*, 85(1):016407, 2012.

[286] R. Capdessus, E. d'Humieres, and V. T. Tikhonchuk. Influence of ion mass on laser-energy absorption and synchrotron radiation at ultrahigh laser intensities. *Physical Review Letters*, 110(21):215003, 2013.

[287] I. C. E. Turcu, C. Murphy, F. Negoita, D. Stutman, M. Zepf, J. Schreiber, C. Harvey, R. J. Gray, M. Toma, S. Balascuta, et al. High field physics and QED experiments at ELI-NP. *Romanian Reports in Physics*, 68:S145, 2016.

[288] R. Capdessus. *Dynamics of a collisionless plasma interacting with an ultra-intense laser pulse.* Theses, Université Sciences et Technologies - Bordeaux I, November 2013.

[289] S. V. Bulanov, T. Z. Esirkepov, J. Koga, and T. Tajima. Interaction of electromagnetic waves with plasma in the radiation-dominated regime. *Plasma Physics Reports*, 30(3):196–213, 2004.

[290] H. X. Chang, B. Qiao, Z. Xu, X. R. Xu, C. T. Zhou, X. Q. Yan, S. Z. Wu, M. Borghesi, M. Zepf, and X. T. He. Generation of overdense and high-energy electron-positron-pair plasmas by irradiation of a thin foil with two ultraintense lasers. *Physical Review E*, 92(5):053107, 2015.

[291] R. Capdessus, M. King, and P. McKenna. Radiating electron source generation in ultraintense laser-foil interactions. *Physics of Plasmas*, 23(8):083117, 2016.

[292] A. Di Piazza. Nonlinear Breit-Wheeler pair production in a tightly focused laser beam. *Physical Review Letters*, 117(21):213201, 2016.

[293] E. P. Liang, S. C. Wilks, and M. Tabak. Pair production by ultraintense lasers. *Physical Review Letters*, 81(22):4887, 1998.

[294] G. Sarri, W. Schumaker, A. Di Piazza, M. Vargas, B. Dromey, M. E. Dieckmann, V. Chvykov, A. Maksimchuk, V. Yanovsky, Z. H. He, et al. Table-top laser-based source of femtosecond, collimated, ultrarelativistic positron beams. *Physical Review Letters*, 110(25):255002, 2013.

[295] V. Tsytovich and C. B. Wharton. Laboratory electron-positron plasma-a new research object. *Comments on Plasma Physics and Controlled Fusion*, 4(4):91–100, 1978.

[296] C. M. Surko, M. Leventhal, A. Passner, and F. J. Wysocki. A positron plasma in the laboratory-how and why. In *AIP Conference Proceedings*, volume 175, pages 75–90. AIP, 1988.

[297] C. P. Ridgers, C. S. Brady, R. Duclous, J. G. Kirk, K. Bennett, T. D. Arber, A. P. L. Robinson, and A. R. Bell. Dense electron-positron plasmas and ultraintense γ rays from laser-irradiated solids. *Physical Review Letters*, 108(16):165006, 2012.

[298] V. S. Popov. Schwinger mechanism of electron-positron pair production by the field of optical and X-ray lasers in vacuum. *Journal of Experimental and Theoretical Physics Letters*, 74(3):133–138, 2001.

[299] R. Alkofer, M. B. Hecht, C. D. Roberts, S. M. Schmidt, and D. V. Vinnik. Pair creation and an X-ray free electron laser. *Physical Review Letters*, 87(19):193902, 2001.

[300] C. D. Roberts, S. M. Schmidt, and D. V. Vinnik. Quantum effects with an X-ray free-electron laser. *Physical review letters*, 89(15):153901, 2002.

[301] M. Jirka, O. Klimo, M. Vranic, S. Weber, and G. Korn. QED cascade with 10 PW-class lasers. *Scientific Reports*, 7(1):15302, 2017.

[302] S. S. Bulanov. Pair production by a circularly polarized electromagnetic wave in a plasma. *Physical Review E*, 69(3):036408, 2004.

[303] M. Marklund and J. Lundin. Quantum vacuum experiments using high intensity lasers. *The European Physical Journal D*, 55(2):319, 2009.

[304] A. Di Piazza, C. Müller, K. Z. Hatsagortsyan, and C. H. Keitel. Extremely high-intensity laser interactions with fundamental quantum systems. *Reviews of Modern Physics*, 84(3):1177, 2012.

[305] B. King and T. Heinzl. Measuring vacuum polarization with high-power lasers. *High Power Laser Science and Engineering*, 4, 2016.

[306] B. B. Pollock, C. E. Clayton, J. E. Ralph, F. Albert, A. Davidson, L. Divol, C. Filip, S. H. Glenzer, K. Herpoldt, W. Lu, et al. Demonstration of a narrow energy spread 0.5 GeV electron beam from a two-stage laser wakefield accelerator. *Physical Review Letters*, 107(4):045001, 2011.

[307] M. J. Duff, R. Capdessus, C. P. Ridgers, and P. McKenna. Multi-stage scheme for nonlinear Breit–Wheeler pair-production utilising ultra-intense laser-solid interactions. *Plasma Physics and Controlled Fusion*, 61(9):094001, 2019.

[308] D. J. Stark, T. Toncian, and A. V. Arefiev. Enhanced multi-MeV photon emission by a laser-driven electron beam in a self-generated magnetic field. *Physical Review Letters*, 116(18):185003, 2016.

[309] S. Fujioka, Z. Zhang, K. Ishihara, K. Shigemori, Y. Hironaka, T. Johzaki, A. Sunahara, N. Yamamoto, H. Nakashima, T. Watanabe, et al. Kilotesla magnetic field due to a capacitor-coil target driven by high power laser. *Scientific Reports*, 3:1170, 2013.

[310] A. Gopal, M. Tatarakis, F. N. Beg, E. L. Clark, A. E. Dangor, R. G. Evans, P. A. Norreys, M. S. Wei, M. Zepf, and K. Krushelnick. Temporally and spatially resolved measurements of multi-megagauss magnetic fields in high intensity laser-produced plasmas. *Physics of Plasmas*, 15(12):122701, 2008.

[311] R. J. Mason and M. Tabak. Magnetic field generation in high-intensity-laser-matter interactions. *Physical Review Letters*, 80(3):524, 1998.

[312] R. N. Sudan. Mechanism for the generation of 10. 9 G magnetic fields in the interaction of ultraintense short laser pulse with an overdense plasma target. *Physical Review Letters*, 70(20):3075, 1993.

[313] L. D. Landau, E. M. Lifshitz, and L. P. Pitaevskij. *Course of theoretical physics. Vol. 10: Physical Kinetics.* Oxford, 1981.

[314] S. S. Bulanov, T. Z. Esirkepov, A. G. R. Thomas, J. G. Koga, and S. V. Bulanov. Schwinger limit attainability with extreme power lasers. *Physical Review Letters*, 105(22):220407, 2010.

[315] A. Gonoskov, A. Bashinov, S. Bastrakov, E. Efimenko, A. Ilderton, A. Kim, M. Marklund, I. Meyerov, A. Muraviev, and A. Sergeev. Ultrabright GeV photon source via controlled electromagnetic cascades in laser-dipole waves. *Physical Review X*, 7(4):041003, 2017.

[316] H. Hu, C. Müller, and C. H. Keitel. Complete QED theory of multiphoton trident pair production in strong laser fields. *Physical Review Letters*, 105(8):080401, 2010.

[317] D. Tong. Classical dynamics. *Wilberforce Road*, 2005.